

On the excess velocity of Taylor-droplets in square microchannels

Vom Fachbereich Produktionstechnik

der

UNIVERSITÄT BREMEN

zur Erlangung des Grades
Doktor-Ingenieur
genehmigte

Dissertation

von

Thorben Helmers, M.Sc.

Gutachter:

Prof. Dr.-Ing. Jorg Thöming

Fachgebiet Chemische Verfahrenstechnik, UFT, Universität Bremen

Prof. Dr.-Ing. habil. Michael Dreyer

AG Mehrphasenströmungen, Fachgebiet Strömungsmechanik, Universität Bremen

Tag der mündlichen Prüfung: 14.10.2019



Thorben Helmers, M.Sc.

On the excess velocity of Taylor-droplets in square microchannels

Dissertationsschrift

Gutachter: Prof. Dr.-Ing. Jorg Thöming und Prof. Dr.-Ing. habil. Michael Dreyer

Universität Bremen

*Fachgebiet Umweltverfahrenstechnik (UVT) in enger Kooperation mit dem
Fachgebiet Chemische Verfahrenstechnik (CVT)*

Zentrum für Umweltforschung und nachhaltige Technologien (UFT)

Fachbereich Produktionstechnik

Leobener Str. 6

28359 Bremen, Germany

Abstract

This thesis deals with the movement of Taylor-droplets in microscopic multiphase flows. Taylor-droplets are small compartments of a disperse phase in a confined geometry (e.g., capillary or microchannel) that are separated from the wall by a thin wall film. Due to the strict confinement on the small length scales, they allow a fluid mechanic to examine highly complex conditions in a very controlled environment. The success of microfluidic approaches is based on their ability to open new process windows and the miniaturization is accompanied by higher selection rates as well as improved inherent security. This is possible since microfluidic approaches offer high transport gradients based on the short diffusion lengths and achieve enhanced heat- and mass-transfer, narrow residence time distribution and high surface to volume ratio. However, microfluidic approaches use a numbering-up approach. Thus, exact knowledge of the residence time and pressure drop is crucial for stable reactor operations. Unfortunately, no comprehensive description of the instantaneous droplet velocity is available.

This thesis reports a phenomenological model to improve the description of the instantaneous droplet velocity. The chosen approach should be seen as a holistic-hybrid between measurement methodology, high-speed image averaging and semi-analytic greybox modeling. It can be used to better determine the residence time or improve models for the pressure drop or mass-transfer. Furthermore, for the first time the influential parameters on the excess velocity (the deviation of the droplet velocity from the calculation of superficial velocity) are described for squared microchannels. To fulfill this task, four research aims are defined and successfully accomplished.

Different valuable benefits arose on this journey besides the final model: A novel non-invasive and cost-efficient measurement device based on near-infrared (NIR) photometry is developed and successfully tested, the flow-induced Taylor-droplet cap deformation is effectively correlated to the Ca -number and genetic algorithms are successfully adapted for model adjustment. Model validation drives the development of a novel refractive index matching (RIM) approach, providing two degrees of freedom. After determination of all necessary material parameters, a proof of principle is given. The phenomenology of the model is subsequently validated using carefully performed 3D2C μ PIV measurements. For this purpose, ensemble-image-averaging and ensemble-correlation methods were used. The benefits arising from this work can be utilized by other researchers, e.g. to improve existing models or gain better process knowledge.

Zusammenfassung

Diese Dissertationsschrift befasst sich mit der Bewegung von Taylor-Tropfen in Mikromehrphasenströmungen. Taylor-Tropfen sind eng abgegrenzte Anteile einer dispersen Phase, die sich in einer definierten Geometrie (Mikrokapillare oder Mikrokanäle) bewegen und durch einen Film der kontinuierlichen Phase von den Kanalwänden getrennt sind. Aufgrund der genauen geometrischen Definiertheit und der kleinen Längenskalen ist es Fluidmechanikern/innen möglich auch hochkomplexe Bedingungen in einer genau definierten Umgebung zu untersuchen. Der Erfolg mikrofluidischer Anwendungen basiert auf der Möglichkeit neue Prozessfenster zu schaffen, da mit den Miniaturisierungsprozessen verbesserte chemische Selektivitäten und eine verbesserte inhärente Sicherheit einhergehen. Mikrofluidische Ansätze bieten hohe Transportkoeffizienten, die auf den vorherrschenden kurzen Diffusionslängen basieren, und erreichen dadurch guten Stoff- und Wärmetransport, enge Verweilzeitverteilung und eine hohe spezifische Oberfläche. Da mikrofluidische Ansätze einen Numbering-Up-Ansatz verwenden, ist genaue Kenntnis über die Verweilzeit und den Druckverlust von Einzelreaktoren von Bedeutung.

Die vorliegende Arbeit entwickelt ein phänomenologisches Modell zur Abschätzung der unmittelbaren Tropfengeschwindigkeit. Der gewählte Modellierungsansatz kann dabei als ganzheitliches Hybrid zwischen Messmethodenentwicklung und semi-analytischem Greybox-Modeling gesehen werden. Er kann durch die Abschätzung der Tropfengeschwindigkeit eine genauere Bestimmung der Verweilzeit ermöglichen oder zur Verbesserung verfügbarer Modellsätze zur Beschreibung des Druckverlustes oder des Stofftransports beitragen. Im Rahmen der Modellierung wurden erstmals die Einflussgrößen auf die Tropfen-Exzessgeschwindigkeit (Differenz der Tropfen- und Leerrohrgeschwindigkeit) identifiziert. Zur Erfüllung dieser Aufgabe wurden vier Forschungsziele definiert und erfolgreich bearbeitet.

Neben dem endgültigen Modell ergeben sich auf diesem Weg verschiedene wertvolle Vorteile: Ein neuartiger, nichtinvasiver und kosteneffizienter, auf Nahinfrarot(NIR)-Photometrie basierender, Sensor wird entwickelt, ein erster Prototyp gefertigt und erfolgreich getestet. Die strömungsinduzierte Kappendeformation von Taylor-Tropfen wird erfolgreich mit der Ca -Zahl korreliert und Genetische Algorithmen werden zur Anpassung des Modells verwendet. Zur Validierung der Modellphänomenologie wird ein neuartiger Brechungsindexanpassungsalgorithmus entwickelt, der zwei Freiheitsgrade zulässt. Dieser wird nach umfangreicher messtechnischer Charakterisierung der zugrundeliegenden Stoffsysteme erfolgreich einem Proof of Principle unterzogen. Die Phänomenologie des Modells wird anschließend anhand sorgfältig durchgeführter 3D2C μ PIV-Messungen validiert. Zu diesem Zweck werden auch ensemble-averaging Methoden eingesetzt.

Die Ergebnisse, die sich aus dieser Arbeit ergeben, können von anderen Forschern genutzt werden, um beispielsweise bestehende Modelle zu verbessern oder eine vertiefte Prozesskenntnis zu erlangen.

Danksagung

Die vorliegende Dissertation entstand während meiner Tätigkeit als wissenschaftlicher Mitarbeiter am Institut für Umweltverfahrenstechnik (IUV) und dem Fachgebiet Umweltverfahrenstechnik (UVT) des Fachbereichs 4 Produktionstechnik der Universität Bremen.

Mein besonderer Dank gilt meinem Doktorvater Herrn Prof. Dr.-Ing. Jorg Thöming, der mich in einer schweren und unsicheren Zeit des Umbruchs als Doktorand angenommen und mir die Möglichkeit gegeben hat dieses Thema zu bearbeiten. Für die umfassende Betreuung, die Bestärkung mein Promotionsvorhaben trotz der herausfordernden Rahmenbedingungen erfolgreich abzuschließen und die kostbaren Erfahrungen, die ich in meiner Promotionszeit sammeln konnte, bin ich sehr dankbar.

Bei Herrn Prof. Dr.-Ing. habil. Michael Dreyer möchte ich mich für die Übernahme des Korreferats und die wissenschaftliche Unterstützung, die ich in vielen Gesprächen erfahren durfte, bedanken. Die Vorgehensweisen und systematischen Ansätze, die ich bei der Unterstützung der Lehre zur Stoffübertragung sammeln konnte, haben mir ein festes Gerüst zum Anfertigen dieser Arbeit gegeben.

Herrn Prof. Dr.-Ing. habil. Sven Kerzenmacher möchte ich für die Förderung meines Promotionsvorhabens seit Übernahme des Fachgebiets danken. Ohne seine Unterstützung hätte die Arbeit in dieser Form nicht entstehen können.

Herrn Dipl.-Ing. Ulrich Mießner danke ich für die unzählbaren Stunden des wissenschaftlichen Diskurses, in denen die Ergebnisse dieser Arbeit gereift sind. In ihm habe ich einen großartigen Mentor gefunden, der mir nicht nur die Mikrofluidik nahebrachte und es mir ermöglichte mich bis zur Promotion zu vertiefen, sondern es auch immer schaffte mich wieder aufzubauen. Ohne ihn wäre diese Arbeit nicht denkbar gewesen.

Herrn Philip Kemper, M.Sc. danke ich für die großartige und tolle Zusammenarbeit während meiner Promotionszeit. Seine zahlreichen Verbesserungsvorschläge haben meine wissenschaftliche Arbeit und diese Dissertationsschrift sehr vorangebracht. Ebenso danke ich Herrn Dipl.-Ing. Johannes Erben, der mich durch sein wertvolles Lektorat sehr unterstützt hat. Herrn Dipl.-Ing. Ralf Nieswandt danke ich für die umfassende Unterstützung bei den zahlreichen Reparaturen der in die Jahre gekommenen Messtechnik und die viele Ratschläge in elektrotechnischen Fragestellungen.

Besonders danken möchte ich auch Herrn Dr.-Ing. Stefan Hubert. Ohne die vielen Gespräche und langen Büroabende im Rahmen unseres gemeinsamen ersten Forschungsprojektes als

junge Promovenden wären insbesondere die metaheuristischen und statistischen Ansätze dieser Arbeit - und damit das präsentierte Modell - so nicht zustande gekommen.

Abschließend möchte ich mich bei allen Kollegen/innen und Ehemaligen für die gute Zusammenarbeit, die schöne gemeinsame Zeit und die vielen tollen Momente am IUUV und UVT bedanken. Dies gilt auch für die zahlreichen Studenten/innen, die ich im Laufe meiner Promotionszeit betreuen durfte und die mit ihren Arbeiten einen Anteil am Entstehen dieser Dissertation hatten.

List of publications

In the following, the complete list of peer-reviewed publications including contributions of Thorben Helmers can be found. All of them are written during his employment as a PhD student at the University of Bremen before the submission of this thesis:

- U. Mießner, **T. Helmers**, R. Lindken, J. Westerweel. *An analytical interface shape approximation of microscopic Taylor flows*. *Exp Fluids* (2019) 60: 75. doi:10.1007/s00348-019-2719-0
- **T. Helmers**, J. Thöming, U. Mießner. *Retrieving accurate temporal and spatial information about Taylor slug flows from non-invasive NIR photometry measurements*. *Exp Fluids* (2017) 58: 160. doi:10.1007/s00348-017-2441-8
- S. Hubert, **T. Helmers**, F. Groß, A. Delgado: *Data driven stochastic modelling and simulation of cooling demand within breweries*. *Journal of Food Engineering* (2016). doi:10.1016/j.jfoodeng.2015.06.032
- S. Hubert, F. Baur, A. Delgado, **T. Helmers**, N. Rübiger. *Simulation modeling of bottling line water demand levels using reference nets and stochastic models*. *Proceedings of SC '15 Winter Simulation Conference* (2015). doi:10.1109/WSC.2015.7408339
- S. Hubert, L. Pettigrew, **T. Helmers**, U. Mießner, F. Groß, N. Rübiger, A. Delgado: *Simulation-based optimisation of wastewater and composition for on-site treatment in the food and beverage industry utilising reference nets in combination with genetic algorithms*. *Proceedings in Applied Mathematics and Mechanics* Vol. 14 (2014), S. 811-812. doi:10.1002/pamm.201410386

Contents

1 Prologue	1
1.1 Introduction	2
1.2 Micro process engineering	3
1.3 Microscopic multiphase flows for heterogeneous catalysis	5
1.4 What to expect from this thesis	6
2 Microscopic Taylor flows: theory and applications	9
2.1 Recent applications in engineering and biosciences	10
2.2 Hydrodynamic fundamentals of microscopic Taylor flows	11
2.3 Microfluidic droplet sensing devices	16
2.4 Micro particle image velocity (μ PIV)	18
2.5 Refractive index matching	21
3 Retrieving accurate temporal and spatial information about Taylor slug flows from non-invasive NIR photometry measurements	23
3.1 Overview	24
3.2 Model development	25
3.2.1 Conceptual approach	25
3.2.2 Geometric properties	26
3.2.3 Transmission signal shape and dI/dx slope derivation	28
3.2.4 Droplet shape estimation	29
3.3 Simulation	30
3.3.1 Fundamentals of raytracing calculation	30
3.3.2 Setup and fluid properties	32
3.3.3 Examination of signal characteristic	33
3.3.4 Evaluation of numerical stability	34
3.4 Sensitivity analysis	35
3.5 Validation	38
3.5.1 Flow dependency of the simulated spatial signal	39
3.5.2 Experimental setup	40
3.5.3 Experimental validation results	41
3.6 Conclusion	44
4 Determining the flow-related cap deformation of Taylor droplets at low Ca-numbers using ensemble averaged high-speed images	47
4.1 Overview	48
4.2 Microfluidic fundamentals	48
4.3 Materials and methods	50
4.3.1 Experimental setup	50

4.3.2	Ternary fluid system for Re and Ca adjustment	51
4.3.3	Ensemble image averaging and curvature detection	52
4.3.4	Determination of droplet velocity	56
4.3.5	Experimental procedure	57
4.4	Results and discussion	58
4.5	Conclusion	63
5	Modeling the excess velocity of low-viscous Taylor droplets in square microchan-	
	nels	65
5.1	Overview	66
5.2	Model development	66
5.2.1	Concept of excess velocity	67
5.2.2	Model specification	71
5.2.3	Model calibration	75
5.2.4	Model validation	79
5.3	Discussion	82
5.4	Conclusion	83
6	Refractive index matching (RIM) using double binary mixtures for Re, Ca and	
	viscosity adjusted μPIV-measurements	85
6.1	Overview and concept	86
6.2	Material and methods	87
6.2.1	Basic mixture compounds	87
6.2.2	Determination of material properties	88
6.2.3	Calculating mass-fractions and the superficial velocity	89
6.3	Experimental results	90
6.3.1	Properties of binary mixtures	90
6.3.2	Properties of RI-matched double-binary mixtures	92
6.4	Discussion	96
6.4.1	Features and limits of the double-binary approach	97
6.4.2	Proof of principle	98
6.5	Conclusion	100
7	Validating the influence of viscous coupling on the excess velocity of Taylor-	
	droplets using μPIV measurements	101
7.1	Overview	101
7.2	Material and methods	102
7.2.1	Experimental setup and material properties	102
7.2.2	Validation of correlation depth and adjustment of ensemble averaging	106
7.2.3	Hydrodynamic determination of channel height	108
7.2.4	Design of experiments	109
7.3	Results and discussion	110
7.3.1	Local flow structure in the gutters of Taylor-droplets	111
7.3.2	Local flow structure of entire Taylor-droplets cross-section	113
7.4	Conclusion	116
8	Conclusion and outlook	117
A	Appendix for Chapter A	121

B Appendix for Chapter 5	123
C Appendix for Chapter 6	125
C.1 Dynamic interfacial tension measurements	125
C.2 Experimental setup for proof of principle	125
D Appendix for Chapter 7	129
D.1 Influence of surfactants on the flow	129
D.2 Validation of μ PIV approach	129
D.3 Supplementary μ PIV measurements	130
E Supervised student works	135
Bibliography	137

Prologue

“ *Science is not abstract but, as a product of human work, also closely linked in its development to the peculiarity and fate of the people who devote themselves to it.*

— **Emil Fischer**
(German chemist)

This thesis deals with the movement of Taylor droplets in microscopic multiphase flows. Taylor droplets are small compartments of a disperse phase in a confined geometry (e.g., capillary or microchannel), that are separated from the wall by a thin wall film. In various fields of classical process engineering, the use of Taylor flows and their special microscopic features to facilitate new process capabilities became important in the recent century. However, the beginning of the microscopic era took place earlier. Inspired by the famous talk "There's Plenty of Room at the Bottom" held by Richard Feynman on 29th December 1959, new ideas awoke to use the specific opportunities of micro- and nanoscale structures to solve macroscale problems. This did not only apply for engineered particles or concepts of micromachines, but also for fluidic flows (Bretherton, 1961). Driven by the general euphoria for nuclear technology after World War II, it is not surprising, that one of the first applications of microscale flows was uranium enrichment (Becker et al., 1979). The new ways of thought pattern paved the way for new manufacturing principles like LIGA (German abbr.: lithography, electroplating and molding) or DRIE (deep reactive-ion etching) which made today's microscopic and lab-on-a-chip approaches possible in the first place.

It is a charm of microfluidic devices that they work without moving parts. All arising flow arrangements are based on self-organization due to the inherent counterplay of forces, transferred mass and energy. In this way, microfluidic approaches stood in contrast to at that time prestigious mass-transfer machines (Mersmann et al., 1986) that represent the opposite extreme of artificially imposed forces. In mass-transfer machines all forces are explicitly exerted to reach the desired hydrodynamics. Albeit having the benefit of high intensity mass- and heat-transfer caused by the active agitation, these advantages are paid by the price of high operational costs and susceptibility to mechanical failures. This might be a reason, why mass-transfer machines, unlike microfluidics, did not find widespread usage today.

In microscopic multiphase flows, liquid-liquid as well as liquid-gas, the strict confinement on the small length scales reduces the problems to its essentials. This allows a fluid mechanist, to examine highly complex conditions in a very controlled environment. Nevertheless, the fundamental interrelation of small droplets exhibits rich and interesting phenomenology. In part of the actual long way from uranium-enrichment to analytic tasks and the productions of fine chemicals, this thesis should serve as a courageous step towards better understanding

of the movement of Taylor droplets in multiphase flows. As the following will show, this enhanced understanding may improve the design and operation of reactors, as well as it makes a valuable contribution to the general understanding of microscopic multiphase flows.

1.1 Introduction

In a modern world with limited resources and a not deniable climate change, modern engineers have to face concerns of sustainability besides the art of engineering. Since it is an aim of mankind to further increase the wealth, this can be done only by process intensification rather than exploiting more and more natural resources. From a process engineer's point of view, especially platform chemicals and daily use goods with a high consumption move into focus due to their large CO₂-footprint. Numerous of these substances are produced in chemical processes utilizing heterogeneous catalysis, where the educts and the catalyst reside in different flow phases, whereby the catalyst often is immobilized at the guiding reactor wall structures. May this range from Fischer-Tropsch-processes for coal liquification and gas-to-liquid application, Haber-Bosch-processes for nitrogen fixation and fertilizer production or various processes of organic synthesis (Kobayashi et al., 2006).

Besides mass-balances of the reactors, the efficiency of the performed processes is significantly influenced by the hydrodynamic and mass-transfer capability of the reactors. This holds especially true for heterogeneous catalysis, since educts and catalysts are in different thermodynamic phases and therefore the behavior of the interfacial surfaces between the flow phases and the mass-transfer through the interfacial surface is important. An optimized counterplay based on precise process knowledge allows to increase the chemical selectivity, save educts and process-energy and finally increase the profit.

Heterogeneous catalysis is often performed in devices that supply a large contact area between the distinct flows phases and the catalysts. The design of reactors ranges from classical bubble-columns, over falling film reactors to high complex structures like monolithic reactors. The decision of which reactor to utilize for operation is mostly based on the boundary conditions of the chemical processes (reaction kinetics, flow properties and reaction heat). Therefore especially monolith based reactors (e.g., exhaust gas cleaning Fig. 1.1) are state of the art, since they provide a high surface to volume ratio, a good process heat conduction and an eminent mechanical stability, which allows to operate them with gas-liquid and liquid-liquid multiphase flows (Schäfer et al., 2016).

For the time after World War II, especially in the 70s an 80s, numerous studies and large research efforts have been dedicated to understand the formation and movement of disperse phase in two-phase flow systems. Beginning on the topics of single droplet formation and single droplet movement, the research moved further on to the field of swarm turbulence. Additionally, considering at first only hydrodynamic and mass-transfer issues, today superimposed chemical reactions are actual research topics as special research programs (SPP) by the German Research Foundation (DFG) show. It is interesting to notice, that today's research efforts again utilize the defined compartment of single bubbles to gain knowledge of the underlying coupling between local hydrodynamic, mass-transfer and chemical reaction.

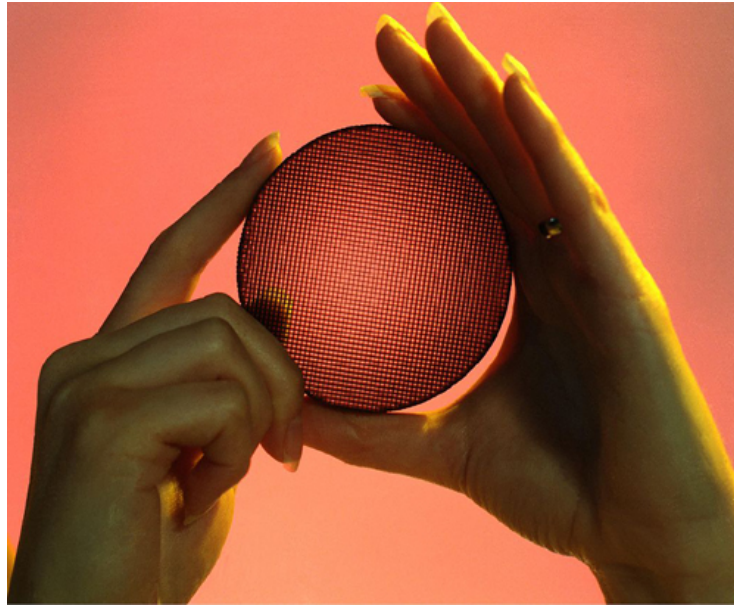


Fig. 1.1.: Low temperature oxidation catalyst developed by NASA. *Image under public domain by Lineberry (2013)*

Therefore it is not surprising that from this unique combination of narrow restricted boundary framework and excellent possibilities, the evolution from microscopic multiphase flows to the novel field of micro process engineering originated. Today, micro process engineering offers a well-developed toolbox to precisely define driving forces such as pressure, temperature and concentration gradients and their resulting transfer rates. The corresponding reaction rates can result in new process windows and often lead to increased selectivity and yield which delivers significant process intensification (Ehrfeld et al., 2004; Seeberger and Blume, 2007).

1.2 Micro process engineering

Starting in first measurements of droplets in round capillaries (Bretherton, 1961) arising from the question, why bubbles move with a different velocity than the calculated superficial velocity, the attention fastly turned to the specific flow phenomena on the micro scale (films, concentration boundary layer, bubble wake). Although the consideration of this microscopic length-scale has been of interest in fluid-dynamics for a long time, e.g. for the examination of turbulence (Kolmogorov microscales) or modeling purpose (laminar boundary layer), the orderly conditions in the well defined microscopic region and their counterplay with the flow are still suspect of hydrodynamic studies (Kastens et al., 2015; Kastens et al., 2017; Schurr et al., 2017).

In the years of the turn of the millennium, different chemical companies discovered the powerful capabilities of microscopic flows and developed a product portfolio. The success of microfluidic approaches is based on their ability to open new process windows and, because the miniaturization is accompanied by higher selection rates as well, improved inherent security. This is possible since microfluidic approaches offer high transport gradients

based on the short diffusion lengths and achieve enhanced heat- and mass-transfer, narrow residence time distribution and high surface to volume ratio.

Especially the possibility to perform reactions and processes with high selectivity and improved product purity, is useful for the production of pharmaceuticals or fine chemicals with high retail prices for limited quantities. In contrast to classical processes, microfluidic solutions usually rely on numbering up instead of a scale up, to keep surface and flow well defined. To reach the desired yield, a number of microfluidic devices can be used in parallel: the idea of a modular micro-factory was born. Examples for these commercial approaches were introduced by *Ehrfeld Mikrotechnik BTS* or by *BASF*. These modular micro-plants provide a versatile toolbox of possibilities, ranging from mixing, separation to extraction. Applications are typically realized in devices with a well-defined structure and geometry (so-called microreactors or microchannels). A big advantage lies in the expandability and modularity of these approaches.

Such a modular approach for the generation of specific engineered microparticles is shown in Fig. 1.2 a) , a micro-factory for educational purpose in b):

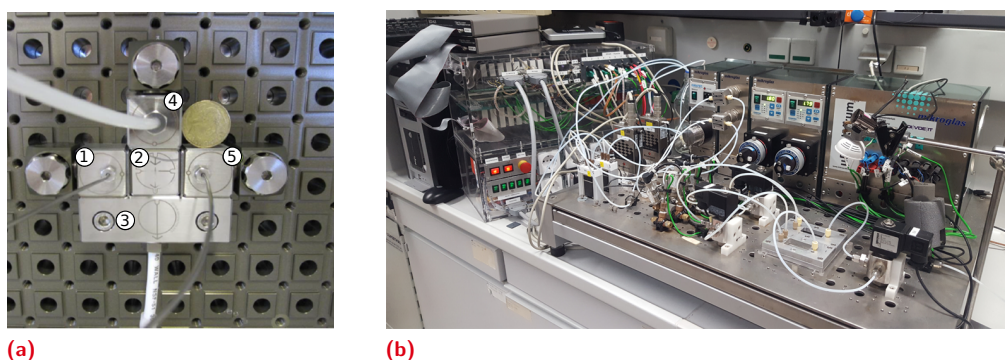


Fig. 1.2.: Different microfluidical approaches for microparticles based production of catalysts. a) modular "MikroJet"-reactor from *Ehrfeld Mikrotechnik BTS* with gas-supply (4), feed (1+5) and outlet (3), b) microplant "BMBF μ Pr@tikum" for educational purpose, characterization of mixing efficiency and catalyst production utilizing two parallel micromixers, micro-gearpumps, clean-in-process and full online process control

After this first generation, a microfluidic renaissance appeared within the last 10 years and microfluidic multiphase flows found a large number of applications mainly in form of chemical like biological analytical applications or utilization of the microfluidic mechanisms for new specific unit operations (Lau, 2015). Furthermore, the public perception has switched to lab-on-a-chip devices and modular microchannel-platforms mostly by university spin-offs (*Little Things Factory GmbH* or *micronit microfluidic*). After all, a modification and adaptation of large scale procedures to novel microfluidic processes, that cannot be optimally applied in meso- or large scale reactors, took place. An overview of this recent second generation applications is given in Sec. 2.1.

1.3 Microscopic multiphase flows for heterogeneous catalysis

In contrast to large scale multiphase flows, the behavior of microscopic flows is more predictable as there are no complex interactions such as swarm turbulence (Kück et al., 2018; Mießner et al., 2017) commonly found in large scale multiphase flows. Additionally, the reproducibility of e.g. droplet-based Taylor flows is a key for the application of microscopic multiphase flows (Kreutzer et al., 2005c). Nevertheless, a good understanding of the underlying hydrodynamics is crucial for a reliable reactor-design and stable operations, making hydrodynamic measurements important.

For this kind of experimental flow analysis, a large selection of possible microreactors, microchannels and materials are available. These range from photo-etched COTS (commercial off-the-shelf) reactors (Fig. 1.3 a)) to tailor-made DRIE-etched reactors made of silicon (Fig. 1.3 b)) as they are used in this thesis.

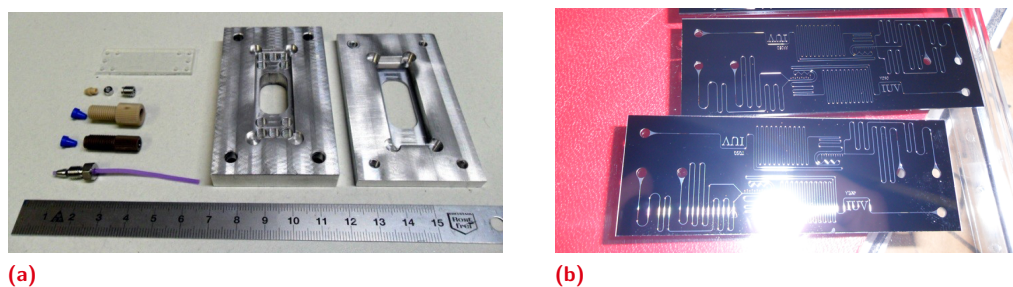


Fig. 1.3.: Labscale microreactors for fluidic measurements. a) COTS photo-structured glass microreactor from *micronit* with common fittings and reactor holder, b) tailor-made DRIE-etched silicon microreactors with high-complex multi-purpose layout

Chemical reactions utilizing heterogeneous catalysis are often performed in monolith reactors as a support for the solid catalyst. In these reactors, a high number of parallelized channels with hexagonal or square channel cross-sections offer a high specific reaction area for wall fixated catalysts of small thickness. This results in a better heat transfer through the walls and better mechanical stability than circular capillaries (Gascon et al., 2015). For process control and stabilization, as well as precise reactor design, knowledge of the underlying fluidic terms is crucial. The high grade of parallelity complicates the prediction of the hydrodynamics and the resulting pressure drop (Kreutzer et al., 2005d; Huerre et al., 2014).

The educts and products of various reactions reside in different hydrodynamic phases, such that a multiphase flow establishes in these reactors. Often these reactors are operated in the Taylor flow regime, which is explained in detail in Sec. 2. Taylor flows typically require a precise control of flow and droplet characteristics to ensure their specific capabilities regarding short diffusion lengths and ensuring a high energy- and mass-transfer. Throughout the entire process, appropriate measurement concepts are necessary to keep the flow conditions inside the desired operational window. Furthermore, the temporal stability of a generated Taylor slug flow is an important parameter to ensure constant reaction rates and sufficient reaction selectivity due to steady gradients and interfacial areas for heat- and

mass-transfer. Since microfluidic process plants are commonly based on a numbering up approach, continuous process control is crucial to guarantee an efficient production in all modular devices (Antweiler et al., 2015). As measurements in pilot-scale monolith-reactors show, an important first step towards process intensification is to feed all reaction tubes equally. This requires a good understanding of the underlying hydrodynamics and derived quantities, e.g. pressure drop, droplet velocity or droplet residence time. This thesis reports a phenomenological model to improve the description of the instantaneous droplet velocity. It can be used to better determine the residence time or improve models for the pressure drop or mass-transfer.

1.4 What to expect from this thesis

This thesis features the holistic development of a semi-analytic fluidic model. The chosen approach should be seen as a holistic-hybrid between measurement methodology, high-speed image averaging and semi-analytic greybox modeling. The new and fascinating topic of metaheuristic approaches and machine learning will be used for this, as well as state-of-the-art measurement techniques like micro particle image velocimetry (μ PIV).

The main aim of this thesis is the development of a phenomenological model to predict the excess velocity (relative velocity difference between the instantaneous droplet velocity and the superficial velocity) of low-viscous Taylor droplets in rectangular microchannels at moderate Ca -numbers. The development of this kind of model is challenging, since comprehensive analytical and deterministic descriptions of the excess velocity in non-circular microchannels have not been reported yet and existing models for circular capillary (Bretherton, 1961) cannot be transferred to rectangular microchannels. Furthermore, the influences acting on droplets and therefore changes in the excess velocity up to 30 % (Fuerstman et al., 2007) are often interpreted as statistic fluctuation and not systematic behavior (Beer et al., 2009; Korczyk et al., 2011; Peng et al., 2015; Zeng et al., 2015a). Additionally, non-invasive and cost-efficient measurement techniques, that allow a more in-depth observation of the Taylor-flow fluctuation behavior for frequency analysis over a necessarily longer time period, are not available at the time of publication.

The aim of this work is **(I)** to introduce a non-invasive measurement technique, that is capable of performing long-term measurements in microscopic Taylor-flows and define the influences on the instantaneous droplet velocity; **(II)** to quantify and correlate this influences, that could serve as a force indicator, based on dimensionless quantities; **(III)** to generate a semi-analytic (greybox) model to phenomenologically describe the excess velocity based on a priori known extrinsic parameters and **(IV)** to introduce a refractive index matching approach that allows to establish Taylor-flows at the identified dimensionless parameters to resolve the local flow field in and around the droplet at characteristic points to validate the phenomenology of the model. The urgency for applicable modeling approaches shows in a most recent publication, that was published shortly before the finalization of this thesis (Rao and Wong, 2018).

The structure of this thesis orientates on the basic model concept from Hangos and Cameron (2001). The essential steps of modeling have been sequentially divided into five thesis-

chapters. The link between the research aims and corresponding chapters is given in Fig. 1.4:

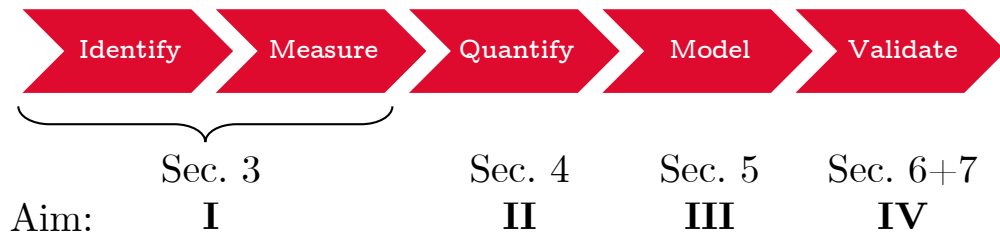


Fig. 1.4.: Steps for model development and corresponding sections of this thesis

At first relevant and the excess velocity influencing flow properties are identified. A novel, non-invasive measurement device based on near infrared photometry is developed and an emitter detector array is simulated to study the correlation between sensor signal and flow state. A first prototype was successfully built and validated (Sec. 3). The identified parameters (Ca, Re) are then quantified via high-speed images developing an image averaging approach to overcome optical restrictions (Sec. 4). A model containing these parameters is introduced and validated with literature data. Measurements were carried out by the developed NIR-sensor and additional high-speed camera measurements are performed (Sec. 5). The phenomenology of the model is validated at local particle-based measurements using 3D2C μ PIV-measurements, applying a novel refractive index matching (RIM) double-binary mixture system, which is introduced and validated (Sec. 6 and 7).

The storyline of this thesis orientates closely on the research articles published by the author. Thus, the chapters report in a dedicated manner on different aspects of the global model development. The author favored and explicitly chose this structure, as it allows to break down the ambitious model-assignment into well-defined work packages. At first, an overview over the state of science is given and the fundamental methods and materials are explained, while modifications of the methods or new approaches that originate from the scientific efforts of this work are addressed in the following chapters. The work closes with a chapter-crossing conclusion and outlook.

Microscopic Taylor flows: theory and applications

“ *If I have seen further it is by standing on the shoulders of giants.* ”

— Isaac Newton

(English physicist and mathematician)

Numerous benefits and applications arise from the confined hydrodynamics of microscopic Taylor flows. Although this seems to imply the simplicity of the theoretical description of Taylor flows, this most fundamental representation of an oriented two-phase flow allows to discover highly complex hydrodynamic interrelations. The well defined boundary conditions allow to focus on the inherent scope of local flow phenomena, that are difficult to describe in macroscopic flows because of masking superimposed phenomena.

In the Taylor flow regime, the disperse phase is separated from the wall by a thin film of the continuous phase and does not fill the entire cross-section of the microchannel. The remaining space between the droplet interface and the microchannel corners is occupied by the continuous phase, which is referred to as gutters (van Steijn et al., 2008). The droplets are typically longer than the channel diameter, which leads to separated elongated disperse phase instances. The continuous phase segments between the droplets are called slugs. The droplets of Taylor flows act as stirred batch microreactors, and the slugs provide good mixing and mass-transfer to the channel walls.

This combination of well mixed slugs, thin wall films with high concentration gradients, inner droplet circulation and the confinement of the different droplets, renders microscopic Taylor flows an excellent possibility to observe a variety of interesting flow phenomena and utilizes them for various explanatory approaches. A rising number of publications confirms the scientific interest in microfluidic multi-phase flows (Chou et al., 2015)

In this chapter the fluidic fundamentals, most important terms and dimensionless quantities are presented. A dedicated scientific examination utilizing these values, is done in the corresponding chapters.

2.1 Recent applications in engineering and biosciences

Already towards the end of the first decade of the 2000s, the versatile possibilities of microfluidic approaches have been recognized (Ehrfeld et al., 2004; Seeberger and Blume, 2007; Angeli and Gavriilidis, 2008; Dietrich, 2009; Huebner et al., 2008). Microscopic multiphase flows facilitate a wide field of possible applications since they provide short diffusion layers in the flow structures. For several applications and improved unit operations, examples range from general chemical reactions (Song et al., 2006) to chemically catalyzed processes transferred from macro- to microscale like fluorination (Chambers et al., 2003; Lang et al., 2012), heterogeneous or multiphase catalysis (Kobayashi et al., 2006; Tanimu et al., 2017; Rossetti, 2018), photo-catalysis (Yusuf et al., 2018) to syngas production (Chen et al., 2018), extraction (Kralj et al., 2007), to mixing tasks (Wong et al., 2004) or the usage of reactions in monolith reactors (Kreutzer et al., 2005a).

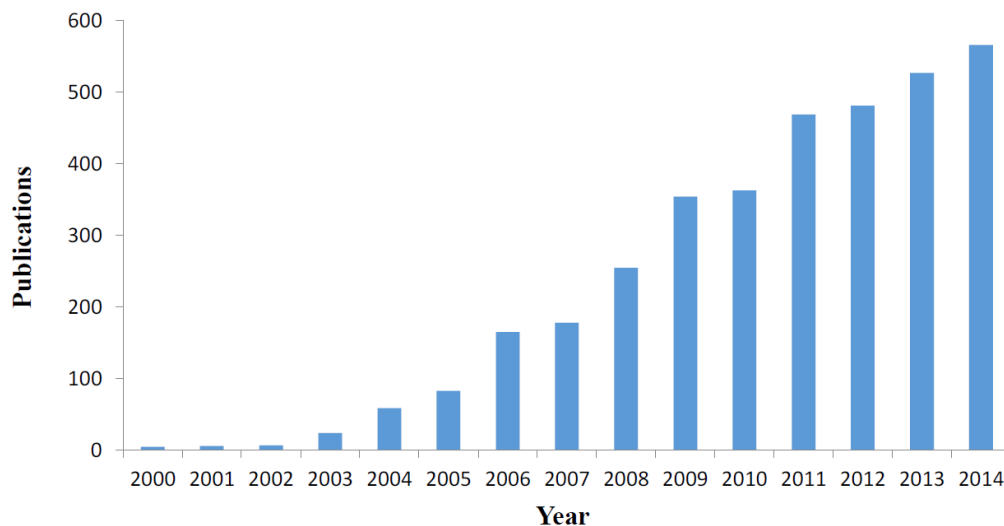


Fig. 2.1.: Number of publications on droplet microfluidics in the past 15 years. *Reprint from Chou et al. (2015) under the Creative Commons Attribution License (CC BY 4.0)*

The great interest in liquid-liquid multiphase flows also held on in recent years (Zhao and Middelberg, 2011; Chou et al., 2015; Shi et al., 2019), showing in an increasing number of publications (Fig. 2.1). This may be caused by the fact, that the process driving forces such as pressure, temperature and concentration gradients and their resulting improved heat- and mass-transfer rates can be precisely adjusted (Haase et al., 2016; Sattari-Najafabadi et al., 2018). The corresponding reaction rates can result in new process windows and often lead to an increased selectivity and yield, which delivers significant process intensification. This could mean fewer hazards or higher selectivity (Sun et al., 2016) or sustainable operation modes close to the optimal working point (Magnaudet and Eames, 2000; Ern et al., 2012).

Especially droplet based microfluidics is utilized since the 2010s for analytic approaches since the well defined and allegedly easy-to-control flow structures allow to adjust droplet formation frequency and other droplet properties (Ward et al., 2005; Cubaud and Mason,

2008; Prileszky et al., 2016; Cao et al., 2018). Most prominent examples are found in genetic analysis (Hosokawa et al., 2017) or cell isolation techniques (Chen et al., 2014). Furthermore, microscopic Taylor flows serve as cell carriers for biological analysis (Clausell-Tormos et al., 2008; Mazutis et al., 2013; Chou et al., 2015; Wolf et al., 2015) and pharmaceutical applications (Kang et al., 2014; Piao et al., 2015). But also for other chemical analytical tasks like precise handling of small sample volumes (Garstecki et al., 2006b; Whitesides, 2006), high-speed processing without cross-contamination (Seemann et al., 2011) or reaction screening in a droplet chain (Jin et al., 2018), they are utilized.

The large specific surface area in combination with the small boundary layers and droplets acting as confined reaction chambers, enable more selective chemical reactions (Ahmed et al., 2018; Scheler et al., 2018) or improved catalytic processes (Abiev and Lavretsov, 2012; Abiev, 2013). Microscopic flows furthermore find use in thermal applications (Leung et al., 2010; Magnini et al., 2013). CFD-calculations enable relatively easy access to the parameterization of liquid-liquid Taylor flows (Rocha et al., 2017)

2.2 Hydrodynamic fundamentals of microscopic Taylor flows

At first glance, microscopic Taylor flows appear to be a defined multi-phase flow form. Despite being seen as a solely academic object of investigation, new challenges arose in combination with novel reactor designs: let it be to describe the rise of steam bubbles in cooling water in confined tubes (Yan et al., 2014) or the usability in heterogeneous catalysis in monolith reactors (Kreutzer et al., 2005c).

The representation of the two-phase flow was at first mainly based on the volumetric flow rate ratio of the continuous and disperse phase among other influential parameters (Fig. 2.2). With increasing ratio of the gaseous phase (Fig. 2.2 a) - d), the gaseous disperse phase becomes more prominent and the two-phase flow transitions from bubble-swarm like behavior (a) + b)) to a more orderly flow (c) + d)).

The volume flow rate ratio α compares the different feed volume flows (Q_d for the disperse phase and Q_c for the continuous phase) and is therefore related to the void fraction ε_d , which is often utilized to describe macro-scale multiphase flows:

$$\alpha = \frac{Q_d}{Q_c} = \frac{\varepsilon_d}{(1 - \varepsilon_d)} \quad (2.1)$$

If elevated void fractions of the disperse phase are reached, the orderly flow structures change towards co-flowing structures (like a falling film, Fig. 2.2 g) + h)). This work focuses on the Taylor flow regime, that is shown in Fig. 2.2 c) + d). In contrast to this work, the depicted flows are driven by buoyancy. Thus, the behavior of rising bubbles or droplets can be described with the Morton number Mo . Please note that in this work the dimensionless

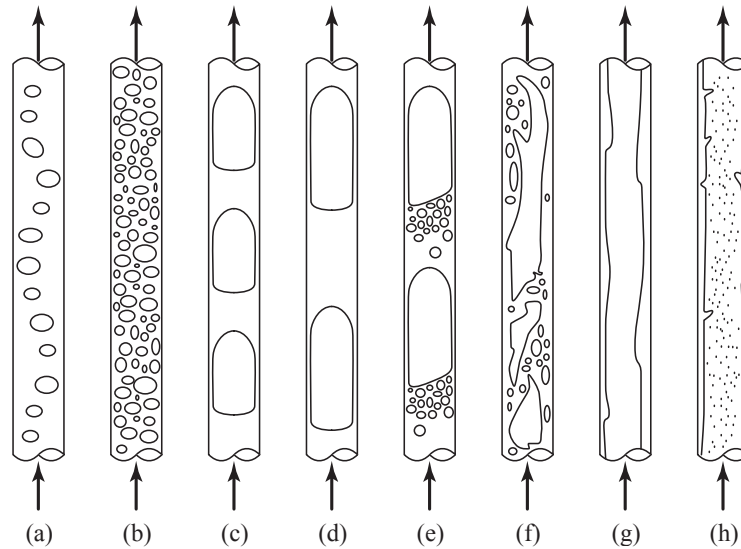


Fig. 2.2.: Sketch of observed flow patterns in capillary channels. (a,b): bubbly flow, (c,d) segmented flow (a.k.a. bubble train flow, Taylor flow, capillary slug flow), (e) transitional slug/churn flow, (f) churn flow, (g) film flow (downflow only), (h) annular flow. Reprinted from *Chemical Engineering Science* 60, Michiel T. Kreutzer, Freek Kapteijn, Jacob A. Moulijn, Johan J. Heiszwolf, *Multiphase monolith reactors: Chemical reaction engineering of segmented flow in microchannels*, 5895-5916, (2005) with permission from Elsevier.

quantities are based on the material parameters of the continuous phase, since it provides the wall contact and drives the disperse phase flow.

$$Mo = Bo \cdot Oh^2 \quad (2.2)$$

The Mo -number combines two dimensionless quantities. The Bond number Bo describes the ratio of buoyancy and interfacial tension forces

$$Bo = \frac{\Delta\rho g d^2}{\sigma} \quad (2.3)$$

with the density difference between both phases $\Delta\rho$, the gravitational acceleration g , a characteristic length d and the interfacial tension σ .

The Ohnesorge number Oh connects the viscous forces, inertia forces and surface tension forces (Ohnesorge, 1936) and originally provides mainly information regarding the material properties of the disperse phase flow system and droplets being dispersed. It can also be interpreted as a description of the viscosity influence on the deformation of droplets and can be used as a material classification when working with surfactants to manipulate flow properties. In case of this thesis, the Oh -number is utilized to characterize the dominant bulk phase material properties independent of the flow-related kinetic forces:

$$Oh = \frac{\eta_c}{\sqrt{H\rho_c\sigma}} = \sqrt{\frac{Ca}{Re}} \quad (2.4)$$

This definition reveals the influence of two additional dimensionless quantities, which are considered later in this section. In microchannels with a microscale cross-section, the Bo -number reaches only small values, since the channel diameter as the characteristic length influences Bo quadratically. As one can see in Eq. 2.2, in microfluidic applications Oh is the main influential parameter on Mo .

In other words: microscopic multiphase flows are mainly influenced by interfacial and viscous forces rather than by buoyancy and inertia forces due to the small size of the droplets and channel structures. The capillary number Ca describes the ratio between viscous and interfacial forces and determines the flow regime of the microscopic two-phase flow. Most prominently, the capillary number can be used to describe changes in the droplet shape (Taha and Cui, 2006; Mießner et al., 2019)

$$Ca = \frac{u_0 \eta_c}{\sigma} \quad (2.5)$$

Herein, η_c denotes the dynamic viscosity of the continuous phase, σ the interfacial tension between the bulk and the droplet phase and u_0 the superficial velocity of the entire flow. The latter can be expressed as

$$u_0 = \frac{Q_{tot}}{A_{ch}} = \frac{Q_d + Q_c}{W \cdot H} = \frac{Q_d + Q_c}{H^2 \cdot ar} \quad (2.6)$$

with Q_{tot} being the total volume flow summing up the disperse (Q_d) and continuous (Q_c) phase volume flow. The microchannel's cross-sectional area A_{ch} calculates from the channel width W and channel height H , where also the channel aspect ratio $ar = \frac{W}{H}$ can be used to replace e.g. the channel width W .

For energetic considerations, knowledge of the Reynolds number Re , quantifying inertia forces and viscous forces, is of importance, since it is commonly related to range the external flow conditions of the Taylor droplets:

$$Re = \frac{\rho_c u_0 H}{\eta_c} \quad (2.7)$$

Herein, ρ_c is the continuous phase density and H represents the channel height as hydrodynamic relevant length.

Additionally, the viscosity ratio

$$\lambda = \frac{\eta_d}{\eta_c} \quad (2.8)$$

between both phases has a significant influence on the pressure drop and instantaneous velocity of a Taylor-droplet (Direito et al., 2017; Shams et al., 2018; Ładosz and Rudolf von

Rohr, 2018) since it indicates the momentum coupling into the disperse phase. Please note, that the definition of λ differs within the mentioned publications.

After the dimensionless quantities have been discussed, the structure of Taylor flows and wording used in this thesis is described in the following: in common droplet-laden multi-phase flows, depending on the given dimensionless quantities, the droplets flow irregularly inside the channel (Fig. 2.3 A). If the correct kinetic energy and void fraction ε_d is reached, the droplet starts to occupy almost the entire channel cross-section and the flow parts into Taylor-droplets and continuous phase sections. The latter is referred to as plugs or slugs (Fig. 2.3 B). It is a specific feature of microscopic Taylor-flows, that the droplet stays separated from the wall by a thin continuous phase wall film (see e in Fig. 2.3, in this work δ is used). Depending on the cross-sectional geometry of the microchannel, the Taylor-droplet does not fill the whole channel and small continuous phase compartments in the corner of the channel are formed (Fig. 2.3 D). The gutters allow the continuous phase to bypass the droplet, which leads to deviations of the instantaneous droplet velocity from the superficial velocity, that can not be described by the Bretherton film theory (Bretherton, 1961) for circular cross-sections.

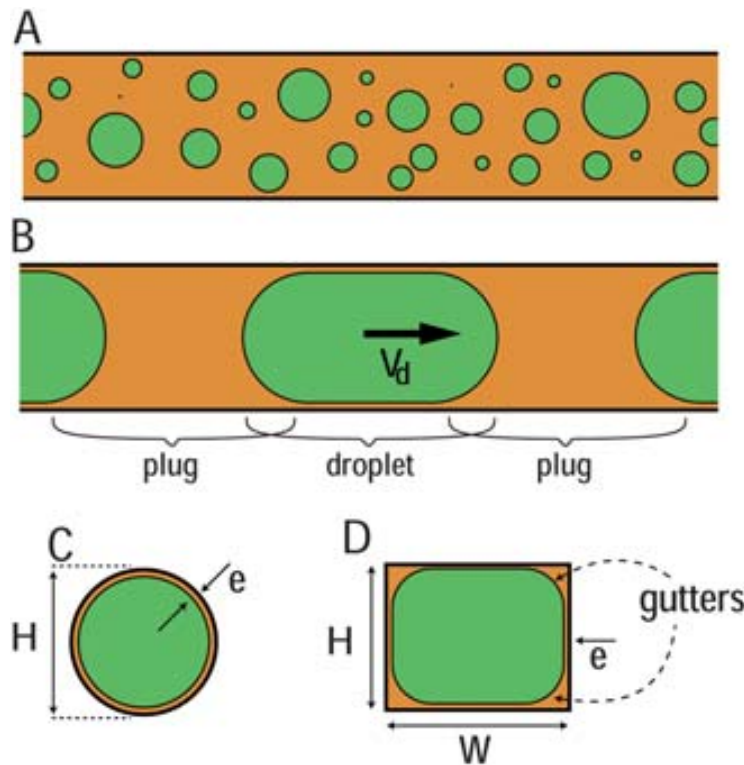


Fig. 2.3.: A) Dispersed flow: small droplets immersed in a carrier fluid. B) Slug flow: a succession of plugs and droplets. C) Cross-section view of a large moving droplet in a circular capillary of diameter H , featuring the thin lubrication film of thickness e . D) Cross section view of a large moving droplet in a rectangular capillary, featuring thin lubrication films and corners gutters. (sic!) Reprinted from *Lab on a Chip* 10, Charles N. Baroud, Francois Gallaire, Remi Dangla, *Dynamics of microfluidic droplets*, 2037-2039, (2010) with permission from Royal Society of Chemistry.

Regarding the droplet velocity, different phenomena can appear. In many applications, Taylor droplets in rectangular horizontal microchannels move with a velocity different from the superficial velocity, because the droplet does not fill the entire channel cross-section and the

continuous phase can bypass the droplet through the gutters. An early description is given by Wong et al. (1995), who derive these phenomena analytically and declare two possible regimes.

In the first regime, the fluid in the gutters moves slower than the droplet, dissipating kinetic energy. For the gutters, Abiev (2017) reported an inversed pressure gradient, indicated by the local surface curvature. For circular microchannels, this results in an inverse flow of the wall film and the droplet moves faster than the superficial velocity.

In the second flow regime, which holds true for long and highly viscous droplets (Wong et al., 1995; Shams et al., 2018; Rao and Wong, 2018), more energy is dissipated through the larger wall film area and through viscous dissipation in the droplet. Consequently, the flow in the gutters moves from the droplet back to the front. Thus, the droplet moves slower than the superficial velocity.

For both regimes, the thin wall film resists the motion of the droplet, resulting in a pressure difference with a higher value at the back and a lower value at the front of the droplet. The transition between both regimes is described by a critical flow rate and depends on the droplet length and the channel aspect ratio (Wong et al., 1995). Jakiela et al. (2011) focus experimentally on the influence of the momentum coupling between both phases (represented by λ) and also reveal a dependence of the droplet velocity on the droplet length. For short low viscous droplets ($\lambda < 1$), the droplets move faster than the superficial velocity and the droplet behavior is assigned to the first flow regime. Highly viscous droplets ($\lambda > 1$) move either faster or slower than the superficial velocity, depending strongly on the droplet length. This shows, that no holistic description of the instantaneous droplet velocity is available. The presented possible influential parameters already have been mentioned in literature. However, a distinct description apart from correlations does not exist.

The uniform distribution of bubbles and slugs in Taylor flows lead to a characteristic evolution of the local hydrodynamics. A Poiseuille flow profile, as it occurs for microscopic single-phase flow, is characterized by a velocity maximum in the center of the channel and shows a parabolic flow profile. In Taylor flows, this flow field is altered by the interaction of two immiscible phases. As a result, a recirculation in the droplets as well as in the slug arises (Fig. 2.4).

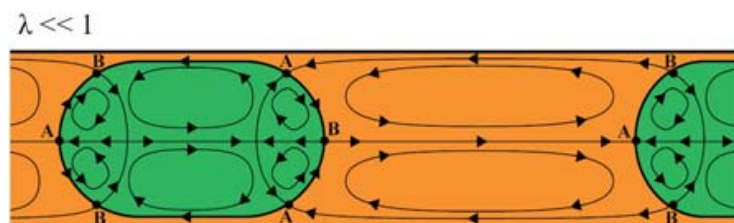


Fig. 2.4.: Topology of the counter-rotating recirculation zones induced by the presence of the interface. The stagnation points on the interface are classified between the converging points A and diverging points B. For non-viscous drops, there are 6 recirculation zones inside the droplet and 2 outside., (sic!) Reprinted from *Lab on a Chip* 10, Charles N. Baroud, Francois Gallaire, Remi Dandla, *Dynamics of microfluidic droplets*, 2037-2039, (2010) with permission from Royal Society of Chemistry.

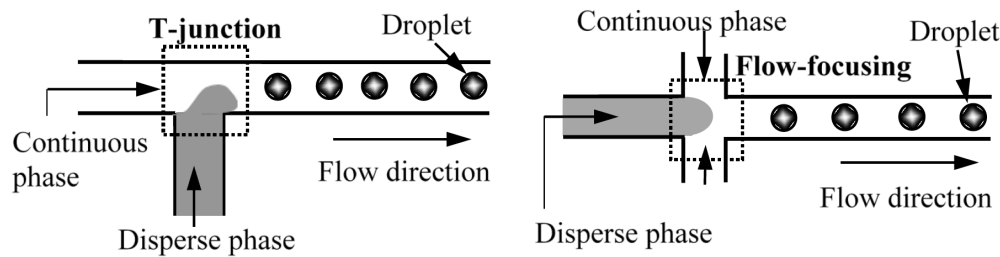


Fig. 2.5.: Continuous-flow emulsion-based droplet microfluidics from T-junction and flow-focusing. Reprint from Chou et al. (2015) under the Creative Commons Attribution License (CC BY 4.0)

For low-viscous droplets ($\lambda \leq 1$) at moderate Ca - and Re -numbers, three vortex structures form within the droplets. A main toroidal vortex in the droplet center is induced by shear from the channel walls and two secondary compensational vortices at the rear and front droplet caps are formed. These vortices inside the Taylor droplet lead to the formation of local stagnation points between droplet and slug. Depending on the local hydrodynamics, these are converging stagnation points at the center of the front and rear cap (Fig. 2.4 A) and diverging stagnation points moved towards the entrance of the gutters (Fig. 2.4 B). Please note, that the denotation was chosen regarding mass-transfer from the continuous phase in the disperse phase: transfer towards the disperse phase and absorption of the transferred component into the dispersed phase takes place mainly at the converging stagnation points. The local flow in the disperse phase moves the absorbed substances towards the divergent stagnation points where the surface is depleted and the substances are transported into the droplet. The concentration gradients are then equalized by the inner toroidal vortices.

The formation process of Taylor droplets in microchannels is only marginally addressed, since this work focuses on the movement of fully developed Taylor droplets in sufficient spatial and temporal distance from the droplet formation point. In microfluidic approaches, droplets are mainly generated in geometrical defined 2D-structures (so called junctions). These part into symmetrical (flow-focusing) and non-symmetrical (T-shape, Y-shape) concepts (Fig. 2.5).

The different occurring energetic regimes of droplet formation (squeezing, dripping, threading) depend mainly on Ca and Re and are well examined (Garstecki et al., 2006a; Gu et al., 2011; Glawdel et al., 2012a; Fu and Ma, 2015; van Loo et al., 2016). In the last years, especially the modeling of the droplet formation has been the topic of many publications (Zhou et al., 2006; Glawdel et al., 2012b; Chen et al., 2015; Wang et al., 2017) and is in focus of experimental and simulative studies (van Steijn et al., 2007; Gupta et al., 2014; Yao et al., 2015).

2.3 Microfluidic droplet sensing devices

Taylor flows typically require a precise control of flow and droplet characteristics to ensure their specific capabilities regarding short diffusion lengths and ensuring high energy- and mass-transfer. Throughout an entire microprocess, appropriate measurement concepts are necessary to keep the flow conditions inside the desired operational window. Furthermore, the temporal stability of a generated Taylor slug flow is an important parameter to ensure

constant reaction rates and sufficient reaction selectivity due to steady gradients and interfacial areas for heat- and mass-transfer. Since microfluidic process plants are commonly based on a numbering up approach, continuous process control is crucial to guarantee an efficient production in all modular devices (Antweiler et al., 2015).

A large number of measurement techniques applicable for microfluidic processes are available. Besides invasive technologies like anemometry or electric current measurements (Burlage et al., 2013) several non-invasive measurement principles can be utilized to capture the actual properties of Taylor slug flows. Voltammetry (Gu and Fisher, 2013), capacitance (Antweiler et al., 2015; Isgor et al., 2015; Yesiloz et al., 2015) or optics are applied (Weber et al., 2014; Yue et al., 2013). Additionally tracer-based measurement techniques can be used to classify the instantaneous flow conditions. Unfortunately, the addition of tracers always leads to a contamination of the fluidic system and the tracer may interact with chemical reactions or the local hydrodynamics. This explains, why the use of measurement techniques like micro particle image velocimetry (μ PIV) or light induced fluorescence (LIF) is mostly restricted to research and development purposes.

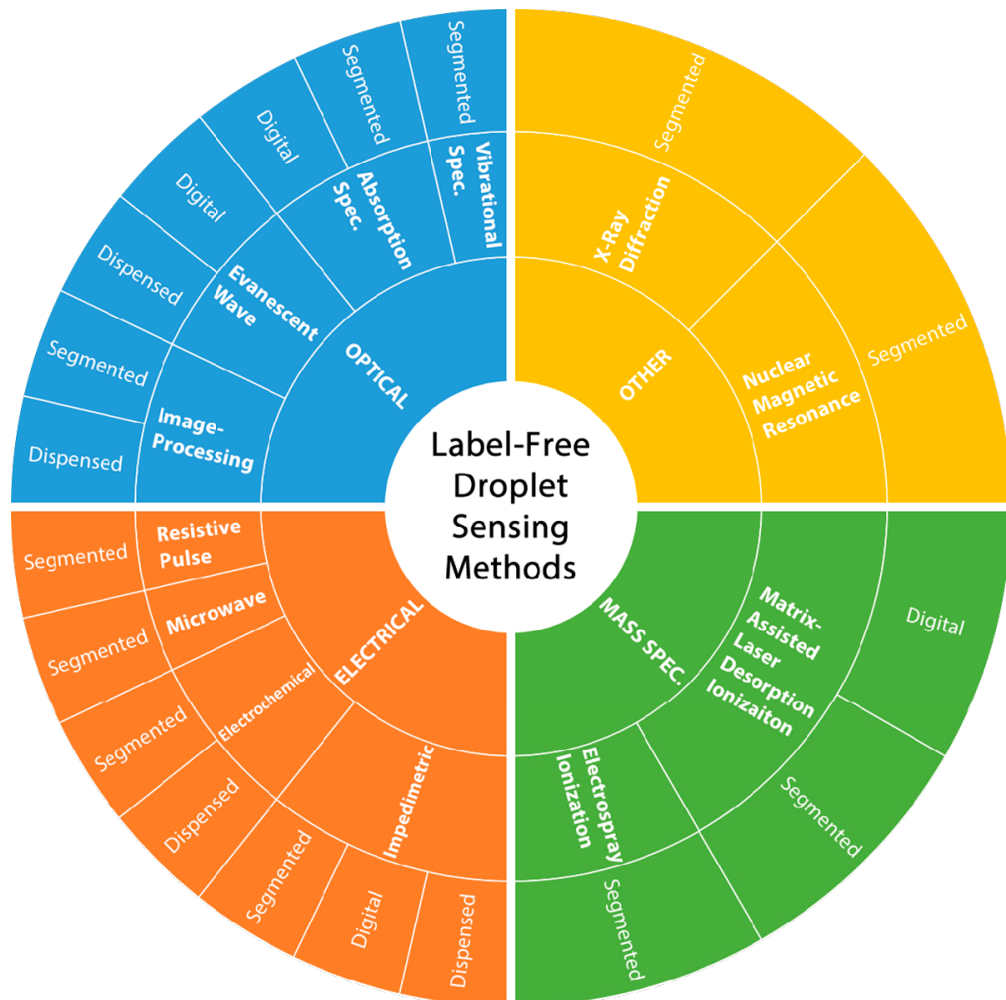


Fig. 2.6.: Classification of label-free droplet sensing methods. The main droplet sensing methods (optical, electrical, mass-spectroscopy and other) are listed in the inner circle, followed by sub-classes and droplet platform used for those sub-classes. *Reprint from Kalantarifard et al. (2018) under the Creative Commons Attribution License (CC BY 4.0)*

In contrast, label free optical techniques are convenient due to their good access for most process control parameters of Taylor-flows (frequencies, droplet- and slug lengths). Unfortunately, they often need complex and cumbersome devices like microscopes with attached high-speed cameras or image post-processing (Guo et al., 2013; Saint Vincent et al., 2012) which diminish the flexibility, and advantages and allow only short term measurements. Furthermore, external devices inhibit the development of embedded lab-on-a-chip systems due to their macroscopic nature. A recent overview over non-invasive techniques is given by (Kalantarifard et al., 2018), who divides the principles into electrical, optical, mass-spectroscopic and other (Fig. 2.6).

However, a cost-efficient and suitable technique useful for model development is not available. Thus, a simple but effective photometric approach, which can be included directly in the chip layout, appears appropriate to regain space in the microreactor periphery and contributes to the aim of realizing a long-term measurement technique for multiphase flows. Photometric principles can provide simple and cheap measurements and can be easily integrated into microreactors. But so far, they only deliver temporal information (Kraus et al., 2004; Nguyen et al., 2006; Weber et al., 2014) and are unable to measure all relevant parameters for modeling purpose (droplet frequency, droplet velocity and droplet length).

2.4 Micro particle image velocity (μ PIV)

Particle image velocimetry (PIV) is an established measurement technique for the examination of multi-phase flows. While PIV-measurements in the past were complicated due to the need for manual postprocessing of the data and especially hard to obtain experimental conditions (precise timing, intensive light sources, complicated analogue image acquisition and development of the film material), today's researchers can luckily utilize the tremendous advantages of computer controlled timing, excellent laser light-sources and powerful time-efficient software-based post-processing. Since the 2000s new mathematical concepts drastically increased the quality of the resolved measurement data using correlation approaches (Meinhart et al., 2000). Since the focus of this work is on measurements on the micro-scale, a further development of PIV, the so-called μ PIV, is used in this work. Thus, especially the specific features of μ PIV are described in this chapter (volume illumination instead of laser-sheet illumination). For a detailed introduction on PIV itself, the author would like to refer to the prominent literature (Adrian and Westerweel, 2011).

μ PIV is mentioned as a non-invasive measurement technology, although it requires an addition of tracer particles, which can be optically detected to determine the desired velocity field. Typically, these particles require to have a low density deviation from the bulk liquid to prevent sedimentation. Furthermore, particles with bulk density reduce the drag between tracer particles and the bulk liquid phase, which would lead to a measurement error. This is especially relevant at flow compartments with high positive or negative accelerations. Therefore, the tracer particle material attributes are adjusted to the bulk phase. For the measurements in this work, polystyrene (PS) particles are used since they provide a low density deviation to water and n-hexane as bulk phases (see App. D.2 for details) and the measurements are performed at moderate Re ($Re < 2.5$).

For the measurements of multi-phase flows, the tracer particles need to be seeded into both phases to measure the flow field of both phases simultaneously. To overcome optical distortions caused by refraction and reflection at the interfacial areas, a refractive index matching (RIM) is crucial (this is described in detail in Sec. 2.5). In those cases, the flow phases cannot be discriminated optically anymore, since the interface is invisible due to RIM. Thus, the seeding of the individual phases can be varied, such that a seeding gradient between the phases allows a threshold detection (Mießner et al., 2019).

In modern μ PIV applications the illumination of the seeded flow is mostly performed by pulsed laser-light. The usage of a laser-device allows to reach a high illumination intensity at defined excitation wavelengths and a high temporal precision of the laser pulses. Typically, the laser illuminates the particles at short and energy-rich wavelengths and the fluorescence answer of the particles, which is shifted to higher wavelengths and therefore lower energy, is used for particle imaging to overcome the restrictions caused by the volume illumination. For the separation of excitation and fluorescence wavelength equipment like of fluorescence microscopy is utilized: a dichroic mirror transmits the excitation light to the substrate (microchannel), while only the fluorescence information can pass to the acquisition system (lowpass filter).

The quality of the gathered data is limited by the microscope's objective: the size of the captured image is determined by the field of view and magnification, while the depth of field calculates the contributing depth information (Raffel et al., 2018).

$$DOF = \frac{RI \lambda}{NA^2} + \frac{n_d \epsilon}{NA M} \quad (2.9)$$

RI is the refractive index of the immersion medium between objective and substrate, λ the light wavelength of the fluorescence signal, ϵ the minimal detectable area and NA the numerical aperture:

$$NA = n_D \sin(\theta) \quad (2.10)$$

Here, θ represents the opening angle of the objective. Often the numerical aperture NA is given for air. For the case of immersion objectives, NA can be corrected if the RI of the immersion medium is known.

Since fluorescent particles are used, intensity information from outside the DOF can be detected. The range contributing to the correlation is called depth of correlation and indicates, in which distance from the focal plane the fluorescence signal is still detected by the evaluation algorithm. This distance can exceed the DOF, since also particles outside the focal plane are registered due to emitted out of plane fluorescence light. By increasing the distance to the focal plane in positive or negative z -direction, the fluorescence signal loses intensity until the particles are undetectable. A mathematical description is given by (Bourdon et al., 2006).

The recording of the image information is mostly achieved using high quantum efficient digital cameras, that allow to capture double-image in a defined temporal difference Δt . The temporal difference between these two frames of a double-images is defined precisely. The acquisition frequency of double-images amounts to about 4 Hz. A special PIV camera equipped with two CCD-chips is used. The timing between laser-pulse and camera-triggering is controlled with a micro-controlled timing-unit.

Prior to the PIV-evaluation, different image-enhancement steps are performed to diminish illumination gradients over the image and remove out-of-focus fluorescence light. This improves the image quality of the raw data and supports the correlation. In the following PIV-analysis, the two frames of a double image are divided into rectangular areas, the interrogation windows, which serve as a search grid (Fig. 2.7).

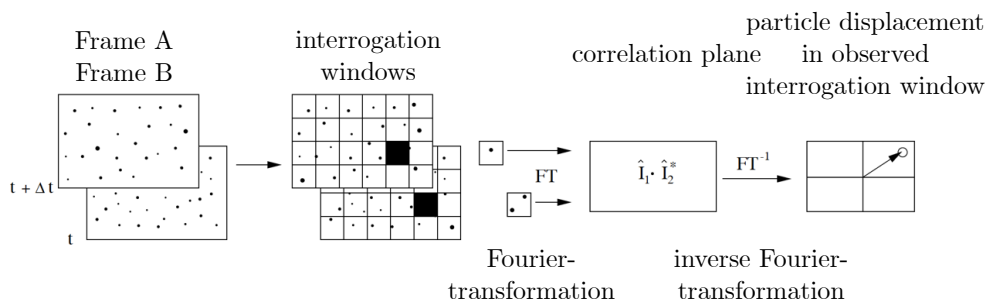


Fig. 2.7.: Analysis of double frame/single exposure recordings: the digital cross-correlation method
Adapted by permission from Springer: *Image Evaluation Methods for PIV* by Markus Raffel, Christian E. Willert, Fulvio Scarano 2018

If enough particle information is available in the corresponding particle images, the algorithm is able to determine the displacement of the interrogation windows in the two image frames. The displacement is determined using a correlation function of the intensities in both images. After carrying out a Fourier transformation, the correlation plane is determined by multiplication of the transformed intensities and subsequent back transformed into the time domain.

Fig. 2.8 represents the particle offset of a pair of particle images of an interrogation window of 64 px x 64 px. The resulting correlation plane indicates the displacement of the particles in the interrogation window.

In many applications the seeding density can not be chosen such, that within every double-frame sufficient information is provided for a reconstruction of the entire vector field. Thus, a sequence of double images can be acquired and the inherent information of the sequential measurements combined. At a single image pair, the direction of movement of the tracer particles is directly evident. If an image is directly averaged from several shots, the vector information can only be averaged at fixed positions. A reliable averaging of the individual images is only given at low Re numbers, when the flow can be considered stationary and measurements over a longer timespan can be combined. By using an ensemble PIV algorithm, an average calculation of the correlation planes is performed. As a results, the average particle offset per interrogation window and not per particle position is determined. Negative

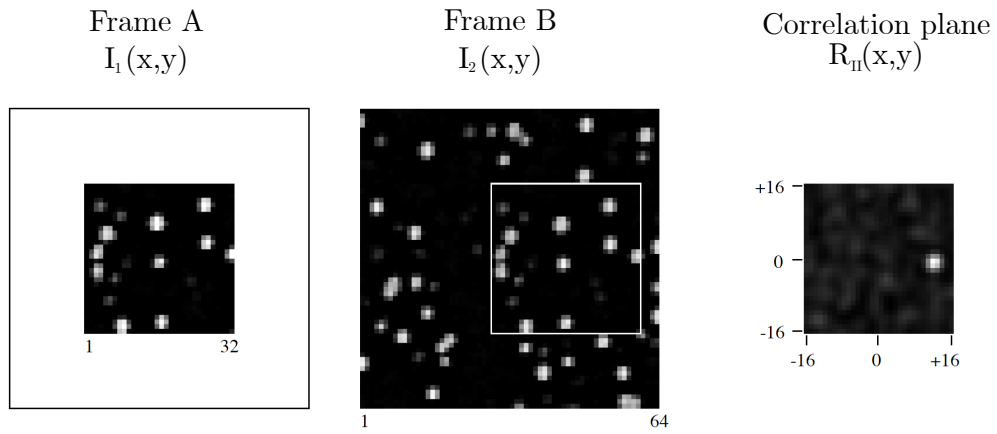


Fig. 2.8.: The cross-correlation function R_{II} (right) as computed from real data by correlating a smaller template I (32x32 pixel) with a larger sample I' (64x64 pixel). The mean shift of the particle images is approximately 12 pixel to the right. The approximate location of best match of I within I' is indicated as a white rectangle. Adapted by permission from Springer: *Image Evaluation Methods for PIV* by Markus Raffel, Christian E. Willert, Fulvio Scarano 2018

influences like Brownian motion can be reduced or removed from the calculated velocity distribution.

A number of different μ PIV-studies have been performed in the last years. Beginning with highspeed confocal scanning microscopy, Kinoshita et al. (2007) and Oishi et al. (2011) acquired multiple measurement planes with 2D velocity information. Recent measurements have been carried out at different DOC by Ma et al. (2014) and Liu et al. (2017).

2.5 Refractive index matching

Experimental characterization of the local flow field around droplets is preferably carried out by non-invasive measurements. Besides techniques using electrical or magnetical properties of the liquids to examine the local flow field, they so far do not reach the spatial and temporal resolution of optical approaches. The most prominent approaches, particle tracing velocimetry (PTV) and particle image velocimetry (PIV) are well established optical measurement techniques. PIV allows a higher particle seeding of the flow and therefore better spatial resolution. For the application with the specific requirements of microscopic multiphase flows, it was successfully adapted as μ PIV as the previous chapter showed.

In addition to the advantage of being a non-invasive measurement technique, the nature of the optical measurement principle requires undisturbed optical accessibility of the interrogated region. Besides intensity variation by the illumination, distortion at the interfacial areas by refraction or reflection may lead to unwanted optical displacement and increased measurement errors (Fig. 2.9). While the effects outside the interrogation area can be compensated by adjustment of the experimental design (e.g., avoiding spheroid surface and use of corrective optics), for the use in multiphase flows this measurement technique needs a refractive index matching (RIM) of the flow phases. This creates new challenges since often the material and flow properties (density, viscosity, interfacial tension) change in the

process of refractive index matching. A broad overview of possible liquid-liquid as well as solid-liquid refractive index matching approaches is given in the works of Budwig (1994) and Wright et al. (2017)

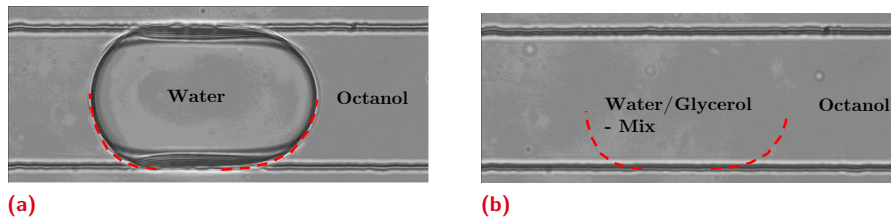


Fig. 2.9.: Example of refractive index matching for a Taylor-flow using an octanol-water/glycerol flow based on the measurements of Mießner et al. (2019). The interfacial area is marked (red dashed line). a) unmatched flow of octanol and water b) RI-matched flow of octanol and water/glycerol mixture

Several approaches have been made using refractive index matched systems to mimic special application cases like specific rheology for blood (Najjari et al., 2016; Brindise et al., 2018) or high-density differences for a buoyant jet (Clément et al., 2018; Krohn et al., 2018). In terms of bubbly/droplet-based multiphase flows in general, besides the sole material parameters, it is desirable to also tune the flow to distinct Ca - or Re - numbers or specific viscous coupling coefficient λ . For parameter studies, mostly simulations exist (Rao and Wong, 2018) or the measurements are experimentally limited to a narrow parameter range at missing or weak refractive index matching (Kovalev et al., 2018).

This is caused by the problem that the influence of the different experimental parameters cannot be shown independently because Ca and Re cannot be altered independently at simultaneous refractive index matching. Nonetheless, independently tuneable Re and Ca , at different viscous coupling λ would be preferable. No approach to deliver this for microscopic Taylor flows with RI matching is yet reported, although the viscosity ratio is a point especially addressed in recent publications.

In microscopic liquid-liquid flows RIM with one degree of freedom solely allows matching the RI of one phase to the other. The material properties of the phases like density, viscosity and interfacial tension are fixed for the desired RI. The governing dimensionless numbers such as Re , Ca may only be parameterized hydrodynamically (superficial flow velocity) or geometrically (microchannel diameter). The monetary effort to experimentally parameterize the diameter of the microchannel is high, while the velocity alters both quantities simultaneously.

Alternatively, surfactants could be added to solely change the interfacial tension of the material system. Surfactant concentration well below the critical micelle concentration does not significantly change the viscosity of the host phase. Albeit this approach indeed addresses Ca only, the use of surfactants introduces severe effects such as altering the hydrodynamics of the flow as well as its mass-transfer properties.

Retrieving accurate temporal and spatial information about Taylor slug flows from non-invasive NIR photometry measurements

” *What we observe is not nature itself, but nature exposed to our method of questioning.*

— **Werner Heisenberg**
(German physicist)

A substantial first approach for a successful model development is the identification and measurement of the underlying influential effects of the model. In case of the Taylor droplet excess velocity, especially for the instantaneous droplet velocity, the droplet length and the frequency of droplet formation is important. Unfortunately, a suitable, cost-efficient and non-invasive measurement technique for microscopic multiphase flows was so far not available. This might explain, why oscillations of the droplet formation frequency and length, that occur in combination with the excess velocity, are often mistaken as stochastic fluctuation. Additionally, the expectable periodic pattern repetition is correlated to the residence time and extends beyond the possible recording times of highspeed camera devices. The aim to retrieve all parameters from a non-invasive and long-term measurement capable single-sensor, is the main subject of the next chapter. Outcome of the work documented in this chapter is a well functioning and successfully validated sensor-prototype (Fig. 3.1). Furthermore, the droplet cap curvature is identified as a geometric factor, that is correlated to the excess velocity.

The presented approach uses geometric disperse phase surface properties to retrieve the instantaneous velocity information from a single sensor's time-scaled signal. For this purpose, a photometric sensor system is simulated using a ray-tracing algorithm to calculate spatially resolved near-infrared (NIR) transmission signals. At the signal position corresponding to the rear droplet cap, a correlation factor of the droplet's geometric properties is retrieved and used to extract the instantaneous droplet velocity from the real sensor's temporal transmission signal. Furthermore, a correlation for the rear cap geometry based on the *a priori* known total superficial flow velocity is developed, because the cap curvature is velocity sensitive itself.

The model for velocity derivation is validated, and measurements of a first prototype showcase the capability of the device. Long-term measurements visualize systematic fluctuations in droplet lengths, velocities, and frequencies, that could otherwise, without the observa-

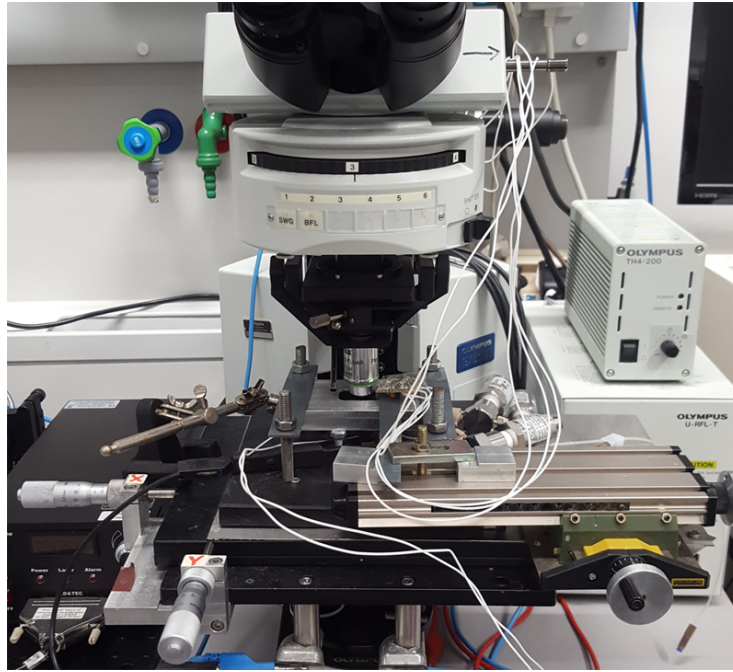


Fig. 3.1.: NIR-photometry sensor-prototype mounted on *Olympus BX-51 W* fluorescence microscope in measurement configuration

tion on a larger timescale, have been identified as measurement errors and not systematic phenomena.

What follows is based on (Helmerts et al., 2017). *Adapted by permission from Springer: Retrieving accurate temporal and spatial information about Taylor slug flows from non-invasive NIR photometry measurements by Helmerts, Thorben, Thöming, Jorg and Mießner, Ulrich. Experiments in Fluids 2017*

3.1 Overview

Optical techniques are convenient due to their good access for most process control parameters of Taylor-flows (frequencies, drop- and slug lengths). On the other hand, the need for necessary complex and cumbersome devices like microscopes with attached high-speed cameras and image post-processing (Guo et al., 2013; Saint Vincent et al., 2012) diminish the flexibility and advantages and allow only short term measurements. Furthermore, external devices inhibit the development of embedded lab-on-a-chip systems due to their macroscopic nature.

Thus, a simple but effective photometric approach, which can be included directly in the chip layout, appears appropriate to regain space in the microreactor periphery and contributes to the aim of realizing a long-term measurement technique for multiphase flows. Up to now, such photometric principles only deliver temporal information (Kraus et al., 2004; Nguyen et al., 2006; Weber et al., 2014) and are unable to measure all relevant parameters.

To obtain exact spatial information like the interfacial area and droplet length, the instantaneous disperse phase velocity u_d of each droplet is crucial. The most prominent approach of using the superficial droplet velocity as a reference can only achieve a diminished accuracy due to reported droplet velocity fluctuations of up to 30% (Fuerstman et al., 2007). The velocity of each individual droplet needs to be measured simultaneously with the time signal.

One possible option to measure the precise droplet velocity is a second pair of emitter and sensor with defined distance on the chip (Revellin et al., 2006; Long et al., 2012). For highly integrated embedded sensor systems or a large number of flow systems in a numbering-up approach, this appears non-practical due to monetary and practical reasons. Instead, a measurement system using only a single sensor location offers the possibility to integrate the system directly into the microreactor layout without significantly increasing the overall size or metrological complexity. Furthermore, it can enhance the experimental flexibility in scientific applications due to spatial reasons.

In this chapter, a versatile method to extract the instantaneous droplet velocity from a single photometric sensor signal without further material required is suggested to enable measurements in highly integrated devices for enhanced Taylor flow applications.

3.2 Model development

3.2.1 Conceptual approach

The largest disadvantage of single light path photometric sensors is their capability to resolve only temporal information and frequency properties so far. This kind of sensors is unable to directly identify the spatial dimensions of Taylor slug flows without knowledge of the corresponding instantaneous disperse phase velocity. To address this challenge, a new method is proposed to retrieve this information from a single sensor time signal. This method uses the representation of characteristic geometric properties of the disperse phase within the time signal.

The geometric properties and shape of the Taylor-flow's disperse phase responds to the mean flow conditions. Thereby the bubble cap curvature depends directly on the channel geometry and the actual mean flow conditions (Mießner et al., 2019). The missing link between the temporal measurement signal $I(t)$ and the corresponding spatial information $I(x)$ is a correlation between the spatial position of the disperse phase with respect to the sensor center position and its corresponding photometric transmission intensity $I(x)$.

When passing the photometric sensor, the disperse phase caps cause a spatial distinct intensity change $\frac{dI}{dx}$ in the sensor signal depending on their shape. This particular spatial and cap-sensitive intensity change is also present in time scaled measurement signal $I(t)$, where it is scaled by the instantaneous droplet velocity u_d . An a priori modeling and simulation of the intensity change caused by a droplet passing the sensor system delivers this spatial factor.

This factor can be expressed mathematically by extending the definition of the disperse phase velocity with the modeled spatial intensity change $\frac{dI}{dx}$ and the measured temporal intensity change $\frac{dI}{dt}$ (Eq. 3.1).

$$u_d = \frac{dx}{dt} \Rightarrow u_d^{NIR} = \frac{dx}{dI} \frac{dI}{dt} \quad (3.1)$$

Using the equality of $\frac{dx}{dI} = \frac{1}{\frac{dI}{dx}}$ allows to retrieve the instantaneous droplet velocity u_d^{NIR} directly from the measured intensity information $\frac{dI}{dt}$ using the disperse phase cap intensity change $\frac{dI}{dx}$ (Eq. 3.2).

$$u_d^{NIR} = \frac{1}{\frac{dI}{dx}} \frac{dI}{dt} \quad (3.2)$$

The curvature fluctuation of the caps is found to be small in relation to fluctuation in the droplet velocity on a broad range of capillary numbers. Thus, velocity fluctuations do not cause significant changes in the aspect ratio of the cap geometry. This holds especially true for the rear cap shape (Taha and Cui, 2006) since the cap geometry only changes linear, when the Ca_0 -number is changed logarithmic.

If the total superficial velocity u_0 of a Taylor flow is known, the geometric features of the droplet caps within the flow can be considered temporally and spatially quasi invariant. In this case, the cap geometry serves as a spatial reference to the temporal intensity signal of the photometric sensor. Nevertheless, to identify other possible influences of the superficial velocity u_0 on the curvature, a sensitivity analysis of the velocity fluctuation impact is provided in section 3.5.1.

To quantify the rear cap related intensity information $\frac{dI}{dx}$, a simplified ray tracing method is used to calculate time-invariant spatially resolved photometric signals, which allow to convert the temporal intensity signal into the corresponding actual disperse phase dimensions and position. Because the disperse phase velocity u_d^{NIR} is retrieved from geometric properties of the rear cap, the influence of the cap shape itself on the NIR intensity signal $\frac{dI}{dx}$ has to be identified in the respective spatial and temporal signal (Sec. 3.4). Detailed information about the simulation is provided in the following sections.

The complete sequence of the model for droplet velocity determination is depicted in Fig. 3.2.

3.2.2 Geometric properties

The general design of the simulation consists of a rectangular channel with a simplified disperse phase geometry of the Taylor flow. Above and below the reactor a NIR-LED serves as an emitter and a photodiode as a receiver for the light rays (Fig. 3.3). The disperse phase position related intensity change of transmitted light is used to determine the velocity. The sensor/emitter combination operates in the near infrared domain (NIR) so absorption effects

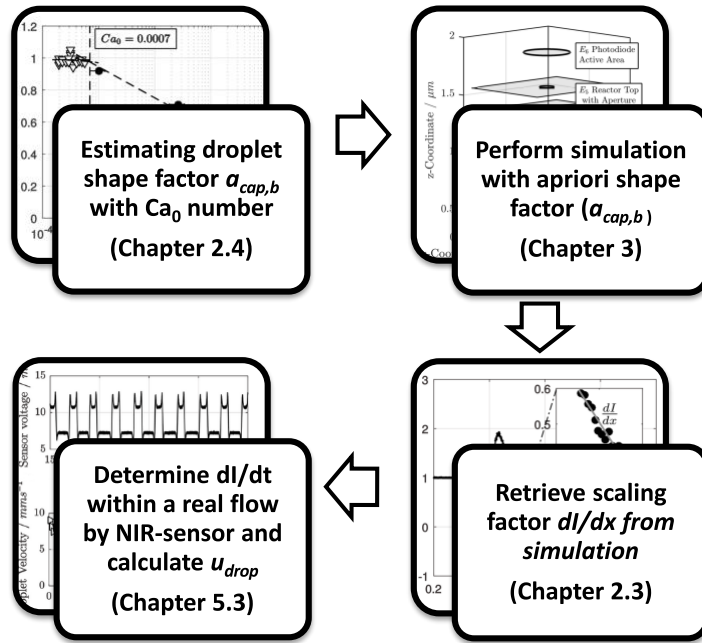


Fig. 3.2.: Complete sequence for droplet velocity u_d^{NIR} determination. At first, the droplet shape factor $a_{cap,b}$ is estimated using the presented correlation. A raytracing simulation is performed and the scaling factor $\frac{dl}{dx}$ is retrieved from the simulation results. The droplet velocity can be obtained from time-scaled measurement results.

enhance the signal contrast between the two immiscible phases of a Taylor-flow. Refraction of light emphasizes the interface position in the received detection signal.

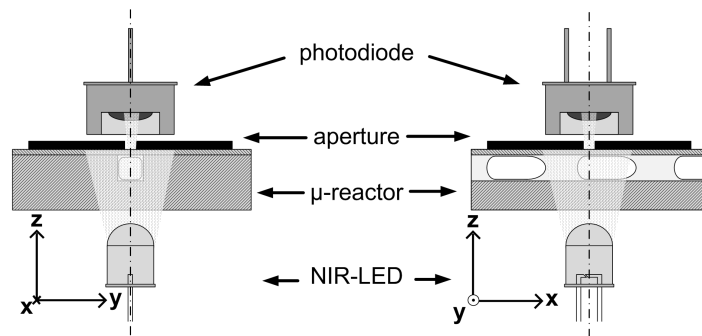


Fig. 3.3.: Cross and longitudinal section of the NIR photometry setup. A top-mounted NIR-sensor aligns with a bottom mounted LED-emitter. An aperture restricts stray light such that the signal to noise ratio of the Taylor slug flow is enhanced

Within the microchannel, a simplified defined disperse phase geometry moves through the sensor system in a square microchannel with an aspect ratio of 1. To keep the simulation on a moderate level, the disperse phase shape is modeled as simple geometric bodies and hydrodynamic influences are ignored. The droplet's x - z cross-section shape is set to be circular and the elongated center part is modeled as a cylindrical surface (geometric cylinder). The disperse phase caps are chosen to have ellipsoidal shapes (half geometric ellipsoid) with a parameterized x - y aspect ratio $a_{cap,f}$ and $a_{cap,b}$ (Fig. 3.4). These rear cap aspect ratio are retrieved from the superficial velocity u_0 using the correlation provided in the next

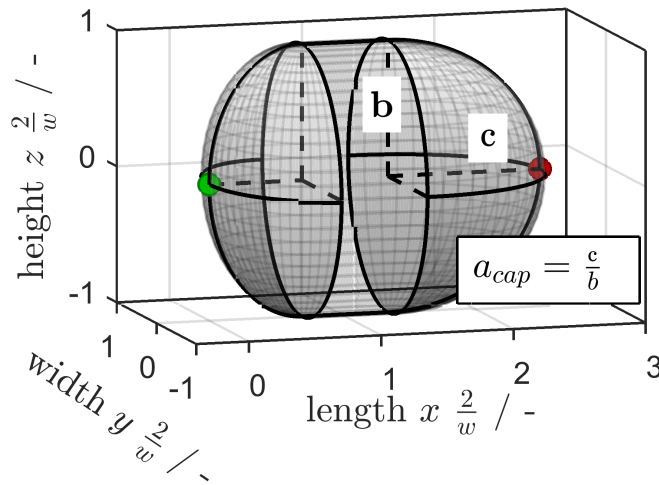


Fig. 3.4.: Sketch of the simplified simulated disperse phase shape as used for the simulations. The surface consists two ellipsoidal caps (front and back), described by respective aspect ratio $a_{cap,i}$, and a cylindrical center

chapter (Chapter 3.2.4). The minimum disperse phase length remains to be the sum of both ellipsoidal x-axis intercepts.

Certainly, the simplifications induce a shape deviation in comparison to a disperse phase shape under the influence of a real flow. Within a real Taylor flow, the resulting thickness of the thin wall film and the cap shape due to the flow induced interfacial forces differ from the model. However, keeping in mind the purpose of this simulation, the author considers this discrepancy acceptable compared to the computational effort needed to implement a full fluid-mechanic simulation.

3.2.3 Transmission signal shape and dl/dx slope derivation

The expected shape of the droplet's transmission signal has been described by Nguyen et al. (2006) and Revellin et al. (2006). By considering the absorption behavior, the movement of the rear disperse phase cap past the sensor causes a transition between the transmission levels of both pure substances. Thus the caps of the droplet must locate in the slopes of the signal. This is also proven by the simulation in Chapter 3.3.3 and a typical droplet-to-continuous phase change in the transmission signal from high (disperse phase) to low (continuous phase) is shown in Fig. 3.5. In order to retrieve the signal slope characteristic $\frac{dl}{dx}$, all data points between the normalized reference value of 0.4 and 0.6 are chosen. In this range the influence of the focal points of the bubble shape is the lowest as the sensitivity analyses (Chapter 3.4) will show. Due to the fact that the simulation uses a simplified droplet shape model, the highest agreement between simulation and reality is found in this signal range of the rear drop signal.

The chosen datapoints are approximated by a linear fit (Fig. 3.5) with the MATLAB function "polyfit", hence the slope of the fit then directly equates $\frac{dI}{dx}$ and numerical fluctuation from the simulation or noise in measurements are damped. Furthermore a linear fit serves as a central difference over the whole area, whereas a higher order fit would be sensitive to the exact point where the slope is derived.

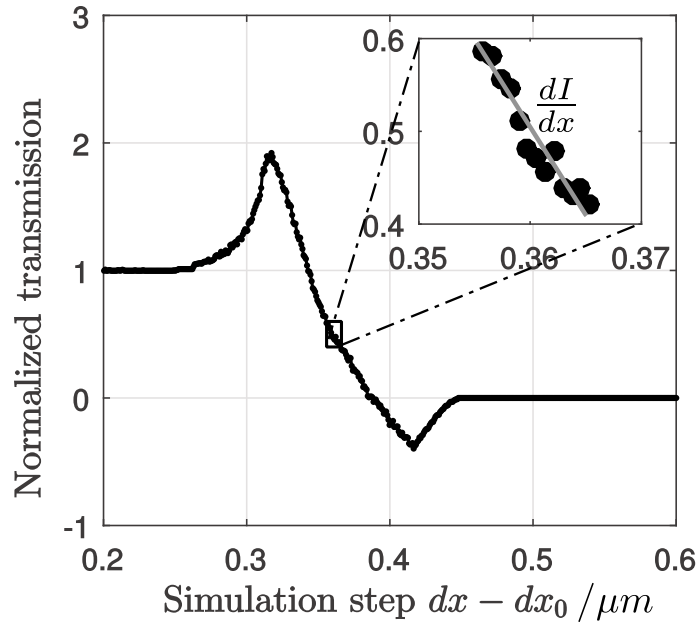


Fig. 3.5.: Transmission signal for a droplet's rear passing the sensor system. The data point of the transmission signal (●) are approximated by a linear fit (-) within a window of [0.4 .. 0.6] to retrieve the slope dI/dx at a normalized transmission value of 0.5

3.2.4 Droplet shape estimation

The spatial reference signal slope $\frac{dI}{dx}$ derives from the rear curvature of the droplet. Therefore, an a priori known hydrodynamic parameter is needed to estimate the droplet shape and enable retrieving accurate simulation results. Taha and Cui (2006) reported on the shape of rear bubble caps, unfortunately their data only covers Ca -number beyond 0.001. Because plenty of application take place at lower Ca -numbers, additional data is needed. Physical considerations of the surface energy of confined interfaces with dominating interfacial tension forces lead to a circular cross section ($a_{cap,i} = 1$) for small Ca -number Taylor slug flows. Own high-speed camera measurements from this work prove this assumption (Chapter 3.5.2).

When both datasets are combined, two regimes occur: For $Ca \leq 0.0007$, the rear cap shape remains to be approximately spherical, while beyond $Ca \geq 0.0007$ a logarithmic behavior as stated in Fig. 3.6 can be found. Since the instantaneous disperse phase velocity u_d is not available, the total superficial velocity of the flow is used to derive the Ca -number and hence the rear cap aspect ratio. An analysis of the presumed slope deviation caused by the difference between u_d and u_0 is given in Chapter 3.5.1 and found to be acceptable for the presented approach.

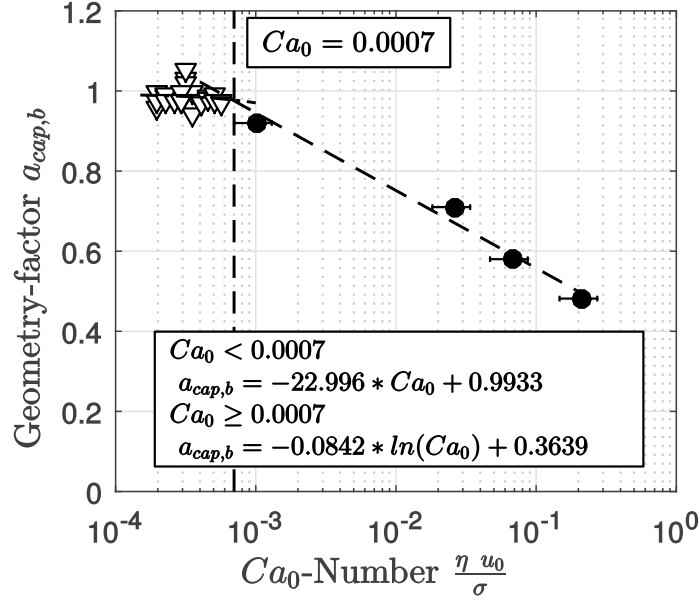


Fig. 3.6.: Dependency of the rear cap aspect ratio $a_{cap,b}$ on the superficial velocity Ca_0 -number. Graph is based on data (●) published by Taha and Cui (2006) and extended by own measurements for low Ca-Numbers (▼). (---) Logarithmic regression of the entire data set (—) Linear regression of own data. The deviation that originates from the usage of u_0 versus u_d (up to +/-30% difference) when calculating the Ca from Taha and Cui (2006) is addressed in Chapter 3.5.1

3.3 Simulation

A simplified ray tracing method is applied to simulate the influence of absorption and refraction of light at all relevant surfaces in the pathway between NIR-source and -detector. The desired spatially correlation factor $\frac{dI}{dx}$ is derived and an understanding of the NIR transmission signal is generated (Fig. 3.5). Material properties and geometric dimensions of the simulation are chosen such, that a comparison between simulation and experiments is feasible. For the described simulations *Mathworks MatLab 2015a* serves as the simulation environment.

3.3.1 Fundamentals of raytracing calculation

The light rays passing through the microchannel and disperse phase are influenced by the different material and optical properties of the experimental design. Considering light as an electromagnetic wave and applying conservation of energy and momentum, the change of wave speed caused by an optical density variation modifies the propagation direction under any angle of incidence other than 90° . Snell's law describes this behavior (Eq. 3.3) using the material's index of refraction (n_1, n_2) along with the angle of incident (θ).

$$\frac{\sin \theta_1}{\sin \theta_2} = \frac{n_2}{n_1} \quad (3.3)$$

The calculation of effects caused by refraction at different surfaces is improved by the fast algorithm of Bec (1997) using vector and matrix calculation.

In addition to refraction, light rays can be reflected when a critical angle of incident exceeded (Eq. 3.4):

$$\theta_{crit} = \arcsin\left(\frac{n_2}{n_1}\right) \quad (3.4)$$

An efficient algorithm for reflection calculation is also described in Bec (1997).

Additional to idealized refraction and reflection, partial reflection occurs on all real surfaces, depending on the angle of incidence and lowers the intensity of refracted light beams. The amount of partly reflected light (R_0) for a particular angle of incident (θ) can be approximated when the refractive indexes (n_1, n_2) are known (Schlick, 1994):

$$R_\theta = R + (1 - R)(1 - \cos(\theta))^5 \quad (3.5)$$

Herein R denotes the reflection coefficient:

$$R = \left(\frac{n_1 - n_2}{n_1 + n_2}\right)^2 \quad (3.6)$$

By considering Snell's Law (Eq. 3.3) using Bec's algorithm (Bec, 1997) and Schlick's Approximation (Eq. 3.5) idealized reflection, partial reflection, total reflection and refraction of light are included in the simulation.

Additional to changing the path of the light rays due to refraction and reflection, an absorption of the light energy occurs within the light path between sensor and emitter. This effect is described with the Lambert-Beer-Law (Eq. 3.8), where ϵ denotes a material specific extinction coefficient, c the concentration and d the path length of the light ray through the absorbing medium:

$$E_\lambda = \lg \frac{I_0}{I_1} = \epsilon_\lambda \cdot c \cdot d \quad (3.7)$$

For pure substances the decreased light intensity (I_1) can be described as

$$I_1 = I_0 \cdot e^{-k_\lambda \cdot d} \quad (3.8)$$

and the corresponding pure substance absorption coefficients (k_λ) are shown in Tab. 3.1.

Tab. 3.1.: Absorption and refraction coefficients of materials used

Substance	Refractive index $n_{\lambda=1450nm}$ [-]	Absorption coefficient $k_{\lambda=1450nm}$ [1/mm]
Borosilicate glass	1.5200 (Jedamzik, 2007)	0.9000 (Company, 2016)
Si	3.4794 (Salzberg and Villa, 1957)	neglectable (Green and Keevers, 1995)
Air	1.0000 (by definition)	0 (by definition)
Deionized water	1.3200 (Kedenburg et al., 2012)	1.26 (Vögele and Buback, 1993)
n-dodecane	1.4200 @589nm (Wohlfarth, 2008)	0.03 (Vögele and Buback, 1993)

Tab. 3.2.: Relevant geometric parameters of the simulation layout

Attribute	Size
Channel width w	0.20 mm
Channel height h	0.20 mm
LED diameter d_{LED}	1.00 mm
LED opening angle α_{led}	15°
Aperture diameter d_{ap}	0.13 mm
Photodiode active area A_{photo}	0.02 mm ²
Thickness of Si-layer	0.30 mm
Thickness of cover glass	0.20 mm

Utilizing this optical behavior and physical properties, the most prominent features of the sensor signal are represented well (Chapter 3.5.2).

3.3.2 Setup and fluid properties

The raytracing simulation is linked up to the simple experimental set up (Sec. 3.2.2) and varies basic geometric, fluidic and material properties. The emitted light travels through a number of surfaces and volumes of different refraction and absorption properties (Tab. 3.1) and geometries (Tab. 3.2). Inputs for the simulation are the flow-invariant and a priori known parameters displayed in Tab. 3.1 and Tab. 3.2 and the superficial Ca-Number Ca_0 , from which the curvature factor $a_{cap,b}$ is calculated (Sec. 3.2.4).

A cylindrical disperse phase body with attached elliptic caps of defined aspect ratio has been chosen over a physically detailed interface representation to reduce the calculation time (Sec. 3.2.2). The simulation setup consists of plain surfaces at which refraction and reflection can occur. The channel side walls as well as first and second order path changes due to full and partial reflection are included in the simulation. In between the planes absorption of light energy takes places proportional to the distance traveled (Eq. 3.8). Due to practical experiences during premeasurements at a physical prototype, an aperture is placed in the light path to shield background radiation. The resulting signal intensity directly depends on the detected vector amount (refraction) and their respective amplitude decrease (absorption).

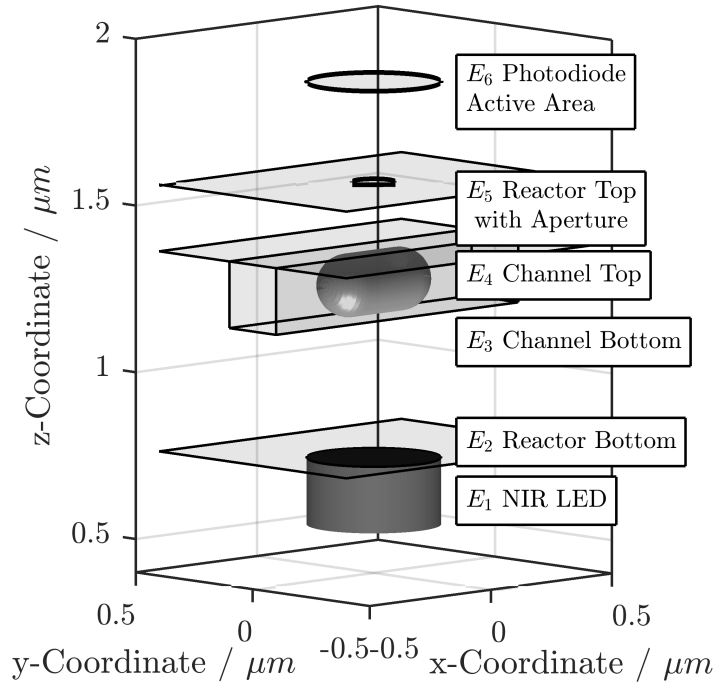


Fig. 3.7.: Overview of the simulation setup. Light beams are initiated at LED-plane E_1 with a divergence of 15° and finally detected at sensor-plane E_6 . The disperse phase interacts with the light between planes E_3 and E_4 . Therefore piercing points of the light rays with the droplets are determined to calculate refraction, reflection and absorption like described in Chapter 3.3.1

An overview of the surfaces belonging to the channel geometry is given in Fig. 3.7. Considering the NIR-LED to be a point source at the origin, equidistant unity vectors represent the emitted light rays. The divergence of the vector field is chosen to achieve a solid angle of 15° across an initial surface E_1 as it is common for NIR-LEDs. This initial vector field allows calculating the piercing points on the next plane E_2 and the respective distances between the planes. These distances influence the absorption, while the angle of incident with respect to the surface normal \mathbf{n} allows the calculation of refraction or reflection for the several light beams.

The procedure is repeated at the respective planes E_i until the light rays reach the top surface of the channel E_4 . Within the channel between E_3 and E_4 refraction as well as partial and total reflection can occur at the droplet surfaces as well as on the channel walls and back reflected in the droplet. Subsequently, the aperture in plane E_5 is modeled with a logical operation that only allows vectors inside the actual aperture radius pass to the photodiode. The sum of the lengths of vectors finally piercing the detector plane E_6 form the desired integral intensity signal value.

3.3.3 Examination of signal characteristic

A number of authors describe the shape of the photometric transmission signals and remarkable characteristics (Nguyen et al., 2006; Revellin et al., 2006). However, an accurate

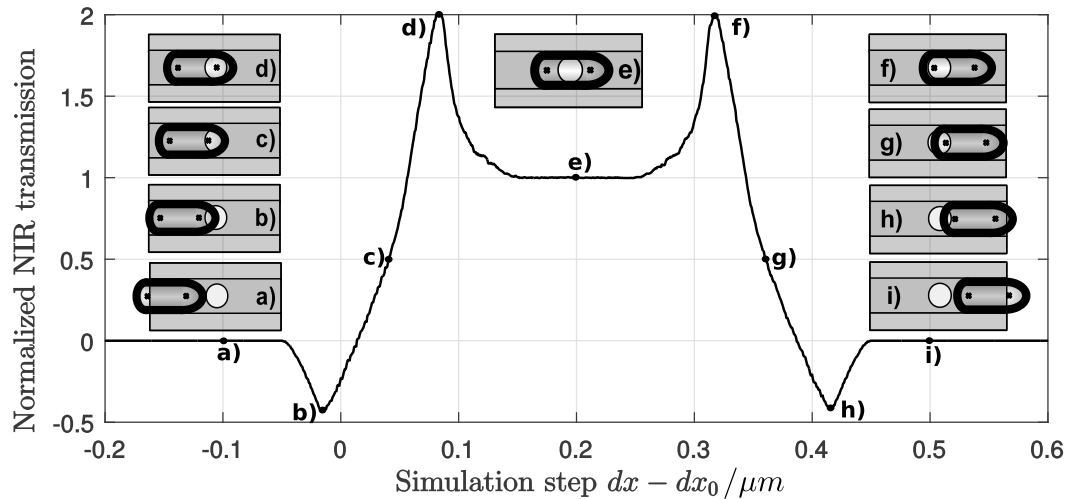


Fig. 3.8.: Characteristic features of the simulated droplet signal a)-i) in constellation with the actual disperse phase position. a) No influence of the disperse phase. b) Interface deflects light from the aperture. c) Focus point enters the aperture area. d) A Maximum is reached when focus fully overlaps the aperture. e) The Signal of the disperse phase body. f-i) Reverse order of events

explanation is missing. Following the procedure outlined in Sec. 3.3.2 the disperse phase shape acts as additional surface added between the planes E_3 and E_4 of the channel geometry and the droplet position inside the channel is varied with respect to the emitter-detector system in order to generate the droplet position related intensity signal. Therefore the modeled droplet is moved dx stepwise per simulation run until the droplet has entirely passed the sensor-emitter system (Fig. 3.8) and the partial intensity signal is generated.

Within Fig. 3.8 letters a)-i) mark the characteristic features of the signal. A base plateau can be noted depending only on the absorption properties of the continuous phase and the refraction at the channel walls. At this point the droplet has not yet approached the proximity of the aperture a). When the aperture is reached, the interface reflects part of the light vectors away from the aperture and consequently reduces the signal intensity b). After an increasing part of disperse phase covers the aperture area, the resulting NIR transmittance rises along with the signal intensity c). Refraction at the curved shape of the disperse phase creates a focal point. Hence, the light intensity increases to a maximum beyond the level of disperse phase adsorption, when the focus enters the aperture area d). After the front focus point veers way from the aperture, a transmission plateau establishes e), which represents the disperse phase body. The reversed order of effects occur when the rear cap of the disperse phase passes the aperture (f)- i)).

3.3.4 Evaluation of numerical stability

Two different aspects of the simulation have to be considered to evaluate the numerical performance of the calculation and simulation setup. At first the concept of using a linear fit to retrieve the transmission slope of the disperse phase from a time signal needs to be examined and as a second step the overall accuracy needs to be evaluated.

For the first step, a simulation run uses default settings to deliver a normalized transmission signal in the spatial domain along with its spatial rear transition slope $\frac{dI}{dx}$ from the disperse to the continuous phase. Successively, it is transformed into a temporal signal using a discretionary initial droplet velocity u_d^{init} . The corresponding time dependent rear slope $\frac{dI}{dt}$ is then determined with the approach of Chapter 3.2.3 with the *MATLAB* function *polyfit*. By multiplying the slopes from the spatial and time scaled signal the disperse phase velocity (u_d^{NIR}) is subsequently derived (Eq. 3.2). A comparison of u_d^{NIR} with the discretionary applied scaling-velocity u_d^{init} delivers a deviation that serves as a numerical benchmark of the slope derivation method.

Simulations at various discretionary velocities u_d^{init} from (1 - 1000) $\mu\text{m/s}$ show that the relative numerical error

$$\epsilon_{u_d}^{rel} = \frac{u_d^{NIR} - u_d^{init}}{u_d^{init}} < 10^{-13} \quad (3.9)$$

for the numerical slope derivation via *polyfit* is nearly constant (Fig. 3.9 a)). Considering *MATLAB*'s roundoff error for floating points of type *double* $2.22 \cdot 10^{-16}$ the *polyfit*-function retrieves the corresponding slopes with a satisfactory performance for even high droplet velocities. Thus the approach of using a linear interpolation for slope derivation is kept.

To quantify the overall numerical accuracy of the various trigonometric calculations within the raytracing algorithm, a simulation run with disabled absorption and matched refractive index of both fluid phases is performed. In the case of accurate calculations, no change in the simulated transmission signal should occur as the disperse phase passes the sensor (Fig. 3.9 b)).

The signal deviation lies below 1%. The deviation results from round off error of the surface vector direction calculation at a flat angle of incidence. Thus the numerical accuracy of the simulation is considered satisfactory.

3.4 Sensitivity analysis

In order to access the physics of the sensor concept and check the transferability of the simulation approach, an analysis of the simulation's input parameter is performed regarding their sensitivity towards the transmission and the signal features.

As initial settings, the reference geometry is chosen to match the experimental conditions, and the channel aspect ratio is set to be unity to avoid major discrepancies concerning the simplified disperse phase shape. The actual physical channel dimensions are considered not to be of importance due to the geometrical scalability of the entire constellation. By definition, the received position dependent signals are normalized to the disperse phase (high level - 1) and the continuous phase (low level - 0) to establish a good comparability with the experiment. This convention is used for all further parameter studies.

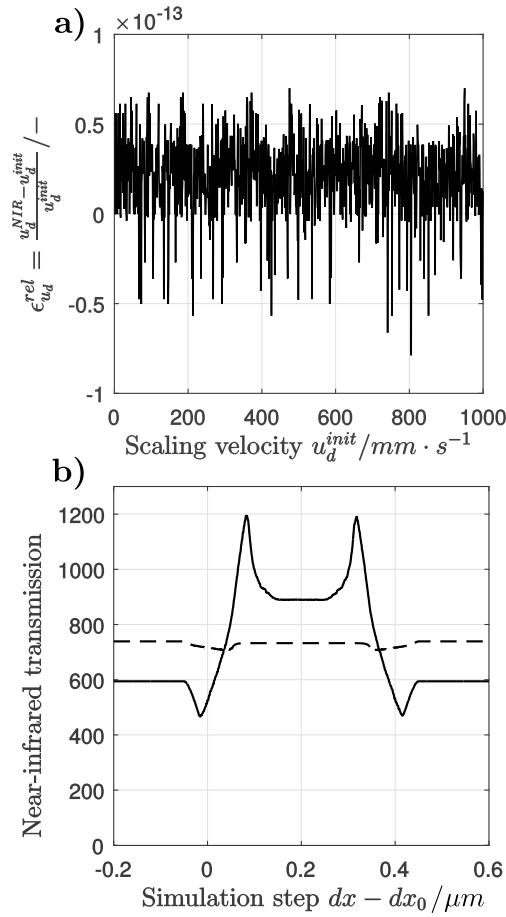


Fig. 3.9.: a) Relative numerical error $\epsilon_{u_d}^{rel}$ of the slope derivation algorithm for various initial scaling velocities u_d^{init} b) Plausibility proof of simulation algorithm. Comparison between system water/n-dodecane (—) and disabled absorption and refraction (---). Minor deviations from the expected straight dashed line are observable. The deviation occurs due to trigonometrical roundup error at flat angle of incident for light rays hitting the droplet

Since flow conditions affect the disperse phase cap geometry, the front end of the droplet stretches while the rear compresses (Taha and Cui, 2006) due to inertial effects. The parameter is varied for $C a_d$ -numbers up to 0.5 according to the proposed correlation ($a_{cap,b} = [0.4..1.0]$). Values $a_{cap,b} > 1$ are just mentioned to identify the optical coherences. In real flows they only appear at the front cap.

The on- and offset of the signal appears to be independent of the cap curvature while the signal peaks change significantly. While sharper caps (aspect ratio $a_{cap} \geq 1$) form the largest focus points and therefore the highest signal peaks, all other geometries distribute the light over a larger area (Fig. 3.10 a). At half level 0.5 between high and low level, the signal slope decreases with reduced aspect ratio. This appears to be counterintuitive since one would expect that a shorter the cap results in a steeper signal slope.

The aperture diameter within the sensor's light path affects the detectable amount of light. The minimum diameter of $d_{ap} = 0.55 w_{Channel}$ ensures a reasonable amount of transmitted energy. The maximum diameter is considered to be $d_{ap} = 0.85 w_{Channel}$ since intensity information from outside the channel does not contribute information about the Taylor flow.

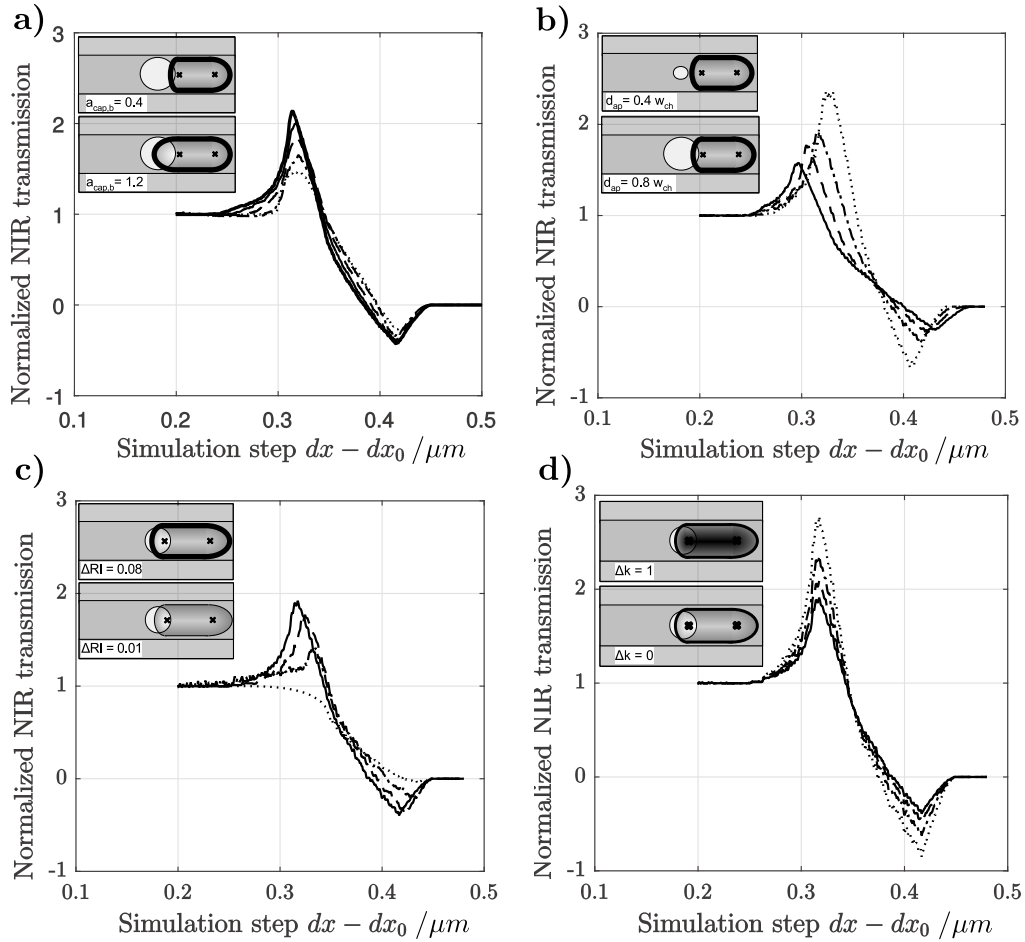


Fig. 3.10.: Normalized transmission for different droplet configuration in the sensitivity analysis. **a)** Influence of the disperse phase cap geometry $a_{cap,b}$ on the resulting NIR transmission signal. Despite the smaller dimension of the compressed disperse phase back, the slope decreases due to the interplay of shape a focal effect. Elongated high aspect ratio caps generate sharper focus points and result in a steeper signal. $a_{cap,b} = 1.2$ (—) $a_{cap,b} = 1.0$ (---) $a_{cap,b} = 0.8$ (- - -) $a_{cap,b} = 0.6$ (---) $a_{cap,b} = 0.4$ (-----) **b)** Influence of the aperture diameter on the resulting NIR transmission signal. The aperture restricts the amount of stray light, thus enhances the signal to noise ratio. Smaller apertures produce higher relative peak values due to the chosen signal normalization convention. $d_{ap} = 0.85w_{ch}$ (—) $d_{ap} = 0.75w_{ch}$ (- - -) $d_{ap} = 0.76w_{ch}$ (---) $d_{ap} = 0.55w_{ch}$ (-----) **c)** Influence of the refractive index difference $\Delta RI^* = (RI_c - RI_d)$ on the resulting NIR transmission signal. system water/n-dodecane $\Delta RI^* = -0.08$ (—) $\Delta RI^* = -0.053$ (- - -) $\Delta RI^* = -0.027$ (---) $\Delta RI^* = 0$ due to a matched refractive index no peaks appear (-----). The signal peaks seem to increase with a RI^* , but this is based on the signal normalization. Higher RI^* lead to large peaks in the not normalized signal, but are also increasing the disperse phase transmission plateau because of light fociation crosswise the channel **d)** Influence of the absorption difference $\Delta k^* = (k_c - k_d)/k_c$ on the resulting NIR transmission signal. $\Delta k^* = 1$ (—) $\Delta k^* = 0.66$ (- - -) $\Delta k^* = 0.33$ (---) $\Delta k^* = 0$ (-----). Variations in the absorption difference of both phases lead to changes in the slope and signal peak in the normalized signal. The peak level in the original signal remains constant because it only depends on the refractive index difference

The size of the aperture strongly influences the normalized signal (Fig. 3.10 b). The smaller the aperture, the more pronounced is the influence of the focus points. The absolute light level decreases with reduced diameter, while the focus points cause a relative exaggeration

of the peak intensity. The signal minima decrement significantly, due to refraction at the disperse phase interface.

Regarding accuracy, a moderate slope is preferable. However, a wider section of the microchannel resulting in less slope change is not preferable, since the large aperture leads to a low signal to noise ratio: Transmitted light from both the interfacial droplet cap area and the cylindrical part enters the detector as well as additional stray light. Contrarily, a smaller aperture shows significant slope differences at the droplet caps due to the large refraction influence.

The clear signal sensitivity to the aperture diameter implies the importance of uniform size throughout the measurement. An aperture diameter of $0.65 w_{Channel}$ for both simulation and experiment has been chosen to implement a good trade-off between the signal slope steadiness and an overall low signal to noise ratio.

Analog to the variation of aperture diameter the refractive index of the disperse phase is changed from the experimental difference applied (n-dodecane/water) towards a refractive index match. The transmission signal shows significant changes in the signal's high and low peaks and a strong influence of the refractive index can be observed (Fig. 3.10 c). In the case of matched refractive indices, a light transmission difference between both phases is visible due to the absorption properties of the liquids. This showcases the capability of the NIR-sensor to even work under difficult optical conditions (RI-matching). Under those circumstances, the characteristic signal peaks vanish and the signal transition between the two levels appears to be steady and almost symmetric.

The absorption difference between both phases has a defined influence on the absolute transmission signal strength, which results especially in a higher signal strength for the disperse phase in case of lower absorption. In the normalized signal, this behavior shows as lower signal peaks and a flattened slope, although the refractive index itself influences the heights of the peaks (Fig. 3.10 d). Thus a larger difference in the absorption of both phases improves the slope characteristics.

The sensitivity analysis clarifies, that the influences on the transmission signal are mainly related to flow invariant properties such as experimental design and material properties. The only velocity dependent parameter is identified to be the droplet shape and therefore the cap aspect ratio (Fig. 3.10 a). The front shape is more sensitive to the flow conditions than the disperse phase rear. Thus, to determine a suitable signal section, it is more accurate to consider the rear cap for the slope derivation. The remaining error due to changes in the assumed droplet shape is discussed in the next chapter.

3.5 Validation

The operation of the sensor concept is validated by the construction of a prototype and measurements of a microscopic Taylor flow at moderate droplet velocities with both, the proposed NIR-sensor and a conventional highspeed-camera.

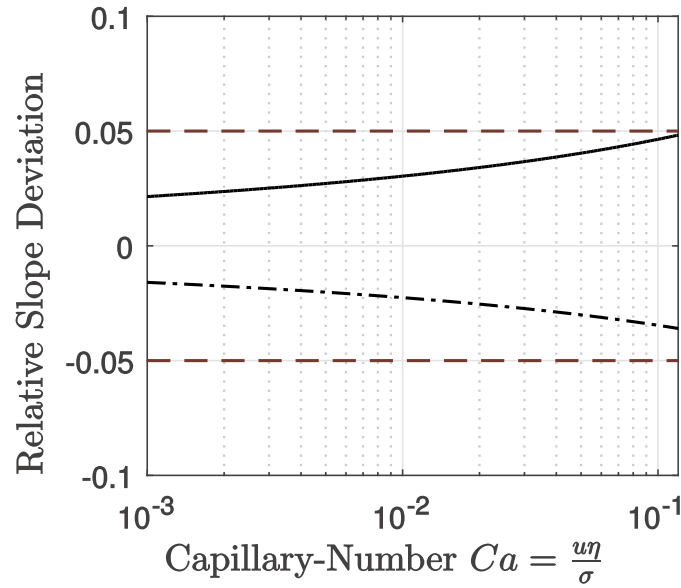


Fig. 3.11.: Relative slope error sensitivity based on a +/- 30% deviation of the Ca-number e.g. inserting the superficial velocity compared to the correct disperse phase velocity. Relative error at +30% Ca (—) and Relative error at -30% Ca (---). The deviation at high capillary numbers is more pronounced than at low values

3.5.1 Flow dependency of the simulated spatial signal

The droplet shape estimation described in Sec. 3.2.4 shows how the shape of the disperse phase differs from cap aspect ratio unity with increasing Ca-number (Taha and Cui, 2006). As already stated the signal's slope caused by the droplet rear cap is used to derive the correlation factor $\frac{dI}{dx}$. Thus, a change of the droplet curvature caused by velocity fluctuations results in a distorted slope and altered correlation factor $\frac{dI}{dx}$.

Unfortunately, velocity differences of about +/- 30% between the disperse phase velocity and the mean velocity of Taylor slug flows are reported. Different authors even contradict in their interpretation (Abiev, 2013; Fuerstman et al., 2007; Jakiela et al., 2011). To evaluate the error caused by the assumption of a uniform droplet shape derived with the superficial velocity u_0 as shown in Fig. 3.6, an analysis of the error propagation is performed. Therefore, the normalized relative slope changes of the transition between disperse and continuous phase at the normalized level of 0.5 is calculated for a Ca-number range of +/- 30% (Fig. 3.11).

The analysis shows that fluctuating flow conditions do not increase the error of the predicted disperse phase curvature significantly. Within an operational window of +/- 30 percent of the total superficial velocity (u_0) even the biggest deviation lies within boundaries of 5% and is considered acceptable for the given purpose (Chapter. 3.3.4). Thus, the superficial velocity (u_0) and thereby the corresponding Ca-number can be used to estimate a proper rear cap aspect ratio ($a_{cap,b}$) for the spatial signal simulation.

3.5.2 Experimental setup

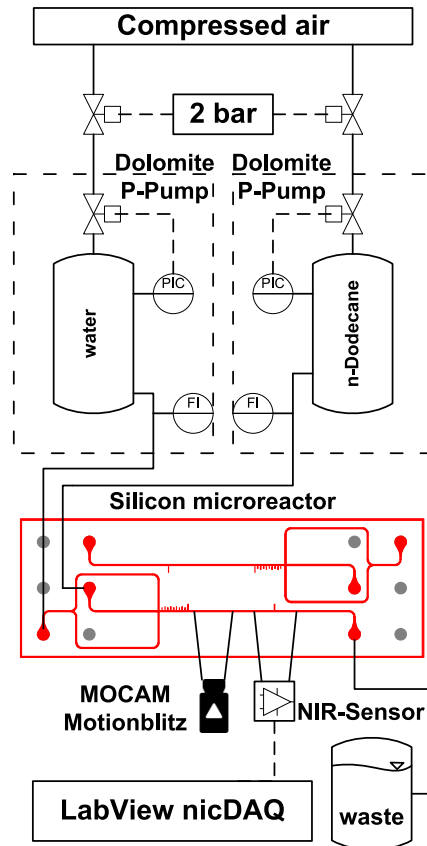


Fig. 3.12.: Experimental design for validating the sensor prototype

Keeping the simulation effort on a low level, a number of simplifications for the droplet shape have been introduced. In order to determine the compliance of simulation and measurement, a sensor prototype has been designed and constructed. A Taylor slug flow is established in a $200\ \mu\text{m}$ diameter microchannel.

As stated in Chapter 3.2.4 the data served by (Taha and Cui, 2006) does not cover the whole relevant Ca_0 -range. To generate further knowledge for lower Ca_0 -numbers, the data is expanded by own measurements. High-speed imaging and image analysis are applied to characterize the droplet shape (rear aspect ratio), and the droplet velocity has been measured. Optical accessibility is achieved via a modified microscope Olympus BX-51 W. For visual data acquisition a high-speed camera (Mikrotron MOCAM Motionblitz) is used at a frame rate of 500 Hz and total measurement time of 2 s each. A self-written adaptive image recognition algorithm detects the interfacial areas to calculate droplet- and slug-lengths, as well as droplet velocity and frequency. Additionally, an edge detection method is used to detect the outer curvature of the droplet front ($a_{cap,f}$) and back ($a_{cap,b}$). An ellipse is fitted into the corresponding center of the droplet's curved interfacial area (Fig. 3.13). The analysis is performed on each high speed image, allowing to detect each droplet several times. Multiple measurement series at different Ca-Number are performed to estimate the droplet velocity influence.

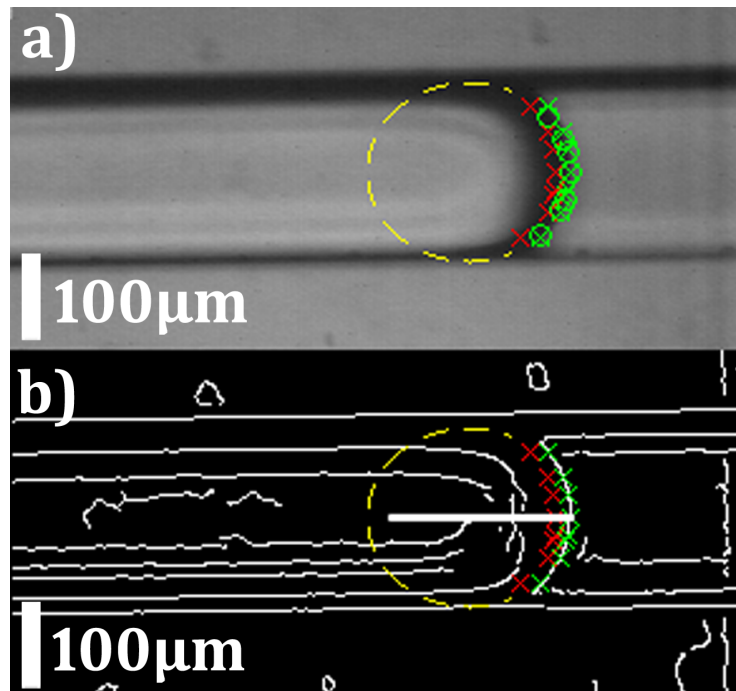


Fig. 3.13.: Example of image recognition algorithm for droplet shape detection. Crosses represent detected points within the interfacial area, circles the used grid point at the droplet outside. a) high speed camera image of an observed droplet with recognized fitted ellipse b) related image of edge detection. Green crosses represent detected points on the droplet outside, red crosses the corresponding center of the curved interfacial area used for ellipsoid fitting

The additional data expands the capillary number dependent cap geometry regression based on the results of (Taha and Cui, 2006) for also low capillary numbers and the droplet-shape can be a priori derived from Ca_0 for the relevant flow-regimes. The results have already been shown in Chapter 3.2.4.

For the validation of the proposed modeled approach, a prototype of the NIR sensor is used in combination with a microfluidic chip (Fig. 3.12). A flow focusing device with a square cross section is fabricated (iX-Factory GmbH, Dortmund) in Silicon using deep reactive ion etching. The channel width is $W = 200 \mu\text{m}$. A LED/photo-diode-system suitable for the NIR domain (wavelength $\lambda = 1450 \text{ nm}$) allows light emission and detection. An aperture to shield stray light is fabricated in plastic with a diameter of about $130 \mu\text{m}$. An analogue circuit amplifies and denoises and stabilizes the signal against external influences. The signal is sampled with a National Instruments DAC at a sampling rate of 20 kHz. A pressure driven flow controlled pump system (Mitos Dolomite P-Pump) is applied to deliver a pulsation-free flow to the flow focusing intersection. All used fluids are filtered to keep particles out of the channel. Before all experiments, the channel is rinsed with deionized water.

3.5.3 Experimental validation results

An intermediate Ca-number Taylor slug flow is chosen to validate the proposed method. The flow is observed simultaneously with a high-speed camera and the presented NIR-sensor. The measurement position for both techniques does not coincide due to the spatial dimension of

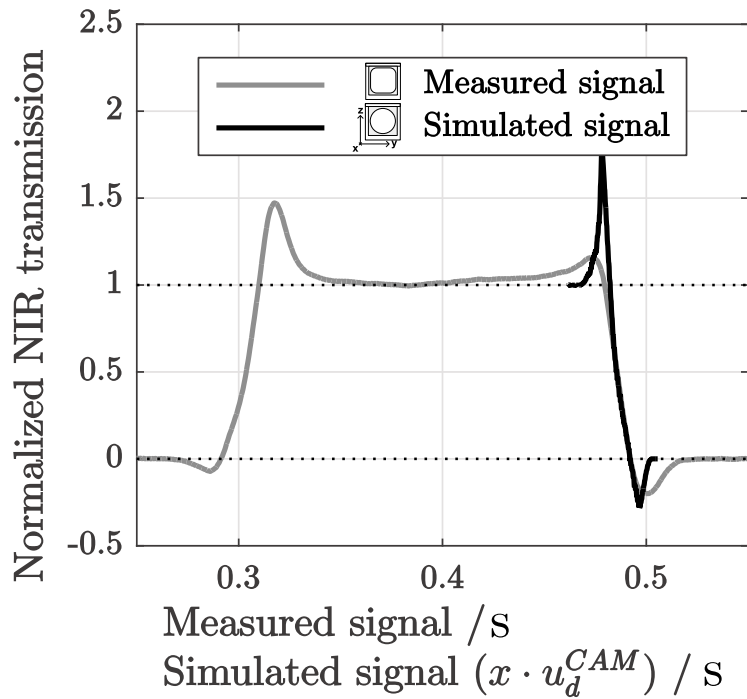


Fig. 3.14.: Measured and simulated NIR transmission signal for the rear cap. The simulated signal derives from using the exact fluidic and geometry parameters of the measurement as input parameters for the simulation. The simulated spatial scaled signal is converted into a time scaled signal by using the measured droplet velocity u_d^{CAM} from highspeed imaging

the microscope objective. Hence, depending on the disperse phase velocity, a residence time between camera registration of a droplet and the NIR detection event has to be taken into account.

The hydrodynamic properties of the Taylor slug flow (droplet length, velocity and cap curvature) are retrieved from the high-speed camera images and used as input parameters for the simulation. Both signals are normalized, whereas no scaling of the x -axis is performed. The signal comparison is depicted in (Fig. 3.14).

The comparison reveals a good agreement between the ray-tracing simulation and the measured signal, although a deviation of the signal peaks can be observed.

This deviation is related to the geometric simplification of the disperse phase shape representation of the simulation. The experimental flow conditions produce a rear cap that adapts to the interdependency of the Laplace-pressure, the geometry and flow conditions. A film separates the disperse phase from the wall. Thus, the center cross section differs significantly from the assumed circular shape. In the rear cap region, this leads to a deviation from the expected ellipsoidal shape of the simulated cap. Since the refraction on a spherical interface provides a more defined focus than other shapes, the peak intensity within the experiment does not reach the simulated signal's intensity. Nonetheless, the simulation captures the curvature of the rear cap well.

In order to validate the entire process of the disperse phase velocity measurement and not only the accordance between model and real droplet, the sensor's velocity results are

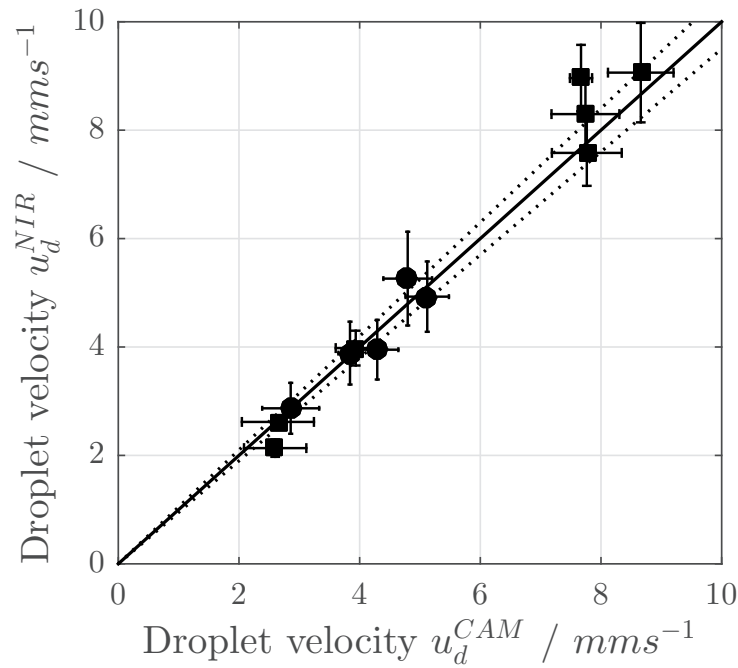


Fig. 3.15.: Comparison of measured velocities by high-speed camera u_d^{CAM} and NIR-sensor u_d^{NIR} for two T-junction microreactors: reactor batch #1 (●) and batch #2 (■). The errorbars depict the standard deviation of both measurement techniques. The relative error of 5% is marked as dotted line (-----)

compared to those retrieved directly from the high speed image sequences (Fig. 3.15). A good agreement between the presented model supported and the validating optical approach is found.

A number of publications report the existence of fluctuations in proposed steady flows (Beer et al., 2009; Korczyk et al., 2011; Peng et al., 2015; Zeng et al., 2015b). However, a thorough investigation is not presented so far. In spite, since long-term effects can only be captured if the fluctuation periods lie within the provided measurement time, authors could perceive them as experimental error. To classify the stability of Taylor flows and identify influential parameters for periodic flow fluctuations a measurement technique capable of performing online long-term measurements is crucial. Additionally, such sensor signals can serve as a parameter for online process control. Thus, long term measurements allow to study the temporal stability of microscopic multiphase flows and offer the possibility to deploy new reactor design guidelines for improved flow stability.

Preliminary flow measurements with the NIR prototype prove the capability of the system and reveal fluctuations in the temporal stability, despite the pulsation free Mitos pumps that keep the volume flows of the two phases constant (Fig. 3.16). Especially the interaction of droplet frequency, length and velocity in combination with downstream geometric properties and the pressure drop hint to relations that are not well examined and understood so far.

This shows the need for carefully monitoring the flow conditions over a longer temporal frame of reference. The measurement time for the presented prototype the measurement time is only restricted by the available hard-disk space.

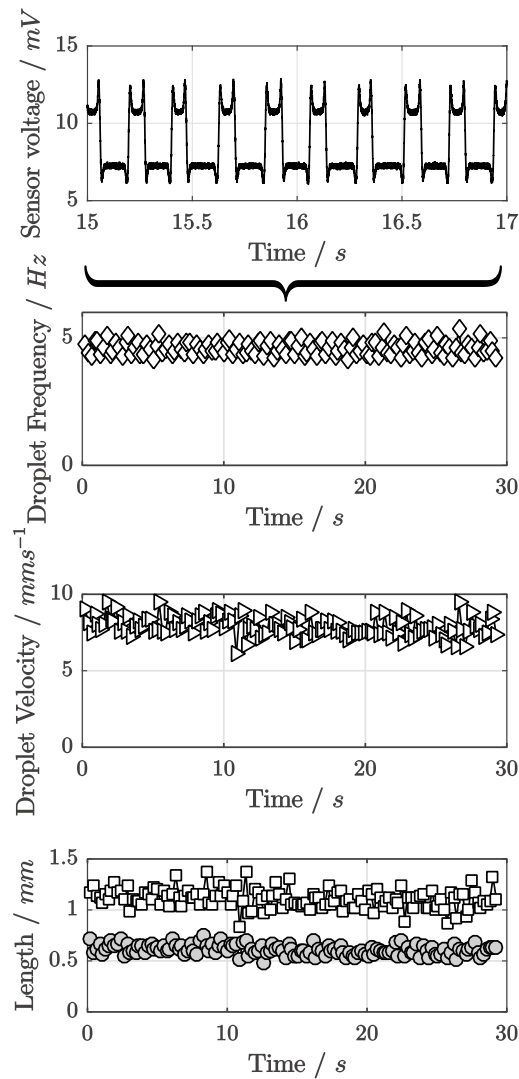


Fig. 3.16.: Resulting data from NIR measurement of a Taylor-Flow at $Ca_0=0.00029$. a) Excerpt of raw NIR-sensor signal at a sampling rate of 20 kHz. b) Analyzed disperse phase frequency over time (\bullet). c) Retrieved droplet velocity u_d^{NIR} (\blacktriangleright) d) Retrieved droplet (\circ) and slug length (\square)

3.6 Conclusion

In this chapter, a new method to derive spatial flow properties of microfluidic Taylor slug flows from a single non-invasive photometric near-infrared sensor is presented. Usually, a sensor pair is needed to retrieve both temporal and spatial flow information, which disqualifies it for embedded systems within highly integrated lab-on-a-chip applications. A second sensor is rendered unnecessary with the presented new approach: The studies identify the disperse phase velocity as a link between the time scaled measurement signal and the desired spatial information. Thus, it can be used to retrieve geometric properties such as disperse phase length from the temporal signal of only one photometry sensor.

The approach combines NIR absorption measurements with simulations of the microfluidic and sensor system. While NIR absorption measurements of the Taylor Flow contribute the

temporal information, simulated NIR signals provide scaling information, that can be used to retrieve the instantaneous droplet velocity from the time scaled measurement signal.

The simulations use a raytracing approach to analyze the sensors NIR transmission signal for a velocity characteristic geometric property. This is found in the slope of the falling transmission signal as a representation of the droplet rear cap passing the sensor. As the measurements and simulations show, the cap curvature itself can be retrieved from the Ca_0 -Number using the total superficial velocity and is only weakly influenced by the instantaneous droplet velocity. It can be used as a geometric input parameter for the simulation and allows to identify the scaling factor in order to retrieve the droplet velocity from time scaled measurements.

The performed simulations are validated by different approaches and show satisfactory agreement with the measurements. A sensitivity analysis shows the good practicability of using the signal slope for the scaling factor determination, because a decreased error-sensitivity can be observed. Thus, influences on the cap curvature caused by changes in the instantaneous droplet velocity during the measurement are compensated.

The new approach shows its capabilities to perform long-term measurements to investigate the stability of Taylor-flows in a first preliminary measurement. This can enhance the process control of especially highly integrated and numbered up flow devices. It was shown, that the droplet cap geometry is geometrically connected to the droplet velocity.

Determining the flow-related cap deformation of Taylor droplets at low Ca -numbers using ensemble averaged high-speed images

“ Experience is what you get when you didn't get what you wanted.

— Randy Pausch
(US american informatician)

The NIR-photometry sensor approach of the previous chapter identified the cap curvature of the droplet as the sensitive parameter, that allows to retrieve temporal, as well as spatial information from the sensor signal. Since no description of the cap curvature is available for the regime of moderate Capillary numbers ($Ca < 0.2$) and no comprehensive studies exist examining the influence of Re and Ca independently, an approach using ensemble image averaging is utilized in this chapter. A new method to reliably measure the droplet deformation is shown, which could act as a flow indicator. The flow-related interface shape deformation of liquid-liquid Taylor flows in square micro channels for $Re < 5$ and $Ca < 0.02$ is quantified by experimental studies and ensemble image averaging. An easy-to-access droplet cap deformation model is utilized, which allows reducing the complex interface curvature information to an ellipse and provide correlation functions to link this deformation ratio to the flow conditions quantitatively. In preparation of the double-binary RIM approach of the following chapter, an experimental approach is introduced using a ternary liquid-liquid material system that allows adjusting Re and Ca independently without surfactant addition by changing the mass-fraction of two liquids forming the continuous phase. In combination, an image processing method to overcome the optical issues arising from the poor image contrast of Taylor droplets with low differences of refractive index to the bulk material is suggested. The presented approach opens the possibility to benchmark numerical studies of the interface deformation and paves the way for improved flow modeling, e.g. pressure drop or relative velocity of Taylor droplets since the flow induced curvature could serve as an indicator of the forces acting on the droplet front and rear.

What follows is based on (Helmert et al., 2019). *Adapted by permission from Springer: Determining the flow-related cap deformation of Taylor droplets at low Ca numbers using ensemble-averaged high-speed images by Helmers, Thorben, Thöming, Jorg and Mießner, Ulrich. Experiments in Fluids 2019*

4.1 Overview

As Abiev (2017) describes, the observed shape of the disperse phase could be used in experiments as a detector indicating the two-phase flow around Taylor droplets and it is therefore interesting for a modeling approach of the excess velocity. The Laplace pressure links the pressure at a surface to the molecular cohesion forces of the fluids in contact and their adhesive interaction across the interface. A superimposed translation causes a change in the local pressure field, exerts additional forces onto the interface and leads to a deformation of the droplet surface curvature (Taha and Cui, 2006; Jakiela et al., 2011; Mießner et al., 2019).

Precise knowledge of the droplet curvature may pave the road for better flow modeling and shows practical concerns: In the previous chapter, a single beam near-infrared photometric sensor was introduced, that is capable of measuring the instantaneous droplet velocity, frequency and droplet length simultaneously. The droplet cap curvature was identified as a relevant calibration factor for the sensor system. A preliminary correlation relates the rear cap deformation to the superimposed flow field properties. Recently Mießner et al. (2019) introduce an analytical estimation of the droplet shape that can be used to improve the evaluation of μ PIV measurements. Their model retrieves the influence of instantaneous flow conditions on the droplet shape from the droplet front and back curvature and therefore requires a reliable description of these properties.

The flow-related evolution of the interface is addressed in simulations (Rocha et al., 2017) and for the viscous flow regime ($Ca > 10^{-2}$) (Sauzade and Cubaud, 2013). However, no systematic experiments to measure the droplet cap curvature of microscopic Taylor flows have been carried out for the capillary flow regime ($Ca < 0.1$, $Re < 5$) at which a variety of lab-on-a-chip devices operate (Vladisavljević et al., 2013).

In this chapter, optical measurements of the interface deformation of liquid-liquid Taylor flow in square channels in the capillary regime ($Re < 5$ and $Ca < 0.02$) are presented to close this gap and successfully correlate the front and back curvature to Ca . An experimental approach is introduced utilizing a ternary liquid-liquid material system that allows adjusting Re and Ca independently by changing the mass-fraction of two liquids forming the continuous phase without the addition of surfactants to tune interfacial tension (Ca). Raw images of the flow at different Ca and Re are recorded with a high-speed camera. An ensemble imaging approach in combination with an adaptive background filter enhances the image contrast for the determination of the droplet cap curvature and reduces the influences of flow fluctuations caused by changes in the flow downstream from the measurement position. In order to access and quantify the deformation of the droplet cap shape, a robust first-order approach is applied, by fitting the cap shape with ellipses (Stone and Leal, 1990).

4.2 Microfluidic fundamentals

The droplet shape dependence on Ca (Taha and Cui, 2006) has been studied qualitatively on a numerical basis. However, an explicit quantitative correlation has not yet been published.

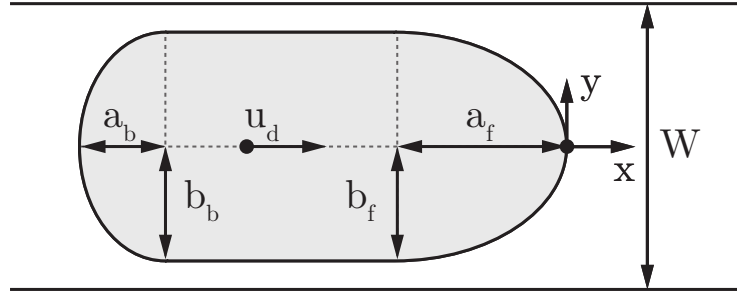


Fig. 4.1.: Declaration of relevant lengths of a droplet flowing through a rectangular microchannel with the droplet velocity u_d . Top-view of x-y-plane, characterizing the droplet with the front (a_f, b_f) and back cap (a_b, b_b), as well as the channel width W

In this work we cover the range $5 \cdot 10^{-5} < Ca < 0.02$ since this is the relevant energy regime for which Taylor Flow formation in microchannels is reported (Fu and Ma, 2015) and the most hydrodynamic models are applied (Han and Shikazono, 2009; Ładosz and Rudolf von Rohr, 2018).

The droplet is geometrically modeled as a combination of a cylindrical body with two ellipsoidal caps: Despite the apparent deviation concerning real three-dimensional Taylor droplets enclosed in square microchannels, the author decided to establish a geometric parameter for the cap deformation of the Taylor droplet, which is easy to access, quantify and compare. Hence, a simplifying but robust approach is applied (Stone and Leal, 1990; Cabral and Hudson, 2006), when fitting the recorded cap shapes with ellipses. As indicated in Fig. 4.1, an elliptic deformation ratio for the cap geometries of the droplets is introduced:

$$k_{c,f} = \frac{a_f}{b_f} \quad (4.1)$$

for the droplet front cap and

$$k_{c,b} = \frac{a_b}{b_b} \quad (4.2)$$

for the droplet back cap. Herein a denotes the major semi-axis of the ellipses and b the minor semi-axis of the ellipse.

For static flow conditions (droplets at rest), both curvatures are identical and spherical $k_{c,f} = k_{c,b} = 1$ (Musterd et al., 2015). Superimposing a flow field, the droplet back gets compressed $k_{c,b} < 1$, while the front is elongated $k_{c,f} > 1$. For moderate Ca the films around the droplet remain thin (Han and Shikazono, 2009), while for higher Ca the film thickness increases and the droplet receives a bullet shape (Abiev et al., 2017).

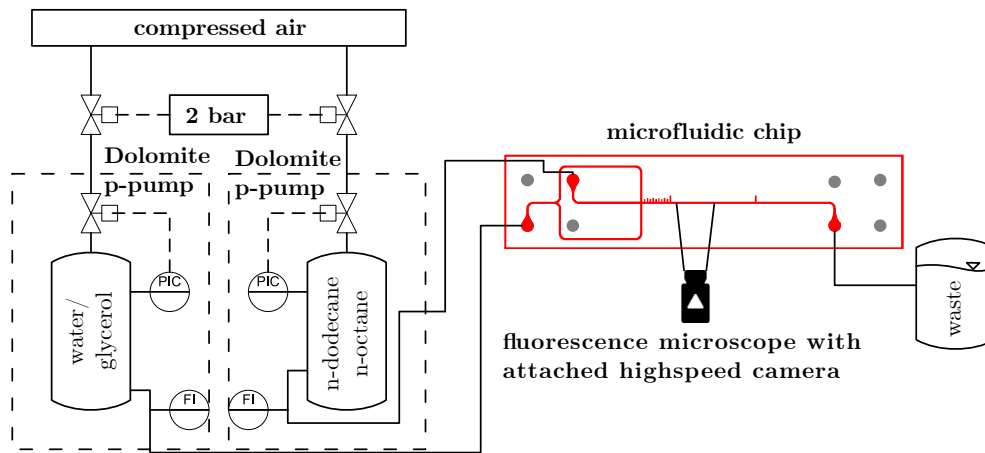


Fig. 4.2.: Experimental setup for a pulsation-free co-current flow through a microfluidic chip made from Si and optical measurements using a fluorescence microscope with attached highspeed camera

4.3 Materials and methods

In order to quantify the interface deformation of Taylor droplets and its relation to the governing flow conditions, a set of experiments is carefully conducted. At first, we describe the experimental setup. Secondly, we present the ternary fluid system for Re and Ca adjustment and subsequently explain the recording mode of the experiments. Finally, ensemble averaging of the recorded images and the curvature detection is explained followed by the determination of droplet velocity.

4.3.1 Experimental setup

The experimental setup of this work (Fig. 4.2) consists of a Silicon-micromixer (manufactured by IMSAS Bremen) using a T-junction for droplet generation and a rectangular cross-section. The channel surfaces are hydrophilized by thermal oxidation with SiO_2 . The geometrical dimensions of the channel are shown in Table 4.1.

Two Dolomite Mitos P-Pumps supply a pulsation-free flow of water/glycerol mixture as a continuous phase and n-dodecane or n-octane as the disperse phase, whereas the flow rates are limited by the used flow meters and camera time resolution ($1 \mu\text{l min}^{-1}$ - $120 \mu\text{l min}^{-1}$). Relevant flow properties such as the droplet shape information, droplet velocity and droplets lengths are recorded with a highspeed camera (Mikrotron MOCAM MotionBlitz) at framerates up to 1 kHz and a resolution of $255 \text{ px} \cdot 292 \text{ px}$. The images are processed by applying ensemble averaging using a MATLAB-script (Sec. 4.3.3).

The microfluidic chip is placed on an Olympus BX51WI fluorescence microscope. For the optical measurements, a Zeiss objective Plan Neofluar 20x with NA of 0.5 to ensure a high light efficiency with an extended depth of focus is used. This allows to record sharp images

of the interface shape. The focal plane is chosen to coincide with the symmetry-plane of the droplet $\frac{H}{2}$.

Tab. 4.1.: Geometrical parameters of the experimental setup

Outer parameter		Unit
channel width W	206	μm
channel height H	197	μm
channel length $\frac{L}{W}$	1000	-
Acquired flowrates	2.59 - 239	$\mu\text{l min}^{-1}$

4.3.2 Ternary fluid system for Re and Ca adjustment

Quantifying the influence of the Ca -number and the Re -number on the cap deformation of Taylor droplets individually, both dimensionless quantities need to be independently accessible. Possible parameters include kinetic, material and geometric properties.

The superficial velocity u_0 as a kinetic property influences both quantities at once and represents one major aspect of the investigation. A change in geometry alters only the Re -number but results in a very expensive setup variation since several different geometrically scaled channel-layouts are needed. Therefore, we rely on the change of material properties.

The surface tension only addresses the Ca -number and is easily accessible when surfactants are applied. However, surfactants accumulate at the interface and cause flow dependent surface tension gradients and a rise of the surface viscosity of the droplet interface (Park, 1992; Olgac and Muradoglu, 2013; Luo et al., 2019). Avoiding this, we focus on the change of viscosity with respect to the change of interface tension, when applying a ternary fluidic material system: We use a trimmed fluid composition of water/glycerol continuous phase against an alkane disperse phase.

If the mass-fraction of glycerol within the continuous phase is varied, viscosity and interfacial tension change simultaneously. However, this change does not happen at the same rate (compare Oh -number). Thus two independent parameters basically determine the flow state at the proposed measurement set. The superficial velocity u_0 introduces the kinetic property change and the mass-fraction of glycerol/ water of the continuous phase ξ_c that accounts for the material properties of the continuous phase.

Given correlations for the essential properties of the continuous phase (interfacial tension σ , mass-fraction ξ_c and density ρ_c , see Eq. 4.3 - 4.5), a combination of Re and Ca results the according kinetic property change u_0 and the mass-fraction of water/glycerol ξ_c ($\xi_c = 0$ indicating pure water, $\xi_c = 1$ indicating pure glycerol).

$$\rho_c = q_{\rho,1} \cdot \xi_c + q_{\rho,0} \quad (4.3)$$

$$\sigma = q_{\sigma,1} \cdot \xi_c + q_{\sigma,0} \quad (4.4)$$

$$\eta_c = q_{\eta,2} \cdot \xi_c^2 + q_{\eta,1} \cdot \xi_c + q_{\eta,0} \quad (4.5)$$

This leads to an equation system that delivers one distinct superficial velocity and glycerol mass-fraction for a specific Re and Ca . Suitable values for u_0 and ξ_c are derived inserting the correlations Eq. 4.4 and 4.5 into the dimensionless quantities and solving the non-linear equation system:

$$Ca = \frac{u_0(q_{\eta,2} \cdot \xi_c^2 + q_{\eta,1} \cdot \xi_c + q_{\eta,0})}{(q_{\eta,1} \cdot \xi_c + q_{\eta,0})} \quad (4.6)$$

$$Re = \frac{u_0 W(q_{\rho,1} \cdot \xi_c + q_{\rho,0})}{q_{\eta,2} \cdot \xi_c^2 + q_{\eta,1} \cdot \xi_c + q_{\eta,0}} \quad (4.7)$$

We combine own measurements with literature data to determine the fitting coefficients (see App. A). The corresponding correlation factors are shown in Tab. 4.2.

Tab. 4.2.: Polynomial coefficients for continuous phase viscosity η_c in mPas, continuous phase density ρ_c in $\text{kg}\cdot\text{dm}^{-3}$ and interfacial tension σ in $\text{N}\cdot\text{m}^{-1}$ for different mass-fractions ξ_c . R^2 denotes the Pearson correlation coefficient

η_c				
range of validity	q_2	q_1	q_0	R^2
$0.00 \leq \xi_c \leq 0.28$	9.6514	1.7769	1.0095	0.9995
$0.28 \leq \xi_c \leq 0.48$	49.223	-21.944	4.5865	0.9995
$0.48 \leq \xi_c \leq 0.64$	82.8	-153.48	36.991	0.9999
$0.64 \leq \xi_c \leq 0.76$	1272.7	-1557.1	488.84	0.9999
ρ_c				
$0.00 \leq \xi_c \leq 1.00$	0	0.2657	0.9938	0.9997
σ				
$0.00 \leq \xi_c \leq 0.70$	0	-0.0206	0.0501	0.9987

4.3.3 Ensemble image averaging and curvature detection

For each parameter set of individual tuned Re and Ca (Fig. 4.5), the front and back curvature of the Taylor droplets is measured from highspeed images (values are given in the appendix of (Helmers et al., 2019)). The glycerol mass-fraction influences the index of refraction of the continuous phase. Small differences of the refractive index between droplet and bulk produce poor contrast with respect to the instantaneous optical interface information. In order to precisely measure the position of the channel wall, the droplet position inside the image and the droplet cap shapes, we remove illumination gradients and enhance the interface information depth with the following image processing steps. We therefore introduce an ensemble image averaging approach (Fig. 4.3), that is explained in the following:

The image time series of the high-speed camera recording contains stationary information (e.g. illumination gradients, channel wall position) and instantaneous information (interfaces of the Taylor droplets). At first, all raw images with the local pixel intensity $I_{(x,y)}$ (Fig. 4.3 a)) are used to create a temporally averaged background image of the entire image sequence

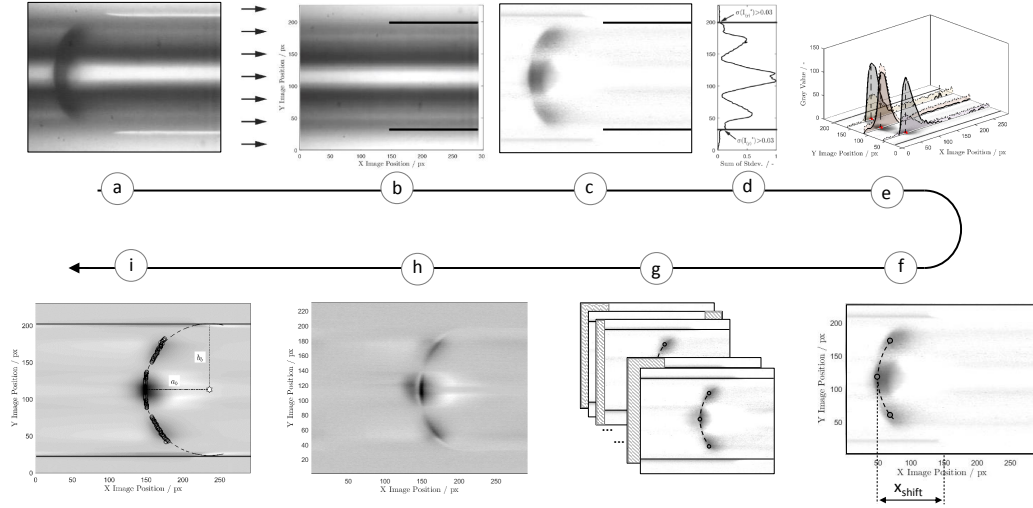


Fig. 4.3.: Scheme of the image processing pipeline and ensemble imaging approach. Overview of image recognition routine for the processed images and their postprocessing steps for small refractive index difference compensation: a) Acquisition of raw highspeed images and calculation of an average background image. b) Average background image. c) Filtered image, that is cleaned from background effects and illumination gradients. It is used for recognition of channel walls by image segmentation. d) Line-wise standard deviation of the image series for wall detection to discriminate between flow induced effects and CMOS-chip noise. e) Within the channel walls (dark, solid lines) three auxiliary lines (white, dashed lines) are defined and the gray values on these lines are analyzed (thin black dashed line raw data, bold solid black line filtered data, see Eq. 4.8). The peaks of these lines are used to identify the interfacial area position at the auxiliary lines (red circles). f) These three points determine the interfacial area position and orientation in each image for further processing. g) Image shifting of all detected interfacial areas to the image center. h) Sum of all shifted droplet images. i) Recognized points x_p (circles) on the interfacial area in the high contrast ensemble averaged image with fitted ellipse x_{ell} (dashed line).

(N -images), which contains only stationary information that does not significantly change within the image time series (Fig. 4.3 b)).

The background image is then used to improve the image quality of every raw image. Therefore the raw images' pixel-intensity $I(x,y)$ is divided by the average background to remove non-homogeneous illumination gradients and to solely receive the instantaneous image information $\hat{I}(x,y)$ (Fig. 4.3 c)).

$$\hat{I}(x,y) = \frac{I(x,y)}{\frac{\sum_{i=1}^N I(x,y)}{N}} \quad (4.8)$$

To discriminate the channel wall from the Taylor flow, the raw image information can not be used since the walls appear blurry. Instead, we divide the image into two segments. The first image segment represents the chip bulk material without any influence of the flow. Here, the intensity fluctuations are mainly caused by the noise of the camera's CMOS-sensors. The second segment shows a direct influence of the flow and therefore exhibits higher fluctuation amplitudes over the sample image sequence. We mathematically discriminate between

flow information and chip-noise by calculating the intensity sum ($\hat{I}^*_{(y)}$) of every horizontal intensity profile over all images of a sequence

$$\hat{I}^*_{(y)} = \sum_x \hat{I}_{(x,y)} \quad (4.9)$$

and subsequently, determine the standard deviation for this intensity sum over the whole time series.

$$\tilde{I}^* = \sqrt{\frac{1}{N-1} \sum_{i=1}^N (\hat{I}^*_i - \bar{I}^*)^2} \quad (4.10)$$

The resulting standard deviation can be evaluated with a threshold analysis (4.3 d)) and allows clear discrimination between the channel void and the channel walls (threshold = 0.05). The transition between the low-intensity standard deviation and the flow related increased standard deviation represents the location of the channel wall.

After the recognition of the wall positions, three reference intensity profiles in flow direction with a distance r from the channel wall are sampled from each corrected image at different channel positions

$$r^+ = \frac{r}{W/2} \quad (4.11)$$

This results in one profile along the channel centerline at $r^+ = 0$ and two profiles at $r^+ = 0.63$ towards the wall position ($r^+ = 1$). Along these reference intensity profiles the highest inverted gray value (darkest point) is identified as the location of the interfacial area (Fig. 4.3 e)). In this manner, three orientation points are obtained: the actual droplet interface position (center line) and references for the droplet cap orientation: the upper and lower orientation points indicate whether a Taylor droplet front or back is detected in the image (Fig. 4.3 f)) with their position relative to the center line reference point.

Avoiding low contrast issues at parameter sets with small refractive index differences between the droplet and the bulk, we apply an approach inspired by ensemble averaging for μ PIV-analysis (Meinhart et al., 2000) and retrieve ensemble averaged images representative for the entire time series of the measurement. An example of the contrast enhancement by the ensemble averaging approach is given in the appendix.

We shift the corrected images of all detected interfaces with similar orientation such, that the centerline position of the interfaces coincides with the image center (Fig. 4.3 g)) x_{shift} along the flow orientation). This results two representative averaged images for each image sequence (front and back cap) with improved contrast (Fig. 4.3 h)), which can be processed at every horizontal intensity profile to locate the interface position. This large number of data points allows a precise fitting of the proposed elliptic interface approximation.

The fitted ellipse follows the equation

$$\frac{x_{ell} - x_{ell,M}^2}{a^2} + \frac{y_{ell} - y_{ell,M}^2}{b^2} = 1 \quad (4.12)$$

Herein $x_{ell,M}, y_{ell,M}$ represent the coordinates of the ellipse center point and a, b are the semi-major and semi-minor axis. We consider

$$b = \frac{W}{2} \quad (4.13)$$

since the fluid films at the walls are thin for the chosen Ca interval (Han and Shikazono, 2009) and define

$$y_{ell,M} = y_{ch} + \frac{W}{2} \quad (4.14)$$

due to symmetry conditions. The x -coordinate of the ellipse center point is fitted to reach a minimum deviation to the recognized points at the interface position. This necessitates the calculation of the ellipse-point distances for each point on the detected interfacial area at each iteration step.

The determination of the distance from a measured interface position (x_p, y_p) to the nearest point on the fitted ellipse (x_{ell}, y_{ell}) of a given optimization step is quadratic, nonlinear and can be described as a minimization problem with boundary conditions. Keeping in mind, that solely numerical solving of the equation system for each point at each iteration step is time-consuming, we decrease the computational effort by a semi-analytical approach. The method of Lagrange multipliers is applied to simplify the optimization problem.

At first, the smallest distance between every data point and the corresponding point on the ellipse $(x_{ell}$ and $y_{ell})$ is identified. We define our objective function as

$$l = \sqrt{(x_{ell} - x_p)^2 + (y_{ell} - y_p)^2} \quad (4.15)$$

For simplification, the minimization of a quadratic term behaves like the minimization of a linear term and l^2 is used to optimize the problem instead of l .

The boundary condition for the optimization problem is the equation of the ellipse itself:

$$\frac{x_M^2}{a^2} + \frac{y_M^2}{b^2} - 1 = 0 \quad (4.16)$$

Introducing the Lagrange-multiplier λ simplifies the problem to a linearization of the boundary condition and objective function:

$$\Lambda_{(x_{ell}, y_{ell}, \lambda)} = (x_{ell} - x_p)^2 + (y_{ell} - y_p)^2 + \lambda \left(\frac{x_M^2}{a^2} + \frac{y_M^2}{b^2} - 1 \right) \quad (4.17)$$

To retrieve the critical points, at which the problem (the distance between ellipse and point) minimizes or maximizes, the gradient is set to zero:

$$\frac{\partial \Lambda}{\partial x} = 0 = 2 \left(\frac{\lambda(x_{ell} - x_m)}{a^2} - x_p + x_{ell} \right) \quad (4.18)$$

$$\frac{\partial \Lambda}{\partial y} = 0 = 2 \left(\frac{\lambda(y_{ell} - y_m)}{b^2} - y_p + y_{ell} \right) \quad (4.19)$$

$$\frac{\partial \Lambda}{\partial \lambda} = 0 = \frac{(x_{ell} - x_m)^2}{a^2} + \frac{(y_{ell} - y_m)^2}{b^2} - 1 \quad (4.20)$$

This equation system can be solved fast and easily to retrieve the extreme values (points on the ellipse with the smallest and longest distance). Inserting these values in Eq. 4.15 and using the minimum of both values reveal the minimum distance of each point to this ellipse. A summation of the distances of all points serves as the quality measure for the iteration step (RMS error).

For the next iteration step the ellipse is varied for different x_m and a , while b is set to $\frac{W}{2}$ and y_m to the channel center position. Subsequently, for each data point the distance to the ellipse is calculated. The ellipse with the lowest sum of distances for all points is used.

4.3.4 Determination of droplet velocity

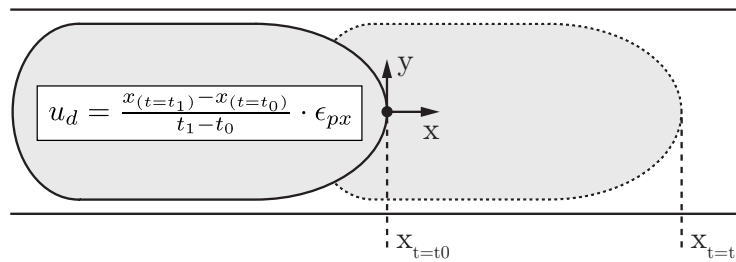


Fig. 4.4.: Droplet velocity determination via image processing. The interface position at time $t = t_0$ is subtracted from the position at $t = t_1$ and multiplied with the image calibration factor ϵ_{px}

The droplet shape depends mainly on Ca , since it is strongly influenced by the viscous flow forces exerted on the droplet's surface. Thus, in order to reference our findings with respect to literature data, the droplet velocity u_d is used.

The determination of the droplet velocity is based on the same images used for shape determination. The droplet position information from the center reference intensity profile is stored for each recognized droplet image and the translation distance of the interface

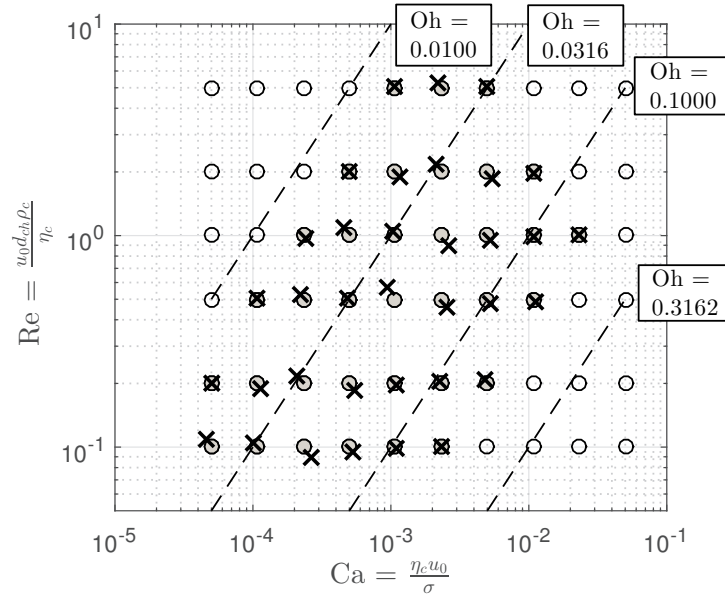


Fig. 4.5.: Overview of fluidic measurement parameters performed for this study. Empty circles represent the points that could not be realized, grey circles represent the parameters accessed in the present set-up. Crosses depict the actual measurement parameter altered by experimental and lab conditions. The resulting errors for Ca and Re are smaller than the marker sizes.

position between the first and last image measured. The average velocity of the droplet is determined by dividing the recognized positions by the time between those image frames (Fig. 4.4):

$$u_d = \frac{x_{imag,2} - x_{imag,1}}{t_{imag,2} - t_{imag,1}} \cdot \epsilon_{px} \quad (4.21)$$

The $\mu\text{m}/\text{px}$ spatial calibration factor ϵ_{px} , which defines the pixel size of the image, is retrieved from the image of a precise calibration target. The droplet velocity determination is performed for each set of 1261 images for every 3 iterations and the standard deviation is calculated.

4.3.5 Experimental procedure

The ternary surfactant-free material system (Chapter 4.3.2) is used to establish a material system of a certain Oh -number. The kinetic parameter u_0 can be changed by tuning the volume flow rate of the pumps. This way we are able to address a wide combination range of Re - and Ca -numbers theoretically.

The measurements are limited, however, in the volume flow range due to the volume flow meters of the Dolomite p-pumps (see Sec. 4.3.1). This restricts the range of measurement (Fig. 4.5) and as a result, we address the system within $0.01 < Oh < 0.2$ (grey circles). Additionally, we prepare the water/glycerol solutions for the bulk phase with a mass-fraction

step width of $\xi = 0.05$ which results in a small disposition of the final experimental points (black crosses) from the ideal planned points (grey circles).

For each targeted Ca/Re -combination three distinct measurements of 1261 images are performed. After each measurement, the pressure pumps are stopped and restarted to ensure independent measurement conditions. Each image sequence of the three measurements allows to detect at least 30 droplets per experimental parameter combination of Re and Ca .

At elevated water/glycerol mass-fractions ξ_c , the optical droplet evaluation aggravates due to the reduced refractive index difference between droplet and bulk. In those cases, n-dodecane is replaced with n-hexane, since it provides a lower refractive index than dodecane and therefore enables measurements at the parameter sets, where the system water/glycerol - dodecane would result in a weak contrast. This is a valid side-step, since the interfacial tension of water/glycerol-dodecane and water/glycerol-hexane is comparable and the material parameters of the continuous phase are used for Re and Ca .

4.4 Results and discussion

At first, we clarify the role of the inertia forces in comparison to the viscous forces (Re) on the Taylor droplet deformation within the addressed parameter range. Next, the influence of the viscous forces is assessed with respect to the interface tension forces (Ca) and a quantification of the cap deformation is delivered. Subsequently, the entire measurements of this study are put into perspective with Taylor droplet velocity data to verify the outcome of this experimental study.

The cap deformation ratio for the front and the back of the Taylor droplets at different Ca is plotted against Re (Fig. 4.6). Our experimental data is supplemented with experimental data from Mießner et al. (2019) and simulation data extracted from Taha and Cui (2006). No trend can be identified in the examined range of $Re = 10^{-5} - 10^1$.

In order to statistically endorse this observation, we apply a two one-sided test procedure (TOST) following Lakens (2017). Usually, the T-Test is performed to reject the null hypothesis, which states the non-existence of a correlation. Therefore, the null hypothesis is formulated explicitly for a single value only (h_0 : property = 0). In order to show that there is no relation, one would need to decline every other possible correlation value, since reliable predictions can only be made if null-hypothesis is declined (falsification principle) (Goertzen and Cribbie, 2010). Non-rejection or "acceptance" of the null-hypothesis is not valid. Thus for a TOST-test, a combined null-hypothesis (h_{01}, h_{02}) is postulated (Schuirmann, 1987). In our case we postulate

Tab. 4.3.: Results of the two one-sided test (TOST) for the cap deformation ratio as a function of Re ($DF = 43, \varepsilon = 0.05, \Delta_{lower} = -0.3, \Delta_{upper} = 0.3$)

	m_i	n_i	R	Z	$Z_{crit, \varepsilon=0.05}$	result
k_f, Δ_{lower}	0.0010	1.0386	0.0087	2.0625	1.645	h_{01} rejected
k_f, Δ_{upper}	0.0010	1.0386	0.0087	-1.9493	-1.645	h_{02} rejected
k_b, Δ_{lower}	-0.0037	0.9219	-0.0443	1.7184	1.645	h_{01} rejected
k_b, Δ_{upper}	-0.0037	0.9219	-0.0443	-2.2935	-1.645	h_{02} rejected

$$h_{01} : R < \Delta_{lower} \quad (4.22)$$

$$h_{02} : R > \Delta_{upper} \quad (4.23)$$

$$h_a : \Delta_{lower} < R < \Delta_{upper} \quad (4.24)$$

with the association interval for the Pearson regression coefficient R in the range of $[\Delta_{lower} = -0.3, \dots, \Delta_{upper} = 0.3]$. If h_{01} and h_{02} are rejected simultaneously, this implies that the population correlation falls within the association interval for h_a .

The procedure for testing the probabilities of the hypotheses is similar to the T-Test (Allen, 1997). Since the standard error of the T-test statistic is related to the chosen association interval of $[\Delta_{lower}, \dots, \Delta_{upper}]$, the normal distribution statistic is preferred. A Fisher z transformation is performed and the corresponding Z-values are used (Fisher, 1915). Depending on the interval border, a left-sided or right-sided probability is applied. For the analysis we chose a significance level $\varepsilon = 0.05$. The properties and results of the TOST-test are shown in Tab. 4.3.

Since $Z < Z_{crit, \varepsilon=0.05}$ for Δ_{upper} and $Z > Z_{crit, \varepsilon=0.05}$ for Δ_{lower} for all tested cases, the targeted significance level ε is reached and the null hypotheses can be rejected. We can state that, based on the measurements, we can not find a statistically confirmed linear correlation for Re in the observed Ca range. Therefore no alternative systematic is coherent. We assume the Reynolds number Re not to significantly influence the cap deformation ratio in the given range.

This is in line with the findings of Kovalev et al., 2018, who identified the Ca -number as the primary influence parameter on the Taylor droplet deformation for moderate Re -numbers. However, at larger Re -numbers a rising influence of inertial forces has been reported (Kreutzer et al., 2005b) when the capillary regime changes towards the viscous regime (Sauzade and Cubaud, 2013).

Concerning the viscous and the surface tension forces (Ca), the cap deformation ratio of Taylor droplets reveals clear trends: In comparison to a resting non-deformed droplet at $k_f = k_b = 1$ (gray dash dotted line, Fig. 4.7) the droplet front is elongated ($k_f > 1$) with rising influence of the viscous forces, while the back cap is compressed ($k_b < 1$). In static conditions ($Ca \rightarrow 0$) the cap curvatures are in correspondence with Musterd et al. (2015).

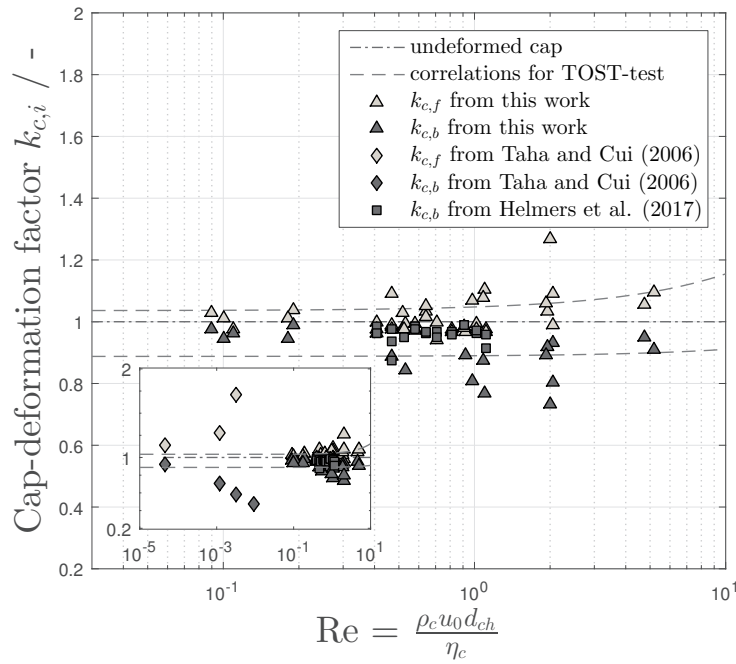


Fig. 4.6.: Measured values for the droplet cap deformation ratios $k_{c,f}$ and $k_{c,b}$ for different Re -numbers at varied Ca regarding Fig. 4.5 extended by literature data. No clear dependence is evident. In an additional TOST-Test for the linear correlation the null-hypotheses h_{01}, h_{02} can be rejected

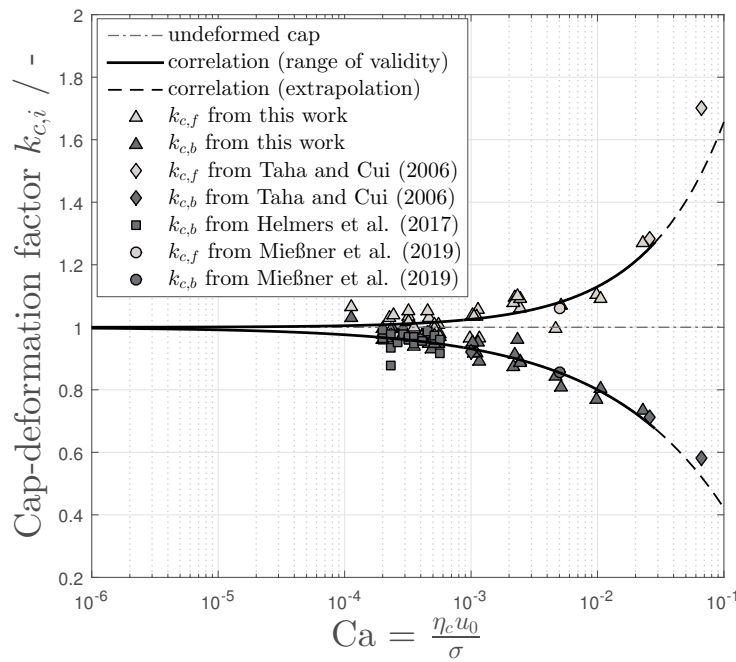


Fig. 4.7.: Measured values and correlation for the droplet cap deformation ratios $k_{c,f}$ and $k_{c,b}$ for different Ca -numbers. For the correlation only data from this work was used, additional data from Taha and Cui (2006) and Mieβner et al. (2019) depict the range of validity of our model ($Ca < 0.02$)

A power regression approach correlates and quantifies the Taylor droplet cap deformation ratio with the Ca -number in accordance to a previous work (Helmers et al., 2017). The

intercept of the deformation axis n_{cap} is set to 1, since for $Ca \rightarrow 0$ it represents the point of the minimum surface energy and therefore a spherical shape.

$$k_{c,i} = m_{cap} \cdot Ca^{c_{cap}} + n_{cap} \quad (4.25)$$

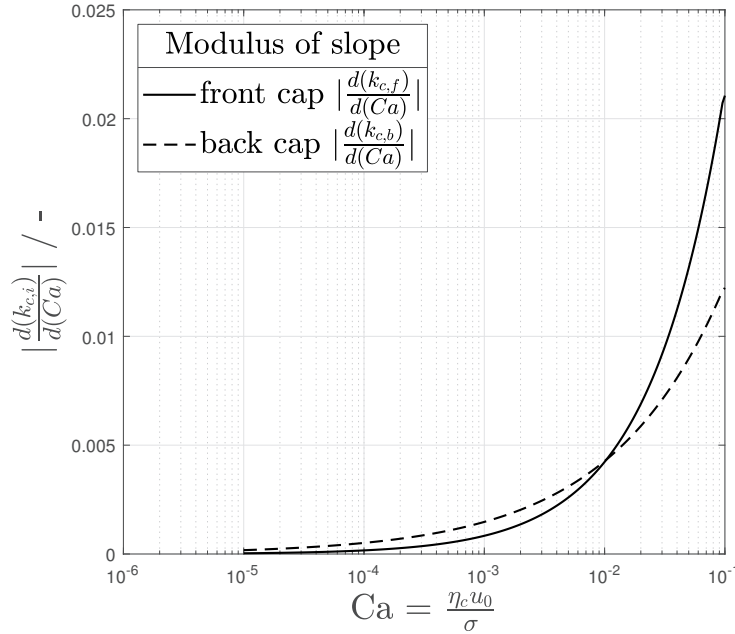


Fig. 4.8.: Modulus of the slope for the flow related cap deformation for rising Ca

A comparison of the correlation with the experimental results in Fig. 4.7 shows a good agreement. To demonstrate the validity of the proposed correlation literature data from Taha and Cui (2006) and Mießner et al. (2019) is used as a test set. An almost perfect match is shown in Fig. 4.9. and the range of validity ($Ca < 0.02$) identified. This lies in the range of the transition between capillary and viscous flow regime, at which especially the influence of the droplet surrounding wall film no longer can be neglected (Han and Shikazono, 2009). The adaption coefficients for the proposed correlations are summarized in Tab. 4.4. Clearly, the Taylor droplet deformation ratios $k_{c,i}$ depend solely on the Ca -number for moderate Re -numbers.

Tab. 4.4.: Values for the fit-functions for droplet shape $k_{c,i}$

Target value	$m_{cap,i}$	$c_{cap,i}$	$n_{cap,i}$
$k_{c,f}$	3.323	0.7041	1
$k_{c,b}$	-1.674	0.4616	1

Rising viscous flow forces cause the droplet cap deformation $k_{c,i}$ to increase. Despite the statement in a previous publication (Helmert et al., 2017), it now becomes obvious, that the droplet back is not generally deformed less with increasing viscous forces ($Ca \uparrow$). Contrarily, the rear cap gets deformed stronger than the front cap for $Ca < 0.008$ as the change of the deformation $\frac{d(k_{c,b})}{d(Ca)}$ shows (Fig. 4.8). Beyond this ($Ca > 0.008$), the frontal deformation is more prominent for an increasing Ca .

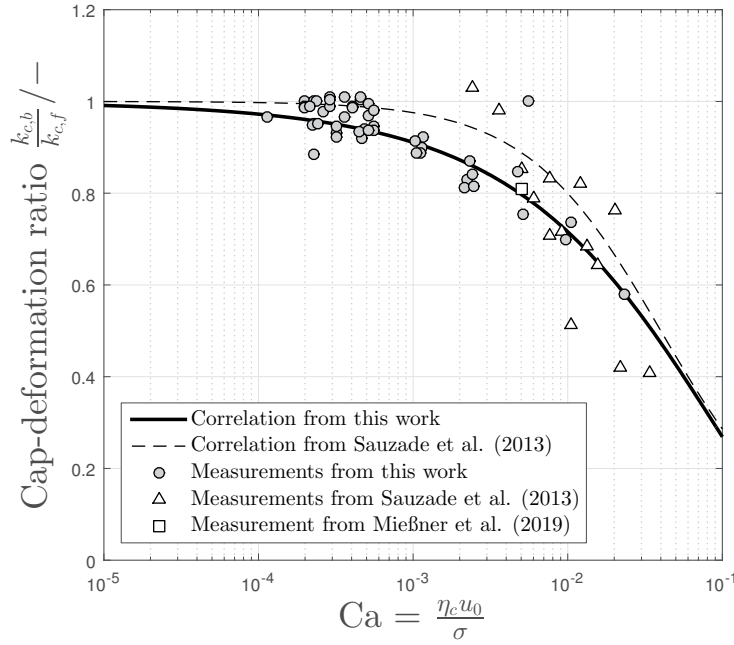


Fig. 4.9.: Comparison of the proposed correlation with measurement data from this work as well as (Mießner et al., 2019) and the correlation from Sauzade and Cubaud (2013). Since Sauzade and Cubaud (2013) base their data on Ca_d with the droplet velocity u_d instead of u_0 , the data is converted using the relative velocity correlation from Jose and Cubaud (2014)

Nevertheless, the absolute forces are stronger at the rear cap. This is in agreement with Wong et al. (2004): The pressure at the front follows $Ca^{\frac{3}{4}}$. The pressure at the back depends with order $\mathcal{O} \approx \frac{3}{4}$ on the film thickness, which in turn correlates with $\frac{\delta}{D} = Ca^{\frac{2}{3}}$ according to Bretherton (1961). The estimation of the exponent results $\approx Ca^{\frac{4}{9}} = Ca^{0.44}$, which is in reasonable agreement with the coefficient found in this work.

Our correlations are compared to measurement data from Mießner et al. (2019) and Sauzade and Cubaud (2013) with respect to the combined deformation ratio of the back and the front cap (Fig. 4.9). Since Sauzade and Cubaud (2013) define their Capillary number Ca_d with the droplet velocity u_d , we convert the measurement data as well as the correlation using the model of Jose and Cubaud (2014) and a mean relative droplet length $\frac{l_d}{w} = 2$ extracted from the images of their publication. Our correlation shows a reasonably good agreement with their experimental data as well as with their correlation.

The velocity data of the measurements serve as a reference to put the measurement range into perspective with experimental data. Jakiela et al. (2011) defined a dimensionless relative velocity between the droplet velocity u_d and superficial velocity u_0 . Values below 1 represent droplet velocities slower than the superficial velocity and larger values faster droplets.

$$u_{rel} = \frac{u_d}{u_0} \quad (4.26)$$

An overview for the relative droplet velocity is given by Jose and Cubaud (2014), who identify the droplet length beside Ca as an influencing factor, whereas data for long droplets

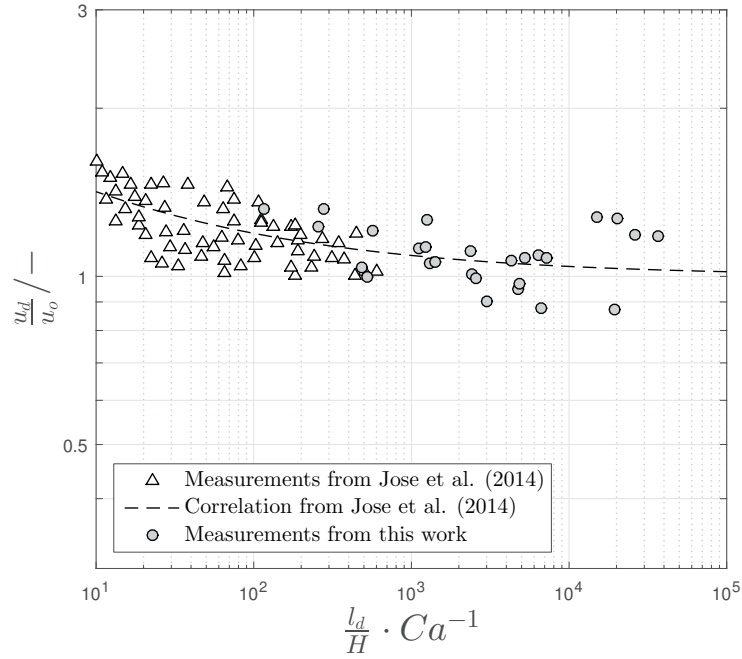


Fig. 4.10.: Measurement data (triangles) and correlation (dashed line) for the relative droplet velocity from Jose and Cubaud (2014) for a Taylor droplet in co-flow. Measurements from this work are added as grey circles

and low Ca is missing, because no stable flow is established for $\frac{l_d}{H}Ca^{-1} > 10^5$ in their design.

The measurements from this study expand their observations and cover the lower Ca at a steady flow, since film drainage is prevented when hydrophilizing the channel walls with SiO_2 . Our measurements are in proper agreement with the correlation of Jose and Cubaud (2014) for the relative droplet velocity (Fig. 4.10). Additionally, our measurements show, that for slow (or long) Taylor droplets (elevated $\frac{l_d}{H}Ca^{-1}$) the relative velocity could also be positive when the wall film is stabilized.

4.5 Conclusion

For the first time, optical measurements of the interface shape of liquid-liquid Taylor flow in square microchannels are used to quantify the relationship between the deformation of the droplet caps (front/back) and the flow conditions in the capillary regime ($Re < 5$ and $Ca < 0.2$) of square microchannels.

An experimental approach using a ternary liquid-liquid material system was introduced and successfully applied, that allows adjusting Re and Ca independently without an addition of surfactants by changing the mass-fraction of two liquids forming the continuous phase. In combination, we report an image processing method to overcome the optical issues arising from the poor image contrast of Taylor droplets with low differences of refractive index to the bulk material.

In the considered flow range no statistically secured influence of the inertia forces (Re) on the Taylor droplet deformation could be detected. The compression of the droplet back cap and the elongation of the droplet front are solely dependent on the rise of the viscous forces with respect to the interface tension forces (Ca). Compression of the back cap appears to happen instantly, as soon as an outer flow field is superimposed. These qualitative findings are in line with numerical investigations of the droplet shape (Rocha et al., 2017). Additionally, a comparison of the Taylor droplet relative velocity with findings from (Jose and Cubaud, 2014) validates the range of flow parameters chosen for this study.

The simplifying interface curvature estimation approach using ellipses allows to reduce the flow related deformation to an easy-to-access droplet cap aspect ratio. Our correlation functions provide the possibility to benchmark numerical studies of the interface deformation and improve analytic modeling approaches (Mießner et al., 2019): The difference of the deformation between the front and back of the Taylor droplets (with rising Ca) indicates a flow related pressure change. This pressure gradient indicator could be used to quantify the rise of relative velocity analytically in surfactant-free, wall-wetting Taylor flows as reported by Jose and Cubaud (2014).

Modeling the excess velocity of low-viscous Taylor droplets in square microchannels

“Failure is an option here. If things are not failing, you are not innovating enough.

— **Elon Musk**

(South African entrepreneur and engineer)

Based on the previous chapter and being motivated by the findings of the measurements with the NIR-photometry prototype, in this chapter a model to determine the excess velocity of Taylor droplets in square microchannels is introduced. This velocity difference between the droplet and the total superficial velocity of the flow has a direct influence on the droplet residence time and is linked to the pressure drop. Since the droplet does not occupy the entire channel cross section, it enables the continuous phase to bypass the droplet through the corners. A consideration of the continuity equation generally relates the excess velocity to the mean flow velocity.

The quantification of the bypass flow is based on a correlation for the droplet cap deformation from its static shape. The cap deformation reveals the forces of the flowing liquids exerted onto the interface and allows estimating the local driving pressure gradient for the bypass flow. The characterizing parameters are identified as the bypass length, the wall film thickness, the viscosity ratio between both phases and the Ca -number. The proposed model is adapted with a stochastic, metaheuristic optimization approach based on high-speed camera measurements. In addition, the model is successfully verified with published empirical data.

This chapter covers the range $5 \cdot 10^{-5} < Ca < 0.1$, since this is the relevant flow regime in which Taylor flow formation in microchannels is reported (Fu and Ma, 2015) and the most hydrodynamic models are applied (Han and Shikazono, 2009; Ładosz and Rudolf von Rohr, 2018).

What follows is based on T. Helmers, P. Kemper, J. Thöming and U. Mießner (2019). "Modeling the excess velocity of low-viscous Taylor droplets in square microchannels". Available via [arXiv:1905.02811](https://arxiv.org/abs/1905.02811).

5.1 Overview

Chemical reactions on the microscale are often performed in monolith reactors. In such reactors, a high number of parallelized channels with hexagonal or square channel cross-section offer a high specific reaction area for wall placed catalysts at small wall thickness. Besides disperse phase size distribution and formation frequency (Fu and Ma, 2015), the actual droplet velocity is essential for the droplet residence time in the reactor. It determines the contact time of the educts and influences the pressure drop of the reactor (Ładosz and Rudolf von Rohr, 2018). In a parallel reactor, an exact knowledge of the pressure drop is especially necessary since a steady educt supply for each individual single reactor is needed to ensure stable and efficient working conditions (Schubert et al., 2016).

Several publications have dealt with the droplet velocity in rectangular capillaries and observed a droplet velocity mostly faster than the superficial velocity (see Sec. 5.2.1). For flows in circular capillaries, where only a thin wall film of the continuous phase is present, this velocity difference is well understood (Abiev, 2017), while for rectangular microchannels a variety of explanations exist, that mostly correlate the relations from measurements (Jose and Cubaud, 2014). This complicates the transfer of results to other flow applications or altered process parameters since local and instantaneous hydrodynamic parameters may not be taken into account by the models and correlations.

This chapter aims to establish a model to determine the droplet velocity from the actual flow conditions: e.g. droplet length, material properties, and the Ca -number. In a first step, a concept for the relative droplet velocity is developed, which relates this velocity to extrinsic parameters, allowing symmetrical scaling. From this concept, the bypass flow through the gutters as well as the film-thickness are identified as the prominent parameters for the excess velocity.

In the next step, a model is developed that uses the surface curvature of the gutters to retrieve the local pressure at the entrance and outlet of the gutter's corner as a driving force. The bypassing gutter flow is calculated based on the counterplay between this driving force and the gutter length, as well as a viscosity correlated resistance factor β . The local droplet curvature at the gutter entrances is derived with an analytical interface shape approximation (Mießner et al., 2019) and a correlation for the droplet cap curvature based on the Ca -number from previous work (Helmers et al., 2019). The model is successfully validated by high-speed camera measurements.

5.2 Model development

In the following a model for the excess velocity of Taylor droplets in rectangular microchannels is developed and validated. For that purpose, the NIR-sensor from Sec. 3, as well as the droplet cap correlation (Sec. 4.4) are used. After identification, the model input parameters are adjusted to measurement data using a metaheuristic approach (Genetic Algorithms). But at first, the modeled property is precisely derived from the continuous equation.

5.2.1 Concept of excess velocity

Based on the instantaneous droplet velocity u_d , that is evident and directly measurable via optical or electrical measurement techniques (Kalantarifard et al., 2018), different explanatory approaches for the deviation of superficial velocity u_0 and droplet velocity u_d have been reported.

Liu et al. (2005) define this relative difference as slipping velocity u_{slip} , Howard and Walsh (2013) as relative drift velocity u_{drift} , Angeli and Gavrilidis (2008) as relative bubble velocity u_{rel} and Abadie et al. (2012) as dimensionless droplet velocity. Jakiela et al. (2011) focus directly on the ratio of $m = \frac{u_d}{u_0}$ and name this quotient droplet mobility according to Bretherton (1961). For this work, we like to summarize these approaches as a slipping velocity:

$$u_{slip} = \frac{u_d - u_0}{u_d} = 1 - \frac{u_0}{u_d} \quad (5.1)$$

In those concepts, the desired quantity is scaled with an intrinsic value such as the instantaneous droplet velocity, which leads to normalization effects as values $u_{slip} < 1$ and $u_{slip} > 1$ are not normalized symmetrically (Fig. 5.1). This behavior has to be taken into account when experimental or simulative data is interpreted.

In this approach, we scale the velocity difference with the superficial velocity as an extrinsic property and, staying in the term of extrinsic denomination, define it as an excess velocity

$$u_{ex} = \frac{u_d - u_0}{u_0} = \frac{u_d}{u_0} - 1 \quad (5.2)$$

In this manner, u_{ex} provides values around 0 for droplet velocities equal the superficial velocity (plug flow), while positive and negative values indicate droplets, which are moving respectively faster or slower than the superficial velocity.

The advantage of this extrinsic concept stands out in a comparison of both approaches (Fig 5.1). The first shown intrinsic concept (slip velocity) leads to an asymmetrical scaling behavior especially for droplets with $u_d < u_0$, since $u_{slip} < 0$ decreases stronger than $u_{slip} > 0$ would increase. For applications like balancing or process modeling, a linear behavior is mandatory, to prevent an additional bias of the modeled quantities towards any direction $u_d < u_0 \vee u_d > u_0$.

A description for the excess velocity can be derived from the volume flows around moving droplets (Eq. 5.3). The continuity equation describes the interrelation between the gutter flow and the outer driving flows and it delivers the relation between the total flow (Q_0) and the volume flow fractions of the disperse (Q_d) as well as the continuous phase (Q_c). Considering the unit cell of a single slug and an adjoining droplet, the continuous phase

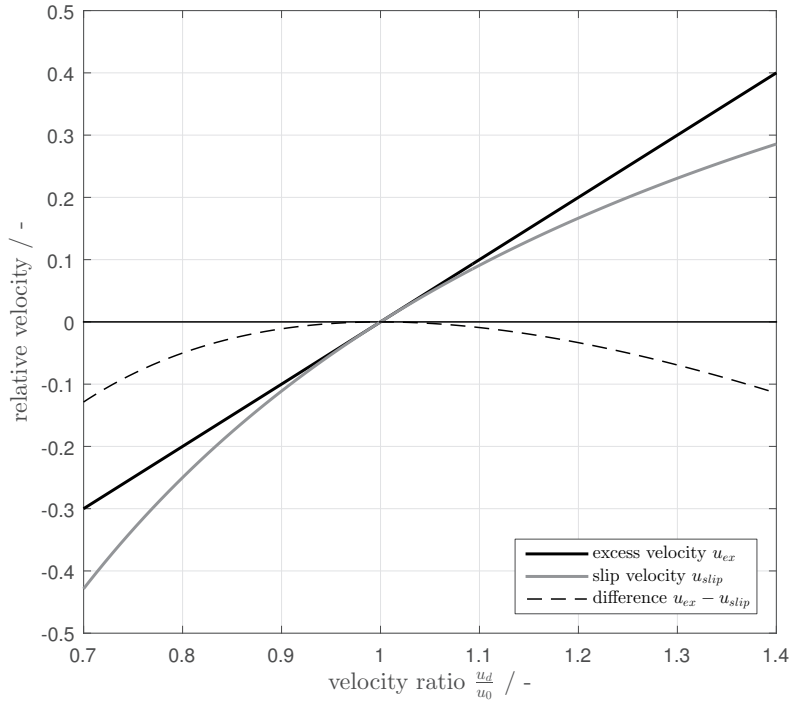


Fig. 5.1.: Comparison of different concepts of calculating the relative droplet velocity: excess velocity from this work (black solid line), slip velocity (grey solid line) and difference of both concepts (black dashed line)

parts into the volume flow of the slug (Q_s), the flow through the gutters (Q_g) and through the wall film (Q_f):

$$Q_0 = Q_d + Q_c = Q_d + (Q_s + Q_g + Q_f) \quad (5.3)$$

If we depict the flows at a moving Taylor droplet (Fig. 5.2 a) and introduce a stationary control surface Γ (Fig. 5.2 b), velocities can be retrieved from the balances, while two differing flow states are possible: In the case of a droplet passing Γ , the slug volume flow through the control surface is $Q_s = 0$ (since there is no slug present). For a slug passing Γ , only the slug volume Q_s is present. As one can see, the use of a stationary point of view leads to instationary terms within the balances.

If the coordinate system is changed from a fixed frame to a moving frame system by moving the control surface with an arbitrary velocity u_{rel} , the balances become stationary and relative velocities become visible (Fig. 5.2 c). For this moving coordinate system, an additional volume flow Q_{rel} adds to the balances that results from the transformation of the coordinate system (Fig. 5.2 d):

$$Q_{rel} = u_{rel} \cdot A_{ch} \quad (5.4)$$

This changes Eq. 5.3 to:

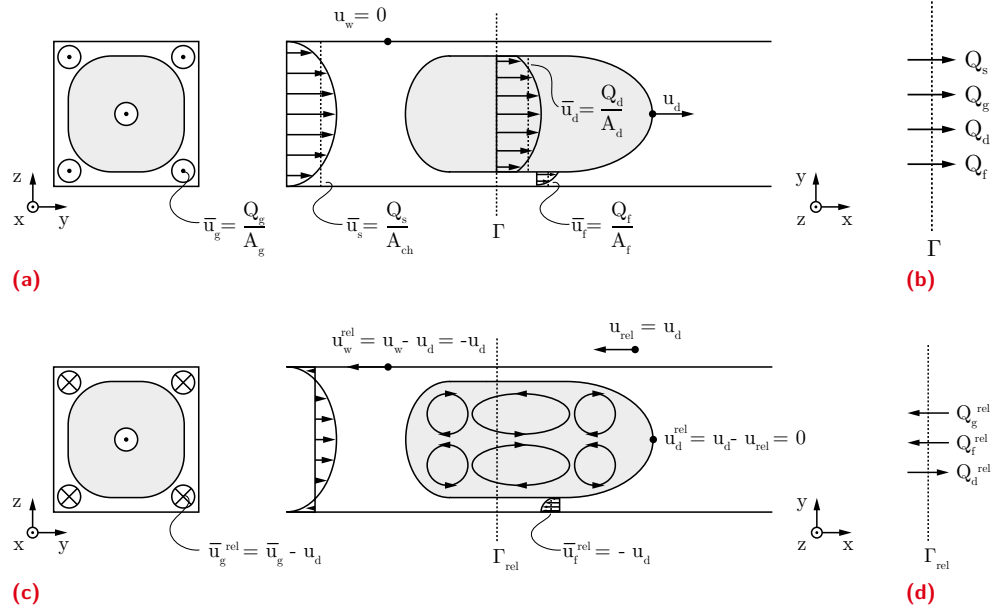


Fig. 5.2.: Prominent averaged and local velocity for a flowing droplet, overlined entities represent area-averaged velocities. The film flow is not shown in this drawing. a) Velocities for a fixed point-of-view (fixed frame), b) flow balance at a steady control surface c) velocities for a moving point-of-view with the velocity u_d (moving frame) d) flow balance at a moving control surface

$$Q_0 - Q_{rel} = Q_d + Q_g + Q_f - Q_{rel} \quad (5.5)$$

With knowledge of the specific areas for each distinct volume flow rate, the averaged velocities can be calculated. Following 5.3 a) + c) we conclude for the gutter area A_g of all four gutters

$$A_g = 4 \left[\left(\overline{R_g}^2 - \frac{\pi \overline{R_g}^2}{4} \right) + 2\delta \overline{R_g} + \delta^2 \right] \quad (5.6)$$

with δ denoting the wall film thickness and $\overline{R_g}$ representing the mean dynamic gutter radius, which is described later in Sec. 5.2.2. For the cross-sectional film area A_f we state with the aspect ratio $ar = WH^{-1}$

$$A_f = \frac{4\delta}{H} H^2 \left(\frac{1 + ar}{2} - 2 \frac{\overline{R_g} + \delta}{H} \right) \quad (5.7)$$

The droplet cross-sectional area A_d is delivered combining A_g and A_f :

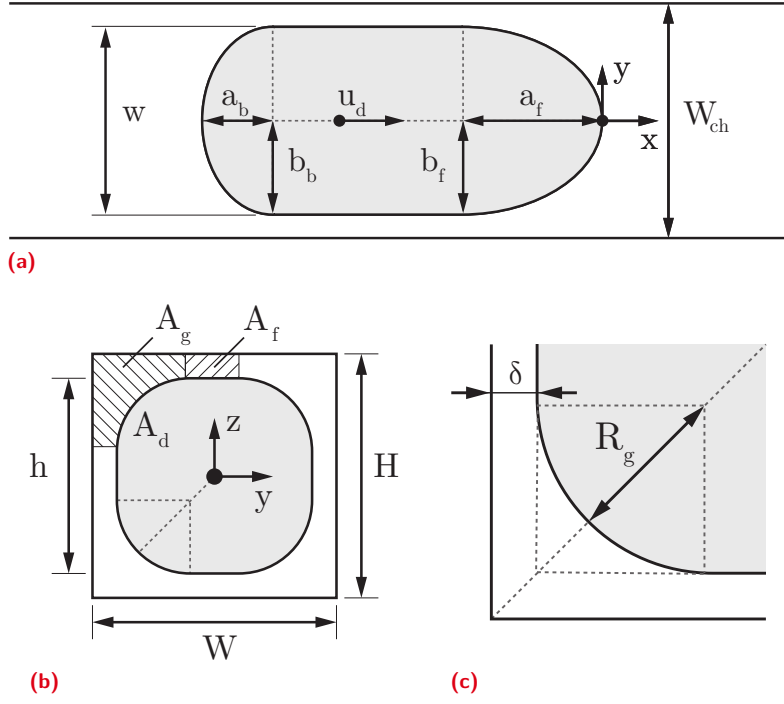


Fig. 5.3.: Declaration of relevant geometry for the model of a Taylor-droplet flowing through a rectangular microchannel with the droplet velocity u_d . a) Top-view of x-y-plane, characterizing the droplet with the front (a_f, b_f) and back cap (a_b, b_b), as well as the channel width W and droplet width w b) droplet front-view in y-z-plane with the droplet area A_d , gutter area A_g , film area A_f , channel height H and the droplet height h . Only one representation of each area is shown c) close-up of the droplet corner region with gutter radius (R_g) and the film-thickness δ

$$A_d = A_{ch} - (A_g + A_f) \quad (5.8)$$

With the cross-sectional areas of the droplet, the gutter and the wall film, the volume flow rates can be rearranged to area-averaged velocities and Eq. 5.5 becomes

$$u_0 A_{ch} - u_{rel} A_{ch} = \bar{u}_d A_d + \bar{u}_g A_g + \bar{u}_f A_f - u_{rel} A_g - u_{rel} A_d - u_{rel} A_f \quad (5.9)$$

Herein \bar{u}_d , \bar{u}_g and \bar{u}_f are area-averaged velocities of the droplet, gutter and film.

For the droplet ($Q_d = \bar{u}_d A_d - u_{rel} A_d$) and the film volume flow ($Q_f = \bar{u}_f A_f - u_{rel} A_f$), the transition velocity u_{rel} equals the stagnation point velocity u_d , since we assume incompressibility, mass-conservation, a stagnant film and a stationary droplet shape (Rocha et al., 2017)

$$\bar{u}_d = u_d \stackrel{!}{=} u_{rel} \quad (5.10)$$

Additionally we assume the averaged velocity in the thin wall films to be insignificant for $Ca < 0.2$

$$\overline{u_f} \approx 0 \quad (5.11)$$

Therefore Eq. 5.9 simplifies to

$$(u_0 - u_d)A_{ch} = \overline{u_g^{rel}}A_g + (0 - u_d)A_f \quad (5.12)$$

Herein $\overline{u_g^{rel}} = \overline{u_g} - u_d$ represents the relative gutter velocity, which dissipates flow energy within the gutter. Simplification and combination with Eq. 5.2 leads to

$$\frac{u_d}{u_0} - 1 = u_{ex} = -\frac{\overline{u_g^{rel}}A_g}{u_0A_{ch}} + (u_{ex} + 1)\frac{A_f}{A_{ch}} \quad (5.13)$$

We neglect the terms that are small of higher order (see Appendix B) and retrieve an expression for the excess velocity:

$$u_{ex} = -\frac{Q_g^{rel}}{Q_0} + \frac{A_f}{A_{ch}} \quad (5.14)$$

The relative gutter volume flow (Q_g^{rel}) and the cross-sectional area of the wall film (A_f) are the most prominent influencing quantities for the excess velocity. Thus the proposed model aims to especially determine these quantities.

5.2.2 Model specification

The considerations of the previous section identify the volume flows significantly determining the excess velocity. In a second step, we clarify the relevant influential parameters on these volume flows and their interconnection.

For the proposed modeling approach, we adapt a greybox model following Hango and Cameron (2001). Our model is developed from engineering principles, hydrodynamic considerations (see Sec. 5.2.1) and well-defined equations, whereas the initialization of a part of the influential parameters is based on measured data. The underlying relations can be described as an intermediate concept between a black box (completely based on measurement data) and a white box model (based only on analytically well-known equations and engineering principles).

As depicted in the previous chapter (Sec. 5.2.1), we assume a droplet flowing through a rectangular microchannel with its properties: The thin wall film cross-section A_f is

determined by Eq. 5.7 and depends on the channel height H , the channel aspect ratio ar and the film thickness δ . To determine δ , we apply the model of Han and Shikazono (2009), which holds for $Ca < 0.2$.

The relative volume flow through the gutter (Q_g^{rel}) is derived from the pressure difference along the gutters as suggested by Abiev (2017). Therefore knowledge of the relevant pressures is crucial. It can be determined from the dynamic interface deformation caused by the moving liquids through the gutters in flow direction (Abate et al., 2012). Stagnant droplets have a static cap shape with a circular outline according to Musterd et al. (2015). When set into motion, the moving liquids exert forces onto the interface and cause a dynamic shape deformation (Rocha et al., 2017).

A model proposed by Mießner et al. (2019) allows to approximate the droplet shape and gutter diameter. The model implies that the deformation difference of the dynamic droplet cap shape between the droplet front and back results in a change of the gutter radius from the static shape. The cross-sectional gutter area A_g widens asymmetrically from back to front with the growing gutter radii to accommodate the relative volume flow Q_g^{rel} of the continuous phase through the gutter. The gutter entrance at the droplet front is therefore larger than the gutter exit of the droplet back. Utilizing their model, the dimensionless radius of these gutters can be calculated from the flow related curvature of the droplet.

The gutter radius $k_{g,i}$ is therefore defined as a fraction of the droplet height h . For the case of present wall films the term is expressed as follows:

$$k_{g,i} = \frac{R_{g,i}}{h} = \frac{R_{g,i}}{H - 2\delta} \quad (5.15)$$

In order to simplify the geometry, we define a mean gutter radius \overline{R}_g using Eq. 5.15:

$$\overline{R}_g = \frac{k_{g,f}(H - 2\delta) + k_{g,b}(H - 2\delta)}{2} \quad (5.16)$$

$$= \frac{(H - 2\delta)(k_{g,f} + k_{g,b})}{2} \quad (5.17)$$

which is also used for the mean cross-sectional area A_g derived with Eq. 5.6.

In a previous work (Helmers et al., 2019), a quantification of the droplet cap deformation with an elliptic approximation of the cap outline is introduced

$$k_{c,f} = \frac{a_f}{b_f} \quad (5.18)$$

$$k_{c,b} = \frac{a_b}{b_b} \quad (5.19)$$

The ratio of the semi-major a and semi-minor axis b of the droplet cap curvature is introduced as deformation ratios $k_{c,i}$ at the droplet front and back. They become $k_{c,f} = k_{c,b} = 1$ when describing the static circular droplet cap shape of the droplet front and back. For the dynamic cap shape, under the influence of the moving liquids, the droplet front appears elongated $k_{c,f} > 1$ and the back cap is compressed in flow direction $k_{c,f} < 1$. Hence we introduce a correlation to describe these relations: The cap curvature only depends on the Ca -number for moderate flows ($Re < 5$):

$$k_{c,i} = m_{cap} \cdot Ca^{c_{cap}} + n_{cap} \quad (5.20)$$

With the correlation approach from a recent publication and the model from Mießner et al. (2019), we are able to calculate the Laplace pressure at the gutters. We assume a linear connection between the gutter front and the back of the droplet body, since the curvature of the gutter in flow direction is negligibly small. In this case, the mean interface curvature at the gutter entrance and its exit depends on the gutter radii only and the flow induced Laplace pressure difference equals:

$$\Delta p_{g,f} = \sigma \left(\frac{1}{R_{g,f}^{stat}} - \frac{1}{R_{g,f}} \right) \quad (5.21)$$

$$\Delta p_{g,b} = \sigma \left(\frac{1}{R_{g,b}^{stat}} - \frac{1}{R_{g,b}} \right) \quad (5.22)$$

Those deformation related pressures at the droplet front and back provide a link to the driving pressure difference Δp_{LP} along the gutter length in the flow direction. Due to symmetry, the static terms cancel out:

$$\begin{aligned} \Delta p_{LP,fb} &= \Delta p_{g,f} - \Delta p_{g,b} \\ &= \sigma \left(\frac{1}{R_{g,f}} - \frac{1}{R_{g,b}} \right) \end{aligned} \quad (5.23)$$

Using the dimensionless expression from Eq. 5.15 this results in

$$\Delta p_{LP,fb} = \sigma \left(\frac{1}{k_{g,f}(H - 2\delta)} - \frac{1}{k_{g,b}(H - 2\delta)} \right) \quad (5.24)$$

$$= \left(\frac{\sigma}{H} \right) \frac{1}{(1 - \frac{2\delta}{H})} \left(\frac{k_{g,b} - k_{g,f}}{k_{g,f} \cdot k_{g,b}} \right) \quad (5.25)$$

for the flow induced pressure difference as a driving force.

The relative volume flow rate through the four gutters Q_g^{rel} can be modeled as a laminar pressure driven flow (Bruus, 2008) and it is linked to this pressure difference with a hydrodynamic resistance Ω :

$$Q_g^{rel} = \frac{1}{\Omega} \Delta p_{LP,fb} \quad (5.26)$$

The hydrodynamic resistance Ω is defined by Ransohoff and Radke (1988) and Shams et al. (2018) as

$$\frac{1}{\Omega} = \frac{\overline{R}_g^{-2}}{\beta} \frac{A_g}{\eta_c \overline{l}_g} \quad (5.27)$$

Besides the mean gutter length \overline{l}_g , herein β is a dimensionless factor, that represents the geometrical obstructions of the gutter flow, as well as the viscous coupling of both flow phases. In accordance with the simulation results of Shams et al. (2018), we declare an influence from the viscosity ratio λ of the flow phases to take care of the viscous coupling effects:

$$\beta = m_\beta \cdot \lambda^{c_\beta} + n_\beta \quad (5.28)$$

The mean gutter length \overline{l}_g can be derived from the droplet length l_d , if the gutter distance $\Delta x_{g,i}$ from the caps is subtracted:

$$\overline{l}_g = l_d - \Delta x_{g,f} - \Delta x_{g,b} \quad (5.29)$$

The gutter distance from the front and back droplet tip $\Delta x_{g,i}$ was defined by Mießner et al. (2019) as

$$\Delta x_{g,i} = k_{c,i} \frac{H}{2} \left[\left(ar - \frac{2\delta}{H} \right) + \left(1 - \frac{2\delta}{H} \right) (1 - 2k_{g,i}) \right] \quad (5.30)$$

The above stated considerations lead to the final description for the relative volume flow through the gutters

$$Q_g^{rel} = \frac{\overline{R}_g^{-2}}{\beta} \frac{A_g}{\eta_c \overline{l}_g} \Delta p_{LP,fb} \quad (5.31)$$

Herein \overline{l}_g and Δp_{LP} depend on \overline{R}_g as the preceding considerations show. Thus \overline{R}_g has the most prominent influence feature besides β . Inserting Eq. 5.31 and Eq. 5.28 in Eq. 5.14 delivers

$$u_{ex} - \frac{A_f}{A_{ch}} = \frac{1}{Ca} \frac{1}{\beta} \frac{\overline{A}_g}{A_{ch}} \frac{\overline{R}_g^2}{l_g H} \frac{1}{(1 - \frac{2\delta}{H})} \left(\frac{k_{g,b} - k_{g,f}}{k_{g,f} \cdot k_{g,b}} \right) \quad (5.32)$$

expanding with $\frac{W}{\overline{W}}$ and inserting l_g (Eq. 5.29) we receive the final expression for the excess velocity:

$$u_{ex} = \frac{1}{Ca} \frac{1}{\beta} \frac{W}{l_d} \frac{\overline{A}_g}{A_{ch}} \frac{\overline{R}_g^2}{\left(1 - \frac{\Delta x_{g,f}}{l_d} - \frac{\Delta x_{g,b}}{l_d}\right)} \frac{1}{A_{ch}} \frac{1}{(1 - \frac{2\delta}{H})} \left(\frac{k_{g,b} - k_{g,f}}{k_{g,f} \cdot k_{g,b}} \right) + \frac{A_f}{A_{ch}} \quad (5.33)$$

It has to be pointed out that the model is usable within the capillary regime $Ca < 0.02$ since the model for the wall film-thickness from Han and Shikazono (2009), the analytic interface model from Mießner et al. (2019) and the droplet curvature correlation from a recent work (Helmert et al., 2019) are valid in this range. At higher Ca in the viscous regime, different flow conditions with thicker wall films (Jose and Cubaud, 2014) as well as a higher influence of Re are reported (Kreutzer et al., 2005b).

5.2.3 Model calibration

The final expression for the excess velocity (Eq. 5.33) depends on accessible data like W , ar and l_d as well as on \overline{R}_g , β , $k_{g,f}$, $k_{g,b}$, $\Delta x_{g,f}$ and $\Delta x_{g,b}$, whereas the latter are also related to the gutter radii \overline{R}_g . As shown in the previous section, the parameters can be calculated from the droplet cap curvatures $k_{c,f}$ and $k_{c,b}$ and via a measurement based model calibration. The 6 parameters $m_{cap,f}$, $m_{cap,b}$, $n_{cap,f}$, $n_{cap,b}$, $c_{cap,f}$, $c_{cap,b}$ influencing the cap deformation at the droplet front and back and additionally the dimensionless resistance factor β with m_β , c_β and n_β need to be adjusted.

For model calibration, we use the dataset presented in (Helmert et al., 2019) in combination with supplementary measurements in the data range of low Ca and redefine n_{cap} within an interval around 1. Nevertheless, for $Ca \rightarrow 0$ it represents the point of minimal surface energy and equates a spherical shape. This approach allows to improve the convergence of solvers. Out of further a priori considerations ($\beta > 0$, $n_{c,f} \approx 1$), we additionally define the boundaries for the search space of the solver in Tab. 5.1. We allow the solver to adapt the correlation coefficient from (Helmert et al., 2019) to the presented model, since correlations of measurement data unavoidably include measurement errors that might bias the solver results.

Beneath the fixed boundaries of the search space, a hydrodynamic boundary condition is applied to improve the convergence of the used optimization algorithms. For a rising Ca , the difference between $k_{g,f}$ and $k_{g,b}$ must increase, because of the pressure difference between

Tab. 5.1.: Boundaries of input values for optimization

parameter	lower boundary	upper boundary
$m_{cap,f}$	1.00	9.90
$c_{cap,f}$	0.40	1.50
$n_{cap,f}$	1.00	1.005
$m_{cap,b}$	-2.50	-1.00
$c_{cap,b}$	0.30	0.75
$n_{cap,b}$	0.995	1.00
m_β	0.00	10.00
c_β	0.50	1.5
n_β	0.50	20

Tab. 5.2.: Weight factors ω_i of the loss-function for GA optimization

ω_1	ω_2	ω_3
3.0	5.0	3.7

the droplet front and back increases with higher Ca (Abiev, 2017) and the droplet front elongates, which leads to a larger front gutter radius, while the droplet rear flattens out. This is expressed by the gutter radius increase for an increasing Ca :

$$\frac{dk_{g,f}}{dCa} > \frac{dk_{g,b}}{dCa} \quad (5.34)$$

The large number of influence parameters leads to a highly nonlinear optimization problem with numerous local minima. Most gradient-based algorithms, which tend to converge to local optima, are not suitable for this type of optimization problem. This would result in an enormous number of randomly initialized solver calls to cover the whole search space. In contrast, stochastic and metaheuristic approaches cover the search space to solve the statistical part of the greybox model by finding the global optimum.

The quality of a solver result (e.g. deviation between measured data and estimation) is quantified by the loss-function of the problem. For the model calibration, we define

$$\mathcal{L} = \omega_1 \left(\sum \frac{|k_{c,b} - k_{c,b}^{\mathcal{M}}|}{k_{c,b}^{\mathcal{M}}} + \sum \frac{|k_{c,f} - k_{c,f}^{\mathcal{M}}|}{k_{c,f}^{\mathcal{M}}} \right) + \omega_2 \sum \frac{|u_d - u_d^{\mathcal{M}}|}{u_d^{\mathcal{M}}} + \omega_3 \sum \frac{|\psi - \psi^{\mathcal{M}}|}{\psi^{\mathcal{M}}} \quad (5.35)$$

with the weights of the individual properties $\omega_1, \omega_2, \omega_3$ following Tab. 5.2. Values with an upper index \mathcal{M} denote values estimated by the model and values without an upper index represent the calibration data. The first two sums serve as calibration data-sets for the hydrodynamic flow properties, since they contain the flow related deformation and therefore the hydrodynamic influences. The differences of the velocity u_d serves as a parameter for the actual droplet velocity and therefore the flow resistance β . This is necessary, since otherwise no representation for β is available.

An additional factor ψ is introduced to maintain the overall integrity of the model: The excess velocity depends on extrinsic measurable values such as the dimensionless quantities and geometrical properties as well as varying flow properties like the gutter length. Thus, it is appropriate to separate the measurable quantities from the model based quantities. In doing so, one can directly compare the quantities received from the correlation with measurement data adjusted for material and flow properties. The separation of those terms leads to the equilibrium function ψ (Eq. 5.36 + 5.37). Herein Eq. 5.36 represents the data from our measurements and Eq. 5.37 only data from our modeling assumptions and geometry. For a well-adjusted model, the measured data for ψ (upper equation) should correspond with the modeled values for ψ (lower equation).

$$\psi = \left(u_{ex} - \frac{A_f}{A_{ch}} \right) C_a \beta \frac{l_d}{\overline{W}} \quad (5.36)$$

$$\psi^{\mathcal{M}} = \frac{\overline{A_g}}{A_{ch}} \frac{\overline{R_g}^2}{\left(1 - \frac{\Delta x_{g,f}}{l_d} - \frac{\Delta x_{g,b}}{l_d} \right)} \frac{1}{A_{ch} \left(1 - \frac{2\delta}{H} \right)} \left(\frac{k_{g,b} - k_{g,f}}{k_{g,f} \cdot k_{g,b}} \right) \quad (5.37)$$

The calibration procedure is based on a Genetic Algorithm (GA). Within the GA, every possible solution is emulated as a genetic code of population individuals. During the optimization process, the different solutions (individuals) can be combined (mated) to generate mixed solutions (children) with a combined genome. The decision, which solutions are actually combined, is based on the error (fitness value of loss function) of the solution. Within a so-called ranking sampling, the best solutions combine stronger than weak solutions (survival of the fittest), which leads to an improvement of the over-all population over the generations. Like in natural populations, random mutations of the genome can improve the overall fitness of a population. Transferred to a solver this means that the population is able to leave local optima, if mutated individuals (solutions of partly random parameters) have a higher fitness value and therefore significantly change the genome pool of the population.

For good optimization results it is necessary to emulate a sufficiently sized genome pool, thus a high number of emulated individuals is preferred. This in turn results in a massively increased calculation demand, because for each iteration step every single individual and the children must be evaluated (Whitley, 1994). Additionally, the Genetic Algorithm is typically performed for several iterations to identify local optima.

To decrease the amount of time-consuming iteration steps of the GA and thereby reduce overall calculation time, we utilize a three-step stochastic and gradient free approach:

In the first step, a random population at the feasible borders of the problem is generated for the Genetic Algorithm and a genetic optimization performed. The convergence point of the GA is initialized via Latin Hypercube Sampling processed by a following fast-converging Pattern Search Algorithm (PSA) (Davey, 2008) that results in an improved minimum as the final convergence point. The properties of both algorithms are shown in Tab. 5.3. The algorithm finally merges at the values shown in Tab. 5.4. The results are discussed in the following.

Tab. 5.3.: Properties of used solver algorithms

Genetic algorithm	
Population size	200 individuals
Creation function	Random feasible population
Scaling function	Ranking
Selection function	Stochastic uniform
Mutation function	Adaptive feasible
Crossover function	Scattered
Pattern Search algorithm	
Search method	Latin Hypercube
Poll method	Complete poll

For the flow induced cap curvature, we again find the corresponding interrelation from the previous section and Helmers et al. (2019). For both cap deformation ratios k_f and k_b an exponential behavior as a function of the Ca -number is visible (Fig. 5.4). This proves the assumption of our previous work (Helmers et al., 2017) and agrees to Mießner et al. (2019). Our additional boundary condition (Eq. 5.34) is satisfied for all values as the graphs for the gutter radii $k_{g,i}$ show.

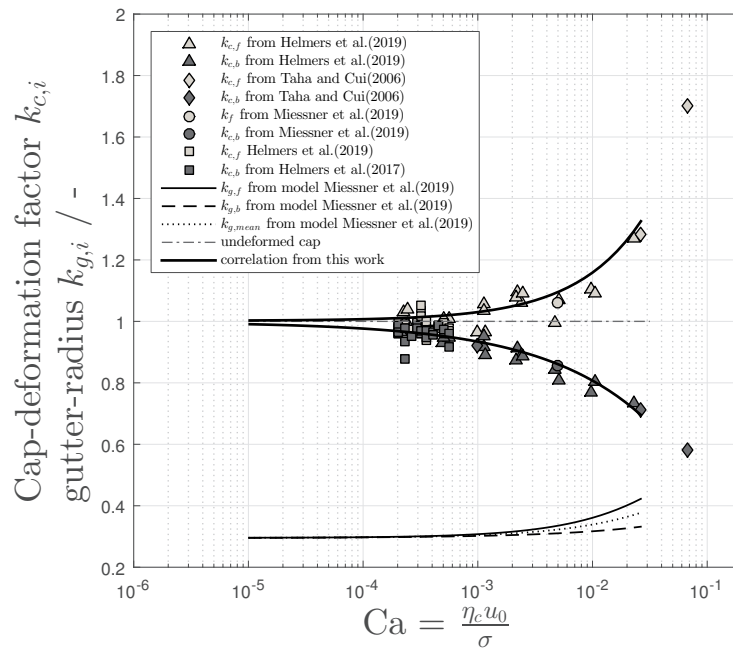


Fig. 5.4.: Measured values and model for the droplet cap deformation ratios $k_{c,f}$ and $k_{c,b}$ for different Ca -numbers. Additionally, the calculated dimensionless gutter-radii $k_{g,f}$, $k_{g,b}$ based on the model of Mießner et al. (2019) are shown

Rising viscous forces, indicated by a rising Ca -number, deform the droplet interface more strongly. At static conditions ($Ca \rightarrow 0$) the cap curvatures are in correspondence with Musterd et al. (2015) roughly circular ($k_{c,f} = k_{c,b} \approx 1$). The back cap is compressed with respect to the main flow direction ($k_{c,b} < 1$) and the front cap elongated ($k_{c,f} > 1$) if viscous forces rise in comparison to the static case.

The size of the gutter radii rises with the increasing influence of the viscous forces, since the bypass flow in the gutter increases and needs to be accommodated by the gutters. The gutter entrance is always larger in diameter than the exit radius ($k_{g,f} > k_{g,b}$).

For the resistance factor β no fitting data is available since it can not be measured directly. Therefore β is fitted based on the velocity data from high-speed camera measurements and the application of parameters for the droplet deformation. The resulting droplet velocities in comparison with the measured values are shown in Fig. 5.5. The measurements fit reasonably well within the range of inevitable velocity fluctuations caused by Taylor flow stability of +/- 10 % range described by (van Steijn et al., 2008).

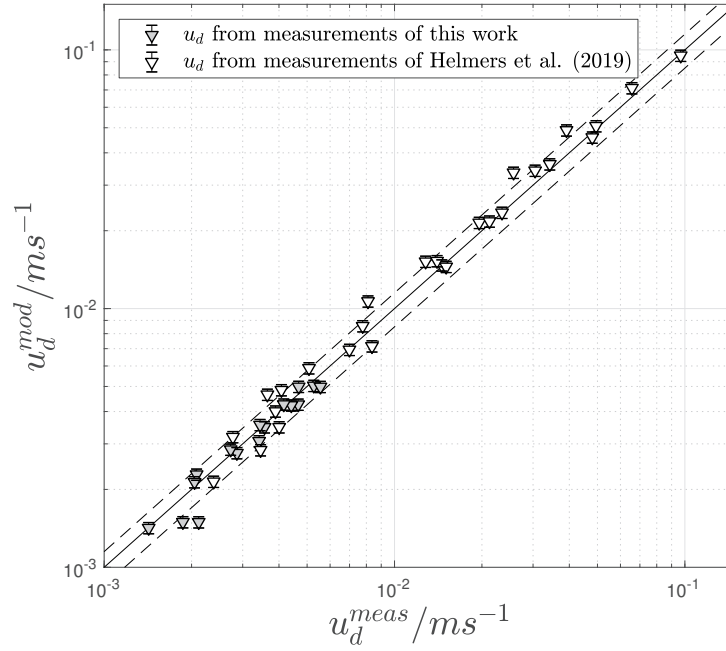


Fig. 5.5.: Parity plot for the droplet velocity of measured droplets and corresponding data from the model after adaption of the dimensionless resistance factor β . The values situate fairly good within the fluctuation range of 10 % as reported by Fuerstman et al. (2007) and van Steijn et al. (2008)

All adaption coefficients for the proposed model are summarized in Tab. 5.4.

Tab. 5.4.: Values for the fit-functions for droplet shape k_i and resistance β

Target value	m_i	c_i	n_i
k_f	4.8761	0.7465	1.0021
k_b	-1.6967	0.4745	0.9980
β	6.1280	1.2105	1.4541

5.2.4 Model validation

For a first validation step the calibration functions ψ and ψ^M are considered. In case of a hydrodynamic well-adjusted model, both functions should coincide, and the model based shape deviations (ψ^M) equals the combination of measured properties (ψ). The corresponding data and the values for our model agree well at high Ca numbers (Fig. 5.6),

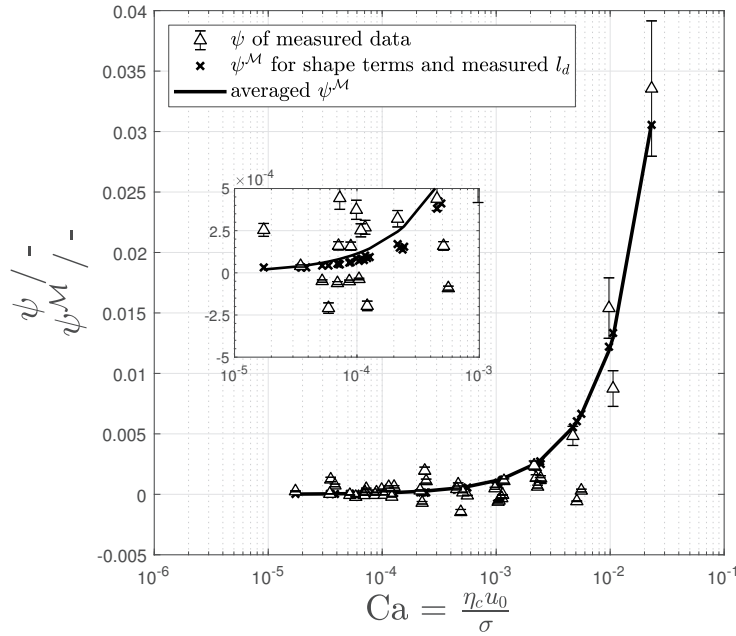


Fig. 5.6.: Measured data ψ (triangles) and modeled data ψ^M for averaged droplet lengths (solid line) over the Ca -number. Crosses depict the values for the actually measured droplet lengths

whereas a deviation for lower Ca -numbers can be observed. This can be explained by the fact that the excess velocity itself is a relative quantity and it is therefore stronger influenced at lower absolute values (low Ca -number). Thus an inevitable constant measurement deviation for velocity and volume flows caused by the experimental equipment results in a higher error for low excess velocities. Especially for $Ca < 10^{-4}$ the resulting volume flows are situated at $Q_0 \approx 2 \cdot 10^{-6}$ l/min and even minor deviations lead to high errors for the excess velocity. Thus, we consider our model approach to represent the measurements reasonably well and our fit coefficients to be valid.

Besides the hydrodynamic validation, the chosen assumptions for β are compared with available simulation data. We find a dependence of the gutter flow resistance β on the viscosity ratio λ . The latter can be interpreted as an indicator for the viscous coupling of both flow phases (Fig. 5.7). In case of a highly viscous continuous phase ($\lambda < 1$) the strongest velocity gradients are found inside the droplet, while for a viscous disperse phase ($\lambda > 1$) larger velocity gradients and therefore energy dissipation is found inside the gutter-flow, resulting in a larger β .

This approach agrees with the simulations from Shams et al. (2018), who improved the model of Ransohoff and Radke (1988) by introducing the viscous coupling of the disperse and the continuous phase. For our case of $\lambda = 0.1 - 1.4$ and a contact angle $\theta = 0$ Shams et al. (2018) report a β between 20-30 for a co-current flow. Our values are shifted by a constant offset, while the slope and therefore the dependence on λ is similar. We consider a constant offset to be caused by the use of a different flow field specifications. Shams et al. (2018) describe a concurrent flow in a fixed frame specification, while in this work we determine Q_g^{rel} within a moving frame flow specification. The coordinate transformation only changes the offset of the function, while the hydrodynamic influence (the slope) must remain identical. Additionally within the simulation of Shams et al. (2018), they assume

a contact line between disperse phase, continuous phase and the wall in their problem definition. Although for the solution shown in Fig. 5.7 the contact angle for the continuous phase is nearly 180° , the existence of a contact line introduces an additional resistance. Thus regarding β the model is considered plausible.

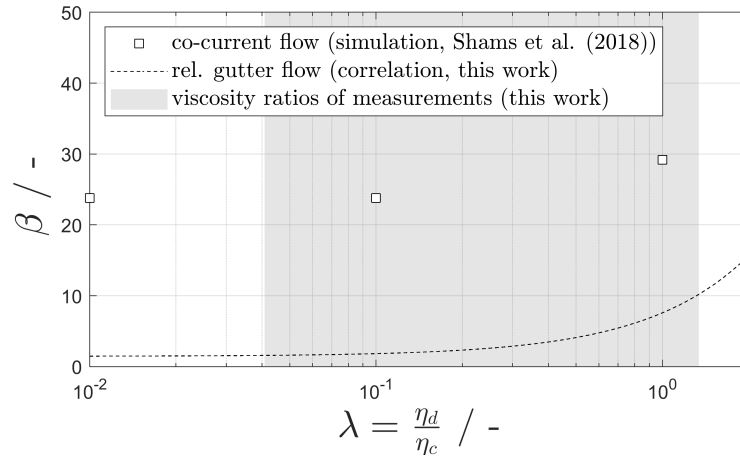


Fig. 5.7.: Comparison of calculated resistance factor β (squares) and correlation (dashed line) of the proposed model. The data of the simulation from Shams et al. (2018) is shown as squares. The λ -dependency of both works agree well, while our values are offset-shifted. This is caused by different flow specifications of both works: fixed frame specification (Shams et al., 2018), moving frame specification (this work)

The integrity of the model itself and the correlation for β has been successfully proven, but due to the mentioned experimental restrictions, we can not directly compare the modeled and experimental determined excess velocities u_{ex} . Instead we compare the results of the proposed model to different published approaches.

A suitable correlation for the prediction of the excess velocity in the first regime was introduced by Jose and Cubaud (2014), who identify the Ca -number and the ratio of the droplet length $\frac{l_d}{H}$ as characteristic properties (Fig. 5.8). It has to be mentioned, that the model of Jose and Cubaud (2014) for non-wetting droplets ends at $\frac{l_d}{HCa^{-1}} > 600$, since for larger values they observe the disperse phase to wet the channel walls. This results in intensified dissipation and a higher pressure drop and thereby inhibits a gutter flow from the droplet front to the back. This phenomenologically equals the second flow regime as mentioned by Wong et al. (2004), but lacks the thin wall film and results in a much larger pressure drop. Furthermore, the viscosity ratio λ is not included in their correlation.

A comparison of the proposed phenomenological model with Jose and Cubaud (2014) correlation Fig. 5.8 shows good agreement. At very low Ca -numbers ($Ca < 10^{-4}$), our model results in a slightly increased excess velocity. We regard this behavior of the model as not physical. The effect results from the mathematical counterplay of the terms $\lim_{Ca \rightarrow 0} \frac{1}{Ca} = \infty \leftrightarrow \lim_{Ca \rightarrow 0} k_{g,f} - k_{g,b} = 0$ within Eq. 5.33. In order to achieve a stable solver convergence, we accepted a small residual deviation for the static case $Ca \rightarrow 0$ for the front and back shape of 0.1%. Due to the relative character of the excess velocity, this unfolds a significant influence at low Ca values. Unfortunately, additional measurement validation concerning the shape deviation at very low Ca is not possible in our experimental design, since the

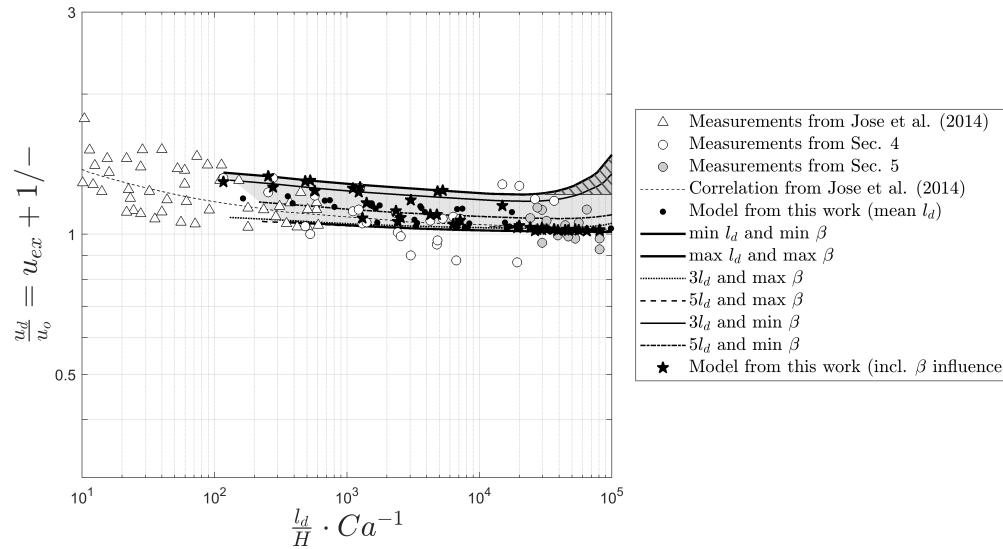


Fig. 5.8.: Comparison of the proposed model (stars) and measurements (triangles) with the measurements (circles) and correlation from Jose and Cubaud (2014) for a Taylor droplet in co-flow. The inclination for low Ca -numbers (hatched area) is discussed within the text. Since the influence of l_d correlates linearly with Δp_{LP} instead of Ca in our model and β is not included in the x -axis normalization, we additionally show the borders of our model for the minimum/maximum l_d and β of our measurements

expected shape deviation is smaller than the blurriness of the interfacial area in the images itself and therefore lies within the measurement deviation.

5.3 Discussion

The interfacial area of a Taylor droplet in rectangular channels can be divided into the front and back cap regions, the wall films and the gutter interface. Neglecting the caps, the main momentum input into a droplet is transferred across the wall film and the gutter interface area. An increasing channel aspect ratio and droplet length result a growing wall film area, i.e. an enlarged dissipation interface.

As we showed in Sec. 2.2, the behavior of the Taylor droplet's excess velocity can be parted in two possible regimes and the viscosity ratio λ has a strong influence on the hydrodynamic mechanisms.

Within the first regime the fluid in the gutter flows slower than the droplet, exerting a drag force and leading to a positive excess velocity $u_{ex} > 0$. These drag forces influence the droplet shape, leading to a flattened droplet back and elongated droplet front. We characterize this shape variation with a correlation (Sec. 5.2.3). As it can be seen from the measurements, the data falls into this flow regime, as our resulting droplet shape indicates in accordance with Wong et al. (1995).

The influence of the droplet length in the plug flow regime and $\lambda < 1$, where larger droplets have an $u_{ex} \approx 0$, is in agreement with Jakiela et al. (2011) and their later publication Jakiela et al. (2012). Additionally, they find an elongation of the dynamic droplet length

in comparison to the static droplet length, which is also covered by the shape correlation, since for rising the Ca -number the droplet front elongates stronger than the droplet back is compressed. Recently published simulations by Kumari et al. (2019) show that also for larger Re -numbers $u_{ex} \approx 0$.

Our concept of deriving the excess velocity from the gutter pressure drop, that is inverted to the flow direction (larger pressure at the front gutter entrance) is in accordance with Abiev (2017). Nevertheless, the averaged pressure is still higher at the droplet back than on the droplet front due to the overall droplet pressure drop, since the droplet needs a driving force for its translation.

For the second flow regime identified by Wong et al. (1995), where the viscous dissipation in the film and droplet leads to a bypass flow from the droplet back to the front and therefore a negative droplet excess velocity (for large λ and long droplets), the proposed model can be adapted, if the gutter-shape-difference term is revised or a resistance coefficient for the film is added. As the viscosity ratio λ rises, more momentum will be dissipated via the wall films. This extra momentum is dissipated at the gutter interface, which results in a slower droplet velocity, forcing the continuous phase to bypass the droplet reversely. As the hydrophilic channel in the experimental setup did not allow to establish a water-in-oil two-phase flow for a $\lambda \ll 1$, droplet shape correlations for the case of $\lambda \gg 1$ should be performed in future work. Therefore, although we assume a systematic inversion of the gutter radii ratio back to front as a consequence of the reversed gutter flow direction, we like to mention that with the current shape correlation our model only works for the case of low viscous disperse phase ($\lambda \lesssim 1$) like gas/liquid or low viscous oil/water flows.

The influence of the channel aspect ratio as mentioned by Wong et al. (2004) is incorporated in the proposed model: a higher aspect ratio results in lower excess velocities. This can be explained by the larger drag forces acting on a larger relative wall film area caused by the flattened channel geometry.

5.4 Conclusion

In this chapter, a model to determine the relative droplet velocity of Taylor flows in square microchannels for moderate Ca -numbers and low to moderate viscosity disperse phase ($\lambda \lesssim 1$) was developed. The proposed model is based on the relative volume flow through the gutters, as well as the wall film thickness. The flow through the gutters is determined from the pressure drop described by the Laplace-pressure difference between the gutter entrances.

The model uses the gutter radii to obtain the resulting pressure gradient that drives the continuous phase through the gutters. Measurements at different Ca and Re in a surfactant-free fluid system from a previous publication (Helmers et al., 2019) were used to derive the radii at the gutter entrances from the surface shape model proposed by Mießner et al. (2019) and calibrate the model parameters.

The model is successfully validated with an intrinsic approach comparing the congruence of measurement data and calibrated model parameters. Additionally, the proposed model was successfully compared to the phenomenological correlation of Jose and Cubaud (2014). The comparison with the most prominent approaches shows that the proposed model and the chosen influential parameters are valid for moderate and small viscosity ratios. The excess velocity is determined by viscous dissipation within the droplet and the gutters as well as the drag of the thin wall films. The relation is characterized by the Ca -number, viscosity-ratio λ , the dimensionless gutter-length l_g , the aspect ratio ar and the wall-film thickness A_f . Furthermore, the proposed model can close the gap for $\frac{l_d}{HCa^{-1}} > 600$ and allows the calculation of the excess velocity for moderate Ca -numbers ($Ca < 0.02$).

For the future, the influence of surfactants and highly viscous droplets ($\lambda \gg 1$) on the excess velocity should be investigated to extend the model, since an excess velocity $u_{ex} < 1$ was not included into the model so far. It is suggested to include this function in the modeling of the wall film resistance. Especially local spatially resolved measurement techniques, e.g. μ -PIV measurements should be appropriate for this task.

Refractive index matching (RIM) using double binary mixtures for Re , Ca and viscosity adjusted μ PIV-measurements

“ *Success is a lousy teacher. It makes smart people think they can't lose.* ”

— **Bill Gates**

(US-American investor, philanthropist,
humanitarian)

An exact understanding of the underlying hydrodynamic interrelations of multiphase flows is the key for successful reactor layout and reaction control. To examine the local hydrodynamic behavior, non-invasive optical measurements techniques like particle tracking velocimetry (PTV) particle image velocimetry (PIV) are the methods of choice, since they provide precise velocity measurements with excellent spatial resolution. Such optical approaches require refractive index matching (RIM) of the involved flow phases to prevent optical distortion due to light refraction and reflection at the interfaces. Established RIM approaches often provide a single degree of freedom, which is sufficient to solely match the RI of the flow phases. With that, the material properties (Oh number) are fixed and the relevant dimensionless numbers (Ca , Re) may only be altered hydrodynamically or geometrically.

To avoid expensive geometric scaling of the microchannels, in this chapter an approach using two binary mixtures (double-binary mixtures) is introduced, which uses an additional degree of freedom. The approach allows examining liquid-liquid two-phase flows at a distinct velocity while being able to change the material combination (Oh -Number). Therefore Ca and Re can be chosen individually and the RIM provides undisturbed optical access. Four different binary mixtures are presented to be used, e.g. with Taylor droplets. The relevant material parameters are successfully correlated to measurement data, which delivers a system of equations that determines the mass-fractions and the velocities to address Re and Ca individually. A proof-of-principle for the proposed double binary mixture RIM-approach is successfully established using μ PIV raw images.

What follows is based on T. Helmers, P. Kemper, U. Mießner and J. Thöming (2019). Refractive index matching (RIM) using double-binary liquid-liquid mixtures. Available via *arXiv:1905.02819*.

6.1 Overview and concept

Deep insight into the hydrodynamic interaction of the distinct flow phases enables to tune e.g. the mass-transfer rates towards more sustainable operation modes close to the optimal working point (Magnaudet and Eames, 2000; Ern et al., 2012). To achieve this, numerical simulation and CFD-calculations enable relatively easily a parameterized study of e.g. liquid-liquid Taylor flows (Rocha et al., 2017). Dimensionless numbers (Re , Ca) and material property ratios (Oh) can be set freely and independently to identify e.g. critical operation modes.

The dimensionless quantities are based on the material parameters of the continuous phase since it is the phase that provides the wall contact and drives the flow of the disperse phase. The capillary number compares the viscous forces with the interfacial tension forces $Ca = \frac{u_0 \eta_c}{\sigma}$ and it is based on the superficial velocity u_0 , the dynamic viscosity η_c of the continuous phase and the interfacial tension σ . The Reynolds number relates the inertia forces to the viscous forces $Re = \frac{\rho_c u_0 H}{\eta_c}$, where ρ_c denotes the density of the continuous phase and H the height of the microchannel. The Ohnesorge number $Oh = \sqrt{\frac{Ca}{Re}}$ removes the hydrodynamic influences and solely remains as a material parameter. Please note that for macroscopic liquid-liquid flows, the set of dimensionless variables changes with the growing influence of inertia and gravitational forces to Re , We and $Mo = Bo Oh^2$. Where the Weber number $We = Ca Re$ represents the inertia forces compared to the interfacial tension forces. Mo introduces the buoyancy dependence of the flow's material system (Araújo et al., 2012) when combining the Bond number $Bo = \frac{\Delta \rho g d^2}{\sigma}$ with the Ohnesorge number. Since buoyancy forces are small ($Bo \ll 1$) in microfluidic applications, we base the RIM system on the Oh number only.

Preferably non-invasive experimental methods need to be applied to investigate the hydrodynamic behavior of liquid-liquid multiphase flows supporting the numerical findings. Even in microchannels, a high spatial resolution of an entire flow field is accessible with e.g. optical measurement techniques (Park and Kihm, 2006; Kinoshita et al., 2007; Khodaparast et al., 2013). However, undistorted optical access is necessary to avoid measurement deviation due to light refraction and reflection.

Often the hardware related refraction effects of the setup can be compensated by adjusting the experimental design e.g. avoiding curved surfaces and using of corrective optics. The curved interfaces of microscopic liquid-liquid flows are commonly counteracted applying refractive index matching with one degree of freedom (Mießner et al., 2008; Ma et al., 2014; Liu et al., 2017). A broad overview of possible liquid-liquid, as well as solid-liquid refractive index matching possibilities, is given in the works of Budwig (1994) and Wright et al. (2017). Recently, several approaches have been made using refractive index matched systems to mimic special application cases like specific rheology for blood (Najjari et al., 2016; Brindise et al., 2018), high-density differences or for a buoyant jet (Clément et al., 2018; Krohn et al., 2018).

In microscopic liquid-liquid flows RIM with one degree of freedom allows solely matching the RI of one phase to the other. The material properties of the phases like density, viscosity

and interfacial tension are fixed for the desired RI. The governing dimensionless numbers such as Re , Ca may only be parameterized hydrodynamically (superficial flow velocity) or geometrically (microchannel diameter). The monetary effort to parameterize the diameter of the microchannel is high, while the velocity alters both quantities simultaneously.

Alternatively, surfactants could be added to change solely the interfacial tension of the material system. Surfactant concentration well below the critical micelle concentration does not significantly change the viscosity of the host phase. Albeit this approach indeed addresses Ca only, the use of surfactants introduces severe effects such as altering the interface viscosity of the flow as well as its mass-transfer properties.

In this part of the work, an approach is suggested using two immiscible binary mixtures to match refractive indices (Saksena et al., 2015; Cadillon et al., 2016), i.e. adding an additional degree of freedom to the system by introducing a binary mixture for each of the liquid phases. The now flexible material system provides an entire range of RI to match the immiscible binary liquid mixtures optically. Hence, the simultaneous velocity related change of Ca and Re may be compensated for by adequately adapting the material composition of the mixtures (Oh).

The mass-fraction dependent material properties of the involved mixtures are carefully determined, dedicated correlation functions and an optimization algorithm to calculate the necessary information to use this RIM system is provided. A proof of principle is given using μ PIV raw-images of two fluorescence particle-seeded microscopic Taylor flows at two Re and constant Ca at different channel heights.

Recently, the viscosity ratio of the immiscible phases λ is reported to influence the local hydrodynamics of microscopic Taylor droplets (Rao and Wong, 2018). However, their measurements are limited to a narrow parameter range without refractive index matching (Kovalev et al., 2018; Liu et al., 2017). Therefore, the author suggests four combinations of well quantified double-binary mixtures for the disperse as well as the continuous phase. This allows to additionally alter the viscosity ratio of the flow phases by changing the flow system.

6.2 Material and methods

Within this section, the choice of the basic mixture compounds, the experimental procedures to retrieve the properties of the fluids and the numerical approach are described. All measurements are referenced to mass-fractions ξ to compensate non-linearities (e.g., excess volume while mixing or when preparing solutions).

6.2.1 Basic mixture compounds

For the binary mixtures of this work, we focus to mainly use nontoxic, non-hazardous, newtonian substances. A wide range of addressable refractive indices is accomplished, when mixing substances of high and low RI in each phase. The polar phase is chosen to

be aqueous for practical reasons. The range of RI of the aqueous binary mixture is defined when using either DMSO or glycerol as newtonian liquid to elevate the RI. The nonpolar phase is based on hexane, as it represents a tradeoff between a lower RI and hazardous properties. The nonpolar binary mixture is complemented by either anisole or sunflower-oil, which establishes a high RI range. Rheometry measurements show that in the observed range sunflower-oil also behaves newtonian.

Combining the suggested aqueous mixtures with the non-polar systems, the viscosity ratio λ between the phases of the flow can be changed by either inverting the flow phases or changing the combination of the materials. For that reason, characterize different binary mixtures for the polar as well as for the non-polar phase are introduced and characterized. Please note that the viscosity ratio cannot be chosen freely. However, it is possible to choose a ratio below or above unity to investigate the hydrodynamic consequences.

For low viscous mixtures with viscosity ratio below one, water/DMSO and n-hexane/anisole are used, while for high viscosity ratio we propose to apply water/glycerol and n-hexane/sunflower oil.

With these mixtures, a broad range of refractive indices is reached, laying between the pure substance's RI of n-hexane ($RI = 1.3753$) and glycerol/DMSO ($RI \approx 1.47$). The material properties of the binary mixtures (density, viscosity, interfacial tension), as well as the refractive, are given in Sec. 6.3.

6.2.2 Determination of material properties

The **refractive indices** of the used fluids were measured using a Krüss Abbe refractometer AR2008, tempered at 20°C. The refractive indices were measured using a light wavelength of 589 nm (Sodium D1-line) with three independent measurements each. The refractometer uses a liquid film between two prisms to measure the angle of total reflection, from which the refractive index is calculated. For volatile or liquids with low viscosity or low surface tension, no stable film forms between the prisms, which leads to a high deviation. For this reason, the refractive indices of the n-hexane/anisole system for high mass-fractions of anisole could not be acquired reliably. Instead, literature data is used in this case.

The **interfacial tension** of the double binary mixtures was measured using a Lauda TVT drop tensiometer with a syringe of 2.5 ml and a stainless steel capillary at a temperature of 20°C. The interfacial tensions were acquired using the volume drop method: A droplet was formed at a capillary tip. Based on the balance of buoyancy and surface tension the droplet pinched off into the continuous phase. The dispersed droplet was detected with a light barrier and the interfacial tension was calculated from the droplet volume.

The interfacial tension is a time-dependent property for nonpure or mixed systems. Thus, as part of the measurement of the dynamic interfacial tension, droplets with differently aged interfacial area were formed. The interfacial tension for infinite time σ_{inf} can be derived depending only on bulk diffusion of surface-active substances. Therefore the interfacial tensions were correlated following Wilkinson (1972) and Sinzato et al. (2017). Within this

work, the droplet formation times and therefore the surface age lie between 2.5 s and 60 s. The procedure is described in detail in Appendix C.1.

The light barrier, which detects the detachment of the ascending droplets, cannot work properly when the refractive indices are matched. Thus, the mass-fraction of the nonpolar phase is deliberately detuned such that a sufficient detection difference exists between the refractive indices of both phases ($\Delta RI = 0.01$). The droplet detachment, as well as the interfacial tension, are determined at these detuned fluid compositions. The actual interfacial tension for the matched case is then retrieved by linear interpolation using the lever rule. The linear interpolation is considered valid since only the mass-fraction of one of both phases is varied and the change in the mass-fraction is kept small.

The measurements of the **viscosities** of the volatile compounds (n-hexane/anisole) were performed using a Malvern Kinexus Ultra Plus with solvent trap, cone-plate setup, 1 degree opening angle and a stationary shear rate table $10 \text{ s}^{-1} \dots 100 \text{ s}^{-1}$ with 5 % stationarity tolerance. The remaining measurements were performed using a Bohlin Rheometer CS and a 30 ml double-gap system. All measurements were performed at 20°C.

The **densities** of the mixtures are mostly retrieved from literature data.

6.2.3 Calculating mass-fractions and the superficial velocity

The main merit of the double-binary mixture flow system is the ability to address different Re and Ca independently of each other. Keeping in mind the definition of Re and Ca , this can be stated as an optimization problem with the superficial velocity u_0 as the objective value. The mass-fractions of the continuous phase ξ_c and disperse phase ξ_d are the control variable, which influences the material properties.

If the fluid properties of the pure substances as well as of the mixtures are known, Ca and Re can be calculated. Because the user needs to establish the flow at a distinct Re and Ca , the equations can be changed such that the superficial velocity u_0 for both numbers is a function of the continuous phase mass-fraction ξ_c :

$$u_{0,Re} = \frac{Re \cdot \eta_c(\xi_c)}{\rho_c(\xi_c) \cdot d} \quad (6.1)$$

$$u_{0,Ca} = \frac{Ca \cdot \omega(\xi_c)}{\eta_c(\xi_c)} \quad (6.2)$$

The problem defines as a minimization problem to find u_0 , where the difference of $u_{0,Ca} - u_{0,Re} \approx 0$. Depending on the material property function (given in Sec. 6.3.1), the problem is not necessarily strictly monotonous. Therefore the use of numerical solvers is strictly advised. After input of the desired Re and Ca , this program automatically determines the necessary superficial velocity u_0 and mass-fraction of both phases. For a minimum residuum of this optimization ($u_{0,Re} = u_{0,Ca}$), the correct u_0 is known as well as the corresponding

mass-fraction of the continuous phase ξ_c . The mass-fraction of the disperse phase ξ_d can be calculated via the refractive index of the continuous phase.

6.3 Experimental results

Within this section, the material properties of the binary and RI-matched double-binary mixtures are experimentally investigated.

6.3.1 Properties of binary mixtures

To solve the optimization problem of finding the correct mass fractions of the RI-matched case, a solver needs a steady optimization function to work with. However, the measurement data consists of discrete points including a measurement error: A transition of the discrete data sampling to continuous functions is necessary. Here, the data is correlated with polynomial approaches for simplicity.

The equation for a polynomial function follows

$$y = A_3 \cdot \xi^3 + A_2 \cdot \xi^2 + A_1 \cdot \xi + A_0 \quad (6.3)$$

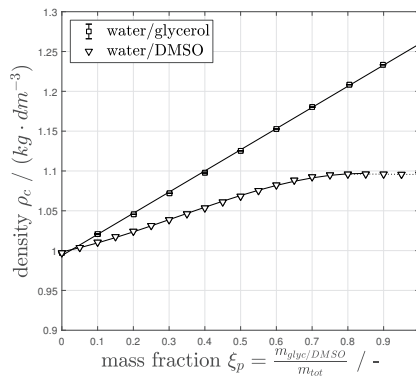
where y is the desired property (e.g., density, viscosity or interfacial tension), ξ the mass-fraction of the mixture and A_3 - A_0 fitting coefficients for the polynomial. The polynomial coefficients for the different material properties as well as the experimental data and the range of validity are shown in the following.

At first, the **densities** of the binary mixtures are investigated in Fig. 6.1 a) for the polar and in Fig. 6.1 b) for the nonpolar media. The system water/glycerol shows a nearly linear behavior, while the system water/DMSO shows a peak at approximately $\xi = 0.8$. This is caused by nonlinear mixing behavior due to the similarity of water/DMSO and also affects the viscosity. The system n-hexane/anisole shows a nearly linear behavior, while n-hexane/sunflower oil shows a deviation from linearity. The correlations extracted from the measurement and literature data are shown in Tab. 6.1.

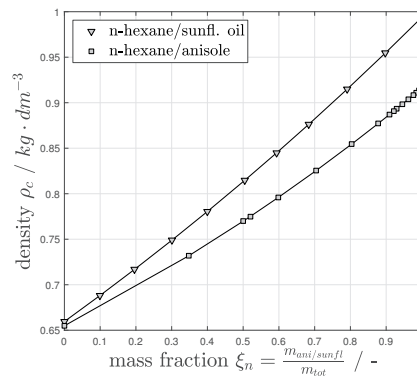
Tab. 6.1.: Correlation coefficients for the densities of binary mixtures

mixture	range	A_3	A_2	A_1	A_0
water / glycerol	$0.00 < \xi_p < 1.00$	0	0	0.2657	0.9938
water / DMSO	$0.00 < \xi_p < 0.85$	-0.1935	0.1883	0.0958	0.9984
	$0.85 < \xi_p < 1.00$	0.2667	-0.7371	0.6742	0.8919
hexan / anisole	$0.00 < \xi_n < 1.00$	0	0.129	0.2021	0.6610
hexan / sunflower oil	$0.00 < \xi_n < 1.00$	0.0081	0.0507	0.2025	0.6549

In Fig. 6.2 the **refractive index** of the water/glycerol mixture features a linear behavior (empty squares), while water/DMSO shows a nonlinearity for higher DMSO mass-fractions



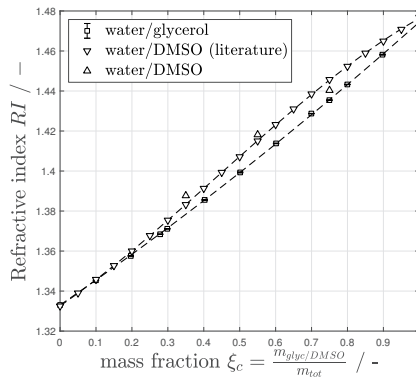
(a)



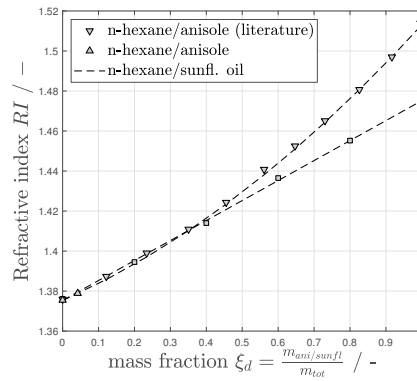
(b)

Fig. 6.1.: Densities for the binary fluid mixtures of each phase a) polar phase for the system water/glycerol (empty squares, own measurements) and water/DMSO (empty downside triangles, LeBel and Goring (1962)) b) non-polar phase for the system n-hexane / anisole (filled downside triangles, Al-Jimaz et al. (2005) and n-hexane/sunflower oil (filled squares, González et al. (1996))

(Fig. 6.2 a) , triangles). For the nonpolar substances the system n-hexane/sunflower-oil (filled squares) behaves nearly linear, while n-hexane/anisole (filled triangles) increases the slope indicating non-linear dependence (Fig. 6.2 b)). For all mixtures, the measurements confirm the available literature data. The correlation coefficients are shown in Tab. 6.2.



(a)



(b)

Fig. 6.2.: Refractive indices for the fluid mixtures a) polar phase for the system water/glycerol (empty squares, own measurements) and water/DMSO (empty downside triangles, LeBel and Goring (1962), upside triangles own measurements) b) non-polar phase for the system n-hexane / anisole (filled downside triangles, Al-Jimaz et al. (2005), upside triangles, own measurements) and n-hexane/sunflower oil (filled squares, own measurements)

The **viscosities** of the four binary mixtures are given in Fig. 6.3. Both of the highly viscous mixtures (water/glycerol Fig. 6.3 a) and hexane/sunflower-oil Fig. 6.3 d) exhibit similar behavior. As intended, with a higher mass-fraction of the more viscous substances, the viscosity rises. The less viscous mixtures water/DMSO (Fig. 6.3 b)) and n-hexane/anisole (Fig. 6.3 c)) show different behavior. While the viscosity of n-hexane/anisole mixtures increases quadratically with a rising mass-fraction of anisole, the viscosity of water/DMSO reaches a peak at $\xi = 0.70$. For n-hexane/anisole no own measurements could be performed, since the high evaporation rate of the volatile hexane/anisole mixture leads to a significant

Tab. 6.2.: Correlation coefficients for refractive index

mixture	A_3	A_2	A_1	A_0
water / glycerol	0	0.0182	0.1232	1.3300
water / DMSO	-0.0631	0.0834	0.1235	1.3300
hexan / anisole	0	0.0588	0.0790	1.3753
hexan / sunflower oil	0	0	0.0999	1.3753

deviation in the mass-fraction of the mixture during the measurement. Instead, literature data is used. The correlation coefficients are shown in Tab. 6.3.

Tab. 6.3.: Correlations coefficients for viscosity

mixture	range	A_4	A_3	A_2	A_1	A_0
water / glyc.	$0.00 < \xi_p < 0.28$	0	0	9.6514	1.7769	1.0095
	$0.28 < \xi_p < 0.48$	0	0	49.223	-21.944	4.5865
	$0.48 < \xi_p < 0.64$	0	0	182.8	-153.48	36.991
	$0.64 < \xi_p < 0.76$	0	0	1272.7	-1557.1	488.84
	$0.76 < \xi_p < 1.00$	0	10863.4	-21776.31	14652.78	-3289.78
water / DMSO	$0.00 < \xi_p < 0.50$	0	3.6080	2.4412	1.7748	0.8995
	$0.50 < \xi_p < 0.89$	0	-11.9506	0.4866	16.9060	-4.2424
	$0.89 < \xi_p < 1.00$	0	130.6611	-355.8453	315.2710	-88.0846
hexan / anisole	$0.00 < \xi_n < 1.00$	0.7284	-0.4838	0.3969	0.1302	0.3117
hexan / sunfl. oil	$0.00 < \xi_n < 0.63$	0	19.1488	0.4864	0.1616	0.3140
	$0.63 < \xi_n < 1.00$	0	1309.0133	-2622.0800	1774.9866	-399.4200

6.3.2 Properties of RI-matched double-binary mixtures

In addition to the direct properties of the individual binary mixtures that have been discussed in the previous section, the properties of the coupled **RI-matched** material systems (double-binary mixtures) are discussed in this section. Since the double-binary system consists of four substances, the interfacial tension is influenced independently and possibly nonlinearly by the mass-fractions of both binary mixtures. Thus to obtain a manageable experimental effort for the required measurements, the interrelations are linearized and the system is simplified: For the use in RI-matched measurements, only the mass-fractions of the matched solution need to be observed. As it is visible in Fig. 6.4 and 6.5, this simplifies the problem to a two-dimensional problem.

To retrieve the specific mass-fractions of both phases for the matched case, the correlations for the RI of both phases are equated and a fit function is numerically retrieved. The behavior of the RI-matched double-binary systems is a combination of the binary mixtures. The results are shown for all double-binary mixture systems in Fig. 6.4.

The system water/DMSO-hexane/anisole (Fig. 6.4 (c)) shows the most prominent non-linear behavior. This is caused by the larger increase of the RI of anisole for elevated anisole mass-fractions and the nonlinearity of water/DMSO. For the system water/glycerol-hexane/anisole (Fig. 6.4 (a)) this behavior is not prominent since the binary mixture water/glycerol in contrast to water/DMSO is nearly linear. As expected from the binary mixture's behavior, this also holds for the system water/glycerol-hexane/sunflower-oil (Fig. 6.4

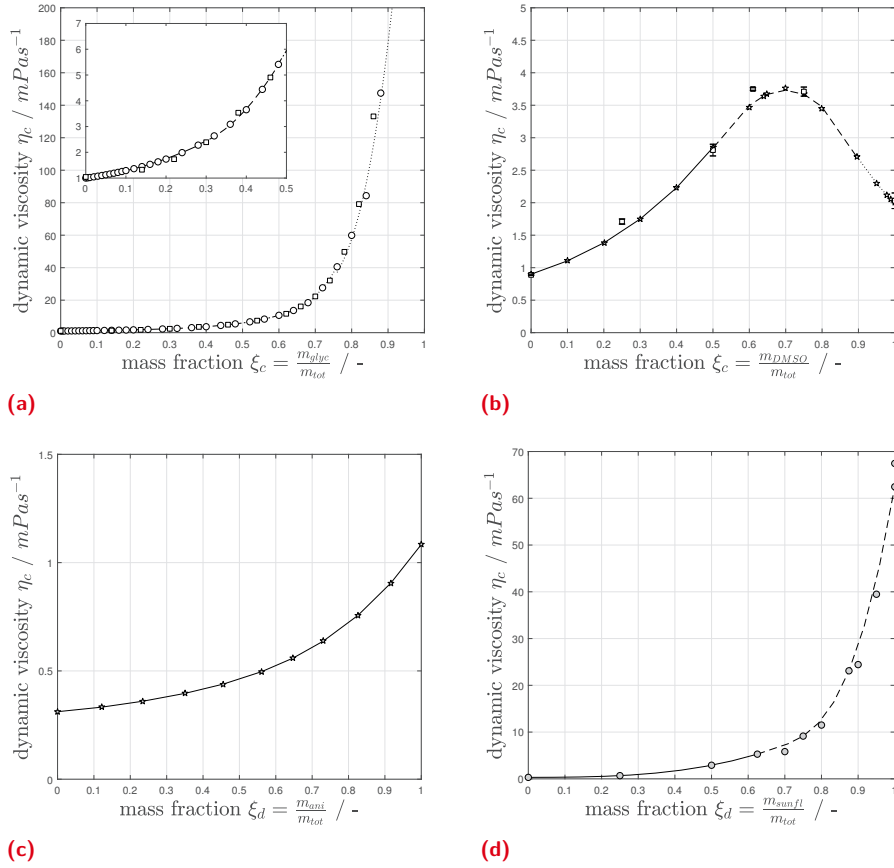


Fig. 6.3.: Viscosities for the fluid mixtures at 20 °C a) polar phase water/glycerol (empty circles, Weast (1989), empty squares own measurements) b) polar phase water/DMSO (empty stars, LeBel and Goring (1962), empty squares own measurements) c) non-polar phase n-hexane / anisole (filled stars, Al-Jimaz et al. (2005)) d) non-polar phase n-hexane/sunflower oil (filled circles, own measurements)

(b)), while again caused by water/DMSO, for water/DMSO-n-hexane/sunflower-oil nonlinearities are present at higher DMSO mass-fractions (Fig. 6.4 (d)). The correlation coefficients for the matched systems are shown in Tab. 6.4.

Tab. 6.4.: Correlation coefficients for the mass-fractions of RI-matched double-binary mixtures (range of validity for all correlations: $0.32 < \xi_p < 1$)

mixture	A_4	A_3	A_2	A_1	A_0
water/glycerol - hexane/anisole	-4.599	12.318	-12.348	6.632	-1.237
water/glycerol - hexane/sunfl. oil	0	0	0.182	1.233	-0.423
water/DMSO - hexane/anisole	-3.623	9.629	-10.027	5.908	-1.098
water/DMSO - hexane/sunfl. oil	0	-0.631	0.835	1.236	-0.453

Additionally to the refractive index, the densities, interfacial tension and viscosities for the different matched mass-fraction have to be considered for the calculation of the desired dimensionless quantities (Re , Ca , λ). Every matched system consists of two binary mixtures with exactly one RI for the matched case and one specific mass-fraction and viscosity for the polar as well as the disperse phase. Changing the mass-fraction of one phase, the

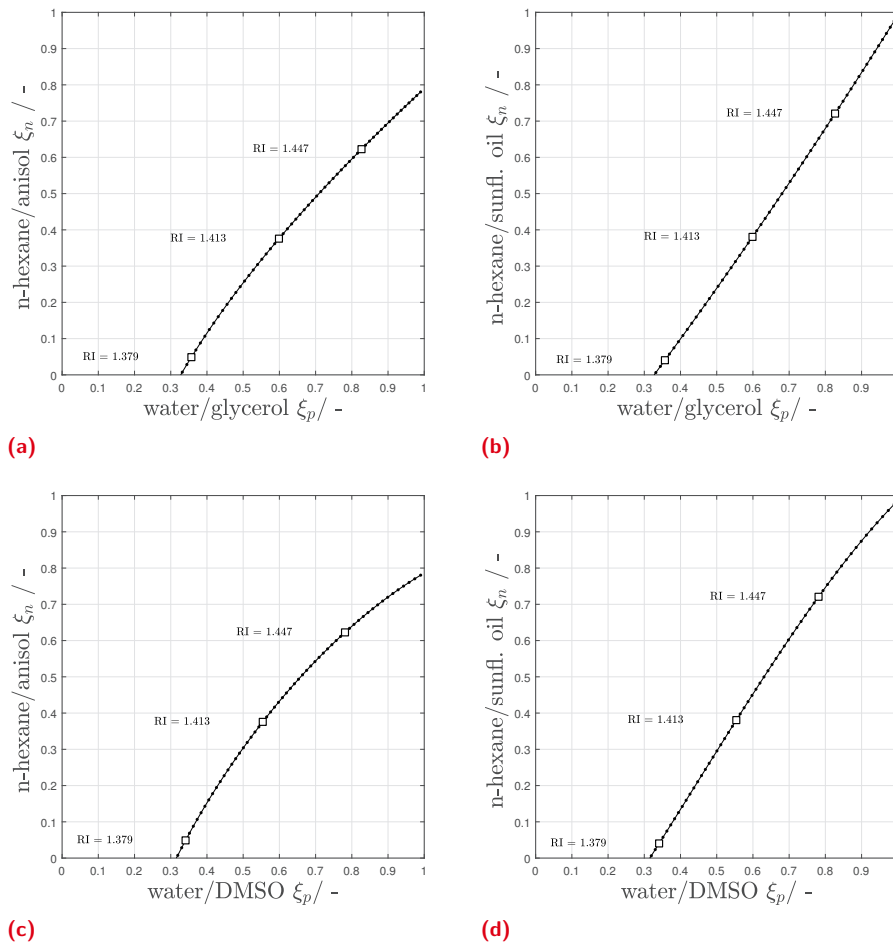


Fig. 6.4.: Mass-fractions of RI-matched double-binary mixtures with matched RI along the graph. a) water/glycerol - n-hexane/anisole b) water/glycerol - n-hexane/sunflower-oil c) water/DMSO - n-hexane/anisole d) water/DMSO - n-hexane/sunflower-oil. Large circles represent a $\Delta RI = 0.068$ step, small dots the interiorly intermediate steps $\Delta RI = 0.0034$

mass-fraction of the other phase needs to be adjusted to keep the RI matching. This changes the viscosity ratio, as it also depends on the ratio of the binary mixtures of each phase.

For the determination of the dimensionless quantities Re , Ca , Oh of microscopic two-phase flows, especially the **viscosity** of the continuous phase is important, since it influences the dimensionless quantities the strongest. Therefore the viscosities for the continuous phase of the high viscous systems are shown (Fig. 6.5).

At first, the polar phase is depicted as the continuous phase, resulting in the graphs of Fig. 6.5. The combinations with water/glycerol show a broad range of available continuous phase viscosities.

Considering the viscosities of both flow phases, the viscosity ratio λ of the respective RI-matched material systems can be calculated. The results are shown in Fig. 6.6 separated for polar and nonpolar continuous phase:

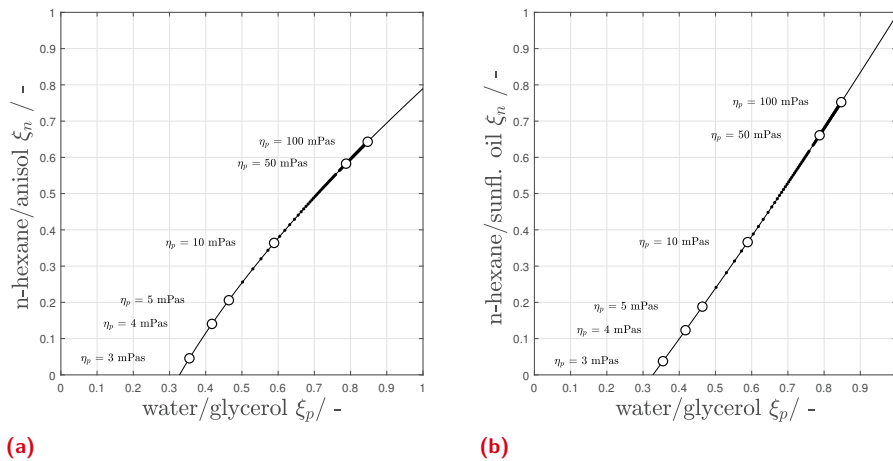


Fig. 6.5.: Polar continuous phase viscosity η_p along the mass-fractions for matched mixtures. a) water/glycerol - n-hexane/anisole b) water/glycerol - n-hexane/sunflower-oil. Large circles represent a logarithmic scale, small dots the interiorly intermediate steps. Low viscous continuous phase systems are not shown since the continuous viscosity does not change significantly over the RI-matched mass regions

In Addition to the determination of the material properties that depend only on the binary mixtures themselves, also the interfacial tension needs to be described. Since it depends on the forces of the energetic state of the interfacial area, the determination for a quaternary fluid system is complex. For the following measurements, only the interfacial tension of the RI-matched case is of interest. Thus, we only determine values at the mass-fractions of the RI-matched interfacial tensions to minimize the experimental effort.

Due to the measurement restrictions (see in Sec. 6.2.2), we perform the measurements at slightly detuned refractive indices and linearly interpolate the interfacial tension for the matched case between the results. The measurement data, as well as the derived correlations, are shown in Fig. 6.7.

The interfacial tension between the RI-matched liquids exhibits different behavior for each system. The system water/glycerol- hexane/anisole (Fig. 6.7 a)) shows an unpredictable interfacial tension development for rising mass-fractions of glycerol or anisole. The interpolated values of the single measurements deviate around the correlation function. This is a sign for strong nonlinear interrelations between the four substances. Probably caused by weaker intermolecular forces between glycerol and anisole depending on the composition of the mixture. The system water/glycerol - hexane/sunflower-oil shows a minimum for equivalent fractions of all four substances ($\xi_p \approx 0.5$, $\xi_n \approx 0.5$), while the interfacial tension increases for higher amounts of glycerol or sunflower oil (Fig. 6.7 b)).

The systems involving water/DMSO expose a decreasing interfacial tension with decreasing mass-fraction of n-hexane. Especially the water/DMSO - hexane/anisole shows a very low interfacial tension for lower mass-fractions of hexane (Fig. 6.7 c)), which is caused by a diminished structural difference to hexane. Water/DMSO - n-hexane/sunflower-oil shows a similar decrease of the interfacial tension (Fig. 6.7 d)).

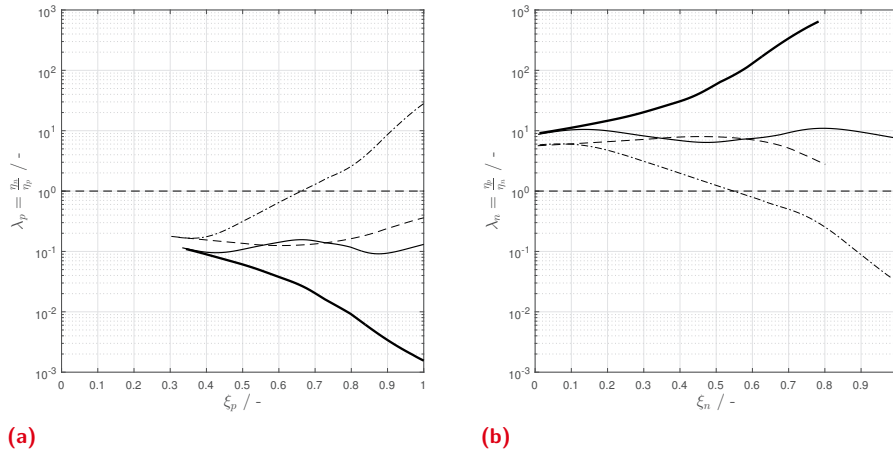


Fig. 6.6.: Viscosity ratios λ_n and λ_p for the different systems. System water/glycerol - n-hexane/anisole (bold solid line), system water/glycerol - n-hexane/sunflower-oil (thin solid line), system water/DMSO - n-hexane/anisole (dashed line), system water/DMSO - n-hexane/sunflower-oil (dash-dotted line). a) continuous phase: polar b) continuous phase: nonpolar.

The most significant deviations (Fig. 6.7 a) and b)) are situated in a range of 2 mPas. Please note, that the derived fitting function represents an averaging attempt to describe the complex 4-material-system. Therefore, a deviation between the correlation and the interpolated data of single measurements can be caused by either the linearization or confined effects at distinct mass-fractions as well as measurement errors. Since the results of the single measurements are based on at least 20 independent droplets (5 droplets x 4 formation times), we consider possible measurement errors to attribute from diminutive contaminations of the volume tensiometer. The correlation coefficients for the interfacial tension for all four systems are shown in Tab. 6.5.

Tab. 6.5.: Correlations coefficients for interfacial tension (range of validity $0.32 < \xi_p < 1.00$)

mixture	A_2	A_1	A_0
wt./glycerol - hex./anisole	-26.002	-24.007	9.164
wt./glycerol - hex./sunfl. oil	24.029	-34.799	28.538
wt./DMSO - hex./anisole	35.627	-76.700	41.824
wt./DMSO - hex./sunfl. oil	22.616	-52.398	35.929

6.4 Discussion

Based on the material properties of the binary mixtures as well as the double-binary mixtures, which were experimentally determined and successfully modeled with polynomial correlations, we describe the features of the double-binary approach in this section and deliver a proof-of-principle.

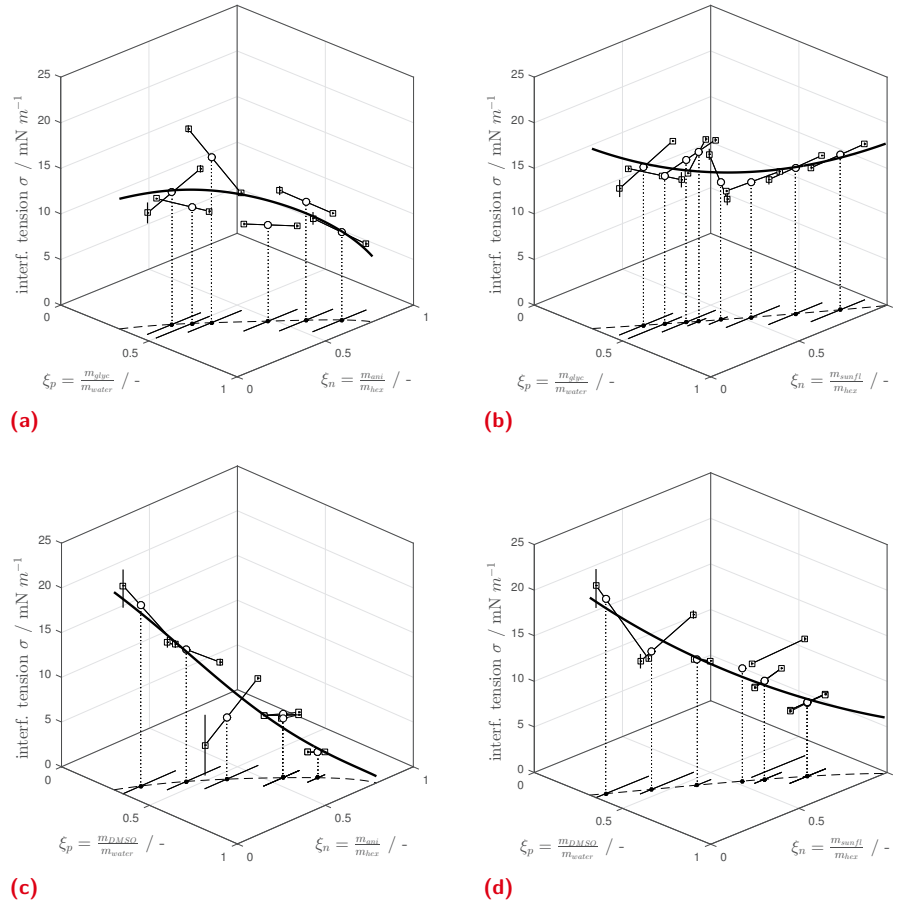


Fig. 6.7.: Interfacial tension σ for the different systems. a) water/glycerol - n-hexane/anisole b) water/glycerol - n-hexane/sunflower-oil c) water/DMSO - n-hexane/anisole d) water/DMSO - n-hexane/sunflower-oil. Actual measurements (squares) are used to interpolate (bars) the interfacial tension at the matched phase composition (circles). The correlation for the matched interfacial tension is the correlated (bold line). Each measurement consists of 5 droplet formation cycles at different droplet formation times. Within each cycle, at least 5 droplets are formed to ensure reproducibility

6.4.1 Features and limits of the double-binary approach

The proposed double-binary mixture approach allows tuning the material system of microscopic Taylor flows with an additional degree of freedom. A two-phase flow can now be RI-matched at a specific individually set of Re and Ca individually. This is done via a variation of the mass-fraction of both phases ξ_c , ξ_d and the superficial velocity u_0 . Alternatively, a set of fixed Ca/Re ratios ($\sim Oh$) at distinct RI can be adjusted, allowing to match the system to a specific reactor material. In this way even complex structures or three phase flows can be observed once the flow is matched to the reactor material. Additionally, the flow can be applied at a specific viscosity of the continuous phase (if fluids with a distinct viscosity should be modeled). A graphical representation of the capabilities is given in Fig. 6.8.

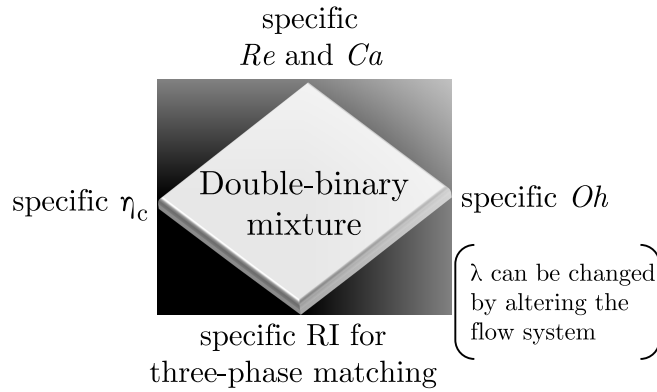


Fig. 6.8.: Features of the double-binary fluid system. Depending on the case of application, Re and Ca can be adjusted individually. Alternatively, a defined continuous phase viscosity η_c , a defined RI or a defined Oh can be chosen. The latter three can only be addressed at a defined Re or Ca , while the other dimensionless quantity is fixed

Based on the conducted measurements and literature data, the proposed double-binary mixture systems are sufficiently described to calculate the relevant dimensionless quantities Ca and Re for all accessible mass-fractions and superficial velocities. These latter two quantities can be calculated by a software solution. Alternatively, they mass-fraction and the superficial velocity can be retrieved graphically from the nomograms presented in Fig. 6.9. The desired Ca and Re are chosen on the according axis and the corresponding matched Oh and RI of both phases, as well as the superficial velocity, can be received. The RI determines the mass-fractions of both phases ξ (Fig. 6.4) and the associated viscosity ratio (Fig. 6.6). Via the continuous phase viscosity (Fig. 6.5) and λ the disperse phase viscosity can be determined. Generally, the systems with a high viscous continuous phase (Fig. 6.9 a) + b)) cover a larger range of possible Ca and Re , while for the lower viscous continuous phase the parameter range is smaller.

6.4.2 Proof of principle

The practicability of the proposed approach for optical measurements and especially the possibility to reach the desired Re and Ca independently while a matched refractive index is proven in an experimental approach. A microscopic Taylor flow is established at two different Re numbers while Ca is held constant. The experimental setup to record the PIV raw-images is described in Appendix C.2.

The capability of the double-binary approach and the quality of refractive index matching is evaluated in three measurement planes at two Re numbers at a steady Ca . Measurements in the symmetry plane (channel center plane), the channel top wall and at an intermediate plane at 0.75 of the channel height are carried out (Fig. 6.10). In the symmetry plane at the half channel height, distortions arising from non-ideal refractive index matching accumulate and can be quantified. The measurements at the channel top allow classifying, if the flow through the gutters can be measured.

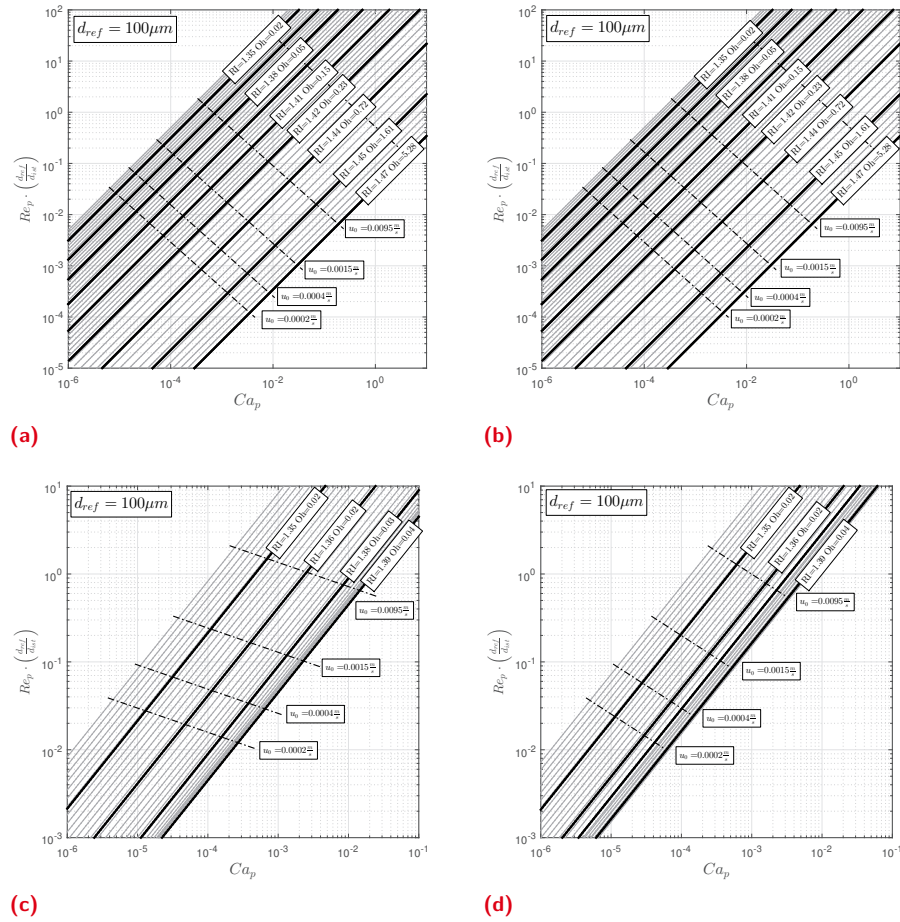


Fig. 6.9.: Nomograms for reachable Ca and Re numbers for a polar continuous phase. a) water/glycerol - n-hexane/anisole b) water/glycerol - n-hexane/sunflower-oil c) water/DMSO - n-hexane/anisole d) water/DMSO - n-hexane/sunflower-oil

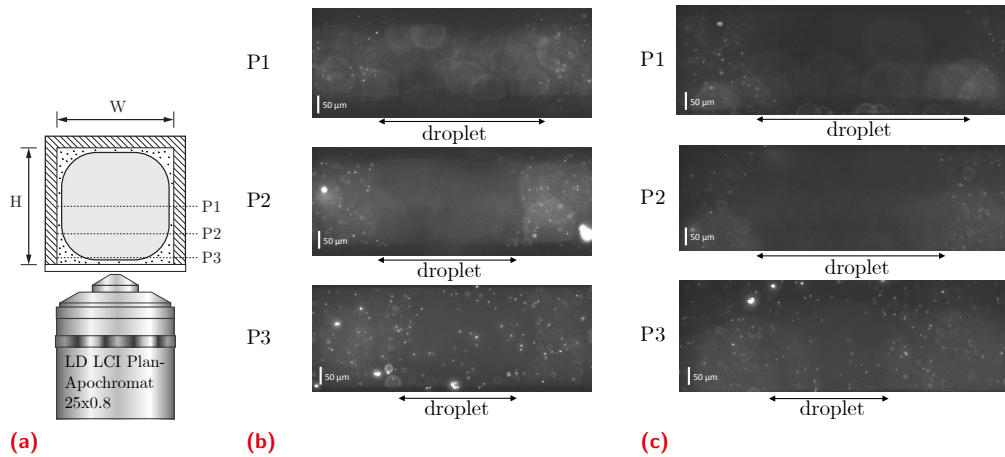


Fig. 6.10.: Exemplary images of a Taylor-flow at two different Re and steady Ca . Water/glycerol is used as the continuous phase and seeded with fluorescent polystyrene particles, n-hexane/sunflower-oil as the disperse phase. Within all measurements no interfacial area is distinguishable, no reflection or distortions of the particles are apparent. a) Cross-section of the microchannel with the measurement planes for proof of principle b) $Ca = 0.005$, $Re = 2.14$, $RI = 1.3838$ $\xi_p = 0.391$ $\xi_n = 0.101$ c) $Ca = 0.005$, $Re = 0.93$, $RI = 1.3958$ $\xi_p = 0.476$ $\xi_n = 0.221$

Within the μ PIV raw images, the droplet interface is not visible. The raw-images in Fig. 6.10 show clearly that the droplet length decreases when the focal plane is moved towards the channel top. This is caused by the curvature of the droplet interface. Only the tracer particles in the focal plane are displayed sharp, while particles on other planes out of focus introduce a blurry signal. Thus, the correlations for the refractive index as well as the solver algorithm works well.

Taylor flows were established and recorded without optical distortion. Thus, the proposed double-binary mixture method works well.

6.5 Conclusion

Within this chapter, a new approach using double-binary mixtures for both immiscible flow phases to establish a refractive index matched microscopic multiphase flows is presented and successfully validated. In comparison to classical mono-binary mixture approaches, Re and Ca can be addressed individually in a material restricted parameter set, since viscosity and interfacial tension (and thus the different flow forces) do not change in the same order of magnitude if the mass-fractions of the phases' binary mixtures are varied. Alternatively, multiphase flows at different Oh at a fixed RI can be established to match the reactor material (e.g. simulating three-phase flows via monolith).

Additionally, two binary mixtures for a polar and nonpolar phase are introduced to enable the investigation of e.g., different viscosity ratios λ or flow systems with simultaneously high or low viscosities are possible too.

Measurements for the relevant material properties (densities, viscosities, refractive index) of the binary mixtures as well as the RI-matched compositions (interfacial tensions) are carried out and compared to literature data to characterize the system. The task to establish multiphase flows at specific Re and Ca independently is identified as an optimization problem and the material properties as well as the interfacial tension are successfully described with correlations that allow the use of a solver algorithm.

In first measurements, the capability to establish refractive index matched Taylor flows at freely chosen Ca and Re is proven. This proof of principle is successfully conducted using recorded μ PIV raw images. With the proposed double-binary RIM-approach the specific influences on the local velocity of droplets can now be independently examined via optical flow visualization techniques (PTV, PIV).

Validating the influence of viscous coupling on the excess velocity of Taylor-droplets using μ PIV measurements

” *A man who dares to waste one hour of time has not discovered the value of life.*

— **Charles Darwin**

(English naturalist, geologist and biologist)

The greybox modeling approach of Sec. 5 identified the gutter length l_g , dimensionless gutter flow resistance β , which is based on the viscosity ratio λ , the aspect ratio ar and the driving force (pressure gradient indicated by droplet cap curvatures) depending on Ca as influential parameters for the excess velocity. In this chapter, the phenomenology of the model and the adjusted input parameters is validated. Based on spatially well-resolved μ PIV measurements utilizing the double-binary RIM approach from Sec. 6, the local flow profile in and outside the droplets is retrieved and examined with respect to the identified model parameters. The velocity information in the gutters of Taylor flows at different Re and λ at a constant $Ca = 0.005$ are acquired as an additional independent measurement set to validate the phenomenology of the model.

7.1 Overview

For the proposed excess velocity model influential parameters like the gutter flow resistance β cannot be measured directly and dedicated literature data for β is not attainable. In the proposed model, β is correlated to the viscous coupling factor λ in accordance with the available literature. Thus, the related correlation factors were retrieved using metaheuristic approaches. This raises the concern, that the model for β might be overfitted to the measured data and does not represent a systematic correlation. Since overfitting is challenging to recognize in the identic parameter set as the model development, it is useful to test against overfitting of the model parameters with additional measurements.

μ PIV measurements are carried out for different Re , λ and gutter lengths l_g applying the double-binary approach from Sec. 6. In carefully conducted μ PIV measurements, the velocity distribution is determined for distinct xy -planes of several z -heights using an inverted microscope with a motorized precision stage and z -drive. The velocity information is

retrieved with the ensemble-correlation method (Sec. 2.4) to decrease the measurement deviation arising from e.g. Brownian motion and to improve the overall quality of the measured vector field.

Considering the microchannel material, it was observed by Mießner et al. (2019) that elastic materials like PDMS might deform during the measurement under the influence of passing Taylor droplets. Gupta et al. (2013) identified the local pressure maxima of a passing droplet, which might be responsible for the deformation. A channel deformation leads to spatial deviations of the interrogated droplets, especially in the proximity of the channel walls. Since elastic channel walls are deformed, the flow is accommodated in a locally increased volume, while the measurements plane (e.g., focal plane of the optical system) remains in place. Thus, the gutter flow is sensitive to the position of the channel wall, since the model is based on the flow through the gutters. It is important to acquire the validation data in a rigid microchannel to avoid deviation caused by deformation of the channel material. An microchannel DRIE-etched in silicon is used for all measurements.

7.2 Material and methods

Different technical domains are associated with the experimental validation of the excess velocity model. These are the setup and the material properties of the liquids, the particles and surfactants used, the verification of the correlation depth, the ensemble averaging method, the hydrodynamic determination of the channel height and the actual design of experiments.

7.2.1 Experimental setup and material properties

The experimental setup for the 3D2C μ PIV-study mainly equals the design of the proof of principle described in App. C.2. Since the 3D2C μ PIV measurements demand a higher instrumental complexity than the proof of principle, the experimental design is reconsidered in detail. This serves the representation and discussion of the experimental results.

As in the proof of principle, a modified Zeiss LSM410 microscope (Fig. 7.1) is used. The integrated continuous wave (CW) lasers of the LSM are deactivated and replaced by a pulsed *New Wave Research Solo-PIV III* laser, which is guided via a laser arm into the beam-scan-system. Utilizing the beam-scan-system of the microscope, the laser beam can be precisely orientated via a motorized concave mirror to maximize the excitation light intensity, thus maximizing the fluorescence intensity yield. After passing the beam-scan-system, the laser light enters the inverted microscope (*Zeiss Axiovert 100*) and is widened by a planoconvex lens. Subsequently, a holographic diffuser equalizes the laser to illuminate the whole sample uniformly. An optical filter set, consisting of a dichroic mirror and lowpass filter, separates the excitation light wavelength from the fluorescence signal. The used microscope objective offers a working distance of $570\ \mu\text{m}$ at a 25x magnification and a depth of field $\text{DOF} = 1.034\ \mu\text{m}$. Alternatively to the laser, a mercury-vapor-lamp can be used to align the microfluidic devices when preparing the μ PIV measurements.

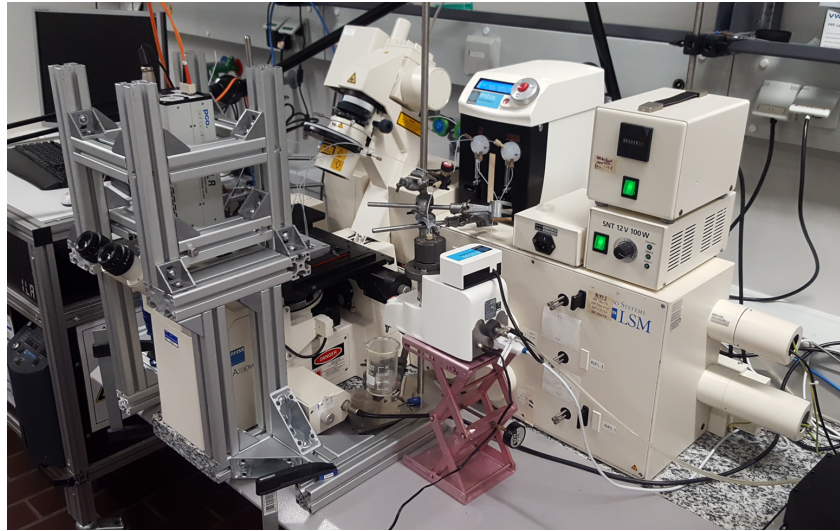
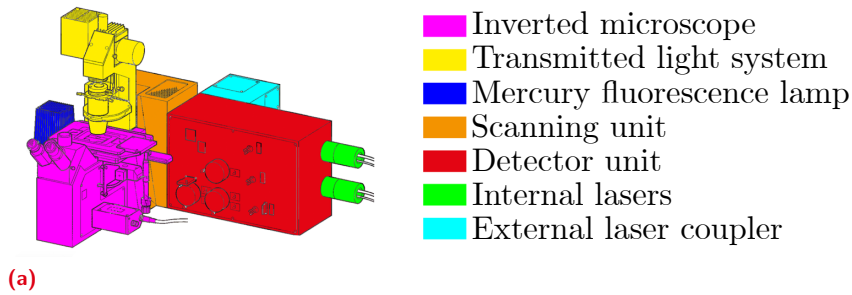


Fig. 7.1.: Adapted confocal-laser-scanning microscope *Zeiss LSM-410* used for the μ PIV measurements. a) schematic drawing of the optical components b) photograph of adapted microscope with peripheral equipment, PIV-camera and external Nd:YAG-laser. *Subfigure a) adapted from (Zeiss, 1995)*

The PIV double-images are recorded by a *PCO sensicam qe 670 LD 3078*, that is mounted on an *Carl Zeiss TV Adapter 2/3" C* with a 0.63 magnification to demagnify the image to the CCD-Chip size of the camera ($6.45 \mu\text{m} \times 6.45 \mu\text{m}$). A possible loss of information is accepted to obtain a wider field of view and to use the entire CCD-chip size of 1376 px x 1040 px. The laser timing and power, as well as the camera timing, are controlled via an *ILA mini PIV-synchronizer*. During the measurements, the time between two images is chosen such, that a particle displacement of 12 px in the flow regions with the highest velocity is obtained. The final interrogation window size (IWS) is 16 px with 50% overlap.

Spherical polystyrene microparticles (*PS-FluoRot-Fi277* from microParticles GmbH, properties in Tab. 7.1) are used as velocity tracer. The particles are purchased as dry powder to exclude possible contamination caused by the preparation of a particle emulsion for shipping by the manufacturer. The fluorescent particles show low dye leaching and high chemical stability for alkanes and fulfill the requirements of a small particle diameter, as well as a small density difference to the liquid phase. The latter ensures a low drag between particles and the flow phase and prevents the deposition of the particles due to inertia. The particle's fluorescence dye is adjusted to the available laser ($\lambda_{ex} = 532 \text{ nm}$) to ensure a high light absorption and an intense fluorescence signal ($\lambda_{peak} = 600 \text{ nm}$). The chosen fluorescence dye (FluoRot) offers an excellent fluorescence signal (560 nm - 850 nm) distinctly shifted from the excitation

wavelength (532 nm). This allows the usage of a dichroic mirror with a cutoff frequency of 550 nm to cover a large wavelength range of the fluorescence signal.

Tab. 7.1.: Properties of used fluorescent tracer particles *PS-FluoRot-1.5*

Property	value	unit
batch	PS-FluoRot-Fi277	-
excitation peak λ_{ex}	530	nm
emission peak λ_{em}	607	nm
density	1.05	g/cm
median diameter	1.61	μm
coefficient of variation (CV)	2.3	%

For the PIV-study of the disperse and continuous phase, both phases require a sufficient seeding with fluorescence particles. Preliminary measurements indicate, that the available PS-particles within the double-binary nonpolar phase sediment and deposit at the walls after preparation. Thus, with these specific particles, a sufficient particle concentration inside the non-polar disperse phase could only be reached in one measurement. This behavior results from the surface properties of the used *FluoRot*-dye coated tracers. Microparticles coated with a different fluorescence-dye (green) do not show this behavior. Unfortunately, the green-labeled particles are not compatible to the μPIV -system ($\lambda_{ex} \ll 532 \text{ nm}$), thus n-dodecane is used as the disperse phase and a one degree of freedom RIM-approach (single-binary mixture) is utilized (Mießner et al., 2008). The refractive index of several water/DMSO mixtures is measured using the method described in Sec. 6.2.2. The measurements indicate, that for a mass-fraction of $\xi_{DMSO} = 0.58$ the refractive index of the binary solution water/DMSO is matched with the RI of n-dodecane (Fig. 7.2)

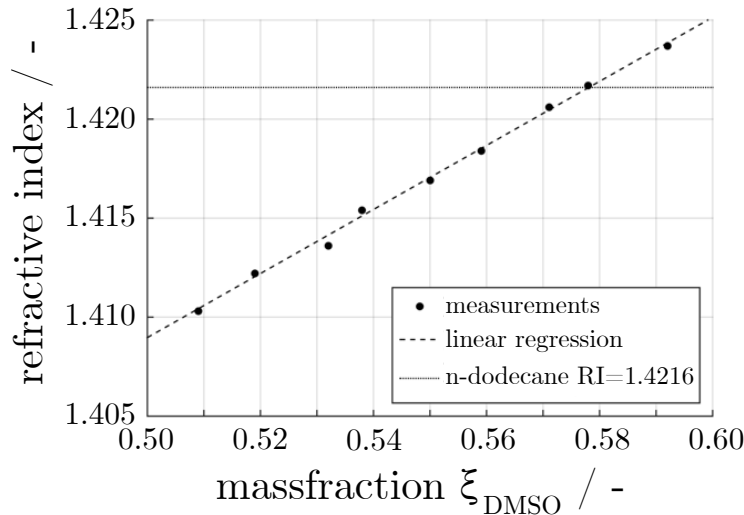


Fig. 7.2.: Measurements of refractive index for water/DMSO-mixture at different mass-fractions ξ . At $\xi = 0.58$ the refractive index of the mixture equals the RI of n-dodecane

To further improve the particle suspension stability, $1 \mu\text{mol/l}$ AOT (Dioctyl sulfosuccinate sodium) is added to the nonpolar phase in consultation with the particle manufacturer. This allows a redispersion of the particles by the flow (visualized in Fig. 7.3) and prevents capillary clogging in the microchannel-feed. The changes of the interfacial tension caused by the addition of AOT is carefully determined.

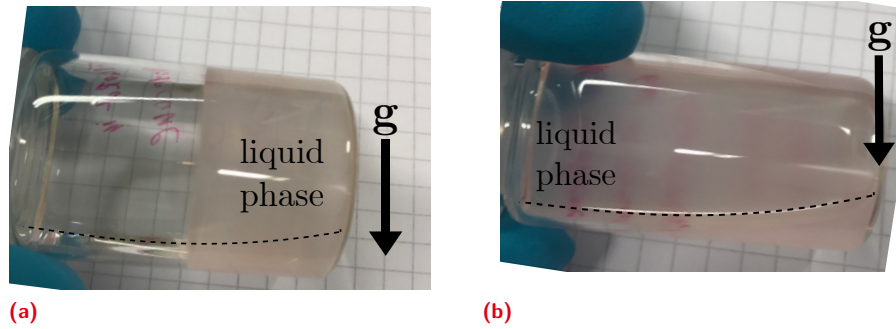


Fig. 7.3.: PS-fluorescence tracer particles in n-dodecane. Without an addition of the surfactant AOT (a), the particles directly deposit at the walls of the snap-cap vial and cannot be redispersed by shaking. After addition of AOT (b) the particles redisperse by movement of the vial

Since the second degree of freedom is omitted in this approach, the Ca -number can only be adjusted by tuning the interfacial tension of the water/DMSO-dodecane system. Thus, a mixture of water/DMSO with added sodium dodecyl sulfate (SDS), an anionic surfactant with a HLB-value of 40 (Rowe, 2009, p.651–652), is added to the continuous phase. The author is aware, that the addition of surfactants alters the system drastically, as the surfactant may absorb locally to the interfacial area (Olgac and Muradoglu, 2013) and therefore influence the viscosity of the interfacial area and the film thickness.

The properties of the surfactants are shown in Tab. 7.2.

Tab. 7.2.: Properties of used surfactants

Surfactant	molar mass / g mol^{-1}	density / g cm^{-3}	solubility in water / g L^{-1}
AOT	444.559	1.146	8.17
SDS	288.38	1.1	150

The main influences of surfactants on two-phase flows are often linked to the critical micelle concentration (CMC) (Fuerstman et al., 2007). The CMC defines the concentration, at which the surfactant molecules start to orientate as geometrical defined structures (micelles). At concentrations below the CMC, surfactant molecules mainly occur as single molecules and absorb to the liquid's interface. With an increasing surfactant concentration, the interfacial tension is decreased rapidly since the probability of surfactant molecules to absorb into the interfacial area rises. When the CMC is reached, the interface can be considered energetically saturated and only minor changes are achieved when increasing the surfactant concentration. At this point, the formation of even complex micellar-structures enables a lower energy level in the system and the surfactant molecules align depending on the bulk solvent. However, it has to be mentioned, that this explanatory approach is a phenomenological reduction of the real thermodynamic behavior as already below the CMC singular micelles exist. Since in this work the focus lies on the hydrodynamic influence of the surfactants, the author considers this valid. For a detailed thermodynamic and energetic consideration of the solubilization of surfactants and the formation of micelles, please refer to dedicated literature (Butt et al., 2003, p.251).

The CMC depends on the composition of the substance the surfactants are solved in. For that reason, interfacial tension measurements are performed as stated in the appendix of the previous chapter (App. C.1): Different SDS concentrations are dissolved in water/DMSO ($\xi = 0.58$) and the interfacial tension is measured (Fig. 7.4). Additionally, $1 \mu\text{mol l}^{-1}$ AOT is added like in the later experiments for particle dispersion.

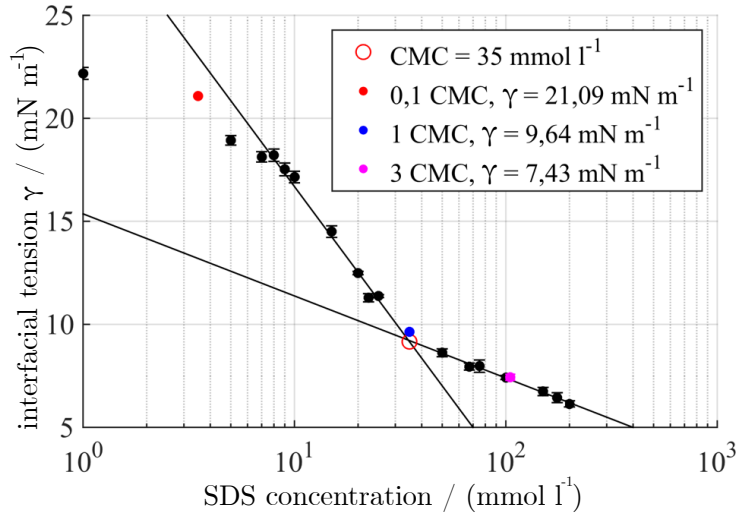


Fig. 7.4.: Measurements of the interfacial tension for different SDS concentrations in a mixture of water/DMSO $\xi = 0.58$ with $1 \mu\text{mol l}^{-1}$ AOT in the n-dodecane fraction

The CMC is retrieved from the point, where the slope $\frac{d\gamma}{dc_{SDS}}$ changes, since for concentrations above the CMC the interfacial tension changes less. Within the measurements, this equals 35 mmol l^{-1}

Please note, that the addition of SDS not only influences the interfacial tension and surface viscosity, but also alters the bulk viscosity of the water/DMSO-mixture. Thus the viscosity ratio λ is also effected. This occurs when concentrations beyond the CMC are applied due to the formation of a lyotropic micelle phase. The corresponding measurements for the viscosity are shown in App. D.1. While the increase of viscosity for concentrations below the CMC is less than 5 %, the concentration beyond the CMC increases the bulk viscosity about 30%. This interrelation needs to be considered when interpreting the variations of the flow field and the change of the excess velocity.

7.2.2 Validation of correlation depth and adjustment of ensemble averaging

A measurement of the flow velocity inside the gutters of Taylor droplets requires the xy flow data from multiple different channels heights (slicewise measurement of the flow in z -direction). As stated in Sec. 2.4 the z -distance between two measurement planes needs to be set bigger than the depth of correlation (DOC). An overlap of measurement planes would not add useful information to the measurement. If the distance between two measurement planes is lower than the DOC, also information from particles outside the interrogated plane are considered and may interfere with the correct particle information from the considered

plane. This results in a loss of information of the reconstructed vector-field and potentially biases the data.

To calculate the DOC, at first the numerical aperture of the objective *Carl Zeiss LD LCI Plan-Apochromat 25x/0.8* is converted to the used water with a RI = 1.333 since instead of air (RI = 1). With the Eq. 2.10 a half opening angle for air as immersion medium can be calculated as $\theta = 53.13^\circ$. From this the numeric aperture for water can be calculated as NA = 1.0666. This results in a depth of field $DOF = 1.034\mu\text{m}$ and a corrected $DOC^{\text{corr}} = 7.034\mu\text{m}$ is retrieved.

To prove the calculations, an image series of stagnant fluorescence particles dispersed in water/DMSO is acquired. Fluorescence particles are dispersed in water/DMSO, placed on a microscope slide and are embedded by a coverslip. The particles are illuminated by a laser and the fluorescence signal is recorded. The z -position of the objective is adjusted for the sharpest image of the interrogated particle and subsequently varied $10\mu\text{m}$ around the focal point, while for every z -step an image is acquired (Fig. 7.5).

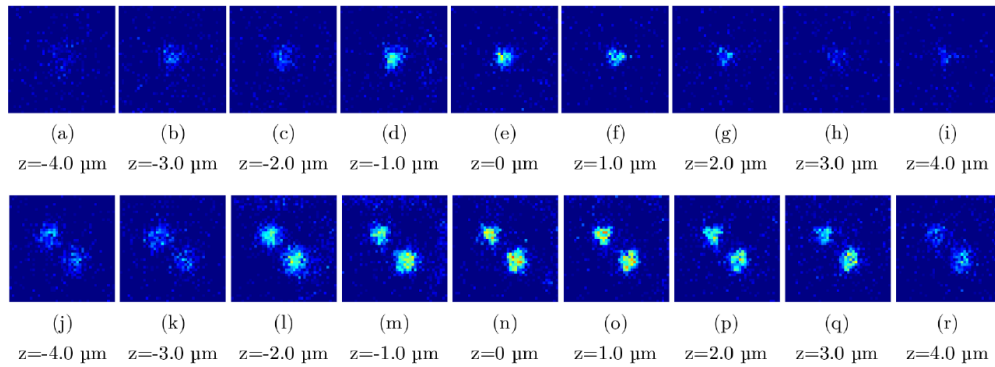


Fig. 7.5.: Validation of calculated depth of correlation using two images series (a) - i) and j) - r) of $1.61\mu\text{m}$ fluorescence particles at different z -positions deviating from the particle (pixel intensity is coded as color). Each single image represents an area of $7\mu\text{m} \cdot 7\mu\text{m}$

Within both image series a rapid decrease of fluorescence intensity and therefore a loss of clear image information is visible at z -position deviations of $3\mu\text{m} - 4\mu\text{m}$ from the focal point (a , i - h , i and j , k - q , r). Thus, depending on the images, a medium DOC^{meas} of $6\mu\text{m} - 8\mu\text{m}$ is retrieved. This is in accordance with the calculated value $DOC^{\text{corr}} = 7\mu\text{m}$. Therefore a mean distance of at least $7\mu\text{m}$ should be chosen between the z -positions of the measurement planes.

The postprocessing of the droplet raw images is performed using an ensemble image averaging approach as described in Sec. 2.4. For the sorting of the raw images, the intensity based sorting and shifting approach by Mießner et al. (2019) is used. As an improvement of this work, the tolerable droplet length deviation over all measurement planes, as well as the used median droplet length, is acquired via an iterative approximation approach: The considered median droplet length is chosen such, that for all 14 measurement planes at least 30 droplets are available for postprocessing. If this number is exceeded, the tolerable droplet length deviation is subsequently decreased until only the desired 30 droplets are remaining. This is performed for several median droplet lengths and finally the median length with the least droplet length deviation over all planes used.

Since the interrogation windows size (IWS) shows a strong influence on the quality of the resulting velocity data, it is validated if the choice of IWS corresponds with the particle displacement of 12 px (Fig. 7.6). Best results are achieved for an IWS of 16 px x 16 px. For lower IWS, the ensemble correlation decorrelates in flow areas with a high velocity. Therefore, an IWS=16 px x 16 px is chosen and coincides well with the targeted particle displacement of the fastest particles of 12 px.

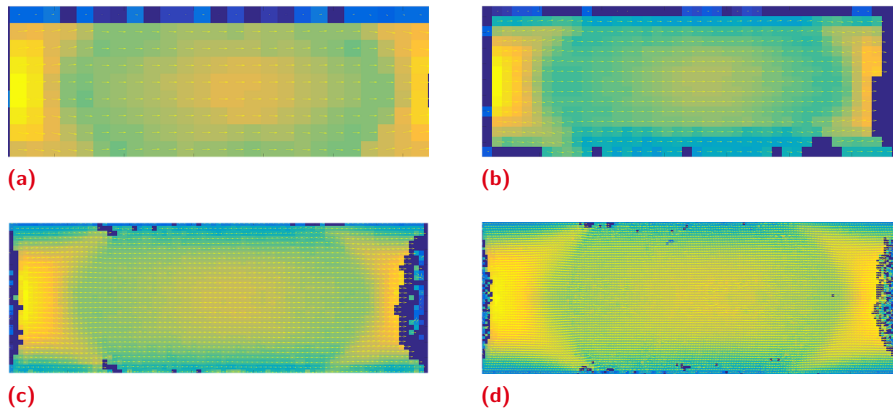


Fig. 7.6.: Velocity field for a flowing Taylor-droplet in a moving reference frame coordinate system (u_d). Effect of different interrogation windows sizes (IWS) on the resolution of the ensemble averaging approach. For all variations identical raw-images and an IWS-overlap of 50% were used. a) IWS=96 b) IWS=64 c) IWS=32 d) IWS=16

7.2.3 Hydrodynamic determination of channel height

The evaluation of the flow fields on different measurements planes requires precise knowledge of the actual channel height to correctly identify the number of measurements planes needed and to define the symmetry plane in the channel center.

The available microchannels are specified with a height of $200\ \mu\text{m}$. However, due to the DRIE-etching process during production, the bottom of the channel is considered nonplanar and the wall roughness of the channel bottom is high. Both could lead to an altered hydrodynamic height. While the wideness of the reactor can be determined via pixel-calibrated measurement in an image of the microchannel top, the channel depth can only be measured by focusing the channel top and bottom and calculating the difference via the moved z -position of the objective. Measurement errors and parallax-effects (decision when the channel top, as well as the bottom, is actually in focus), lead to an unacceptable interval of estimated channel heights between $169\ \mu\text{m}$ - $206\ \mu\text{m}$.

A metrological definition of the hydrodynamic channel height can be performed by establishing an analytically well-defined single-phase flow in the microchannel and measuring the maximum flow velocity for different channel heights by means of μPIV . For a laminar single-phase flow with rectangular cross-section at moderate Re a parabolic profile is expected on each xy -plane of the measurement. Also, a parabolic profile is present in the yz -plane. From the symmetry condition of the rectangular channel, the profile of the entire parabola in yz -direction can be reconstructed with μPIV measurements at discrete channel heights.

The measurement data for the first reactor batch is shown in Fig. 7.7. The assumed half channel height ($100\ \mu\text{m}$) does not coincide with the reconstructed parabola. Instead, the maximum is found at $89\ \mu\text{m}$ and $96\ \mu\text{m}$. Thus, the hydrodynamic channel height can be considered to be $178\ \mu\text{m}$ and $192\ \mu\text{m}$ respectively.

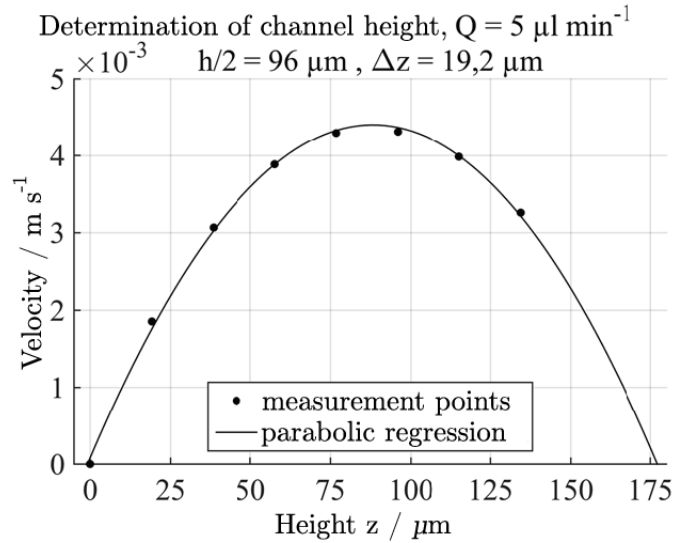


Fig. 7.7.: Determination of hydrodynamic channel height using a single-phase flow with a flow rate of $5\ \mu\text{l min}^{-1}$. The measurement data shows the parabolic regression fitted to the measurement data with the lowest root mean square error (RMSE). The maximum velocity (the maximum of the fitted parabola) does not coincide with the estimated half channel height at $100\ \mu\text{m}$. Instead, the correct channel height (h in this figure) can be determined at the intersection of the abscissa. Only measurements for the first reactor batch with a height of $178\ \mu\text{m}$ are shown

The integrity of the measurement data for a one-phase flow is additionally validated successfully utilizing an approximation of the Navier-Stokes-Equation for rectangular microchannels and is shown in the Appendix (App. D.3).

7.2.4 Design of experiments

The local velocity field of Taylor droplets and the surrounding gutters is measured at different z -planes at a distance dz of at least the $\text{DOC} = 7.034\ \mu\text{m}$. Using the symmetry conditions of rectangular channels, only in half of the microchannel measurements are performed to decrease the amount of data handling. Since the height of the first reactor batch is $H = 178\ \mu\text{m}$, this results 14 measurement planes. For the second batch reactor ($H = 192\ \mu\text{m}$), also 14 measurement planes are chosen to obtain integrity and comparability of the results. The orientation of the measurement planes with obtained velocity data is schematically shown in Fig. 7.8.

The influence of Re , Ca and λ on the local hydrodynamics is evaluated to validate the phenomenology of the proposed excess velocity model. The following measurements are carried out (Tab. 7.3). The gutter length l_g is a posteriori retrieved from the measurements. Supplementary measurements with seeding only in the continuous phase, are shown in die Appendix (App. D.3).

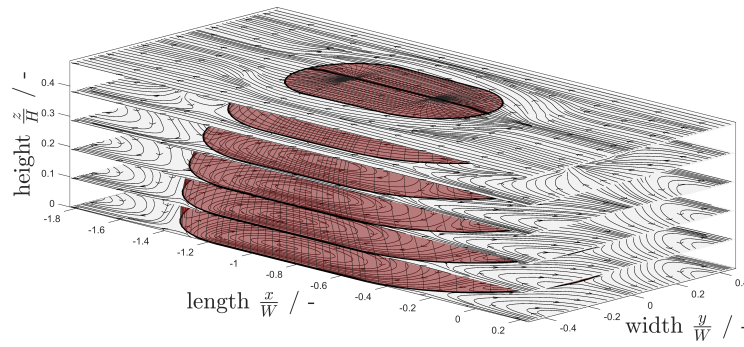


Fig. 7.8.: Orientation of the measurement planes in xy -orientation with velocity data obtained from μ PIV measurements (seeding in both phases). The droplet interface is determined using the shape approximation of Mießner et al. (2019). Only 6 of the 14 measurement planes are shown for reasons of clarity and comprehensibility.

Tab. 7.3.: Carried out measurements for the model validation. All for $Ca = 0.005$

No.	Re	Oh	λ	$\frac{l_g}{w}$	flow system
I	0.93	0.0733	1.032	0.66	water/DMSO - hex/sunfl.
II	2.14	0.0483	0.341	0.83	water/glycerol - dodecane
III	2.06	0.0493	0.336	0.83	water/DMSO/0.1CMC SDS - dodecane
IV	0.93	0.0733	0.333	0.83	water/DMSO/1.0CMC SDS - dodecane
V	0.52	0.0733	0.240	0.83	water/DMSO/3.0CMC SDS - dodecane

Thus the following effects can be observed: within measurements I and II, Re , l_g and λ are varied, but no surfactants are present. Thus, the effect of Re on the local flow can be examined. Following the consideration of the proposed model, Re should not significantly influence the flow field. This effect is expected to be caused by λ . Utilizing measurements II+IV, Re is varied by a surfactant concentration change with a small increase of λ . Thus, the effect of a varied Re with additional surfactants can be observed. In this case, Re is not expected to significantly influence the flow field, because the viscosity ratio stays constant and only the interfacial tension, mobility and viscosity are addressed. In measurements II+V, λ , Re , as well as the surfactant concentration is varied. The effect of Re and λ on the flow structure can be examined. Considering u_{ex} , an increase with a shorter gutter length, as well as a lower λ is expected to become visible.

7.3 Results and discussion

The excess velocity is strongly correlated to the gutter volume flow as it is shown in Sec. 5.2.1. Velocity data retrieved by means of μ PIV allows to visualize the flow profiles in the gutter to derive the mean axial velocity as well as the volume flow distribution in streamwise direction. To simplify the quantification of the volume flow through the gutters, the velocity field is evaluated as far away from the caps as possible to ensure a flow direction pointing predominantly in streamwise direction (x -direction). Thus a number of 9 cross-sections at the longitudinal streamwise center of the Taylor droplets is chosen to average the streamwise

velocity distribution and to measure the volume flow distribution in the gutter. An increase of the excess velocity $u_{e,x}$ is expected to be accompanied by an increasing negative gutter volume flow. Depending on λ , the flow profile should change according to (Rao and Wong, 2018).

7.3.1 Local flow structure in the gutters of Taylor-droplets

The volume flow in the gutters of the droplet is examined using the proposed 3D2C μ PIV methods. The precise knowledge of the droplet interface position is needed to determine the correct gutter flow and to distinguish between the droplet and the continuous phase. Since the flow phases are refractive index matched, the interfacial area cannot be determined directly by optical measurements. Instead, averaged images of the shifted μ PIV-data are used and in the gutter the distance between droplet and wall is determined using a particle seeding gradient between both phases (Fig. 7.9). The results are averaged over all cross-sectional measurements planes, since they have been performed at a nearly identical $Ca = 0.005$ and thus the gutter cross-section is expected to coincide (Mießner et al., 2019).

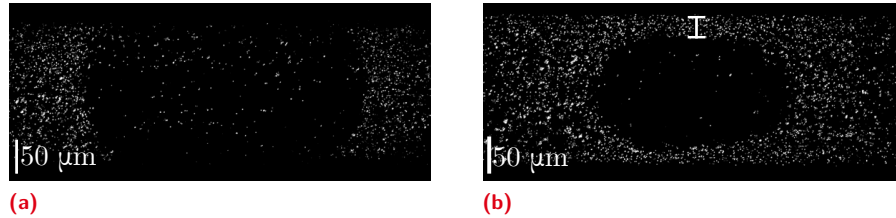


Fig. 7.9.: Summed raw μ PIV images of sorted and shifted Taylor droplet with seeding in both phases at two measurement planes. The different seeding of both flow phases allows discriminating between droplet and continuous phase. a) sum-image in the channel center plane (at channel height $z=89\ \mu\text{m}$) b) sum-image in a plane near the channel top wall with schematic measurement of the gutter size (at channel height $z=13.7\ \mu\text{m}$)

To quantify the relative volume flow in the gutters, the local relative velocity in the x -direction $u_{rel}(\bar{x}, y, z)$ is determined using the stagnation point velocity of the droplet u_d . To minimize the influence of measurement errors at single interrogation windows, the information of 9 yz -planes around the droplet center are averaged (Fig. 7.10):

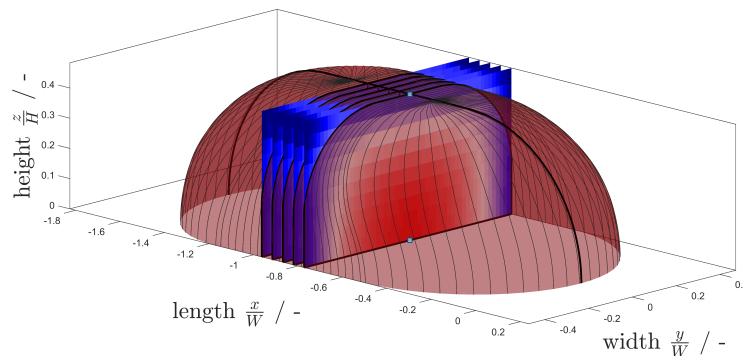


Fig. 7.10.: Orientation of the interrogation planes in y, z -orientation obtained from μ PIV measurements (seeding in both phases). The droplet interface is determined using the shape approximation of Mießner et al. (2019). Only 5 of the 9 planes of the averaging step around the droplet center are depicted for reasons of clarity and comprehensibility

$$u_{rel}(\bar{x}, y, z) = u(\bar{x}, y, z) - u_d \quad (7.1)$$

For the excess volume flow through the gutters, the local relative volume flow distribution in the center cross-section (y/z -plane) of the droplet

$$Q_{ex}(\bar{x}, y, z) = \frac{Q_{rel}(\bar{x}, y, z)}{Q_0} = \frac{u_{rel}(\bar{x}, y, z) \cdot (dy dz)}{Q_0} \quad (7.2)$$

is calculated. The streamwise relative velocities for each interrogation window $u_{rel}(\bar{x}, y, z)$ are multiplied with the reference area, i.e. the product of the stepwidth in y and z direction. Herein the stepwidth $dy = IWS/2$ is caused by the 50% overlap of the interrogation windows (Sec. 2.4) and stepwidth (dz) denotes the distance between two measurement planes.

The calculated excess gutter volume flows ($Q_{ex}(\bar{x}, y, z)$) are shown in Fig. 7.11:

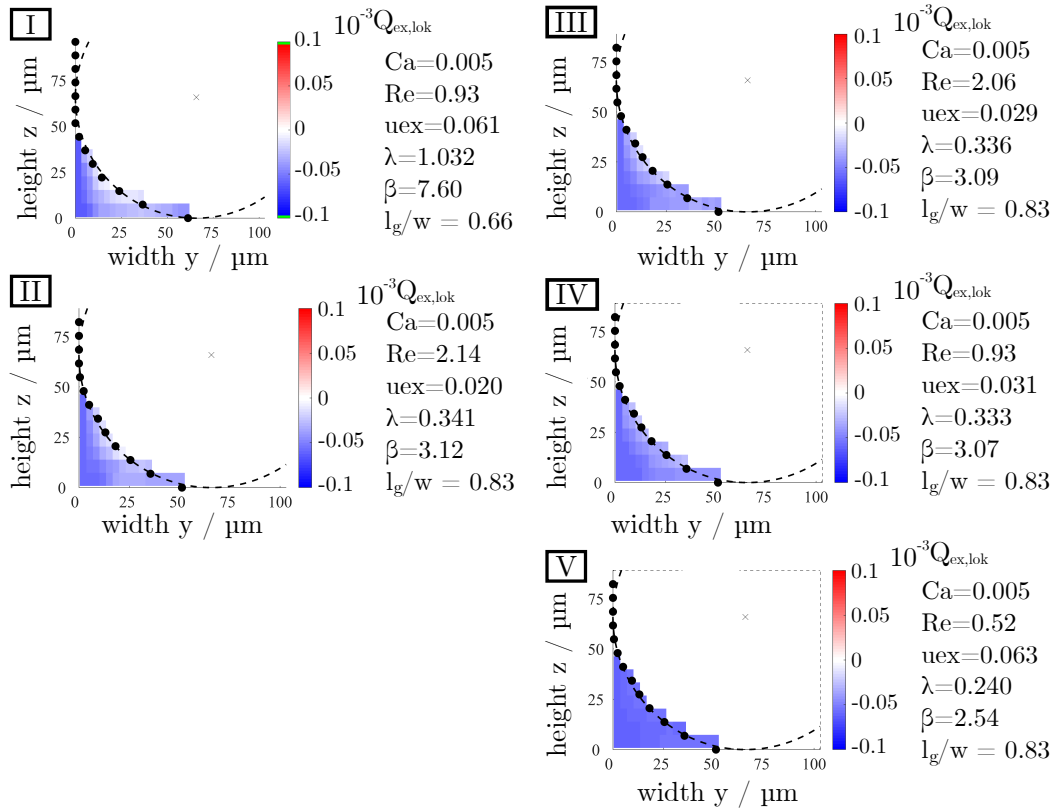


Fig. 7.11.: Local excess volume flows $Q_{ex,loc}$ in the gutters at the droplet center. Red volume flows point in positive x -direction (towards droplet front and the observer), blue into opposite direction

The measurements at an elevated Re and rising λ (II, III) exhibit a gradient in the gutters. In close proximity to the interfacial area on the cross-sectional diagonal, the relative gutter volume flows tend to point towards. This should result in lower excess velocities (Eq. 5.14) of identical gutter length. To validate whether this is caused by Re , λ or the surfactant

concentration measurements **I** and **II** can be compared. Here, an influence of Re cannot be confirmed, since a similar flow distribution is visible in the gutters. Admittedly, a decrease in excess velocity from **I** to **II** is evident, but this is considered to be caused by the much shorter gutter length l_g of **I** and it is supported by the findings of (Jakiela et al., 2011). Based on the measurements it can be postulated that a more viscous disperse phase (larger λ) includes a larger resistance to the forces exerted from the walls. Therefore, the flow in the gutters changes more strongly since energy is more mainly dissipated in the gutters, which leads to a lower excess velocity. To furthermore evaluate the influence of surfactant addition, the flow profile over the entire Taylor droplet and channel cross-section is examined.

7.3.2 Local flow structure of entire Taylor-droplets cross-section

Similar to the previous section, the excess volume flows $Q_{ex}(\bar{x}, \bar{y}, z)$ for each interrogation window are calculated. Since both flow phases are simultaneously seeded with fluorescence particles, the velocity profile across the entire channel cross-section can be retrieved. This allows to identify a variation of the flow profile inside the droplet and to determine how e.g. the viscosity ratio λ influences the flow.

Furthermore, the flow-field in the microchannel center plane is represented with streamlines to observe the influences of λ and Re on the local flow field. Additionally, a possible influence of surfactant addition can be shown. Measurement **I** uses the double-binary mixture approach, while **II-V** apply an one degree of freedom approach utilizing the surfactant SDS to tune the interfacial tension. This allows to compensate the variation with the superficial velocity to adjust Re and to establish a constant Ca .

The velocity measurements of at least 30 averaged droplets are shown in Fig. 7.12. The streamlines are plotted together with the averaged images of the shifted images of the center plane to allow discrimination between the droplet and the continuous phase. The coordinate system is transformed into a moving-frame description with the velocity at the stagnation points of the droplet front (u_d).

The measurements show recirculation of the slug region in the observed image frame at the droplet caps. Also the flow in the droplets is visible. The center torus-vortex is mainly represented, while the two front and back vortices are not clearly visible in the measurements, since the ensemble averaging algorithm decorrelates here. This is caused by the low seeding of the disperse phase due to the deposition of particles from the disperse phase at adjacent walls. A rising surfactant concentration (and continuous phase viscosity) causes the main vortex to position closer towards the droplet's rear cap. At the maximum surfactant concentration (**V**) of 3 CMC the vortex position is altered the most. A displacement of the front and rear secondary vortices can only be anticipated.

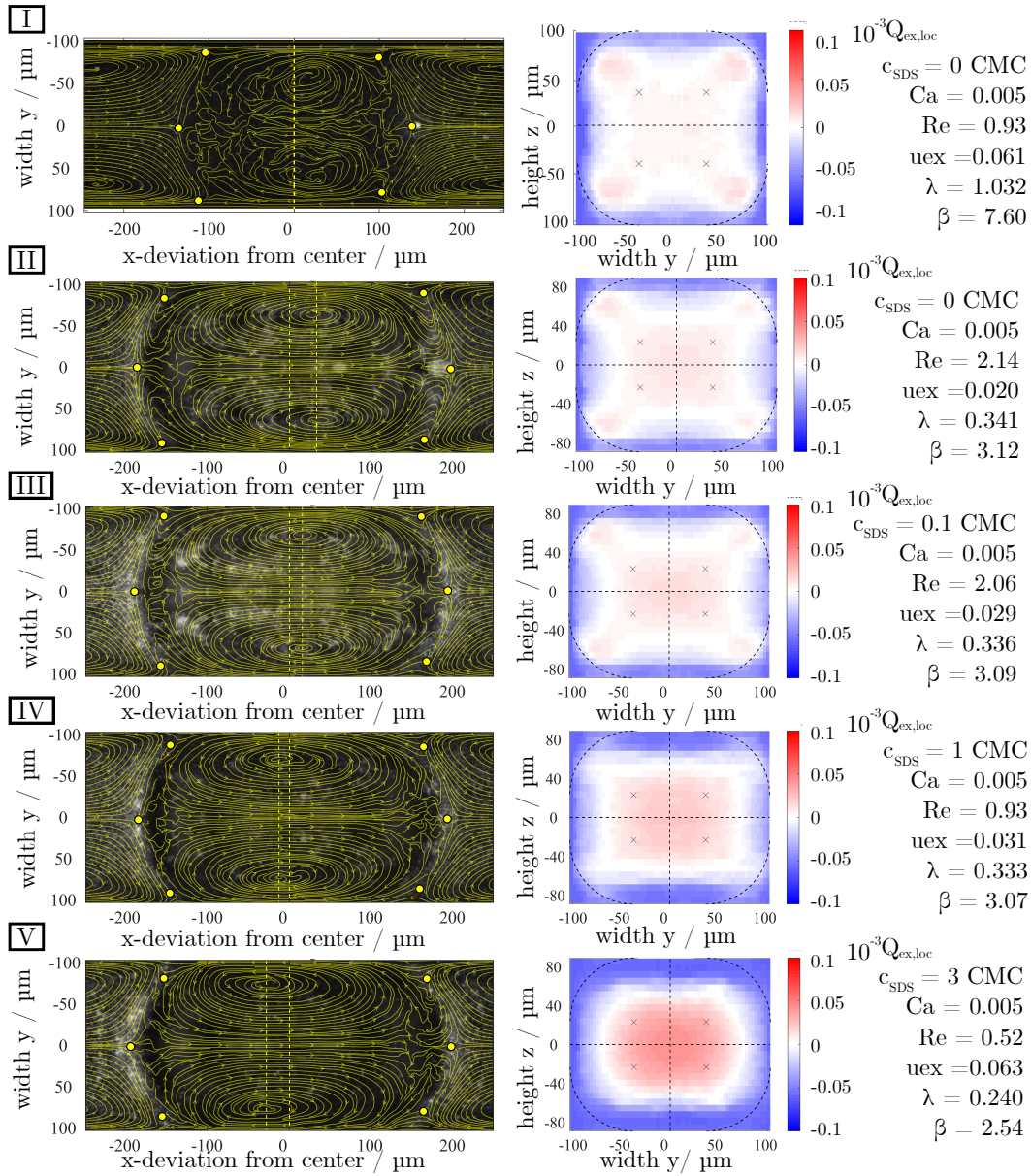


Fig. 7.12.: Streamlines of the flow in channel center plane in z -direction retrieved from ensemble averaged μPIV measurements. The corresponding particle average image is used as background to visualize the position of the droplet. The stagnation point at the interfacial is marked with yellow dots. In addition, local excess volume flows $Q_{ex,loc}$ for the entire longitudinal streamwise droplet center are depicted. Red volume flows point in positive x -direction (towards droplet front and the observer), blue volume flows point in opposite direction. The gutter lengths l_g are retrieved from the images.

At the droplet front and rear cap three stagnation points are visible: At the droplet front there are two converging and one diverging stagnation point, while in the back there are one converging and two diverging. The denomination of the stagnation points was chosen in terms of surfactant transportation towards the interfacial area (perspective seen from the continuous phase, since effective amounts of surfactants were only added to the continuous phase). A comparison of the streamlines for all surfactant concentrations shows no significant differences in the stagnation point position.

A variation of surfactant concentration alters the surface tension and the viscosity of the continuous phase, since the surfactants are added only to the continuous phase. Therefore a change of Re and λ is present and causes variations of the flow field. All measurements show a positive flow in the cross-section of the flow field. For low surfactant concentrations, four additional positively oriented flow filaments at the channel corners and the gutters are visible. Increasing the surfactant concentration, the positive flow is intensified in the channel center, while the flow towards the gutters decreases. Additionally, the regions of flow inversion with respect to the droplet velocity (shown as white flow areas) are moved towards the channel center. This can be interpreted as a decrease of the hydrodynamic cross-section.

Varying the viscosity ratio of the flow, a higher λ leads to a position change of the central vortex towards the droplet front (visible for the measurements without surfactants and higher λ). This effect seems not to be based on Re alone as the comparison with measurement **V** at a lower Re shows. For lower λ and higher surfactant concentration, the vortex moves to the droplet back. The movement of the vortex is assumed to be a consequence of the varied viscous coupling between both phases. If the disperse phase viscosity is low ($\lambda < 1$), the continuous phase dominates the flow and the droplet simply follows. Therefore the main velocity gradients are situated in the droplets (**V**). If the disperse phase is more viscous ($\lambda > 1$), the disperse phase momentum dominates the gutter flow. Thus, the main velocity gradients are positioned closer to the gutters (**I**). The disperse phase forms viscous finger-like structures since the continuous phase is not able to transfer the momentum from the wall into the droplet through the gutter.

The comparison of depicted volume flows only allows a qualitative evaluation of the effects. Nevertheless it is evident, that the addition of surfactants does not lead to a strong immobilization of the interfacial area. In this case, the velocity of the interface would be almost constant at the entire droplet interface (like solid body translation). Alternative visualizations of the flow field with color-coding of the streamwise velocity-component (u for x - and v for y -direction) are given in App. D.3.

The excess velocity of measurements **II** - **V** is below the excess velocity of **I**. Especially the increased gutter resistance β of measurement **I** would let one think of a lower u_{ex} . However, the l_g effect seems to exceed the influence of an increased gutter resistance β , since l_g is notably smaller.

In the case of the presented measurements, an addition of surfactants shows no surfactant specific influence on the local hydrodynamic behavior of Taylor droplets in rectangular microchannels. The changes in excess velocity could be sufficiently explained with the increase of the viscosity ratio λ due to the significant formation of micelles. Specific effects like an immobilization of the interfacial area or moved stagnation points could not be shown.

7.4 Conclusion

Utilizing the novel double-binary mixture approach developed in this work (Sec. 6), 3D2C μ PIV measurements at 14 different channel heights in the rectangular microchannels at a narrow depth of correlation of $7\ \mu\text{m}$ have been carried out. The hydrodynamic height of the channel was experimentally validated and the PIV-approach itself referenced with analytical solutions for laminar flows in rectangular microchannels. Commercially available PS-particles could be dispersed in various mass-fraction of the polar binary mixture system, while for the nonpolar phase only in a single measurement a stable tracer suspension could be reached. This is probably related to the red fluorescence dye, since particle with blue dye form a stable suspension, but could not be used with the available PIV-laser combination. The omitted measurements were replaced by measurements utilizing a classical one degree of freedom RIM-approach with surfactant addition.

An ensemble-image-averaging approach in combination with an improved droplet sorting routine was used to carefully retrieve velocity information in xy -measurement planes at different z -height positions. Based on these measurements, the flow in the droplet gutters and the droplet center was examined in dependency of Ca , Re , λ and the surfactant concentration. The phenomenological aspects of the proposed model have been successfully validated: A longer gutter length l_g and a higher λ lead to a decrease of the excess velocity. Additionally, the flow fields at the microchannel center plane are examined and a change in the position of the central vortex is identified in dependency of λ only. Neither an immobilization of the interface due to the surfactants could be observed, nor a position change of the stagnation points.

Nevertheless, the interrelation between Re and λ for the excess velocity could not be conclusively clarified, since the double-binary mixture system could not be used for all measurements due to a lack of available suspensible tracer particles.

Conclusion and outlook

” *One, remember to look up at the stars and not down at your feet. Two, never give up work. Work gives you meaning and purpose and life is empty without it. Three, if you are lucky enough to find love, remember it is there and don't throw it away.*

— **Stephen Hawking**

(English theoretical physicist and cosmologist)

In this thesis for the first time the influential parameters on the excess velocity have been identified and a phenomenological model was derived. To fulfill this task, four research aims were defined, successfully accomplished and different valuable benefits arose on this journey. A novel non-invasive and cost-efficient measurement device based on near-infrared (NIR) photometry was developed and successfully tested, the flow-induced Taylor droplet cap deformation was successfully correlated to the Ca -number and Genetic Algorithms were successfully adapted for model adjustment. Model validation drove the development of a novel refractive index matching (RIM) approach, providing two degrees of freedom. Including the determination of all necessary material parameters, a proof of principle is given. The phenomenology of the model was subsequently validated using carefully performed 3D2C μ PIV measurements. For this purpose, ensemble-image-averaging and ensemble-correlation methods were used.

With respect to the four research aims, the challenging modeling approach was processed in five chapters, each representing a small step towards the ambitious over-all aim:

Utilizing NIR-emission, a photometric approach, consisting of a diode emitter and detector, was used to non-invasively resolve spatial and temporal information from Taylor flows with only a single detector/emitter unit. The droplet cap geometry was identified as a geometric parameter to translate the temporal signal to spatial droplet information, and the cap curvature was identified to be related to the droplet velocity. A raytracing simulation was carried out, to gain an understanding of the measurement system and the underlying correlations. The cap curvature was identified in a sensitivity analysis as the best factor for a geometrical conversion from temporal to spatial signal via the instantaneous droplet velocity. A prototype was manufactured and the applicability, as well as the measurement principle, successfully validated against highspeed camera measurements.

Based on the gained knowledge of the velocity sensitivity of the droplet cap, optical high-speed camera measurements of the droplet front and rear cap at different Re and Ca were performed to precisely define the influential parameters on the droplet cap. A geometric curvature ratio was introduced to describe the flow induced Taylor-droplet cap deformation.

Based on the performed measurements, the Ca was identified as the influential parameter for moderate Ca and Re , while no statistically significant influence of Re could be determined. Based on the measurement results, a correlation for the cap deformation ratio was retrieved.

A phenomenological model was developed to estimate the excess velocity of Taylor droplets. For this purpose, the concept of excess velocity was introduced and the relevant volume flow was derived from the continuity equation and identified as the relative gutter flow. The droplet cap deformation correlation was used to derive the Laplace pressure at the gutter entrances of the droplet based on Ca . Utilizing an approach to estimate the flow resistance of the gutter and combining it with determined pressure difference as the driving force, the influential parameters for the excess velocity were identified. These are the gutter length l_g , the gutter radius $k_{g,i}$ calculated via a Taylor droplet shape approximation from the cap deformation $k_{c,i}$ and a dimensionless resistance factor β , which implements effects of the viscous coupling.

For phenomenological model validation, a two degree of freedom RIM-approach was introduced, that allows adjusting Re and Ca independently to examine the local flow at these parameters. The latter is done by changing the mass-fraction of both flow phases (while being RI-matched) and varying the superficial velocity to obtain the desired inertia of the system. Four different double-binary mixtures (for each phase one with high and one with low viscosity) were presented, to achieve the possibility to establish Taylor-flows at different λ by altering the materials of the flow system or invert the flow phases. The material parameters for the binary mixture were measured and successfully correlated to enable a software-based determination of the desired mass-fractions and superficial velocity, which combines to the distinct dimensionless numbers. A proof of principle is given presenting raw images of a μ PIV study.

The phenomenology of the model was validated using carefully performed spatially resolved 3D2C μ PIV measurements at 14 z -height-position in two rectangular microchannels. Flow images were acquired using a pulsed Nd:YAG-laser for excitation and a high quantum efficiency double-CCD camera. Spatially resolved velocity information was gathered at 14 planes by using a droplet-sorting and shifting approach, to measure the flow of at least 30 independent droplets. The vector quality is improved by utilizing a correlation-averaging approach. As a result, streamlines of the flow, as well as the yz -plane (gutter cross-section) at the droplet center, are retrieved. The influence of Re on the local flow field was identified to be low, while the viscous coupling λ showed an influence on the local flow field in the droplet and on the excess velocity. In addition it was shown, that the gutter length l_g influences the excess velocity as predicted by the model. The phenomenology of the model was successfully validated.

Looking into the future, the results from this work may pave the way for an improved process modeling. Linked strictly to the excess velocity, the residence time of Taylor-droplets in microreactors directly influence the chemical selectivity of reaction and the process performance. If the residence time can be determined more precisely while designing a reactor, improvements of the processes efficiency without additional efforts or costs could be achieved. This work may help to attenuate the future shortage of resources, as well as

to increase the process yield and profit. Also analytical or general microfluidic approaches that utilize droplet chains, where droplet pressure drop feedbacks on the disperse phase formation, can be improved by a better process knowledge.

The author would be proud if the arisen benefits besides the model can be utilized by other researchers for their work, as the author profited from the enormous knowledge gathered from the numerous contributions of previous studies. The author is aware of possible research topics and applications especially for the NIR-sensor and the RIM-approach, as the topic of Taylor-flow provides sufficient open research questions for upcoming young scientists.

Appendix for Chapter A

A

The correlation coefficients of Tab. 4.2 from Sec. 4.3.2 are carefully retrieved from measurements and literature data. The good agreement of measurement data and the correlations are shown in Fig. A.1.

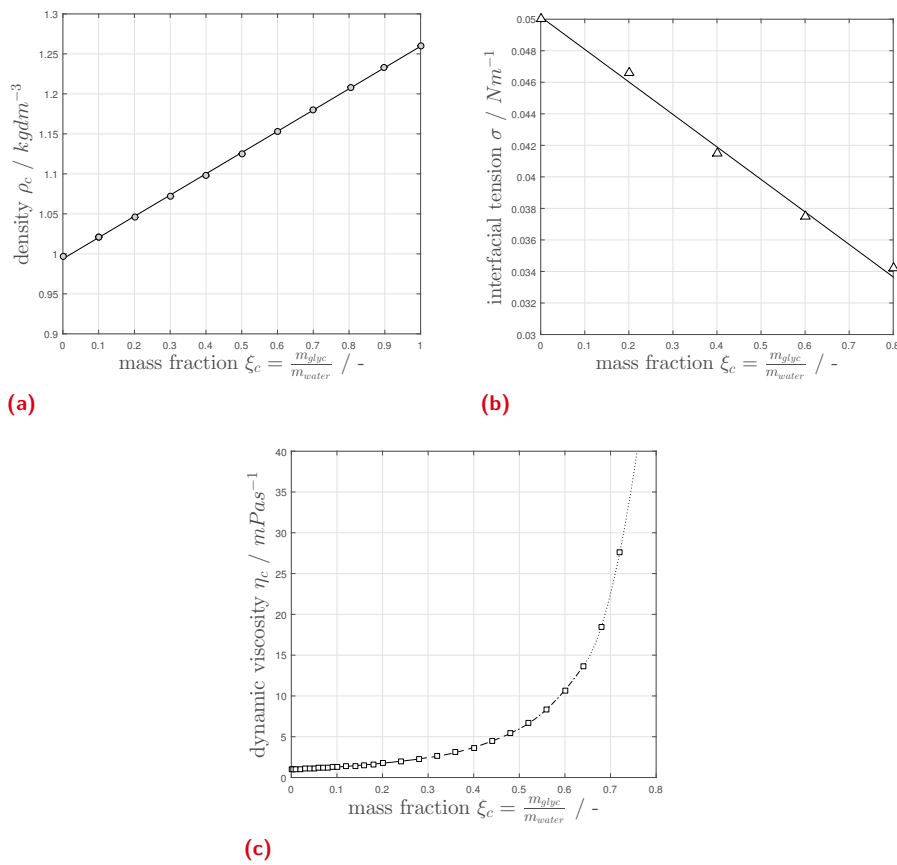
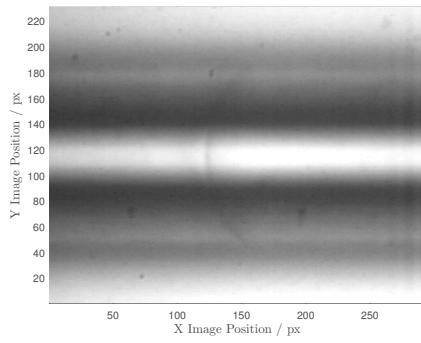
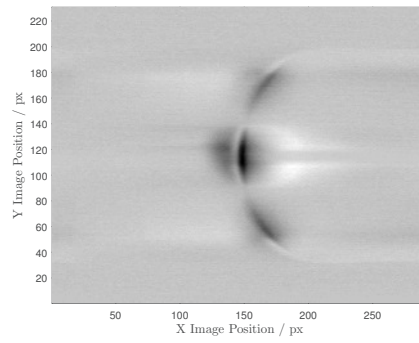


Fig. A.1.: a) Density of the water/glycerol mixture for different mass-fraction ξ_c (own measurements) b) Interfacial tension of water/glycerol mixtures against n-dodecane from Takamura et al. (2012) for 20 °C. for different mass-fraction ξ_c c) Viscosity data from Takamura et al. (2012). Line styles represent the validity range of the different approximations as shown in Tab. 4.2

When the difference in refractive index between continuous and disperse phase decreases (Fig. A.2 a)), the discrimination of the flow phases becomes difficult. To nevertheless determine the droplet cap curvature, it is necessary to use the ensemble averaging approach we showed in Sec. 4.3.3. This results in an ensemble averaged image with a higher contrast of the interfacial area (Fig. A.2 b)).



(a)



(b)

Fig. A.2.: Comparison of raw image and result of ensemble averaging. a) highspeed image of a droplet with small refractive index deviation between continuous and disperse phase b) result of ensemble image averaging approach with applied background filter

Appendix for Chapter 5

Considerations for u_{ex} : Rearranging Eq. 5.13 leads to the equation

$$u_{ex} - u_{ex} \frac{A_f}{A_{ch}} = \frac{Q_g^{rel}}{Q_0} + \frac{A_f}{A_{ch}} \quad (\text{B.1})$$

Our measurements show in agreement with Jose and Cubaud (2014) excess velocities with values $u_{ex} < 0.4$ for $Ca < 0.2$. Additionally we can assume $\frac{A_f}{A_{ch}} < 0.005$ as shown in Fig. B.1. Thus one can say $u_{ex} \frac{A_f}{A_{ch}} < 0.002$ and therefore it can be considered small of higher order and be neglected.

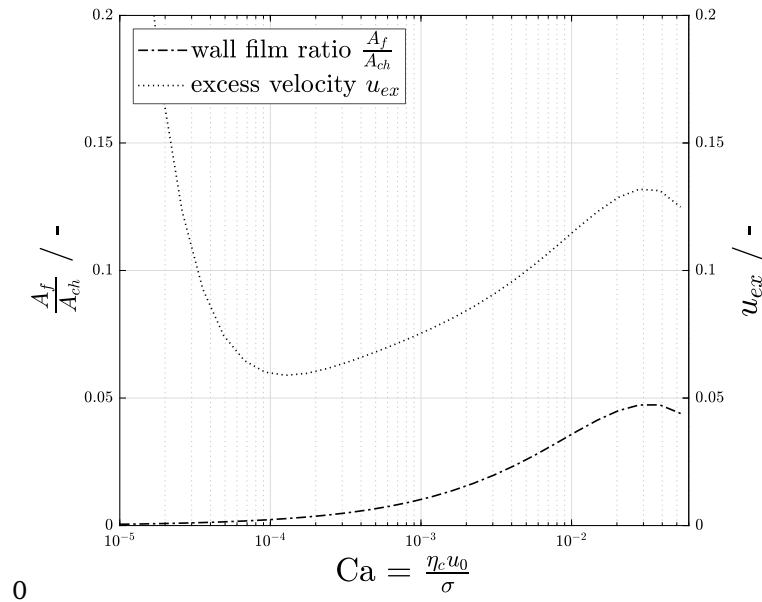


Fig. B.1.: Dimensionless film-area and excess velocity for $\frac{l_d}{W} = 3$ and $\beta = 3.892$ for the proposed model

Appendix for Chapter 6

C.1 Dynamic interfacial tension measurements

The measurement principle for the dynamic interfacial tension measurements using the Lauda TVT is described in the following:

The interfacial tension of the double-binary mixtures is measured using a Lauda TVT drop tensiometer with a syringe of 2.5 ml and a stainless steel capillary at a temperature of 20°C. The interfacial tensions are acquired using the volume drop method: A droplet is formed at the capillary tip and based on the balance of buoyancy and surface tension the droplet pinches off within the continuous phase. The pinched-off droplet is detected by a light barrier.

The balance at the tip of the capillary follows:

$$\gamma = \frac{V_{drop} \Delta \rho g}{\pi d_{cap}} \quad (C.1)$$

herein V_{drop} is the volume of the detached droplet, that can be retrieved from the way the syringe plunger was moved since the last detached droplet. $\Delta \rho$ describes the density difference between the continuous and the droplet phase, g the gravitational acceleration and d_{cap} the diameter of the capillary. Depending on the wetting behavior, the outer or inner diameter, as well as a correction factor, must be used (Wilkinson, 1972).

As Eq. C.1 shows, the wetting behavior (d_{cap}) of the capillary has a large influence on the calculated interfacial tension. The used capillary shows a good wetting behavior for nonpolar media. Thus we choose the nonpolar fluids as the disperse and the polar fluids as the continuous phase to ensure a stable wetting of the capillary.

C.2 Experimental setup for proof of principle

The experimental design follows Fig. C.1: A Si-microchannel (manufactured by IMSAS Bremen) with channel height $H=198 \mu\text{m}$ and nearly rectangular cross-sectional area is located on a Zeiss LSM-210 inverted microscope with a motorized nosepiece and two-axis stage for precision movement. The microscope is controlled via a self-written LabView program using serial port communication.

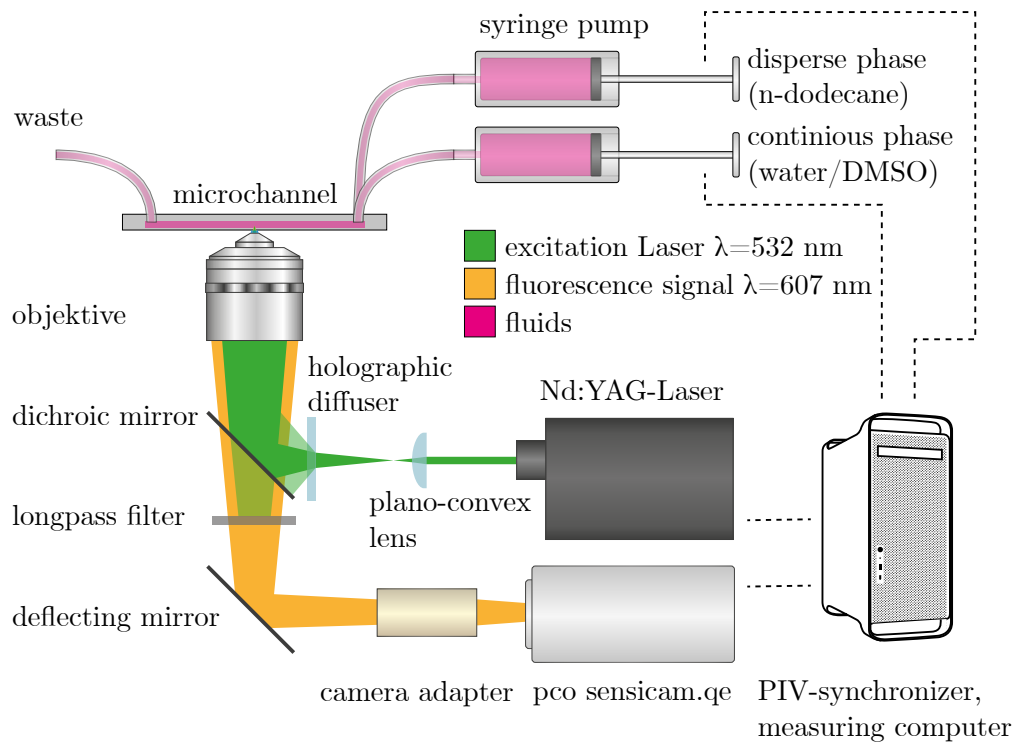


Fig. C.1.: Proof of principle of the double-binary mixture approach. Scheme of the experimental design for μ PIV experiments

The microscope is equipped with a Zeiss LD LCI Plan Apochromat 25x/0.8 objective to provide a high spatial resolution at a small depth of field ($DOF = 1.034\mu\text{m}$) to receive a high resolution in the z -direction. A pulsed Nd:YAG laser (*New Wave Research Solo-PIV III*) with a 15 Hz repetition rate, 50 mJ pulse intensity and a pulse length of 3 ns - 5 ns with frequency doubling (wavelength: $\lambda_{ex} = 532\text{ nm}$) serves as a light source for the measurement. Images of the flow are acquired using an active-cooled high quantum-efficient *PCO.sensicam qe 670 LD 3078* double CCD-camera with an acquisition rate of 4 Hz at a resolution of 1376 px x 1040 px. The continuous phase is seeded with $1.61\mu\text{m}$ particles. The particles are coated with FluoRed as fluorescence dye (excitation peak $530\mu\text{m}$, emission peak $607\mu\text{m}$) and are dispersed in the water/glycerol phase using an ultrasonic bath for 15 min at 20°C .

Two syringe pumps (*Dolomite MitoS Duo XS*) supply a steady flow such, that the volume flow of both phases can be individually controlled. The excitation light from the pulsed Nd:YAG laser is guided into the *Zeiss LSM210* microscope and the laser is widened with a convex lens of short focal length. The illumination is additionally averaged with a holographic diffuser.

A dichroic mirror separates the green excitation light from the red fluorescence light and directs it to the camera. To further improve the cutoff, an additional long-pass filter is mounted in the light-path to shield the camera from laser light (Fig. C.1). A timing unit synchronizes the laser and the camera.

An overview of the experimental and optical parameters is given in Tab. C.1.

Tab. C.1.: Experimental and optical parameters of the experimental design

property	value	unit
channel width W	198	μm
channel height H	192	μm
excitation wavelength λ_{ex}	532	nm
tracer particle diameter d_{tr}	1.6	μm
tracer particle CV	2.3	%
objective magnification	25	-
objective NA	0.8	-
objective DOF	0.859	μm
particle excitation wavelength peak	530	nm
particle emission wavelength peak	607	nm
dichroitic mirror cutoff	552	nm
longpass filter cutoff	550	nm

Appendix for Chapter 7

D.1 Influence of surfactants on the flow

The addition of SDS to the mixture of water/glycerol leads to an increase in the dynamic viscosity of the mixture caused by the surfactants. Below the CMC the viscosity increase is moderate, while for concentration over the CMC the viscosity is increased by up to 30% (Fig. D.1).

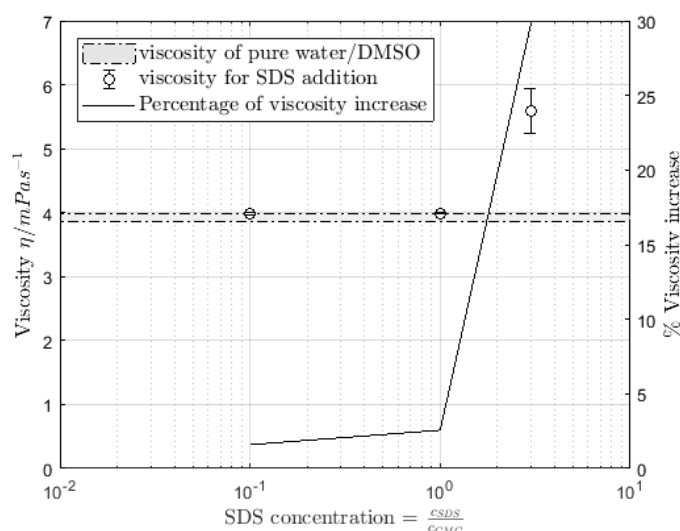


Fig. D.1.: Viscosity measurements for water/DMSO $\xi = 0.58$ with addition of SDS

After solving high concentration of SDS in water/glycerol on a stirring plate, after several minutes the formation of a lyotropic phase can be observed. The formed complexes change the optical and viscous properties of the mixture (Fig. D.2).

D.2 Validation of μ PIV approach

Using the Navier-Stokes-equation for incompressible fluids, the velocity profile for one-phase flows within rectangular microchannels can be determined. The solution of the inhomogeneous differential equation is complex, but a simplified solution is given by Bruus (2008). The restrictions of this solution, as well as the estimated error are given in the mentioned publication.

A comparison of the retrieved μ PIV measurement data and the model shows a good agreement (Fig. D.3).



Fig. D.2.: Deposition of a lyotropic phase formed from micelles in a solution of 7CMC SDS in water/glycerol ($\xi = 0.58$)

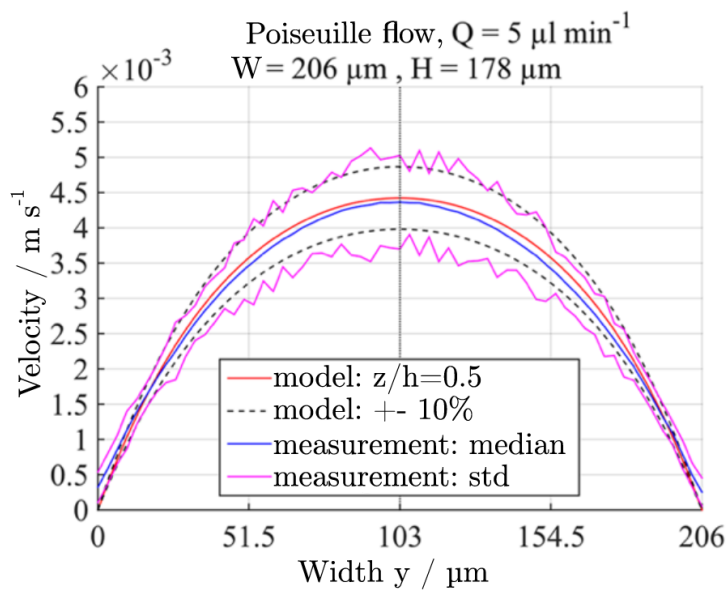


Fig. D.3.: Comparison of μPIV -measurement data and the proposed model from Bruus (2008)

D.3 Supplementary μPIV measurements

The following measurements were acquired with seeding only in the continuous phase and are shown for completeness. Since there were no tracer particles in the droplets, only flow information in the gutters could be obtained. Caused by the bad particle behavior, the measured droplet lengths for the average-shifting algorithm (Mießner et al., 2019) have a deviation of up to 10%. This complicates the identification of the droplet's stagnation points (they appear blurry due to the fluctuating droplet length) and lead to an error in the following results. However, the flow gradients can be considered correct, since the measured u_d applies an equal shift to all measured volume flows Fig. D.4.

Tab. D.1.: Additional measurements with seeding only in the continuous phase. All for $Ca = 0.005$

No.	Re	Oh	λ	$\frac{l_g}{w}$	flow system
VI	2.14	0.0483	0.098	0.62	water/glycerol - hex/sunfl.
VII	0.93	0.0733	0.101	0.92	water/glycerol - hex/sunfl.
VIII	2.00	0.0500	0.303	0.88	water/DMSO - hex/sunfl.
IX	0.93	0.0733	1.032	0.39	water/DMSO - hex/sunfl.

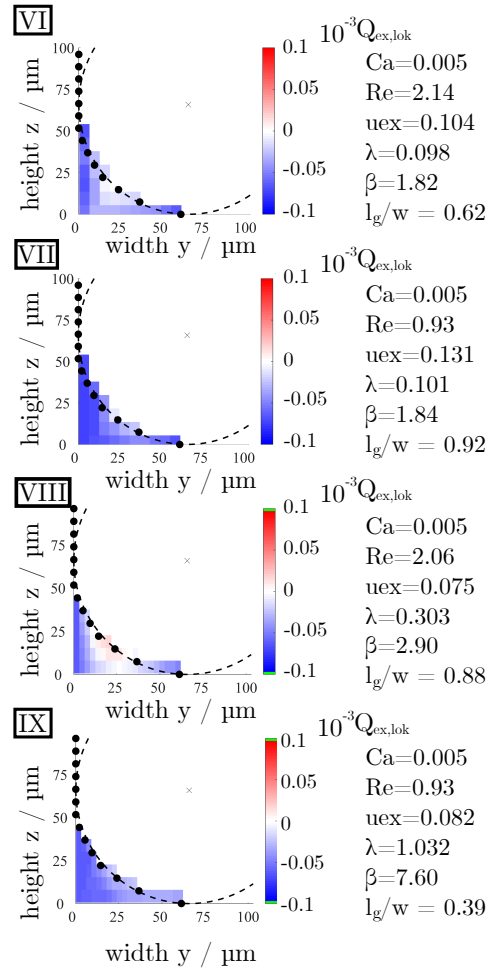


Fig. D.4.: Local excess volume flows $Q_{ex,loc}$ within the gutters at the droplet center. Red volume flows point in positive x -direction (towards droplet front and the observer), blue into opposite direction

Furthermore in addition to the shown measurements in Fig. 7.12, measurements I-V are given in the following with a different color-coding, that represents the u and v component of the flow in the channel center plane.

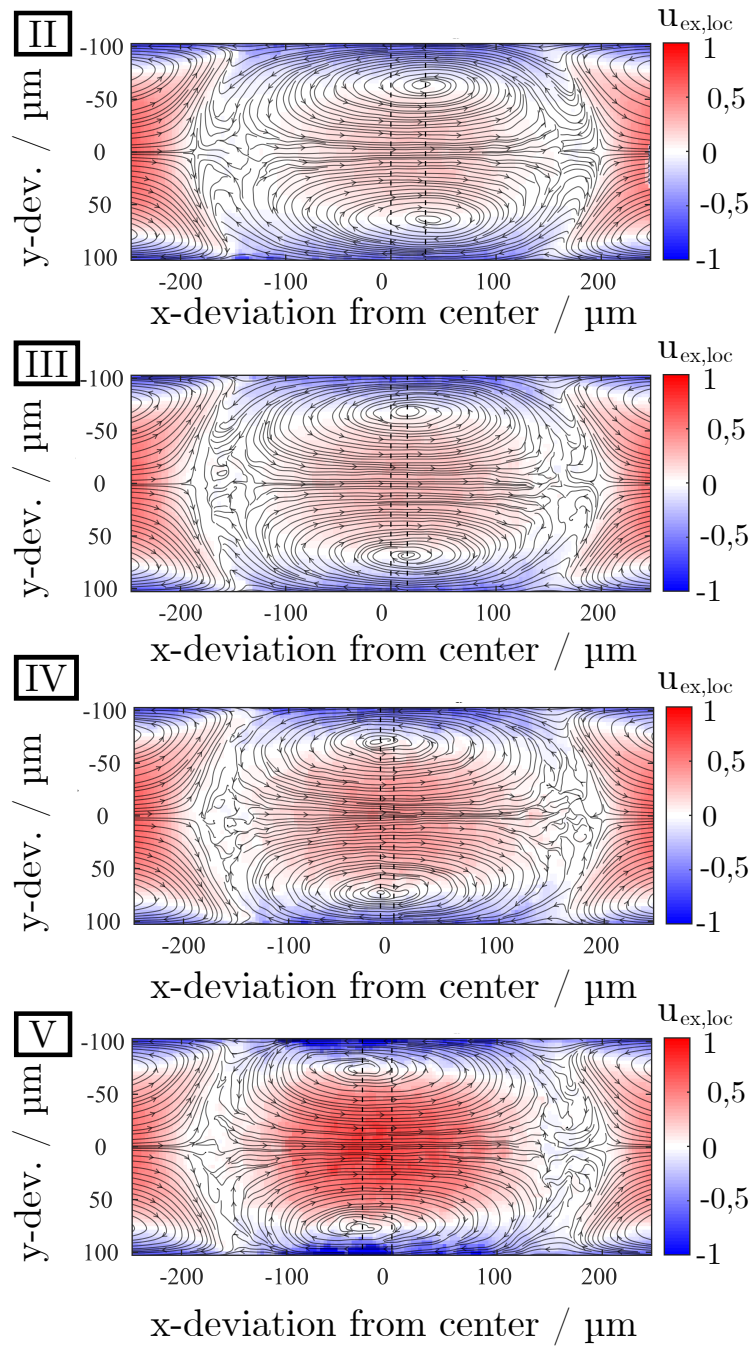


Fig. D.5.: Streamlines of the flow in channel center plane retrieved from ensemble averaged μPIV measurements. The velocity components in x -direction are color-coded

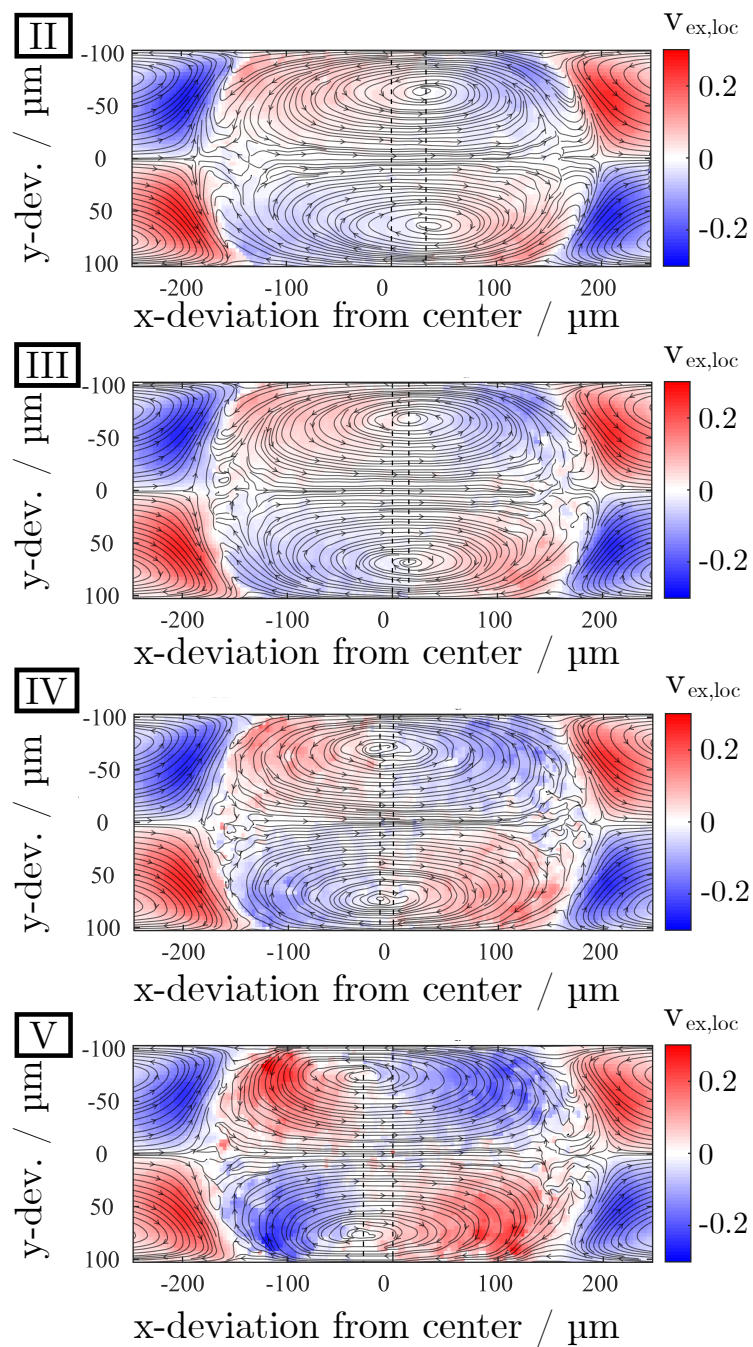


Fig. D.6.: Streamlines of the flow in channel center plane retrieved from ensemble averaged μPIV measurements. The velocity components in y -direction are color-coded

Supervised student works

In the dissertation the results from the supervision of the following students' works are included. The author gratefully thanks all students for the good cooperation.

- **Projects**

- Nowak, S. (2015). "Engineered particles using microreactor technology"
- Austrup, L.; Giesler, J.; Pillarz, M.; Weirauch, L. (2017). "Mikromehrphasenströmung - Konzeption eines Micro Particle Image Velocimetry (μ PIV) Versuchsstandes auf Basis eines konfokalen Laser Scanning Mikroskops (CLSM) inklusive experimenteller Verifikation"
- Diekmann, S.; Ehing, T.; Hehmsoth, N.; Koptelov, A. (2019). "Mikromehrphasenströmung - Entwicklung eines Experimentes zur zeit- und orts aufgelösten Messung der Dispersphasenbildung von Taylor Strömungen"

- **Bachelor theses**

- Knicker, B. (2013). "Mikromehrphasenströmung - Experimentelle Untersuchung der Geometrieabhängigkeit der Dispersphasenbildung in druckgetriebenen flüssig/flüssig Systemen am Beispiel Wasser/Octan"
- Kemper, P. (2014). "Mikromehrphasenströmung - Experimentelle Charakterisierung von Dispergierorganen anhand der Bildungsfrequenz kontinuierlicher Tropfenketten"
- Behrends, G. (2014). "Mikromehrphasenströmung - Untersuchung der Geschwindigkeitsabhängigkeit des NIR-Absorptionssignals von Taylor-Strömungen"
- Lammers, M. (2015). "Mikromehrphasenströmung - Experimentelle Charakterisierung der Tropfenkettendispergierung von Taylor-Strömungen anhand der Bildungsfrequenz am Beispiel einer offenen und modifizierten Y-Kreuzung"
- Weirauch, L. (2015). "Mikromehrphasenströmung – Experimentelle Charakterisierung der zeitlichen Stabilität von Taylor-Strömungen"
- Gozek, M. (2016). "Experimental characterization of disperse phase formation at low Weber-numbers on capillaries in stagnant and concurrent upward flows"
- Meister, B. (2016). "Mikromehrphasenströmung – Experimentelle Untersuchung des Tensideinflusses auf die Dispersphasenexzessgeschwindigkeit in Taylor-Strömungen"
- Koptelov, A. (2017). "Mikromehrphasenströmung - Experimentelle Untersuchung von Materialsystemen zur Brechungsindexanpassung in flüssig/flüssig Taylor Strömungen"
- Hehmsoth, N. (2017). "Mikromehrphasenströmung - Eindimensionale Simulation des Druckverlustes von wandbeeinflussten Tropfenketten (Taylor-Strömung)"
- Vanev, I. (2017). "Mikromehrphasenströmung – Experimentelle Untersuchung des Brechungsindex- und Mischungsverhaltens von Tensiden"

- **Master theses**

- Nowak, S. (2015). "Mikromehrphasenströmung – Experimentelle Überprüfung und Beurteilung der Übertragbarkeit von Dispersphasenbildungsmodelle der Makro- auf die Mikroskala"
- Kemper, P. (2017). "Mikromehrphasenströmung – Untersuchung des Tensideinflusses auf die lokale Hydrodynamik von Taylor-Strömungen"

- Behrends, G. (2017). "Mikromehrphasenströmung – Experimentelle Untersuchung des Tenseinflusses auf die Dispersphasenform in Taylor Strömungen"
- Schütte, T. (2017). "Mikromehrphasenströmung – Experimentelle Untersuchung der Driftgeschwindigkeit in Taylor-Strömungen in Abhängigkeit der Tensidkonzentration"
- Schoebel, J. (2019). "Mikromehrphasenströmung – Untersuchung der Impulskopplung an der Phasengrenzfläche auf die lokale Hydrodynamik von Taylorströmungen"

Bibliography

- Abadie, Thomas; Aubin, Joëlle; Legendre, Dominique and Xuereb, Catherine (2012). „Hydrodynamics of gas–liquid Taylor flow in rectangular microchannels“. In: *Microfluidics and Nanofluidics* 12.1-4, pp. 355–369. DOI: 10.1007/s10404-011-0880-8 (cit. on p. 67).
- Abate, Adam R.; Mary, Pascaline; van Steijn, Volkert and Weitz, David A. (2012). „Experimental validation of plugging during drop formation in a T-junction“. In: *Lab on a chip* 12.8, pp. 1516–1521. DOI: 10.1039/c2lc21263c (cit. on p. 72).
- Abiev, R. (2017). „Analysis of local pressure gradient inversion and form of bubbles in Taylor flow in microchannels“. In: *Chemical Engineering Science* 174, pp. 403–412. DOI: 10.1016/j.ces.2017.09.041 (cit. on pp. 15, 48, 66, 72, 76, 83).
- Abiev, R.Sh. (2013). „Bubbles velocity, Taylor circulation rate and mass transfer model for slug flow in milli- and microchannels“. In: *Chemical Engineering Journal* 227, pp. 66–79. DOI: 10.1016/j.cej.2012.10.009 (cit. on pp. 11, 39).
- Abiev, R.Sh. and Lavretsov, I. V. (2012). „Intensification of mass transfer from liquid to capillary wall by Taylor vortices in minichannels, bubble velocity and pressure drop“. In: *Chemical Engineering Science* 74, pp. 59–68. DOI: 10.1016/j.ces.2012.02.024 (cit. on p. 11).
- Abiev, Rufat; Svetlov, Stanislav and Haase, Stefan (2017). „Hydrodynamics and Mass Transfer of Gas-Liquid and Liquid-Liquid Taylor Flow in Microchannels“. In: *Chemical Engineering & Technology* 40.11, pp. 1985–1998. DOI: 10.1002/ceat.201700041 (cit. on p. 49).
- Adrian, Ronald and Westerweel, Jerry (2011). *Particle image velocimetry*. Vol. 30. Cambridge aerospace series. Cambridge: Cambridge Univ. Press (cit. on p. 18).
- Ahmed, Ishtiaq; Akram, Zain; Bule, Mohammed and Iqbal, Hafiz (2018). „Advancements and Potential Applications of Microfluidic Approaches—A Review“. In: *Chemosensors* 6.4, p. 46. DOI: 10.3390/chemosensors6040046 (cit. on p. 11).
- Al-Jimaz, Adel S.; Al-Kandary, Jasem A.; Abdul-latif, Abdul-Haq M. and Al-Zanki, Adnan M. (2005). „Physical properties of anisole+n-alkanes at temperatures between (293.15 and 303.15) K“. in: *The Journal of Chemical Thermodynamics* 37.7, pp. 631–642. DOI: 10.1016/j.jct.2004.09.021 (cit. on pp. 91, 93).
- Allen, Michael Patrick (1997). *Understanding Regression Analysis*. New York: Plenum Press. DOI: 10.1007/b102242 (cit. on p. 59).
- Angeli, P. and Gavriilidis, A. (2008). „Hydrodynamics of Taylor flow in small channels: A Review“. In: *Proceedings of the Institution of Mechanical Engineers, Part C: Journal of Mechanical Engineering Science* 222.5, pp. 737–751. DOI: 10.1243/09544062JMES776 (cit. on pp. 10, 67).
- Antweiler, Nicolai; Gatberg, Sascha; Franzke, Joachim and Agar, David William (2015). „Neue kosteneffektive Mess- und Regeltechnik für das Numbering-up von reaktiven Pfropfenströmungen in Mikrokanälen“. In: *Chemie Ingenieur Technik* 87.9, pp. 1221–1229. DOI: 10.1002/cite.201500032 (cit. on pp. 6, 17).

- Araújo, J.D.P.; Miranda, J. M.; Pinto, A.M.F.R. and Campos, J.B.L.M. (2012). „Wide-ranging survey on the laminar flow of individual Taylor bubbles rising through stagnant Newtonian liquids“. In: *International Journal of Multiphase Flow* 43, pp. 131–148. DOI: 10.1016/j.ijmultiphaseflow.2012.03.007 (cit. on p. 86).
- Bec, X. (1997). „Faster Refraction Formula, and Transmission Color Filtering“. In: *Ray Tracing News* 10.1 (cit. on p. 31).
- Becker, E.W.; Bier, W.; Bley, P., et al. (1979). „Das Entwicklungspotential des Trenndüsenverfahrens zur U-235-Anreicherung“. In: *Atomwirtschaft* 11 (cit. on p. 1).
- Beer, Neil Reginald; Rose, Klint Aaron and Kennedy, Ian M. (2009). „Observed velocity fluctuations in monodisperse droplet generators“. In: *Lab Chip* 9.6, pp. 838–840. DOI: 10.1039/B818479H (cit. on pp. 6, 43).
- Bourdon, Christopher J.; Olsen, Michael G. and Gorby, Allen D. (2006). „The Depth of Correlation in Micro-PIV for High Numerical Aperture and Immersion Objectives“. In: *Journal of Fluids Engineering* 128.4, p. 883. DOI: 10.1115/1.2201649 (cit. on p. 19).
- Bretherton, F. P. (1961). „The motion of long bubbles in tubes“. In: *Journal of Fluid Mechanics* 10.2, pp. 166–188. DOI: 10.1017/S0022112061000160 (cit. on pp. 1, 3, 6, 14, 62, 67).
- Brindise, Melissa C.; Busse, Margaret M. and Vlachos, Pavlos P. (2018). „Density- and viscosity-matched Newtonian and non-Newtonian blood-analog solutions with PDMS refractive index“. In: *Experiments in Fluids* 59.11, p. 38. DOI: 10.1007/s00348-018-2629-6 (cit. on pp. 22, 86).
- Bruus, Henrik (2008). *Theoretical microfluidics*. Vol. 18. Oxford master series in physics Condensed matter physics. Oxford: Oxford Univ. Press, p. 76 (cit. on pp. 74, 129, 130).
- Budwig, R. (1994). „Refractive index matching methods for liquid flow investigations“. In: *Experiments in Fluids* 17.5, pp. 350–355. DOI: 10.1007/BF01874416 (cit. on pp. 22, 86).
- Burlage, K.; Gerhardy, C.; Praefke, H.; Liauw, M. A. and Schomburg, W. K. (2013). „Slug length monitoring in liquid–liquid Taylor-flow integrated in a novel PVDF micro-channel“. In: *Chemical Engineering Journal* 227, pp. 111–115. DOI: 10.1016/j.cej.2012.08.070 (cit. on p. 17).
- Butt, Hans-Jürgen; Graf, Karlheinz and Kappl, Michael (2003). *Physics and chemistry of interfaces*. 1. ed. Physics textbook. Weinheim: Wiley-VCH. DOI: 10.1002/3527602313 (cit. on p. 105).
- Cabral, João T. and Hudson, Steven D. (2006). „Microfluidic approach for rapid multicomponent interfacial tensiometry“. In: *Lab on a chip* 6.3, pp. 427–436. DOI: 10.1039/b511976f (cit. on p. 49).
- Cadillon, Jérémy; Saksena, Rajat and Pearlstein, Arne J. (2016). „Transparent, immiscible, surrogate liquids with matchable refractive indexes: Increased range of density and viscosity ratios“. In: *Physics of Fluids* 28.12, p. 127102. DOI: 10.1063/1.4968512 (cit. on p. 87).
- Cao, Zhen; Wu, Zan and Sundén, Bengt (2018). „Dimensionless analysis on liquid-liquid flow patterns and scaling law on slug hydrodynamics in cross-junction microchannels“. In: *Chemical Engineering Journal* 344, pp. 604–615. DOI: 10.1016/j.cej.2018.03.119 (cit. on p. 11).
- Chambers, Richard D.; Holling, Darren; Rees, Anthony J. and Sandford, Graham (2003). „Microreactors for Oxidations Using Fluorine“. In: *ChemInform* 34.17. DOI: 10.1002/chin.200317049 (cit. on p. 10).
- Chen, Junjie; Song, Wenya and Xu, Deguang (2018). „Catalytic partial oxidation of methane for the production of syngas using microreaction technology: A computational fluid dynamics study“. In: *International Journal of Hydrogen Energy* 43.31, pp. 14059–14077. DOI: 10.1016/j.ijhydene.2018.05.125 (cit. on p. 10).
- Chen, Xiaoming; Glawdel, Tomasz; Cui, Naiwen and Ren, Carolyn L. (2015). „Model of droplet generation in flow focusing generators operating in the squeezing regime“. In: *Microfluidics and Nanofluidics* 18.5-6, pp. 1341–1353. DOI: 10.1007/s10404-014-1533-5 (cit. on p. 16).

- Chen, Yuchao; Li, Peng; Huang, Po-Hsun, et al. (2014). „Rare cell isolation and analysis in microfluidics“. In: *Lab on a chip* 14.4, pp. 626–645. DOI: 10.1039/c3lc90136j (cit. on p. 11).
- Chou, Wei-Lung; Lee, Pee-Yew; Yang, Cing-Long; Huang, Wen-Ying and Lin, Yung-Sheng (2015). „Recent Advances in Applications of Droplet Microfluidics“. In: *Micromachines* 6.9, pp. 1249–1271. DOI: 10.3390/mi6091249 (cit. on pp. 9–11, 16).
- Clausell-Tormos, Jenifer; Lieber, Diana; Baret, Jean-Christophe, et al. (2008). „Droplet-based microfluidic platforms for the encapsulation and screening of Mammalian cells and multicellular organisms“. In: *Chemistry & biology* 15.5, pp. 427–437. DOI: 10.1016/j.chembiol.2008.04.004 (cit. on p. 11).
- Clément, Simon A.; Guillemain, Anaïs; McCleney, Amy B. and Bardet, Philippe M. (2018). „Options for refractive index and viscosity matching to study variable density flows“. In: *Experiments in Fluids* 59.2, p. 434. DOI: 10.1007/s00348-018-2496-1 (cit. on pp. 22, 86).
- Cubaud, Thomas and Mason, Thomas G. (2008). „Capillary threads and viscous droplets in square microchannels“. In: *Physics of Fluids* 20.5, p. 053302. DOI: 10.1063/1.2911716 (cit. on p. 10).
- Davey, K. R. (2008). „Latin Hypercube Sampling and Pattern Search in Magnetic Field Optimization Problems“. In: *IEEE Transactions on Magnetics* 44.6, pp. 974–977. DOI: 10.1109/TMAG.2007.916292 (cit. on p. 77).
- Dietrich, Thomas R., ed. (2009). *Microchemical engineering in practice*. Hoboken, NJ and Hoboken, NJ: Wiley. DOI: 10.1002/9780470431870 (cit. on p. 10).
- Direito, F.J.N.; Campos, J.B.L.M. and Miranda, J. M. (2017). „A Taylor drop rising in a liquid co-current flow“. In: *International Journal of Multiphase Flow* 96, pp. 134–143. DOI: 10.1016/j.ijmultiphaseflow.2017.07.009 (cit. on p. 13).
- Ehrfeld, Wolfgang; Hessel, Volker and Lowe, Holger (2004). *Microreactors: New technology for modern chemistry*. Weinheim: Wiley-VCH. DOI: 10.1002/3527601953 (cit. on pp. 3, 10).
- Ern, Patricia; Risso, Frédéric; Fabre, David and Magnaudet, Jacques (2012). „Wake-Induced Oscillatory Paths of Bodies Freely Rising or Falling in Fluids“. In: *Annual Review of Fluid Mechanics* 44.1, pp. 97–121. DOI: 10.1146/annurev-fluid-120710-101250 (cit. on pp. 10, 86).
- Fisher, R. A. (1915). „Frequency Distribution of the Values of the Correlation Coefficient in Samples from an Indefinitely Large Population“. In: *Biometrika* 10.4, p. 507. DOI: 10.2307/2331838 (cit. on p. 59).
- Fu, Taotao and Ma, Youguang (2015). „Bubble formation and breakup dynamics in microfluidic devices: A review“. In: *Chemical Engineering Science* 135, pp. 343–372. DOI: 10.1016/j.ces.2015.02.016 (cit. on pp. 16, 49, 65, 66).
- Fuerstman, Michael J.; Lai, Ann; Thurlow, Meghan E., et al. (2007). „The pressure drop along rectangular microchannels containing bubbles“. In: *Lab on a chip* 7.11, pp. 1479–1489. DOI: 10.1039/b706549c (cit. on pp. 6, 25, 39, 79, 105).
- Garstecki, Piotr; Fuerstman, Michael J.; Stone, Howard A. and Whitesides, George M. (2006a). „Formation of droplets and bubbles in a microfluidic T-junction-scaling and mechanism of break-up“. In: *Lab on a chip* 6.3, pp. 437–446. DOI: 10.1039/b510841a (cit. on p. 16).
- Garstecki, Piotr; Fuerstman, Michael; Fischbach, Michael A.; Sia, Samuel K. and Whitesides, George M. (2006b). „Mixing with bubbles: a practical technology for use with portable microfluidic devices“. In: *Lab Chip* 6 (2), pp. 207–212. DOI: 10.1039/B510843H (cit. on p. 11).
- Gascon, J.; van Ommen, J. R.; Moulijn, J. A. and Kapteijn, F. (2015). „Structuring catalyst and reactor – an inviting avenue to process intensification“. In: *Catalysis Science & Technology* 5.2, pp. 807–817. DOI: 10.1039/C4CY01406E (cit. on p. 5).
- Glawdel, Tomasz; Elbuken, Caglar and Ren, Carolyn (2012a). „Droplet formation in microfluidic T-junction generators operating in the transitional regime. I. Experimental observations“. In: *Physical Review E* 85.1. DOI: 10.1103/PhysRevE.85.016322 (cit. on p. 16).

- Glawdel, Tomasz; Elbuken, Caglar and Ren, Carolyn L. (2012b). „Droplet formation in microfluidic T-junction generators operating in the transitional regime. II. Modeling“. In: *Physical Review E* 85.1. DOI: 10.1103/PhysRevE.85.016323 (cit. on p. 16).
- Goertzen, Jason R. and Cribbie, Robert A. (2010). „Detecting a lack of association: An equivalence testing approach“. In: *The British journal of mathematical and statistical psychology* 63.Pt 3, pp. 527–537. DOI: 10.1348/000711009X475853 (cit. on p. 58).
- González, Cristina; Resa, José M.; Ruiz, Aitor and Gutiérrez, José I. (1996). „Densities of Mixtures Containing n -Alkanes with Sunflower Seed Oil at Different Temperatures“. In: *Journal of Chemical & Engineering Data* 41.4, pp. 796–798. DOI: 10.1021/je960053p (cit. on p. 91).
- Green, Martin A. and Keevers, Mark J. (1995). „Optical properties of intrinsic silicon at 300 K“. in: *Progress in Photovoltaics: Research and Applications* 3.3, pp. 189–192. DOI: 10.1002/pip.4670030303 (cit. on p. 32).
- Gu, Hao; Duits, Michel H. G. and Mugele, Frieder (2011). „Droplets formation and merging in two-phase flow microfluidics“. In: *International journal of molecular sciences* 12.4, pp. 2572–2597. DOI: 10.3390/ijms12042572 (cit. on p. 16).
- Gu, Yunfeng and Fisher, Adrian C. (2013). „An AC voltammetry approach for the detection of droplets in microfluidic devices“. In: *The Analyst* 138.16, pp. 4448–4452. DOI: 10.1039/c3an00822c (cit. on p. 17).
- Guo, S.; Wu, F.; Wei, W., et al. (2013). „A novel wavelet denoising method used for droplet volume detection in the microfluidic system“. In: *2013 IEEE International Conference on Mechatronics and Automation*, pp. 1732–1737. DOI: 10.1109/ICMA.2013.6618177 (cit. on pp. 18, 24).
- Gupta, Amit; Matharoo, Harpreet S.; Makkar, Devavret and Kumar, Ranganathan (2014). „Droplet formation via squeezing mechanism in a microfluidic flow-focusing device“. In: *Computers & Fluids* 100, pp. 218–226. DOI: 10.1016/j.compfluid.2014.05.023 (cit. on p. 16).
- Gupta, Raghvendra; Leung, Sharon S.Y.; Manica, Rogerio; Fletcher, David F. and Haynes, Brian S. (2013). „Hydrodynamics of liquid–liquid Taylor flow in microchannels“. In: *Chemical Engineering Science* 92, pp. 180–189. DOI: 10.1016/j.ces.2013.01.013 (cit. on p. 102).
- Haase, Stefan; Murzin, Dmitry Yu. and Salmi, Tapio (2016). „Review on hydrodynamics and mass transfer in minichannel wall reactors with gas–liquid Taylor flow“. In: *Chemical Engineering Research and Design* 113, pp. 304–329. DOI: 10.1016/j.cherd.2016.06.017 (cit. on p. 10).
- Han, Youngbae and Shikazono, Naoki (2009). „Measurement of liquid film thickness in micro square channel“. In: *International Journal of Multiphase Flow* 35.10, pp. 896–903. DOI: 10.1016/j.ijmultiphaseflow.2009.06.006 (cit. on pp. 49, 55, 61, 65, 72, 75).
- Hangos, Katalin M. and Cameron, I. T., eds. (2001). *Process modelling and model analysis*. Vol. v. 4. Process Systems Engineering. San Diego: Academic Press (cit. on pp. 6, 71).
- Helmers, Thorben; Thöming, Jorg and Mießner, Ulrich (2017). „Retrieving accurate temporal and spatial information about Taylor slug flows from non-invasive NIR photometry measurements“. In: *Experiments in Fluids* 58.11, p. 66. DOI: 10.1007/s00348-017-2441-8 (cit. on pp. 24, 60, 61, 78).
- Helmers, Thorben; Kemper, Philip; Thöming, Jorg and Mießner, Ulrich (2019). „Determining the flow-related cap deformation of Taylor droplets at low Ca-numbers using ensemble averaged high-speed images“. In: *Experiments in Fluids* 60.7, p. 113. DOI: 10.1007/s00348-019-2757-7 (cit. on pp. 47, 52, 66, 72, 75, 78, 83).
- Hosokawa, Masahito; Nishikawa, Yohei; Kogawa, Masato and Takeyama, Haruko (2017). „Massively parallel whole genome amplification for single-cell sequencing using droplet microfluidics“. In: *Scientific reports* 7.1, p. 5199. DOI: 10.1038/s41598-017-05436-4 (cit. on p. 11).
- Howard, James A. and Walsh, Patrick A. (2013). „Review and extensions to film thickness and relative bubble drift velocity prediction methods in laminar Taylor or slug flows“. In: *International Journal of Multiphase Flow* 55, pp. 32–42. DOI: 10.1016/j.ijmultiphaseflow.2013.04.005 (cit. on p. 67).

- Huebner, Ansgar; Sharma, Sanjiv; Srisa-Art, Monpichar, et al. (2008). „Microdroplets: a sea of applications?“ In: *Lab on a chip* 8.8, pp. 1244–1254. DOI: 10.1039/b806405a (cit. on p. 10).
- Huerre, Axel; Miralles, Vincent and Jullien, Marie-Caroline (2014). „Bubbles and foams in microfluidics“. In: *Soft matter* 10.36, pp. 6888–6902. DOI: 10.1039/c4sm00595c (cit. on p. 5).
- Isgor, Pelin Kubra; Marcali, Merve; Keser, Mert and Elbuken, Caglar (2015). „Microfluidic droplet content detection using integrated capacitive sensors“. In: *Sensors and Actuators B: Chemical* 210, pp. 669–675. DOI: 10.1016/j.snb.2015.01.018 (cit. on p. 17).
- Jakiela, Slawomir; Makulska, Sylwia; Korczyk, Piotr M. and Garstecki, Piotr (2011). „Speed of flow of individual droplets in microfluidic channels as a function of the capillary number, volume of droplets and contrast of viscosities“. In: *Lab on a chip* 11.21, pp. 3603–3608. DOI: 10.1039/c11c20534j (cit. on pp. 15, 39, 48, 62, 67, 82, 113).
- Jakiela, Slawomir; Korczyk, Piotr M.; Makulska, Sylwia; Cybulski, Olgierd and Garstecki, Piotr (2012). „Discontinuous transition in a laminar fluid flow: A change of flow topology inside a droplet moving in a micron-size channel“. In: *Physical review letters* 108.13, p. 134501. DOI: 10.1103/PhysRevLett.108.134501 (cit. on p. 82).
- Jin, Si Hyung; Jung, Jae-Hoon; Jeong, Seong-Geun, et al. (2018). „Microfluidic dual loops reactor for conducting a multistep reaction“. In: *Frontiers of Chemical Science and Engineering* 12.2, pp. 239–246. DOI: 10.1007/s11705-017-1680-9 (cit. on p. 11).
- Jose, Bibin M. and Cubaud, Thomas (2014). „Formation and dynamics of partially wetting droplets in square microchannels“. In: *RSC Adv* 4.29, pp. 14962–14970. DOI: 10.1039/C4RA00654B (cit. on pp. 62–64, 66, 75, 81, 82, 84, 123).
- Kalantarifard, Ali; Saateh, Abtin and Elbuken, Caglar (2018). „Label-Free Sensing in Microdroplet-Based Microfluidic Systems“. In: *Chemosensors* 6.2, p. 23. DOI: 10.3390/chemosensors6020023 (cit. on pp. 17, 18, 67).
- Kang, D.-K.; Ali, M. M.; Zhang, K, et al. (2014). „Rapid detection of single bacteria in unprocessed blood using Integrated Comprehensive Droplet Digital Detection“. In: *Nature Communications* 5, p. 5427. DOI: 10.1038/ncomms6427 (cit. on p. 11).
- Kastens, Sven; Hosoda, Shogo; Schlüter, Michael and Tomiyama, Akio (2015). „Mass Transfer from Single Taylor Bubbles in Minichannels“. In: *Chemical Engineering & Technology* 38.11, pp. 1925–1932. DOI: 10.1002/ceat.201500065 (cit. on p. 3).
- Kastens, Sven; Timmermann, Jens; Strassl, Florian, et al. (2017). „Test System for the Investigation of Reactive Taylor Bubbles“. In: *Chemical Engineering & Technology* 40.8, pp. 1494–1501. DOI: 10.1002/ceat.201700047 (cit. on p. 3).
- Kedenburg, S.; Vieweg, M.; Gissibl, T. and Giessen, H. (2012). „Linear refractive index and absorption measurements of nonlinear optical liquids in the visible and near-infrared spectral region“. In: *Optical Materials Express* 2.11, p. 1588. DOI: 10.1364/OME.2.001588 (cit. on p. 32).
- Khodaparast, Sepideh; Borhani, Navid; Tagliabue, Giulia and Thome, John Richard (2013). „A micro particle shadow velocimetry (μ PSV) technique to measure flows in microchannels“. In: *Experiments in Fluids* 54.2, p. 1474. DOI: 10.1007/s00348-013-1474-x (cit. on p. 86).
- Kinoshita, Haruyuki; Kaneda, Shohei; Fujii, Teruo and Oshima, Marie (2007). „Three-dimensional measurement and visualization of internal flow of a moving droplet using confocal micro-PIV“. In: *Lab Chip* 7 (3), pp. 338–346. DOI: 10.1039/B617391H (cit. on pp. 21, 86).
- Kobayashi, Juta; Mori, Yuichiro and Kobayashi, Shū (2006). „Multiphase organic synthesis in microchannel reactors“. In: *Chemistry, an Asian journal* 1.1-2, pp. 22–35. DOI: 10.1002/asia.200600058 (cit. on pp. 2, 10).
- Korczyk, Piotr M.; Cybulski, Olgierd; Makulska, Sylwia and Garstecki, Piotr (2011). „Effects of unsteadiness of the rates of flow on the dynamics of formation of droplets in microfluidic systems“. In: *Lab on a chip* 11.1, pp. 173–175. DOI: 10.1039/c01c00088d (cit. on pp. 6, 43).

- Kovalev, Alexander V.; Yagodnitsyna, Anna A. and Bilsky, Artur V. (2018). „Flow hydrodynamics of immiscible liquids with low viscosity ratio in a rectangular microchannel with T-junction“. In: *Chemical Engineering Journal* 352, pp. 120–132. DOI: 10.1016/j.cej.2018.07.013 (cit. on pp. 22, 59, 87).
- Kralj, Jason G.; Sahoo, Hemantkumar R. and Jensen, Klavs F. (2007). „Integrated continuous microfluidic liquid-liquid extraction“. In: *Lab on a chip* 7.2, pp. 256–263. DOI: 10.1039/b610888a (cit. on p. 10).
- Kraus, Tobias; Günther, Axel; Mas, Nuria de; Schmidt, Martin A. and Jensen, Klavs F. (2004). „An integrated multiphase flow sensor for microchannels“. In: *Experiments in Fluids* 36.6, pp. 819–832. DOI: 10.1007/s00348-003-0764-0 (cit. on pp. 18, 24).
- Kreutzer, Michiel; Kapteijn, Freek; Moulijn, Jacob and Heiszwolf, Johan (2005a). „Multiphase monolith reactors: Chemical reaction engineering of segmented flow in microchannels“. In: *Chemical Engineering Science* 60.22. 7th International Conference on Gas-Liquid and Gas-Liquid-Solid Reactor Engineering, pp. 5895–5916. DOI: 10.1016/j.ces.2005.03.022 (cit. on p. 10).
- Kreutzer, Michiel T.; Kapteijn, Freek; Moulijn, Jacob A.; Kleijn, Chris R. and Heiszwolf, Johan J. (2005b). „Inertial and interfacial effects on pressure drop of Taylor flow in capillaries“. In: *AIChE Journal* 51.9, pp. 2428–2440. DOI: 10.1002/aic.10495 (cit. on pp. 59, 75).
- Kreutzer, Michiel T.; Kapteijn, Freek; Moulijn, Jacob A. and Heiszwolf, Johan J. (2005c). „Multiphase monolith reactors: Chemical reaction engineering of segmented flow in microchannels“. In: *Chemical Engineering Science* 60.22, pp. 5895–5916. DOI: 10.1016/j.ces.2005.03.022 (cit. on pp. 5, 11).
- Kreutzer, Michiel T.; Bakker, Jasper J. W.; Kapteijn, Freek; Moulijn, Jacob A. and Verheijen, Peter J. T. (2005d). „Scaling-up Multiphase Monolith Reactors: Linking Residence Time Distribution and Feed Maldistribution“. In: *Industrial & Engineering Chemistry Research* 44.14, pp. 4898–4913. DOI: 10.1021/ie0492350 (cit. on p. 5).
- Krohn, Benedikt; Manera, Annalisa and Petrov, Victor (2018). „A novel method to create high density stratification with matching refractive index for optical flow investigations“. In: *Experiments in Fluids* 59.4, p. 434. DOI: 10.1007/s00348-018-2522-3 (cit. on pp. 22, 86).
- Kück, Ulf Daniel; Mießner, Ulrich; Aydin, Murat and Thöming, Jorg (2018). „Mixing time and mass transfer of rising bubbles in swarm turbulence“. In: *Chemical Engineering Science* 187, pp. 367–376. DOI: 10.1016/j.ces.2018.04.031 (cit. on p. 5).
- Kumari, Sadhana; Kumar, Nilay and Gupta, Raghvendra (2019). „Flow and heat transfer in slug flow in microchannels: Effect of bubble volume“. In: *International Journal of Heat and Mass Transfer* 129, pp. 812–826. DOI: <https://doi.org/10.1016/j.ijheatmasstransfer.2018.10.010> (cit. on p. 83).
- Ładosz, Agnieszka and Rudolf von Rohr, Philipp (2018). „Pressure drop of two-phase liquid-liquid slug flow in square microchannels“. In: *Chemical Engineering Science* 191, pp. 398–409. DOI: 10.1016/j.ces.2018.06.057 (cit. on pp. 13, 49, 65, 66).
- Lakens, Daniël (2017). „Equivalence Tests: A Practical Primer for t Tests, Correlations, and Meta-Analyses“. In: *Social psychological and personality science* 8.4, pp. 355–362. DOI: 10.1177/1948550617697177 (cit. on p. 58).
- Lang, P.; Hill, M.; Krossing, I. and Woias, P. (2012). „Multiphase minireactor system for direct fluorination of ethylene carbonate“. In: *Chemical Engineering Journal* 179, pp. 330–337. DOI: 10.1016/j.cej.2011.11.015 (cit. on p. 10).
- LeBel, R. and Goring, D. (1962). „Density, Viscosity, Refractive Index, and Hygroscopicity of Mixtures of Water and Dimethyl Sulfoxide.“ In: *Journal of Chemical and Engineering Data* (cit. on pp. 91, 93).
- Leung, Sharon S.Y.; Liu, Yang; Fletcher, David F. and Haynes, Brian S. (2010). „Heat transfer in well-characterised Taylor flow“. In: *Chemical Engineering Science* 65.24, pp. 6379–6388. DOI: 10.1016/j.ces.2010.09.014 (cit. on p. 11).

- Liu, Hui; Vandu, Chippla O. and Krishna, Rajamani (2005). „Hydrodynamics of Taylor Flow in Vertical Capillaries: Flow Regimes, Bubble Rise Velocity, Liquid Slug Length, and Pressure Drop“. In: *Industrial & Engineering Chemistry Research* 44.14, pp. 4884–4897. DOI: 10.1021/ie049307n (cit. on p. 67).
- Liu, Zhaomiao; Zhang, Longxiang; Pang, Yan; Wang, Xiang and Li, Mengqi (2017). „Micro-PIV investigation of the internal flow transitions inside droplets traveling in a rectangular microchannel“. In: *Microfluidics and Nanofluidics* 21.12, p. 180. DOI: 10.1007/s10404-017-2019-z (cit. on pp. 21, 86, 87).
- Long, J.; Ji, H.; Wang, B.; Huang, Z. and Li, H. (2012). „Online parameters measurement of Taylor flow in small channels using optical technique“. In: *Instrumentation and Measurement Technology Conference (I2MTC), 2012 IEEE International*, pp. 2322–2325. DOI: 10.1109/I2MTC.2012.6229302 (cit. on p. 25).
- Luo, Zheng Yuan; Shang, Xing Long and Bai, Bo Feng (2019). „Influence of pressure-dependent surface viscosity on dynamics of surfactant-laden drops in shear flow“. In: *Journal of Fluid Mechanics* 858, pp. 91–121. DOI: 10.1017/jfm.2018.781 (cit. on p. 51).
- Ma, Shaohua; Sherwood, Joseph M.; Huck, Wilhelm T. S. and Balabani, Stavroula (2014). „On the flow topology inside droplets moving in rectangular microchannels“. In: *Lab Chip* 14 (18), pp. 3611–3620. DOI: 10.1039/C4LC00671B (cit. on pp. 21, 86).
- Magnaudet, J. and Eames, I. (2000). „The Motion of High-Reynolds-Number Bubbles in Inhomogeneous Flows“. In: *Annual Review of Fluid Mechanics* 32.1, pp. 659–708. DOI: 10.1146/annurev.fluid.32.1.659 (cit. on pp. 10, 86).
- Magnini, M.; Pulvirenti, B. and Thome, J.R. (2013). „Numerical investigation of the influence of leading and sequential bubbles on slug flow boiling within a microchannel“. In: *International Journal of Thermal Sciences* 71, pp. 36–52. DOI: 10.1016/j.ijthermalsci.2013.04.018 (cit. on p. 11).
- Mazutis, L.; Gilbert, J.; Ung, W. L.; Griffiths, A. D. and Heyman, J. A. (2013). „Single-cell analysis and sorting using droplet-based microfluidics“. In: *Nature Protocols* 8, 870–891. DOI: 10.1038/nprot.2013.046 (cit. on p. 11).
- Meinhart, Carl D.; Wereley, Steve T. and Santiago, Juan G. (2000). „A PIV Algorithm for Estimating Time-Averaged Velocity Fields“. In: *Journal of Fluids Engineering* 122.2, p. 285. DOI: 10.1115/1.483256 (cit. on pp. 18, 54).
- Mersmann, Alfons; Voit, Harald and Zeppenfeld, Rolf (1986). „Brauchen wir Stoffaustausch-Maschinen?“. In: *Chemie Ingenieur Technik* 58.2, pp. 87–96. DOI: 10.1002/cite.330580202 (cit. on p. 1).
- Mießner, Ulrich; Lindken, Ralph and Westerweel, Jerry (2008). „Velocity Measurements in Microscopic Two-Phase Flows by Means of Micro PIV“. in: *Proceedings of the 6th International Conference on Nanochannels, Microchannels and Minichannels - 2008*. New York, NY: ASME, pp. 1111–1118. DOI: 10.1115/ICNMM2008-62093 (cit. on pp. 86, 104).
- Mießner, Ulrich; Kück, Ulf D.; Haase, Katharina, et al. (2017). „Experimental Assessment of an Innovative Device to Mimic Bubble Swarm Turbulence“. In: *Chemical Engineering & Technology* 40.8, pp. 1466–1474. DOI: 10.1002/ceat.201600688 (cit. on p. 5).
- Mießner, Ulrich; Helmers, Thorben; Lindken, Ralph and Westerweel, Jerry (2019). „An analytical interface shape approximation of microscopic Taylor flows“. In: *Experiments in Fluids* 60.4, p. 75. DOI: 10.1007/s00348-019-2719-0 (cit. on pp. 13, 19, 22, 25, 48, 58, 60–62, 64, 66, 72–75, 78, 83, 102, 107, 110, 111, 130).
- Musterd, Michiel; Steijn, Volkert van; Kleijn, Chris R. and Kreutzer, Michiel T. (2015). „Calculating the volume of elongated bubbles and droplets in microchannels from a top view image“. In: *RSC Adv.* 5 (21), pp. 16042–16049. DOI: 10.1039/C4RA15163A (cit. on pp. 49, 59, 72, 78).

- Najjari, Mohammad Reza; Hinke, Jessica A.; Bulusu, Kartik V. and Plesniak, Michael W. (2016). „On the rheology of refractive-index-matched, non-Newtonian blood-analog fluids for PIV experiments“. In: *Experiments in Fluids* 57.6, p. 1704. DOI: 10.1007/s00348-016-2185-x (cit. on pp. 22, 86).
- Nguyen, Nam-Trung; Lassemono, Sumantri and Chollet, Franck Alexis (2006). „Optical detection for droplet size control in microfluidic droplet-based analysis systems“. In: *Sensors and Actuators B: Chemical* 117.2, pp. 431–436. DOI: 10.1016/j.snb.2005.12.010 (cit. on pp. 18, 24, 28, 33).
- Ohnesorge, Wolfgang von (1936). „Die Bildung von Tropfen an Düsen und die Auflösung flüssiger Strahlen“. In: *ZAMM - Journal of Applied Mathematics and Mechanics / Zeitschrift für Angewandte Mathematik und Mechanik* 16.6, pp. 355–358. DOI: 10.1002/zamm.19360160611 (cit. on p. 12).
- Oishi, M; Kinoshita, H; Fujii, T and Oshima, M (2011). „Simultaneous measurement of internal and surrounding flows of a moving droplet using multicolour confocal micro-particle image velocimetry micro-PIV“. in: *Measurement Science and Technology* 22.10, p. 105401. DOI: 10.1088/0957-0233/22/10/105401 (cit. on p. 21).
- Olgac, Ufuk and Muradoglu, Metin (2013). „Effects of surfactant on liquid film thickness in the Bretherton problem“. In: *International Journal of Multiphase Flow* 48, pp. 58–70. DOI: 10.1016/j.ijmultiphaseflow.2012.08.007 (cit. on pp. 51, 105).
- Park, Chang-Won (1992). „Influence of soluble surfactants on the motion of a finite bubble in a capillary tube“. In: *Physics of Fluids A: Fluid Dynamics* 4.11, pp. 2335–2347. DOI: 10.1063/1.858475 (cit. on p. 51).
- Park, J. S. and Kihm, K. D. (2006). „Three-dimensional micro-PTV using deconvolution microscopy“. In: *Experiments in Fluids* 40.3, pp. 491–499. DOI: 10.1007/s00348-005-0090-9 (cit. on p. 86).
- Peng, Dongyue; Xin, Feng; Zhang, Lexiang; Yu, Huaizhe and Zhang, Weihua (2015). „Experiments and modeling on bubble uniformity of Taylor flow in T-junction microchannel“. In: *Chemical Engineering Science* 128, pp. 11–20. DOI: 10.1016/j.ces.2015.01.064 (cit. on pp. 6, 43).
- Piao, Yunxian; Han, Dong Ju; Azad, Mohammad Reza; Park, Minsu and Seo, Tae Seok (2015). „Enzyme incorporated microfluidic device for in-situ glucose detection in water-in-air microdroplets“. In: *Biosensors and Bioelectronics* 65, pp. 220–225. DOI: <https://doi.org/10.1016/j.bios.2014.10.032> (cit. on p. 11).
- Prileszky, Tamás A.; Ogunnaike, Babatunde A. and Furst, Eric M. (2016). „Statistics of droplet sizes generated by a microfluidic device“. In: *AIChE Journal* 62.8, pp. 2923–2928. DOI: 10.1002/aic.15246 (cit. on p. 11).
- Raffel, Markus; Willert, Christian E.; Scarano, Fulvio, et al. (2018). *Particle Image Velocimetry: A Practical Guide*. 3rd ed. 2018. Cham: Springer International Publishing. DOI: 10.1007/978-3-319-68852-7 (cit. on p. 19).
- Ransohoff, T.C and Radke, C.J (1988). „Laminar flow of a wetting liquid along the corners of a predominantly gas-occupied noncircular pore“. In: *Journal of Colloid and Interface Science* 121.2, pp. 392–401. DOI: 10.1016/0021-9797(88)90442-0 (cit. on pp. 74, 80).
- Rao, Sai Sashankh and Wong, Harris (2018). „The motion of long drops in rectangular microchannels at low capillary numbers“. In: *Journal of Fluid Mechanics* 852, pp. 60–104. DOI: 10.1017/jfm.2018.521 (cit. on pp. 6, 15, 22, 87, 111).
- Revellin, Rémi; Dupont, Vincent; Ursenbacher, Thierry; Thome, John R. and Zun, Iztok (2006). „Characterization of diabatic two-phase flows in microchannels: Flow parameter results for R-134a in a 0.5mm channel“. In: *International Journal of Multiphase Flow* 32.7, pp. 755–774. DOI: 10.1016/j.ijmultiphaseflow.2006.02.016 (cit. on pp. 25, 28, 33).
- Rocha, Luis A. M.; Miranda, João M. and Campos, Joao B. L. M. (2017). „Wide Range Simulation Study of Taylor Bubbles in Circular Milli and Microchannels“. In: *Micromachines* 8.5, p. 154. DOI: 10.3390/mi8050154 (cit. on pp. 11, 48, 64, 70, 72, 86).

- Rossetti, Ilenia (2018). „Continuous flow (micro-)reactors for heterogeneously catalyzed reactions: Main design and modelling issues“. In: *Catalysis Today* 308, pp. 20–31. DOI: 10.1016/j.cattod.2017.09.040 (cit. on p. 10).
- Rowe, Raymond C., ed. (2009). *Handbook of pharmaceutical excipients*. 6. ed. London: APhA (PhP) Pharmaceutical Press (cit. on p. 105).
- Saint Vincent, Matthieu Robert de; Cassagnère, Sébastien; Plantard, Joël and Delville, Jean-Pierre (2012). „Real-time droplet caliper for digital microfluidics“. In: *Microfluidics and Nanofluidics* 13.2, pp. 261–271. DOI: 10.1007/s10404-012-0955-1 (cit. on pp. 18, 24).
- Saksena, Rajat; Christensen, Kenneth T. and Pearlstein, Arne J. (2015). „Surrogate immiscible liquid pairs with refractive indexes matchable over a wide range of density and viscosity ratios“. In: *Physics of Fluids* 27.8, p. 087103. DOI: 10.1063/1.4928030 (cit. on p. 87).
- Salzberg, Calvin D. and Villa, John J. (1957). „Infrared Refractive Indexes of Silicon Germanium and Modified Selenium Glass“. In: *Journal of the Optical Society of America* 47.3, p. 244. DOI: 10.1364/JOSA.47.000244 (cit. on p. 32).
- Sattari-Najafabadi, Mehdi; Nasr Esfahany, Mohsen; Wu, Zan and Sunden, Bengt (2018). „Mass transfer between phases in microchannels: A review“. In: *Chemical Engineering and Processing - Process Intensification* 127, pp. 213–237. DOI: 10.1016/j.cep.2018.03.012 (cit. on p. 10).
- Sauzade, Martin and Cubaud, Thomas (2013). „Initial microfluidic dissolution regime of CO₂ bubbles in viscous oils“. In: *Physical review. E, Statistical, nonlinear, and soft matter physics* 88.5, p. 051001. DOI: 10.1103/PhysRevE.88.051001 (cit. on pp. 48, 59, 62).
- Schäfer, Thomas; Meitzner, Christine; Lange, Rüdiger and Hampel, Uwe (2016). „A study of two-phase flow in monoliths using ultrafast single-slice X-ray computed tomography“. In: *International Journal of Multiphase Flow* 86, pp. 56–66. DOI: 10.1016/j.ijmultiphaseflow.2016.07.008 (cit. on p. 2).
- Scheler, Ott; Postek, Witold and Garstecki, Piotr (2018). „Recent developments of microfluidics as a tool for biotechnology and microbiology“. In: *Current opinion in biotechnology* 55, pp. 60–67. DOI: 10.1016/j.copbio.2018.08.004 (cit. on p. 11).
- Schlick, Christophe (1994). „An Inexpensive BRDF Model for Physically-based Rendering“. In: *Computer Graphics Forum* 13.3, pp. 233–246. DOI: 10.1111/1467-8659.1330233 (cit. on p. 31).
- Schubert, Markus; Kost, Sebastian; Lange, Rüdiger, et al. (2016). „Maldistribution susceptibility of monolith reactors: Case study of glucose hydrogenation performance“. In: *AIChE Journal* 62.12, pp. 4346–4364. DOI: 10.1002/aic.15334 (cit. on p. 66).
- Schuirmann, Donald J. (1987). „A comparison of the Two One-Sided Tests Procedure and the Power Approach for assessing the equivalence of average bioavailability“. In: *Journal of Pharmacokinetics and Biopharmaceutics* 15.6, pp. 657–680. DOI: 10.1007/BF01068419 (cit. on p. 58).
- Schurr, Daniela; Guhathakurta, Jajnabalkya; Simon, Sven; Rinke, Günter and Dittmeyer, Roland (2017). „Characterization of a Raman Spectroscopic and Holographic System for Gas-Liquid Flows in Microchannels“. In: *Chemical Engineering & Technology* 40.8, pp. 1400–1407. DOI: 10.1002/ceat.201600622 (cit. on p. 3).
- Seeberger, P. H. and Blume, T., eds. (2007). *New Avenues to Efficient Chemical Synthesis: Emerging Technologies*. Vol. 2006/3. Ernst Schering Foundation Symposium Proceedings. Berlin, Heidelberg: Springer-Verlag Berlin Heidelberg. DOI: 10.1007/978-3-540-70849-0 (cit. on pp. 3, 10).
- Seemann, Ralf; Brinkmann, Martin; Pfohl, Thomas and Herminghaus, Stephan (2011). „Droplet based microfluidics“. In: *Reports on Progress in Physics* 75.1, p. 016601. DOI: 10.1088/0034-4885/75/1/016601 (cit. on p. 11).
- Shams, Mosayeb; Raeini, Ali Q.; Blunt, Martin J. and Bijeljic, Branko (2018). „A study to investigate viscous coupling effects on the hydraulic conductance of fluid layers in two-phase flow at the pore level“. In: *Journal of Colloid and Interface Science* 522, pp. 299–310. DOI: 10.1016/j.jcis.2018.03.028 (cit. on pp. 13, 15, 74, 80, 81).

- Shi, Huanhuan; Nie, Kaixuan; Dong, Bo, et al. (2019). „Recent progress of microfluidic reactors for biomedical applications“. In: *Chemical Engineering Journal* 361, pp. 635–650. DOI: 10.1016/j.cej.2018.12.104 (cit. on p. 10).
- Sinzato, Yuri Zeniti; Sousa Dias, Nuno Jorge and Cunha, Francisco Ricardo (2017). „An experimental investigation of the interfacial tension between liquid-liquid mixtures in the presence of surfactants“. In: *Experimental Thermal and Fluid Science* 85, pp. 370–378. DOI: 10.1016/j.expthermflusci.2017.03.011 (cit. on p. 88).
- Song, Helen; Chen, Delai L. and Ismagilov, Rustem F. (2006). „Reactions in droplets in microfluidic channels“. In: *Angewandte Chemie (International ed. in English)* 45.44, pp. 7336–7356. DOI: 10.1002/anie.200601554 (cit. on p. 10).
- Stone, H. A. and Leal, L. G. (1990). „Breakup of concentric double emulsion droplets in linear flows“. In: *Journal of Fluid Mechanics* 211.-1, p. 123. DOI: 10.1017/S0022112090001525 (cit. on pp. 48, 49).
- Sun, Bing; Jiang, Jie; Shi, Ning and Xu, Wei (2016). „Application of microfluidics technology in chemical engineering for enhanced safety“. In: *Process Safety Progress* 35.4, pp. 365–373. DOI: 10.1002/prs.11801 (cit. on p. 10).
- Taha, Taha and Cui, Z. F. (2006). „CFD modelling of slug flow inside square capillaries“. In: *Chemical Engineering Science* 61.2, pp. 665–675. DOI: 10.1016/j.ces.2005.07.023 (cit. on pp. 13, 26, 29, 30, 36, 39–41, 48, 58, 60, 61).
- Takamura, Koichi; Fischer, Herbert and Morrow, Norman R. (2012). „Physical properties of aqueous glycerol solutions“. In: *Journal of Petroleum Science and Engineering* 98-99, pp. 50–60. DOI: 10.1016/j.petrol.2012.09.003 (cit. on p. 121).
- Tanimu, Abdulkadir; Jaenicke, Stephan and Alhooshani, Khalid (2017). „Heterogeneous catalysis in continuous flow microreactors: A review of methods and applications“. In: *Chemical Engineering Journal* 327, pp. 792–821. DOI: 10.1016/j.cej.2017.06.161 (cit. on p. 10).
- van Loo, Stéphanie; Stoukatch, Serguei; Kraft, Michael and Gilet, Tristan (2016). „Droplet formation by squeezing in a microfluidic cross-junction“. In: *Microfluidics and Nanofluidics* 20.10. DOI: 10.1007/s10404-016-1807-1 (cit. on p. 16).
- van Steijn, Volkert; Kreutzer, Michiel T. and Kleijn, Chris R. (2007). „PIV study of the formation of segmented flow in microfluidic T-junctions“. In: *Chemical Engineering Science* 62.24, pp. 7505–7514. DOI: 10.1016/j.ces.2007.08.068 (cit. on p. 16).
- van Steijn, Volkert; Kreutzer, Michiel and Kleijn, Chris (2008). „Velocity fluctuations of segmented flow in microchannels“. In: *Chemical Engineering Journal* 135, S159–S165. DOI: 10.1016/j.cej.2007.07.037 (cit. on pp. 9, 79).
- Vladisavljević, Goran T.; Khalid, Nauman; Neves, Marcos A., et al. (2013). „Industrial lab-on-a-chip: Design, applications and scale-up for drug discovery and delivery“. In: *Advanced drug delivery reviews* 65.11-12, pp. 1626–1663. DOI: 10.1016/j.addr.2013.07.017 (cit. on p. 48).
- Vögele, Hans Peter and Buback, Michael (1993). *FT-NIR atlas*. A SpecBook by chemical concepts. Weinheim [u.a.]: VCH (cit. on p. 32).
- Wang, Xiaoda; Zhu, Chunying; Fu, Taotao; Qiu, Ting and Ma, Youguang (2017). „Critical condition for bubble breakup in a microfluidic flow-focusing junction“. In: *Chemical Engineering Science* 164, pp. 178–187. DOI: 10.1016/j.ces.2017.01.066 (cit. on p. 16).
- Ward, Thomas; Faivre, Magalie; Abkarian, Manouk and Stone, Howard A. (2005). „Microfluidic flow focusing: Drop size and scaling in pressure versus flow-rate-driven pumping“. In: *Electrophoresis* 26.19, pp. 3716–3724. DOI: 10.1002/elps.200500173 (cit. on p. 10).
- Weast, Robert C., ed. (1989). *CRC handbook of chemistry and physics: A ready-reference book of chemical and physical data*. 70. ed., 1989-1990. Boca Raton: CRC Press (cit. on p. 93).

- Weber, Emanuel; Puchberger-Enengl, Dietmar; Keplinger, Franz and Vellekoop, Michael J. (2014). „In-line characterization and identification of micro-droplets on-chip“. In: *Optofluidics, Microfluidics and Nanofluidics* 1.1. DOI: 10.2478/optof-2013-0002 (cit. on pp. 17, 18, 24).
- Whitesides, George M. (2006). „The origins and the future of microfluidics“. In: *Nature* 442, pp. 368–373. DOI: 10.1038/nature05058 (cit. on p. 11).
- Whitley, Darrell (1994). „A genetic algorithm tutorial“. In: *Statistics and Computing* 4.2. DOI: 10.1007/BF00175354 (cit. on p. 77).
- Wilkinson, M.C (1972). „Extended use of, and comments on, the drop-weight (drop-volume) technique for the determination of surface and interfacial tensions“. In: *Journal of Colloid and Interface Science* 40.1, pp. 14–26. DOI: 10.1016/0021-9797(72)90169-5 (cit. on pp. 88, 125).
- Wohlfarth, Ch. (2008). „Refractive index of dodecane“. In: *Refractive Indices of Pure Liquids and Binary Liquid Mixtures (Supplement to III/38)*. Ed. by M.D Lechner. Berlin, Heidelberg: Springer Berlin Heidelberg, pp. 528–530. DOI: 10.1007/978-3-540-75291-2_327 (cit. on p. 32).
- Wolf, A.; Hartmann, T.; Bertolini, M., et al. (2015). „Toward high-throughput chip calorimetry by use of segmented-flow technology“. In: *Thermochimica Acta* 603. Chip Calorimetry, pp. 172–183. DOI: 10.1016/j.tca.2014.10.021 (cit. on p. 11).
- Wong, Harris; Radke, C. J. and Morris, S. (1995). „The motion of long bubbles in polygonal capillaries. Part 2. Drag, fluid pressure and fluid flow“. In: *Journal of Fluid Mechanics* 292.-1, p. 95. DOI: 10.1017/S0022112095001455 (cit. on pp. 15, 82, 83).
- Wong, S.; Ward, M. and Wharton, C. (2004). „Micro T-mixer as a rapid mixing micromixer“. In: *Sensors and Actuators B: Chemical* 100.3, pp. 359–379. DOI: 10.1016/j.snb.2004.02.008 (cit. on pp. 10, 62, 81, 83).
- Wright, Stuart F.; Zadrazil, Ivan and Markides, Christos N. (2017). „A review of solid–fluid selection options for optical-based measurements in single-phase liquid, two-phase liquid–liquid and multiphase solid–liquid flows“. In: *Experiments in Fluids* 58.9, p. 357. DOI: 10.1007/s00348-017-2386-y (cit. on pp. 22, 86).
- Yan, Chaoxing; Yan, Changqi; Shen, Yunhai; Sun, Licheng and Wang, Yang (2014). „Evaluation analysis of correlations for predicting the void fraction and slug velocity of slug flow in an inclined narrow rectangular duct“. In: *Nuclear Engineering and Design* 273, pp. 155–164. DOI: 10.1016/j.nucengdes.2014.03.019 (cit. on p. 11).
- Yao, Chaoqun; Dong, Zhengya; Zhang, Yuchao, et al. (2015). „On the leakage flow around gas bubbles in slug flow in a microchannel“. In: *AIChE Journal* 61.11, pp. 3964–3972. DOI: 10.1002/aic.14895 (cit. on p. 16).
- Yesiloz, Gurkan; Boybay, Muhammed Said and Ren, Carolyn L. (2015). „Label-free high-throughput detection and content sensing of individual droplets in microfluidic systems“. In: *Lab on a chip* 15.20, pp. 4008–4019. DOI: 10.1039/c5lc00314h (cit. on p. 17).
- Yue, Jun; Falke, Floris H.; Schouten, Jaap C. and Nijhuis, T. Alexander (2013). „Microreactors with integrated UV/Vis spectroscopic detection for online process analysis under segmented flow“. In: *Lab on a chip* 13.24, pp. 4855–4863. DOI: 10.1039/c3lc50876e (cit. on p. 17).
- Yusuf, Ahmed; Garlisi, Corrado and Palmisano, Giovanni (2018). „Overview on microfluidic reactors in photocatalysis: Applications of graphene derivatives“. In: *Catalysis Today* 315, pp. 79–92. DOI: 10.1016/j.cattod.2018.05.041 (cit. on p. 10).
- Zeng, Wen; Jacobi, Ian; Li, Songjing and Stone, Howard A. (2015a). „Variation in polydispersity in pump- and pressure-driven micro-droplet generators“. In: *Journal of Micromechanics and Microengineering* 25.11, p. 115015. DOI: 10.1088/0960-1317/25/11/115015 (cit. on p. 6).
- Zeng, Wen; Jacobi, Ian; Li, Songjing and Stone, Howard (2015b). „Variation in polydispersity in pump- and pressure-driven micro-droplet generators“. In: *Journal of Micromechanics and Microengineering* 25.11, p. 115015. DOI: 10.1088/0960-1317/25/11/115015 (cit. on p. 43).

Zhao, Chun-Xia and Middelberg, Anton P.J. (2011). „Two-phase microfluidic flows“. In: *Chemical Engineering Science* 66.7, pp. 1394–1411. DOI: 10.1016/j.ces.2010.08.038 (cit. on p. 10).

Zhou, Chunfeng; Yue, Pengtao and Feng, James J. (2006). „Formation of simple and compound drops in microfluidic devices“. In: *Physics of Fluids* 18.9, p. 92105. DOI: 10.1063/1.2353116 (cit. on p. 16).

Online resources

Company, Sinclair Manufacturing (2016). *Technical Data, optical transmission curves*. URL: <http://www.sinclairmfg.com/datasheets/optical3.html> (visited on Aug. 31, 16) (cit. on p. 32).

Jedamzik, Ralf (2007). *SCHOTT Technical Information: TIE-43 Optical properties of Zerodur*. URL: http://refractiveindex.info/download/data/2007/schott_tie-43_optical_properties_of_zerodur_november_2007_us.pdf (visited on Jan. 30, 17) (cit. on p. 32).

Lau, Birgit (2015). *BASF and top universities jointly develop new process improving the bioavailability of active ingredients*. URL: <https://www.basf.com/global/de/media/news-releases/2015/09/p-15-332.html> (visited on May 10, 2019) (cit. on p. 4).

Lineberry, Denise (2013). *NASA Langley Wins 2012 Commercial Invention of the Year*. URL: https://www.nasa.gov/centers/langley/news/researchernews/rn_2012InventionAward.html (visited on May 9, 19) (cit. on p. 3).

Zeiss, Carl (1995). *LSM 410 invert Laser Scan Microscope (Operating manual)*. URL: <http://www.its.caltech.edu/~bi227/2016/Private/LSM410.Operating.Manual.Full.pdf> (visited on May 10, 19) (cit. on p. 103).

List of Symbols

The following symbols have been used in this thesis. Usually states or origins of the corresponding data is visualized via superscript. Subscript, however, give further information or details on the specified quantity. Symbol above the quantity show mathematical operations like averaging or filtered values.

Acronyms

μ PIV	particle image velocimetry
μ PTV	particle tracking velocimetry
AOT	dioctyl sulfosuccinate sodium
CCD	charge-coupled device sensor
CFD	computational fluid dynamics
CMC	critical micelle concentration
COTS	commercial off-the-shelf
DMSO	dimethyl sulfoxide
DOC	depth of correlation
DOF	depth of field
GA	Genetic Algorithm
HLB	hydrophilic-lipophilic balance
IWS	interrogation windows size
NA	numerical aperture
NIR	near infrared radiation
PDMS	polydimethylsiloxane
PSA	pattern search algorithm

RI	refractive index
RIM	refractive index matching
RMSE	root mean square error
SDS	sodium dodecyl sulfate
TOST	two one-sided tests procedure

Dimensionless Quantities

λ	Viscosity ratio [-]
Bo	Bond number [-]
Ca	Capillary number [-]
Mo	Morton number [-]
Oh	Ohnesorge number [-]
Re	Reynolds number [-]

Greek Symbols

α	opening angle [°]
β	geometric coefficient of resistance [-]
Δ	interval Border [-]
δ	wall film thickness [μm]
ϵ	numerical error
ϵ	spatial calibration factor [$\mu m \cdot px^{-1}$]
ϵ	spectral absorption coefficient [$m^2 \cdot mol^{-1}$]
η	dynamic viscosity [$Pa \cdot s$]
Γ	control surface [-]
Λ	linearized function
λ	Lagrange multiplier for linearization [-]
λ	light wavelength [nm]
Ω	flow resistance [$Pa \cdot s \cdot m^{-3}$]
ω	weight factor [-]
ψ	dimensionless validation function [-]

ρ	density [$kg \cdot m^{-3}$]
σ	interfacial tension [$N \cdot m^{-1}$]
θ	lightray angle from vertical [$^\circ$]
ε	significance level for TOST-Test [–]
ε	void fraction of disperse phase [–]
ξ	mass-fraction [–]
k	pure substance absorption coefficient [m^{-1}]

Roman Symbols

\mathcal{O}	Order [–]
A	correlation factor [–]
A	cross sectional area [mm^2]
a	Rear cap geometry factor [–]
a	semi-major axis of ellipse [μm]
ar	aspect ratio [–]
b	axial cap length [μm]
b	semi-minor axis of ellipse [μm]
c	fitting coefficient [–]
c	radial cap length [μm]
d	characteristic length [m]
d	diameter [mm]
DF	degree of freedom [–]
dI	infinitesimal intensity change [mV]
dt	infinitesimal time change [s]
dx	infinitesimal spatial change [μm]
g	gravitational acceleration [$mm s^{-1}$]
H	channel height [μm]
h	droplet height [μm]
h	test hypothesis [–]

I	image intensity [-]
I	photometric intensity [mV]
i	index [-]
k	curvature ratio [-]
k	dimensionless ratio [-]
l	length [μm]
m	fitting coefficient [-]
N	total number of images [-]
n	fitting coefficient [-]
n	refractive index
Q	volume flow rate [$\mu l \cdot min^{-1}$]
q	fit factor for material properties [-]
R	Pearson correlation coefficient [-]
R	general reflection coefficient
R	radius [μm]
RI	Refractive index [-]
t	image acquisition time [ms]
u	velocity [$mm \cdot s^{-1}$]
W	channel width [μm]
x	cap length till gutter entrance [μm]
x	x coordinate [px]
y	y coordinate [px]
Z	Z value [-]

Superscripts

* sum value

+ dimensionless

\mathcal{M} model calibration data

CAM highspeed camera recorded

<i>corr</i>	corrected value
<i>init</i>	initial value
<i>meas</i>	measurement data
<i>mod</i>	model results
<i>NIR</i>	acquired by NIR-sensor
<i>rel</i>	relative
<i>stat</i>	stationary

Subscripts

0	superficial
1	inciding lightray or medium 1
1, 2, 3	order of correlation factor
2	refracted lightray or medium 2
β	concerning resistance factor
η	concerning viscosity
λ	at a specific wavelength λ
ρ	concerning density
σ	concerning interfacial tension
<i>a</i>	alternative [–]
<i>ap</i>	aperture
<i>b</i>	droplet rear
<i>c</i>	continuous phase
<i>c</i>	critical
<i>c, b</i>	back droplet cap
<i>c, f</i>	front droplet cap
<i>c, i</i>	front or back droplet cap
<i>cap</i>	capillary
<i>cap</i>	concerning droplet cap curvature
<i>ch</i>	channel

crit critical value

d disperse/droplet phase

drop droplet

ell, M center point of fitted ellipse

ex excess scale concept

ex excitation [–]

f droplet front

f wall film

g gutter

g, b gutter at back of droplet

g, f gutter at front of droplet

g, i i-th droplet gutter

imag, 1 in first image

imag, 2 in second image

LED concerning the LED

lower lower

n nonpolar phase

p point at measured ellipse

p polar phase

photo photodiode

px pixel value

rel relative value

s slug

shift value for image shifting

slip slipping scale concept

t temporal

tot total

tr tracer particle

upper upper

x spatial

Other Symbols

$\hat{}$ filtered value

$\overline{\overline{}}$ area averaged value

\sim stdev. of value

Colophon

This thesis was typeset with \LaTeX using *TeXstudio* environment and the *TeX Live* distribution. Diagrams were created using *MATLAB* and converted to *.eps via "export_fig"-toolbox. Schemes and drawing were mostly done in *Adobe Illustrator* and *Inkscape*. No droplets were harmed in the making of this thesis. The thesis uses the *Clean Thesis* style developed by Ricardo Langner. The design of the *Clean Thesis* style is inspired by user guide documents from Apple Inc.

Download the *Clean Thesis* style at <http://cleanthesis.der-ric.de/>.

Declaration

I declare, that the work was carried out without any unauthorized third party assistance, no other sources or aids than the ones specified have been used and those works/text passages which have been included word by word or by content accordingly from other sources have been indicated.

Bremen, Germany, 13.05.2019



Thorben Helmers, M.Sc.

